NATIONAL KAPODISTRIAN UNIVERSITY OF ATHENS

DEPARTMENT OF PHYSICS

DOCTORAL DISSERTATION

Study of Aerosol, Trace Gases and Water Vapour optical properties, using spectral measurements of solar irradiance

Raptis Ioannis Panagiotis

Physicist

M.Sc. Environmental Physics

Athens 2018

ΕΘΝΙΚΟ ΚΑΠΟΔΙΣΤΡΙΑΚΟ ΠΑΝΕΠΙΣΤΗΜΙΟ ΑΘΗΝΩΝ

ΤΜΗΜΑ ΦΥΣΙΚΗΣ

ΔΙΔΑΚΤΟΡΙΚΗ ΔΙΑΤΡΙΒΗ

Μελέτη των οπτικών ιδιοτήτων αερολυμάτων, αέριων ρύπων και υδρατμών με την χρήση φασματικών μετρήσεων ηλιακής ακτινοβολίας

Ράπτης Ιωάννης Παναγιώτης

Φυσικός

M.Sc. Φυσική Περιβάλλοντος

Αθήνα 2018

Supervising Committee

Professor Emeritus **C. Helmis** (University of Athens)

Senior Researcher **S. Kazadzis** (National Observatory of Athens, Physicalisch Meteorologisches Observatorium Davos, World Radiation Center)

Research Director **E. Gerasopoulos** (National Observatory of Athens)

Examination Committee

Associate Professor, **Deligiorgi D.**(University of Athens)

Associate Professor , **Flocas H.** (University of Athens)

Research Director **Gerasopoulos E.** (National Observatory of Athens)

Senior Researcher , **Gröbner J.**, (Head of WRC IRS, WORCC and WCC-UV Sections, Physicalisch Meteorologisches Observatorium Davos, World Radiation Center)

Professor Emeritus **Helmis C.** (University of Athens)

Senior Researcher **Kazadzis S.** (National Observatory of Athens, Physicalisch Meteorologisches Observatorium Davos, World Radiation Center)

Professor , **Tombrou – Tzella M.** (University of Athens)

And the ground's not cold
And if the ground's not cold
Everything is gonna burn
We'll all take turns, I'll get mine too
This monkey's gone to Heaven
Pixies, Doolitle, 1989

Now, nothing in the Sky looks the same
Thomas Pynchon, Mason & Dixon, 1997

We're not scaremongering
This is really happening
Radiohead, Kid A, 2000

We are stuck because the actions that would give us the best chance of averting catastrophe—and would benefit the vast majority—are extremely threatening to an elite minority that has a stranglehold over our economy, our political process, and most of our major media outlets. It is our great collective misfortune that the scientific community made its decisive diagnosis of the climate threat at the precise moment when those elites were enjoying more unfettered political, cultural, and intellectual power than at any point since the 1920s.
Naomi Klein, This changes everything, 2014

Cover image is Altrarpiece no 1, Group X, 1915 by Hilma af Klint

PREFACE – ACKNOWLEDGMENTS

The current dissertation was conducted at National Observatory of Athens and Physikalisch-Meteorologisches Observatorium Davos/World Radiation Center. The subject of the dissertation was recommended to me by Professor C. Helmis and Senior Researcher S. Kazadzis, both of whom I would like to express my sincere gratitude for trusting, supporting and helping me throughout the entire period of the study. Without their unceasing advising and support, the completion of the present study would have been impossible. Especially S. Kazadzis support me in every possible way, but first has been a constant source of learning, motivation and improvement. His elegant guidance throughout the process made this thesis flow in a smooth manner. Additionally, his ahead planning not only facilitated my work but also equipped me with a lot of supplies for the future. Also, Professor C. Helmis uphold me in difficult conditions, despite all the obstacles in the way, from my first years as an undergraduate student until today. I would also like to acknowledge research director E. Gerasopoulos, member of my advisor committee, for his scientific guidance and advices throughout the years.

Programs that funded my work should be acknowledged , including 'Development Proposals of Research Entities – KRIPIS', which is funded by N.P. 'Competitiveness and Entrepreneurship', Action: 'THESPIA – Development of synergistic and integrated methods and tools for monitoring, management and forecasting of Environmental parameters and pressures', the project 'Aristotelis-SOLAR (50561), Investgation on the factors affecting the solar radiation field in Greece', the H2020 GEO-CRADLE project under grant agreement No 690133 and ACTRIS-2, which has received funding from EU H2020 research and innovation programme (grant agreement No 654109).

In addition, I would like to acknowledge all the tutors at the University of Athens, that taught me the Atmospheric Science and made me eager to go deeper into the research field, associate professors D.Deligiorgi, H. Flocas and M. Tombrou as former professors C. Iakovides and G. Papaioannou. Also, during the period I was working at PMOD/WRC at Davos, guidance and consulting from Dr. Gröbner boosted and enhanced my work. Furthermore, I would like to thank research director V. Amiridis and assistant professor K. Eleftheratos for their advices and help whenever I asked for it. Special thanks to scienists that collaborated for specific issues including Dr. A. Redondas, Dr. A. Arola, Dr. L. Doppler , Dr R. Becker and Dr. A. Cede. In the context of my PhD study I collaborated with several people who contributed in order to complete this work and I am specially thankful to my friends

Dr. P. Kokkalis, Dr. E. Flaounas, Dr. N.Kouremeti and Dr A. Tsekeri for the numerous hours that we spent discussing scientific issues, for helping me in the laboratory and campaigns and for their personal time they spent in my support. Also, I would like to thank Dr. P. Kosmopoulos and Dr. M. Taylor for their collaboration in several issues and their help with the radiative transfer models.

Taking this opportunity, I would also like to express my gratitude to my long gone family, for their sacrifices and their unceasing encouragement and support during my studies and my grief for them not being present at the end of the road. Additionally, I would like to thank express my deepest gratitude to all my friends that stood by me during the difficult recent years and really act like a family to me. Finally, I want to express my gratefulness to Ioanna for her love and support, her endless patience and understanding, and specially for her tolerance and sacrifices while I moved to Switzerland.

Abstract

The subject of the thesis is to study and develop methods for retrieving optical and physical properties of atmospheric components using spectral solar irradiance measurements, while goals of the present thesis is to develop methods to enhance the accuracy of available data of atmospheric variables.

In particular, a method to retrieve Total Ozone Column from Ultraviolet Multifilter Radiometer (UVMFR) measurements was developed, which was applied to a 5 years dataset and was compared with Brewer and satellite retrievals. Enhancement of the method is the quantification of stratospheric temperature and aerosols influence on the retrieval. Also, it is crucial for monitoring purposes that the retrieval was stable throughout the 5 years period. Additionally, the influence of stratospheric temperature and AOD to the retrieved values was investigated and corrections to the retrieved product were applied accordingly. The validation of TOC retrieved with this method compared with state of the art ground based and satellite based TOC retrievals showed good results towards its use in long term or case studies concerning TOC.

Two approaches were used to retrieve Integrated Water Vapour (IWV) from a Precision Solar Spectroradiometer (PSR). The first method was monochromatic, following the approach used in many filter radiometers, and was tested against other retrievals (CIMEL, GPS, MWP, radiosondes) and was found that 946 nm channel provides the most reliable results. The second method was an enhancement, benefiting from the dense spectral recording of PSR, using a spectral window of 934-948 nm to retrieve IWV. This method provided less varied retrievals with better agreement to reference methods.

Also, a method for retrieving Single Scattering Albedo (SSA) in UV wavelengths was developed and applied on 5 years dataset. Retrievals from a collocated CIMEL sun photometer were used to evaluate the products and Study the spectral dependence of aerosol absorption. Strong SSA wavelength dependence is revealed for cases of low Ångström exponents, accompanied by a SSA decrease with decreasing extinction optical depth, suggesting varying influence under different aerosol composition. However, part of this dependence for low aerosol optical depths is masked by the enhanced SSA retrieval uncertainty. Dust and brown carbon UV absorbing properties were also investigated to explain seasonal patterns.

Finally, UV irradiance was calculated and compared using different SSA datasets retrieved at Athens, Greece during 2009-2014; including SSA timeseries

from UVMFR at 332 and 368 nm, SSA from AERONET at 440 nm, from OMI satellite at 342.5 nm and AeroCom climatological database at 300 nm. Irradiances were estimated using a Radiative Transfer Model (RTM). UVA and UVB were estimated and found that using UVFMR retrieved SSA and AOD leads to significant drops. Performance of the modeled data was evaluated using Brewer measurements at 324 nm.

Summarizing, this thesis deals with the improvement of knowledge and retrieval of atmospheric constituents that affect spectrally the Earth – Atmosphere radiative balance such as the total column ozone, the integrated water vapour and the columnar absorption properties of aerosols. For the case of TOC it provides evidence on the validity of a simple method that can be used by filter instruments and can contribute to the enhancement of the TOC measurement stations density worldwide. For IWV a new method is proposed using the advantage of spectral direct sun measurements and for the case of aerosols it contributes to a scientifically open aspect dealing with the SSA columnar retrieval in the UV region.

Περίληψη

Θέμα της παρούσας διατριβής είναι η μελέτη των ατμοσφαιρικών στοιχείων και η ανάπτυξη μεθόδων για τον υπολογισμό φυσικών και οπτικών ιδιοτήτων τους, χρησιμοποιώντας φασματικές μετρήσεις της ηλιακής ακτινοβολίας. Στόχος της μελέτης είναι η ανάπτυξη μεθόδων για την βελτιστοποίηση της ακρίβειας των δεδομένων ατμοσφαιρικών μεταβλητών.

Συγκεκριμένα, αναπτύχθηκε μέθοδος για τον υπολογισμό της κατακόρυφης στήλης όζοντος από τις μετρήσεις του οργάνου UVMFR κι εφαρμόστηκε σε δεδομένα 5 ετών, τα οποία συγκρίθηκαν με μετρήσεις από το όργανο Brewer και από δορυφόρο. Η βελτίωση της μεθόδου περιλαμβάνει την ποσοτικοποίηση της επιρροής στον υπολογισμό, τόσο της στρατοσφαιρικής θερμοκρασίας όσο και του οπτικού βάθους αερολυμάτων. Σημαντική για την χρήση της μεθόδου ήταν η σταθερότητα που έδειξαν τα αποτελέσματα σε μια χρονοσειρά 5 ετών. Η διακρίβωση της κατακόρυφης στήλης όζοντος που υπολογίστηκε με αυτή την μέθοδο, συγκρίθηκε με μετρήσεις από επίγεια και δορυφορικά όργανα πρωτοποριακής τεχνολογίας και τα αποτελέσματα κατέδειξαν ικανοποιητική συμφωνία. Επίσης τα αποτελέσματα είχαν σταθερή ποιότητα σε όλη την χρονοσειρά, υποδεικνύοντας την δυνατότητα μακροπρόθεσμης χρήσης της μεθόδου.

Δυο προσεγγίσεις χρησιμοποιήθηκαν για τον υπολογισμό της στήλης υδρατμών από μετρήσεις PSR. Η πρώτη μέθοδος ήταν μονοχρωματική, ακολουθώντας την προσέγγιση που χρησιμοποιείται στα ραδιόμετρα φίλτρων. Τα αποτελέσματα της συγκρίθηκαν με άλλα δεδομένα (από CIMEL, GPS, MWP, ραδιοβολίσεις) και βρέθηκε ότι το κανάλι των 946nm παρουσιάζει τα πιο αξιόπιστα αποτελέσματα. Η δεύτερη μέθοδος εκμεταλλεύεται την φασματική ανάλυση του οργάνου και υπολογίζει την στήλη υδρατμών χρησιμοποιώντας το φασματικό παράθυρο 934-948nm.

Επίσης, αναπτύχθηκε μέθοδος για τον υπολογισμό της λευκαύγειας μονής σκέδασης στα υπεριώδη μήκη κύματος και εφαρμόστηκε σε μια πενταετή βάση δεδομένων. Δεδομένα από φωτόμετρο CIMEL χρησιμοποιήθηκαν για την αξιολόγηση των αποτελεσμάτων και την μελέτη της φασματικής συμπεριφοράς των απορροφητικών σωματιδίων. Σημαντική φασματική εξάρτηση παρατηρήθηκε στις περιπτώσεις με χαμηλό εκθέτη Ångström, συνοδευόμενα με μείωση της λευκαύγειας μονής σκέδασης και με την μείωση του οπτικού βάθους αερολυμάτων, καταδεικνύοντας την συσχέτιση με τη σύνθεση των αερολυμάτων. Σημαντικό είναι το γεγονός ότι μέρος της φασματικής διακύμανσης δεν μπορεί να προσδιοριστεί εξαιτίας της αβεβαιότητας υπολογισμού της λευκαύγειας μονής σκέδασης. Οι απορροφητικές ιδιότητες στο υπεριώδες της σκόνης και του καφέ άνθρακα ερευνήθηκαν για να εξηγηθούν οι εποχικές διακυμάνσεις.

Τέλος, η υπεριώδης ακτινοβολία υπολογίστηκε και συγκρίθηκε, χρησιμοποιώντας διαφορετικές βάσεις δεδομένων για την λευκαύγεια μονής σκέδασης, για την Αθήνα την περίοδο 2009-2014. Χρησιμοποιήθηκαν δεδομένα από UVMFR, AERONET, AEROCOM και OMI. Η ακτινοβολία εκτιμήθηκε με την χρήση μοντέλου διάδοσης ακτινοβολίας. Οι ακτινοβολίες UVA και UVB υπολογίστηκαν και βρέθηκε ότι χρησιμοποιώντας τα δεδομένα από το UVFMR υπάρχει σημαντική μείωση. Οι επιδόσεις των υπολογισμών του μοντέλου αξιολογήθηκαν με μετρήσεις από Brewer στα 324nm.

Συνοψίζοντας, η παρούσα διατριβή συνεισφέρει στην βελτίωση των κατανόησης και στον υπολογισμό ατμοσφαιρικών συστατικών που επηρεάζουν το φασματικό ισοζύγιο ακτινοβολιών του συστήματος Γη- Ατμόσφαιρα, όπως η στήλη του όζοντος, η στήλη υδρατμών και οι απορροφητικές ιδιότητες των αερολυμάτων. Για την περίπτωση της στήλης όζοντος, παρέχει ενδείξεις για την εγκυρότητα μιας σχετικά απλής μεθόδου που μπορεί να χρησιμοποιηθεί από φωτόμετρο φίλτρου και να συνεισφέρει στην αύξηση της παγκόσμιας επίγειας καταγραφής της μεταβλητής. Η μέθοδος που προτείνεται σχετικά με τους υδρατμούς, εκμεταλλεύεται την τεχνολογική πρόοδο των φασματικών μετρήσεων της ηλιακής ακτινοβολίας. Τέλος σε σχέση με τα αερολύματα υπάρχει σημαντική συνεισφορά στο ανοιχτό επιστημονικό ερώτημα της λευκαύγειας μονής σκέδασης στην υπεριώδη περιοχή του ηλιακού φάσματος.

Εκτεταμένη Περίληψη

Η πρόοδος της επιστήμης της φυσικής της ατμόσφαιρας βασίζεται στην εξέλιξη των επιστημονικών οργάνων και μεθόδων που οδηγεί στη βελτίωση των μετρήσεων των ατμοσφαιρικών συστατικών, οδηγώντας στην κατανόηση των διεργασιών. Η παρατήρηση των ατμοσφαιρικών παραμέτρων είναι πιο έντονη από ποτέ, καθώς οι επίγειες μετρήσεις στον πλανήτη πολλαπλασιάζονται συνεχώς και πραγματοποιούνται με μεγαλύτερη ακρίβεια και οι παρατηρήσεις από δορυφόρους αυξάνονται και βελτιώνονται ποιοτικά και χωρικά με κάθε καινούργια αποστολή. Μια σειρά από ανοιχτά ζητήματα συνεχίζουν να υπάρχουν σε σχέση με την διαθεσιμότητα και την ακρίβεια των μετρούμενων δεδομένων, τα οποία ενίοτε μπορεί να οδηγούν σε εσφαλμένη εκτίμηση της κατάστασης της ατμοσφαίρας και συνοψίζονται στις εκθέσεις της Διακυβερνητικής Επιτροπής για την Αλλαγή του Κλίματος (Intergovernmental Panel on Climate Change- IPCC). Για παράδειγμα, η συνολική συνεισφορά των ανθρωπογενών αερολυμάτων στο ισοζύγιο ακτινοβολιών είναι πλήρως κατανοητή από φυσικής άποψης, αλλά παραμένει ελλιπής η ποσοτικοποίηση της σε παγκόσμια κλίμακα. Βασική πηγή αυτής της απροσδιοριστίας είναι η εκτίμηση των απορροφητικών ιδιοτήτων και των σκεδαστικών χαρακτηριστικών των αερολυμάτων, σε όλες τις περιοχές του φάσματος (IPCC, 2013). Η μελέτη των αλλαγών της στήλης του όζοντος παγκοσμίως υστερεί, λόγω της μη ομογενούς και πυκνής γεωγραφικής κάλυψης των επίγειων σταθμών, καθώς οι περισσότεροι σταθμοί μέτρησης βρίσκονται στα μεσαία γεωγραφικά πλάτη του βορείου ημισφαιρίου (UNEP, 2010). Η πρόγνωση των ατμοσφαιρικών μεταβλητών που σχετίζονται με την υπεριώδη ακτινοβολία και των επιπτώσεων στην υγεία, απαιτούν ακόμη μια λεπτομερή και ακριβή γνώση των οπτικών ιδιοτήτων των αερολυμάτων (Blumthaler, 2018). Εκτός από το οπτικό βάθος αερολυμάτων, που είναι η πιο σημαντική οπτική ιδιότητα για αυτές τις εφαρμογές, το ποσοστό απορρόφησης/σκέδασης των αερολυμάτων σε σχέση την ολική εξασθένιση της ηλιακής υπεριώδους ακτινοβολίας παίζει έναν υπολογίσιμο ρόλο στο τελικό αποτέλεσμα. Αυτά τα ζητήματα αποτέλεσαν κίνητρο για αυτή τη διατριβή, που προσπαθεί να συμβάλλει στην βελτιστοποίηση των μεθόδων υπολογισμού των οπτικών παραμέτρων των ατμοσφαιρικών συστατικών με τελευταίας τεχνολογίας φασματικές μετρήσεις του ηλιακού φάσματος.

Με βάση τα παραπάνω, η παρούσα διατριβή επικεντρώθηκε στα εξής:

- Την μέτρηση της ολικής στήλης όζοντος με την χρήση δεδομένων UV από το όργανο UVMFR. Για την βελτιστοποίηση της ακριβείας των μετρούμενων τιμών πραγματοποιήθηκε έλεγχος της ευαισθησίας της μεθόδου σε σχέση με τα αερολύματα και στην θερμοκρασία της στρατόσφαιρας.

- Την ανάπτυξη μεθόδου για την μέτρηση της ολικής στήλης υδρατμών με την χρήση του φασματοφωτόμετρου PSR. Η μέθοδος εκμεταλλεύεται τις πυκνές φασματικές μετρήσεις του οργάνου, ώστε να προσδιορίσει τους υδρατμούς με μεγαλύτερη ακρίβεια από τις μεθόδους που χρησιμοποιούν φωτόμετρα με φίλτρα (σε ένα μήκος κύματος).

- Την ανάπτυξη μεθόδου για τον υπολογισμό της λευκαύγειας μονής σκέδασης των ατμοσφαιρικών αερολυμάτων στην υπεριώδη περιοχή του ηλιακού φάσματος. Η μέθοδος χρησιμοποιεί συνδυασμό μετρήσεων ολικής και απευθείας ηλιακής ακτινοβολίας στην υπεριώδη περιοχή από το όργανο UVMFR.

- Την μελέτη της επίδρασης του τύπου των αερολυμάτων στη φασματική εξάρτηση της υπεριώδους ακτινοβολίας από τα αερολύματα αυτά. Ο χαρακτηρισμός των αερολυμάτων πραγματοποιήθηκε με την λευκαύγεια μονής σκέδασης σε υπεριώδη μήκη κύματος και η εκτίμηση εφαρμόστηκε σε δεδομένα 5 χρόνων από την Αθήνα.

Τα σημαντικότερα ευρήματα της παρούσας διδακτορικής διατριβής μπορούν να συνοψιστούν στα εξής:

- Η μέθοδος για την μέτρηση ολικής στήλης όζοντος με το όργανο UVMFR εφαρμόστηκε σε χρονοσειρά 5 ετών στην Αθήνα και έγινε σύγκριση με τις αντίστοιχες μετρήσεις από το όργανο Brewer και από αυτές του οργάνου OMI στο δορυφόρο AURA. Σε σχέση με τις μετρήσεις του Brewer βρέθηκε συντελεστής συσχέτισης 98%. Σε σχέση με τις δορυφορικές μετρήσεις OMI βρέθηκαν διαφορές της τάξης του ±3%, με μεγαλύτερες διαφορές τους καλοκαιρινούς μήνες

Επιβεβαιώθηκε ότι τα λάθη στον υπολογισμό του οπτικού βάθους αερολυμάτων (AOD) συνεισφέρει σφάλμα 1 DU για κάθε 0.1 AOD, στον υπολογισμό της στήλης του όζοντος. Επίσης χρησιμοποιώντας του συντελεστές απορρόφησης των Bass-Paur για τον υπολογισμό της στήλης, υπολογίστηκε ότι διαδίδεται επιπρόσθετο σφάλμα 0.5% κατά τον υπολογισμό της στήλης για απόκλιση ενός ˚K στην θερμοκρασία της στρατόσφαιρας.

- Για την περιοχή της Αθήνας παρατηρήθηκε ημερήσια διακύμανση των τιμών του όζοντος με μέγιστα τις απογευματινές ώρες η οποία συνδέεται με τον ημερήσιο κύκλο του τροποσφαρικού όζοντος.

- Δυο διαφορετικές μέθοδοι αναπτύχθηκαν για την μέτρηση της ολικής στήλης υδρατμών με το φασματοφωτόμετρο PSR, η πρώτη με την χρήση μόνο των μετρήσεων

στο μήκος κύματος 946nm, και η δεύτερη χρησιμοποιώντας το ολοκλήρωμα της ακτινοβολίας στα φασματική περιοχή 934-948 nm, η οποία ορίστηκε ύστερα από έρευνα ευαισθησίας της απορρόφησης σε διαφορετικά φασματικά παράθυρα. Πραγματοποιήθηκε σύγκριση των δύο μεθόδων με τις μετρήσεις από το φωτόμετρο CIMEL, το ραδιόμετρο μικροκυμάτων MWP, το δορυφορικό σύστημα GPS και από ραδιοβολίσεις. Με την μονοχρωματική προσέγγιση οι μέσες σχετικές διαφορές με τα άλλα όργανα ήταν μέχρι 3.3%, με R2 μεταξύ 0.87 και 0.95. Για την φασματική προσέγγιση οι μέσες σχετικές διαφορές βρέθηκαν μέχρι 0.75 και το R2 μεταξύ 0.96 και 0.98.

- Η αβεβαιότητα και για τις δύο μεθόδους βρέθηκε μέχρι 0.28 cm υδρατμών.

- Σε απόλυτες τιμές οι διαφορές των μετρήσεων του PSR σε σχέση με τα υπόλοιπα όργανα βρέθηκαν ανάμεσα σε 0.08 και 0.30 cm υδρατμών και σε ακραίες περιπτώσεις έφτασαν το 15%.

- Υπολογίστηκε η λευκαύγεια μονής σκέδασης αερολυμάτων στα 332 και 368 nm, χρησιμοποιώντας 5 χρόνια μετρήσεων UVMFR στην Αθήνα με την χρήση μοντέλου διάδοσης ακτινοβολίας. Η αξιολόγηση των αποτελεσμάτων έγινε με την χρήση των μετρήσεων στα 440nm του φωτόμετρου CIMEL που ήταν εγκατεστημένο στο ίδιο σημείο.

- Για όλη την υπό μελέτη περίοδο οι μέσες τιμές της λευκαύγειας μονής σκέδασης αερολυμάτων ήταν 0.83, 0.87 και 0.90 στα μήκη κύματος 332, 368 και 440nm αντίστοιχα. Η ημερήσια διακύμανση του συντελεστή ήταν περίπου 0.05 για όλα τα μήκη κύματος.

- Στις περιπτώσεις με χαμηλό εκθέτη Ångström, η φασματική διακύμανση της λευκαύγειας μονής σκέδασης ήταν πολύ μεγαλύτερη, με μείωση της στο υπεριώδες, εμφανίζοντας διαφορετική συμπεριφορά αναλόγως τον τύπο των αερολυμάτων. Οι περιπτώσεις αυτές συνδέθηκαν με επεισόδια σκόνης στην περιοχή.

- Ελάχιστες τιμές της λευκαύγειας μονής σκέδασης υπολογίστηκαν για τον μήνα Φεβρουάριο και συσχετίστηκαν με την έντονη παρουσία σωματιδίων καφέ άνθρακα στην περιοχή.

- Η λευκαύγεια μονής σκέδασης στα 332 και 368 nm, μπορεί να υπολογισθεί με αβεβαιότητα ±0.03 για ηλιακές ζενίθιες γωνίες πάνω από 40° και με αβεβαιότητα ±0.04 για όλες τις γωνίες εφόσον το οπτικό βάθος αερολυμάτων στα 368 nm είναι πάνω από 0.2.

- Εκτιμήθηκε η εξασθένιση της υπεριώδους ακτινοβολίας για την Αθήνα με την χρήση των παραπάνω αποτελεσμάτων και αφού συνδυάστηκαν με μετρήσεις και

μοντέλο διάδοσης ακτινοβολίας. Παρατηρήθηκαν διαφορές έως 20% στην εκτίμηση των ακτινοβολιών UVA και UVB όταν δεν λήφθηκε υπόψιν η φασματική εξάρτηση των οπτικών ιδιοτήτων απορρόφησης των αερολυμάτων. Χρησιμοποιήθηκε η λευκαύγεια μονής σκέδασης από ορατά μήκη κύματος αντί της αντίστοιχης στο υπεριώδες και οι μέσες σχετικές διαφορές βρέθηκαν 2% και 8.7% αντίστοιχα για τις ακτινοβολίες UVA και UVB.

- Η χρήση κλιματολογικών τιμών της λευκαύγειας μόνης σκέδασης από την βάση δεδομένων AEROCOM στα 300 nm, για τον υπολογισμό της υπεριώδους ακτινοβολίας, οδήγησε σε μέση σχετική διαφορά 5.7% σε σχέση με τον υπολογισμό από μετρήσεις UVMFR.

- Οι ακτινοβολίες UVA και UVB μειώνονται κατά 12% για κάθε αλλαγή 0.05 στο οπτικό βάθος απορροφητικών αερολυμάτων, σε σχέση με την εκτίμηση εφόσον χρησιμοποιηθούν οι οπτικές ιδιότητες αερολυμάτων στο ορατό φάσμα.

- Συγκρίθηκε η εκτίμηση της ακτινοβολίας στα 324 nm από το μοντέλο διάδοσης ακτινοβολίας με τις μετρήσεις από το Brewer. Η καλύτερη συμφωνία βρέθηκε όταν χρησιμοποιήθηκαν οι τιμές από το UVMFR, όταν και οι μέσες σχετικές διαφορές ήταν 0.86%. Όταν χρησιμοποιήθηκαν κλιματολογικές τιμές ή μετρήσεις από το ορατό οι αντίστοιχες σχετικές διαφορές βρέθηκαν 4.91% και 4.15%.

Table of Contents

1.Introduction

Atmospheric sciences rely on the observational data to move forward. Monitoring of atmospheric variables is denser than ever, as ground stations multiply every single year and satellite retrievals are enhanced with every new mission. Still several open issues rise concerns on the availability or the accuracy of measured data, that could lead to erroneous estimations of the atmospheric state. A major issue is the anthropogenic radiative forcing of aerosols, which is understood from theoretical prospective, but the quantification remains incomplete on global scale as measurements of spectrally varying aerosol extinction, absorption and phase function are needed alongside with cloud radiative properties (IPCC, 2013). Ground based monitoring of stratospheric ozone, in the context of ozone depletion, is still lacking on global coverage, since most stations are located at north hemisphere mid latitudes (UNEP, 2010). Forecasting of health variables related to UV irradiance is still lacking of robust input of aerosol properties (Blumthaler, 2018). Motivated by the above issues, this study provides contributions to the enhancement of methods for retrieving optical properties of atmospheric components using state of the art spectral solar measurements.

Total Ozone Column (TOC) is a variable linked mainly to stratospheric ozone. Brewer and Dobson instruments provide very accurated and well established retrievals of TOC, but are instruments that needs a lot of maintenance to operate properly and the global coverage offered by stations is not satisfactory. These spectrophotometers are the primary ground-based instruments in use (Staehelin et al., 2009). Both instruments have been in operation now for several decades and provide long (decadal) time series of TOC (Redondas et al., 2014, Bais et al., 2015. The World Meteorological Organization (WMO) has initiated actions such as the Ozone Mapping Center (http://lap. physics.auth.gr/ozoness2/) in order to unify such measurements and provide near-real-time TOC for the Northern hemisphere. Although ground-based measurements provide long multi-decadal time series at high temporal resolution, their spatial coverage of the planet is low, especially over oceans and for locations near the equator. Additionally, over the last years a decline of stations recording TOC from surface has been recorded (Braathen, 2012) leading to crucial gaps on the monitoring process. In Montreal Protocol Seminar on Protecting our Atmosphere for Generations to Come, Geneva (Vol. 11). On the other hand, satellite instruments such as TOMS (Bhartia et al., 2004) from 1978 to 2005 and the Ozone Monitoring Instrument (OMI) on board of AURA satellite (Levelt et al. 2006) since 2006, have been providing total ozone measurements globally, but at a rate of only 1–2 measurements per day. Balis et al. (2007) have validated OMI TOC product against Brewer and Dobson ground based

retrievals and found global bias of 0.8%, while at different measuring sites all biases were up to 3%. In 2017 TROPOMI instrument on board Sentinel-5 Precursor, was launched in geostationary orbit and will provide global retrievals in 7X7 km^2 resolution (Veefkind et al.,2012; Butz et al., 2012).

UltraViolet MultiFilter Radiometer (UVMFR) is a portable, relatively easily maintened and affordable instrument, that provides the potential of TOC and SSA retrieval techniques in many occasions and fill important spatial gaps for climate monitoring. Gao et al. (2001) have suggested a spectral method for calculating TOC using measurements at four wavelengths from a UVMFR and showed that daily TOC values agreed with Brewer measurements to within 1.4%. Slusser et al. (1999) retrieved daily TOC values from UVMFR measurements using a look-up table (LUT) generated from a multiple-scattering radiative transfer code and validated them against Brewer and Dobson derived TOC data. Despite using only a relatively small data set (four and five months of daily values, respectively), both studies concurred and showed good agreement between UVMFR and spectrophotometer TOC values. In addition, Tree and Slusser (2004) compared five months of UVMFR recordings at Mauna Loa, Hawaii, to TOMS satellite retrievals (one satellite overpass per day) and also found a good agreement but with a small and systematic underestimation of the TOC. Thus, the potential to retrieve accurate TOC could be an important step to fill spatial and temporal gaps on global datasets. At chapter 4, a method for retrieving TOC is described, applied to a 5 years dataset and validated against Brewer and OMI retrievals.

Water vapour is the most important greenhouse gas and rules the thermodynamic state of the atmosphere, and considered a major climate feedback agent (Hartman et, al 2013). Also, monitoring the quantity of water vapour is important for hydrology, meteorological forecasting and clouds' microphysics. Continuous monitoring of (Integrated Water Vapour) IWV is established through Global Positioning System (GPS) satellite observations (Bevis et al., 1992), which could be used to retrieve IWV anywhere in the globe at relatively high temporal frequencies. The theoretical basis for these measurement is that delays in the signals emitted by GPS satellites are caused by the amount of water in the atmosphere, and through proper calibration, such delays could be expressed as function of the IWV. Thus, as long as there are ground based GPS receivers, after the appropriate post-processing of the received signals, IWV can be retrieved. Microwave Radiometer Profilers (MWP) measure the emitted microwave radiation of the atmosphere and retrieve water vapour vertical profiles and then IWV, providing continuous data at very high frequencies under all weather conditions

(e.g. Güldner and Spankuch, 2001, Güldner, 2013). These instruments provide very high accuracy but are not very common. Measurements from sun-photometers (eg CIMEL, PREDE-POM, MFR) have also been used to calculate water vapour transmittance and, thus, estimate IWV. Filter radiometer recordings in the spectral region around water vapour absorption bands, in the near infrared region, are used to calculate this quantity (Halthore et al., 1997, Campanelli et al., 2018, Nyeki et al., 2005). The World Meteorological Organization (WMO) recommends the use of spectral windows centered around 719, 817 and 946 nm, though the most frequently used is the 946 nm bandpass, which Ingold et al. (2000), showed that provides the most robust results. Global networks of deployed sun-photometric devices are capable of providing IWV time series. The AErosol RObotic NETwork (AERONET) retrieves IWV at more than one five hundred stations around the globe since the 1990's (Holben et al. 1998, https://aeronet.gsfc.nasa.gov/) using the Cimel instrument. Other sun-photometers such as the Precision Filter Radiometers (PFR) (Nyeki et al., 2005) have also been used by the Global Atmosphere Watch (GAW) WMO program to monitor IWV. Furthermore, the SKYNET radiometer network (details on: http://atmos2.cr.chiba-u.jp/skynet/) also retrieves IWV using Prede-POM sunphotometers at many stations (Campanelli et al., 2012, 2014). Finally, national networks of sunphotometers are installed and operating in some countries also provide Integrated Water Vapour (IWV) retrievals, eg. China Aerosol Remote Sensing NETwork (CARSNET) is using the 936nm channel to provide IWV (Che et al., 2016). Schneider et al. (2010) provided a very detailed comparison of different instrument retrievals over a 4-year data set recorded at Izaña Atmospheric Observatory, Tenerife, Spain. They found that MWP is the most precise technique and, in addition, it is independent of weather conditions, while sun-photometric retrievals were limited by cloudy and biased by dry/humid atmospheres, and GPS retrieved IWV showed deviations at lower IWV values. Deviations were also recorded when compared to radiosondes, which was explained by the difference in air masses and time scales among radiosondes and other IWV retrievals.

In recent years, a great improvement on hardware capabilities have made possible to manufacture spectroradiometers that cover a great part of the solar spectrum at very high resolution, like PSR and PANDORA. High spectral resolution enable to retrieve atmospheric variables using varied spectral bandwidths in order to enhance the accuracy. The Precision Solar Spectroradiometer (PSR), designed and manufactured at PMOD/WRC , Davos, Switzerland, is one of the most accurate instruments of this class (Gröbner et al., 2012) .The technique developed in this study, proposes the use of a wider solar spectral range to provide a more accurate

quantification of absorption and IWV calculation and is described and validated in chapter 5.

Aerosol play an important role on climate change understanding, as interaction with radiation include scattering and absorption, which are spectrally varying and show different behavior according to mixture. In addition, indirect effect of aerosols on irradiance through the formation of clouds and the heating of absorbing aerosol layer. High uncertainties remain on the quantification of anthropogenic aerosol related climate change, since the above effects could be mutually eliminated, and various types of aerosol contributes differently to each of them (IPCC, 2013). A comprehensive review of the assessment of the aerosol direct effect, its state of play as well as outstanding issues, is given by (IPCC, 2013) and (Yu et al., 2006). Both emphasize that significant uncertainties in Single Scattering Albedo (SSA) estimations, constitute one of the largest single source of uncertainty in current modeling rate of aerosol climate forcing. SSA is the ratio of scattering to total extinction (scattering plus absorption), and it depends strongly on chemical composition, particle size, mixing state, relative humidity and wavelength.

Hence, there is a need of robust retrievals of absorbing properties of aerosols in the whole of solar spectrum. For example for the same aerosol load (aerosol optical depth), the absorbing nature of aerosols can lead to up to 50% decrease in the erythermal irradiance, compared to only scattering aerosols (Bais et al., 2014). In the visible (VIS) and in the near infrared (NIR) parts of the spectrum, advanced retrieval algorithms for microphysical aerosol properties have been developed in the framework of the Aerosol Robotic Network (AERONET) and the Skyradiometer Network (SKYNET) (e.g., Dubovik and King, 2000; Nakajima et al., 1996). All AERONET stations currently provide inversion based column average SSA retrievals at the visible and near IR wavelengths (i.e., 440nm, 670nm, 870nm, 1020nm). In addition, Goering et al. (2005), Taylor et al (2008) and Kudo et al. (2008) have proposed estimation techniques for the retrieval of spectral aerosol optical properties by combining multi-wavelength measurements using a priori constraints that are applied differently than in the single wavelength methods. SSA retrieval in the ultraviolet (UV) part of the spectrum has large uncertainties and is rarely available. As AERONET does not provide any information about SSA at the UV, compared to the visible and infrared spectral region, only a few publications have dealt with aerosol absorption at UV wavelengths (e.g. Eck et al., 1998; Krotkov et al., 2005a; Bais et al., 2005; Corr et al., 2009). It is envisaged that improvement in measurement accuracy and in the general understanding of aerosol absorption in the UV (and immediate derivatives like the SSA) in various scientific applications, will contribute significantly to enhancing the accuracy of radiation

forcing estimates. For example, desert dust particles (Alfaro et al., 2004), soot produced by fossil fuel burning, and urban transportation, all strongly absorb UV radiation. However, optical properties of other potential UV absorbers like organic, nitrate and aromatic aerosols are still poorly known (Jackbson, 1999). Torres et al., (2007), in an overview study of OMI aerosols products, summarized the algorithmical techniques of SSA satellite retrieval at 388nm, which uses spectral variability between 354 and 388nm , 388nm reflectance and a selection on the aerosol type. They compared to AERONET SSA at 440nm and found a root mean square error of 0.03. Bergstrom et al., 2003 showed that spectra of aerosol SSA obtained in different campaigns around the world differed significantly from region to region, but in ways that could be ascribed to regional aerosol composition. Moreover, results from diverse air, ground, and laboratory studies, using both radiometric and in situ techniques, show that the fractions of black carbon, organic matter, and mineral dust in atmospheric aerosols play a role in the determination of the wavelength dependence of aerosol absorption (Russell et al., 2010). Barnard et al. (2008) and Corr et al., (2009) investigating the variability of SSA in a field study for the Mexico City metropolitan area, found that, in the near-UV spectral range (300 to 400 nm), SSA is much lower compared to SSA at 500 nm indicative of enhanced absorption in the near-UV range. They suggested that absorption by elemental carbon, dust or gas alone could not account for this enhanced absorption leaving the organic carbon component of the aerosol as the most likely absorber. It has been found in many studies that, in addition to dust, the absorbing organic carbon compounds can induce strong spectral absorption increasing towards the shortest UV wavelengths. Sources of these light–absorbing organic carbon compounds (often called as "Brown Carbon", BrC) are various; biomass burning (e.g. Kirchstetter et al.2004), urban smoke (e.g. Liu et al. 2015) and biogenic emissions (e.g. Flores et al. 2014). Corr et al. (2009) presented a review of studies estimating SSA at different wavelengths. For the visible part of the spectrum, two different approaches have been presented. The first (Dubovik et al., 2002), introduced sky radiance measurements in a matrix inversion technique to calculate various aerosol microphysical properties. This methodology has been widely applied in the AERONET. The second (Eck et al.,2003, (Kassianov et al., 2005), proposed the use of radiative transfer model (RTM) calculations, using as input measurements of AOD and the ratio of direct to diffuse irradiance at specific wavelengths. However, in the case of SSA calculations at UV wavelengths, enhanced measurement uncertainties, RTM input assumptions, and interference of absorption by other gases (O3, NO2), make the retrieval more difficult. All reported results concerning UV-SSA, utilize RTM combined with total and diffuse relative

irradiance measurements (Herman et al., 1975; King and Herman 1979; King 1979; Petters et al., 2003; Krotkov et al., 2005b; Corr et al., 2009; Bais et al., 2005) or absolute irradiance measurements (Kazadzis et al., 2010; Ialongo et al., 2010; Bais et al., 2005). The review made by Corr et al. (2009) also presents the major differences in the results of simulations of the SSA, arising from RTM input assumptions, measurement techniques and retrieved wavelengths. An additional problem is that previous studies have dealt with short time periods due to the limited lifespan of experimental campaigns. Moosmuller et al (2012) showed that iron concentration in mineral dust aerosols is linked to lower SSA at 405nm than in 870, which could be a hint for lowest SSA in the UV-VIS range during dust events. Medina et al (2012) found in El Paso-Juarez also large variation in UV range SSA, with lower values than visible wavelengths and showed that on heavy polluted days it can get as low as 0.53 at 368nm. An effort was made to calculate SSA in lower UV wavelengths, using Brewer (Direct and Global Spectral Irradiance at UV range) measurements, at Belgium, revealing lowest values but with high uncertainty (Nikitidou et al, 2013). Recently Schuster et al (2016) have tried to distinguish aerosol types, by their optical properties and assumed that dust particles have higher absorption at UV wavelengths. They used imaginary refractive index spectral dependence to separate from black carbon and infer hematite/goethite in the coarse mode. They found that dust particles containing hematite are highly absorbing in the UV region.

At chapter 6, a method for retrieving SSA at 332 and 368 nm is described, applied on 5 years dataset. Also, the behavior of different types of aerosols, according to ångström exponent, is investigated.

Ultraviolet (UV) solar radiation has a broad range of effects on life on Earth (UNEP et al., 1998;UNEP et al., 2007;UNEP, 2003). It influences not only human beings (e.g. (Diffey, 1991)), but also plants and animals (e.g. Bornman and Teramura, 1993). Furthermore, it causes degradation of materials and functions as a driver of atmospheric chemistry. There are a few studies linking changes of the UV radiation field with changes in the scattering and absorption of aerosols in the atmosphere (e.g. Zerefos et al., 2012). Such changes can be comparable in magnitude to those caused by the decline in stratospheric ozone (Elminir, 2007; Reuder and Schwander, 1999; Krotkov et al., 1998). As an example, analysis of long term UV time series at Thesaloniki, Greece, showed a reduction of 7% of AOD (305nm) per decade was recorded, but the UV Irradiance has increased by 9% (after removing ozone column effect on it) which could only be explained by change in the absorption characteristics of aerosols in the area (Meleti et al, 2009). Moreover, UV variations induced by changes in aerosol optical properties directly

affect tropospheric photochemistry causing: increases in regional O3 (10-20 ppb for Eastern USA) caused by increased UV levels due to the presence of non-absorbing aerosols (Dickerson et al., 1997), decreases in regional O3 (up to 50 ppb for Mexico City and for particular days) caused by strong UV reduction due to absorbing aerosols (Castro et al., 2001). There are also several more scientific issues that may be clarified with accurate knowledge of aerosol absorption properties such as aerosol effects on UV trends may enhance, reduce or reverse effects of stratospheric ozone change, satellite retrieval retrieval algorithms of the surface UV irradiance are directly affected by the presence of absorbing aerosols and the uncertainty in commonly used atmospheric radiative transfer applications and codes.

Future scenarios for simulations of global UV levels are based on ozone recovery, having as their sole input the predicted future decline in columnar ozone. Furthermore, simulations of observed tendency of reduced anthropogenic aerosols in the atmosphere in the US and Europe during the course of the last decade (den Outer et al., 2005) included only cloud and AOD changes in the characterization of likely UV trends. In this regard, changes in the absorbing properties of aerosols on global scales would have had a large effect on the uncertainty budget in any of the above simulations (WMO, 2003). For example, a decrease in aerosol absorption properties accompanied by an AOD decrease in Europe could lead to a significant acceleration of the calculated ozone decline related to UV upward trends (Kazadzis et al., 2009, Zerefos et al., 2012). The discrepancies between ground-based (GB) UV measurements and satellite-derived (OMI, TOMS, GOME) data are directly related to aerosol absorption that is absent from current satellite retrieval algorithms (Tanskanen et al., 2007;Arola et al., 2005). It has been shown that enhanced aerosol UV absorption in urban areas can cause up to 30% overestimation in the satellite retrieved UV radiation (Kazadzis et al., 2009). Radiative transfer algorithms calculating surface UV irradiance, lacks accuracy due to large uncertainties in the input parameters (e.g. levels of ozone, aerosol composition and the surface albedo) used in model calculations. It is now known that the major input source of uncertainty in radiative-transfer model simulations, is aerosol absorption (e.g. Van Weele et al., 2000). In particular, the direct radiative effect of aerosols is very sensitive to mid-visible SSA. For example, a change in SSA from 0.9 to 0.8 can often alter the sign of the direct effect (Yu et al., 2006). Furthermore, availability and quality of observational SSA data do not match with those available for AOD (Krotkov et al., 2005a). This is compounded by the lack of information on the vertical profile of aerosol optical properties such as the SSA at global scales. Only few case studies have dealt with such measurements and have been limited to local scales (Müller et al., 1999).

RTM algorithms calculating surface UV irradiance under clear sky conditions, have important accuracy issues due to uncertainties of input parameters (e.g. levels of ozone, aerosol composition and the surface albedo). The single most important input source of uncertainty in UV RTM, is aerosol absorption (e.g. Van Weele et al., 2000). A change in SSA from 0.9 to 0.8 can often alter the sign of the direct effect (Yu et al., 2006). Although AOD and ångstöm exponent are the most important factors for RTM estimation and there are widely available databases almost globally, SSA observational data lack quantity and quality (Krotkov et al., 2005a). This is compounded by the lack of information on the vertical profile of aerosol optical properties such as the SSA at global scales. Uncertainties in the estimation of SSA could lead to changes on the sign of radiative forcing. Also, SSA is strongly spectral depended, demonstrating different behaviour according to aerosol mixture, which may lead to significant changes as a function of wavelength (Russel et al., 2010). SSA used in RTM calculations refers to the vertical profile (column) of the aerosol extinction coefficient that usually differs significantly from the in-situ measured one. These profiles of the extinction coefficient can be retrieved by airborne in situ vertical profiling of aerosols (Schwarz et al., 2010, Skeie et al., 2011, Andrews et al., 2017). This approach remains very expensive and is rarely used in experimental campaigns. More commonly, retrievals of the mean columnar SSA from sun-photometric instruments are used to scale default climatological profiles used for RTM simulations (Kosmopoulos et al., 2017). Measurements of the mean columnar SSA are available from a large number of sites around the globe, though rarely in the UV (Kazadzis et al., 2016, Andrews et al., 2017).

UV irradiance is less than 10% of the solar irradiance reaching the Earth's surface, even though it is very important for the biosphere. UV solar spectrum is divided in three zones: UVC (<280 nm), where practically all irradiance is blocked by the atmosphere; UVA (315-400 nm), which provides ~90% of the total UV radiation reaching the surface; and UVB (280-315 nm), which is the most harmful for living cells as well as being beneficial for humans at the same time, by defining the creation of vitamin D in the human skin [Asta et al., 2011, Lucas et al., 2015]. Ozone is the dominant attenuator of UVB irradiance and the most important atmospheric factor for its deviations [Bais et al., 2015]. Aerosol attenuation in UV spectral region is also a non- negligible factor for the irradiance reaching the surface and, in some cases, its effects have been found to be as important as those of ozone (Castro et al., 2001, Meleti et al., 2009, Fragkos et al., 2016, Fountoulakis et al., 2016, Lamy et al., 2018)Also, absorbing aerosols indirectly affect irradiance's variability, by reducing the incident UV irradiance and altering lower atmosphere's

photochemistry , thus affecting tropospheric ozone's concentration (up to 50 ppb has been reported) (Castro et al., 2001).

Several factors related to human health are actively related to UV Irradiance estimation, such as DNA damage, Vitamin D Effective Dose and the UV index (erythema) for human exposure to the sun for numerous vulnerable population groups (e.g. pregnant women, light-coloured skins etc., as described by the World Health Organization , 2006). These variables are monitored in few countries through surface networks (Hülsen and Gröbner,2007, WMO/GAW, 2010) but have greater value when forecasted through RTM and are available to the general public (Blumthaler, 2018). Due to the lack of sources for SSA in the UV region, it is a common practice when estimating UV or forecasting health-related variables such as the UV index, to transfer SSA values from available visible wavelengths to UV wavelengths in radiative transfer calculations or just use climatological values (Bais et al., 2010).

Finally, in chapter 7 the absorbing aerosols effect of reducing UV irradiance reaching the surface is quantified. Many instruments and networks are measuring UV irradiance and estimate health related indexes. These data are used for scientific research and climatological estimations, but there is a great need of robust forecasting, in order to inform the authorities and the general public about the health concerns. In that case RTM calculations are usually used, that underestimate the role of spectral dependence of aerosol absorbing properties in the UV spectral range. In this study several runs of RTM were performed using different datasets of SSA in the UV, either measured in the UV or transferred from visible bandwidth or from climatological databases.

2. Theoretical Background

2.1 Solar Radiation

The primary source of energy on planet Earth is the incoming electromagnetic radiation from the Sun. There are two possible viewpoints for describing electromagnetic radiation. A radiation is composed of particles (photons), or it can be viewed as a wave propagating at the speed of light ($c \simeq 3 \times 10^8$ m/s in a vacuum), characterized by its frequency ν (in s^{-1} or in hertz) or, equivalently, by its wavelength $\lambda = c/\nu$ (usually expressed in nm or in μm). Shortwave radiation that reaches the planet is the driving force for the most physical and chemical procedures in the atmosphere and it is the vital part of energy equilibrium of the planet. Radiation emitted from the solar disc, has small variations from the one emitted from the theoretical black body defined by Planck, Stefan-Boltzman and Wien laws, at a temperature of 5788K (Linde, 2004). These variations are caused by emission and absorption by gases and elements at solar disc and the non-isothermal solar atmosphere (Routh, 2018). Maximum radiation is found at a wavelength shorter than the one estimated from Wien's law. An example of the theoretical black body spectrum and the actual observed at the sun is given at figure 2.1.

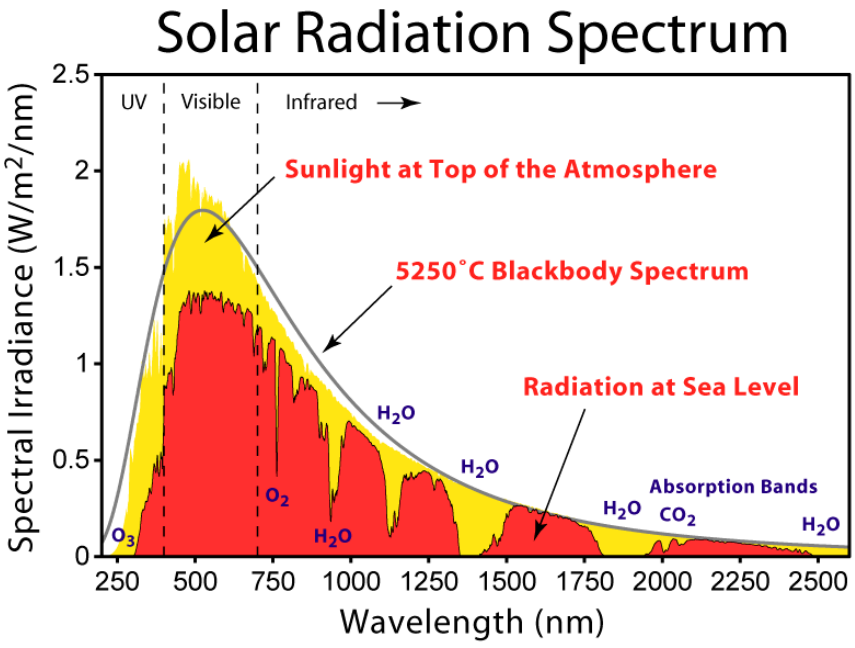

Figure 2.1. A theoretical solar spectrum, where UV, visible and IR regions are signified. The black body curve corresponding to sun's temperature is noted. Spectrum recorded at the top of the atmosphere is shown with yellow. Actual spectrum at earth surface with alongside with the most important molecular

absorbers is shown with red. source: http://www.globalwarmingart.com/wiki/File:Solar_Spectrum_png

The spectrum that is recorded at the Earth's surface has also been transformed when it is propagated through the atmosphere. Gases and water vapour in the atmosphere absorb at very specific wavelengths, where missing (absorbing) lines are observed at the spectrum (Chance et al, 1997). Also, solid matter suspended in the atmosphere, found in the form of particles, called aerosols, absorbs and scatters solar radiation, at the whole spectrum according to their optical and physical properties. Additionally, an important part of radiation's extinction in the atmosphere is caused by scattering caused by air molecules, cloud droplets and ice crystals. Absorption in the spectral region 300-900nm for the major gases in the atmosphere for representative concentrations are shown in figure 2.2. The solar radiation attenuation on an optical path can be described by a parameter called optical depth that is defined as the natural logarithm of the ratio of incident to transmitted radiant power through the atmosphere. The parameter is unitless and solar radiation wavelength dependent.

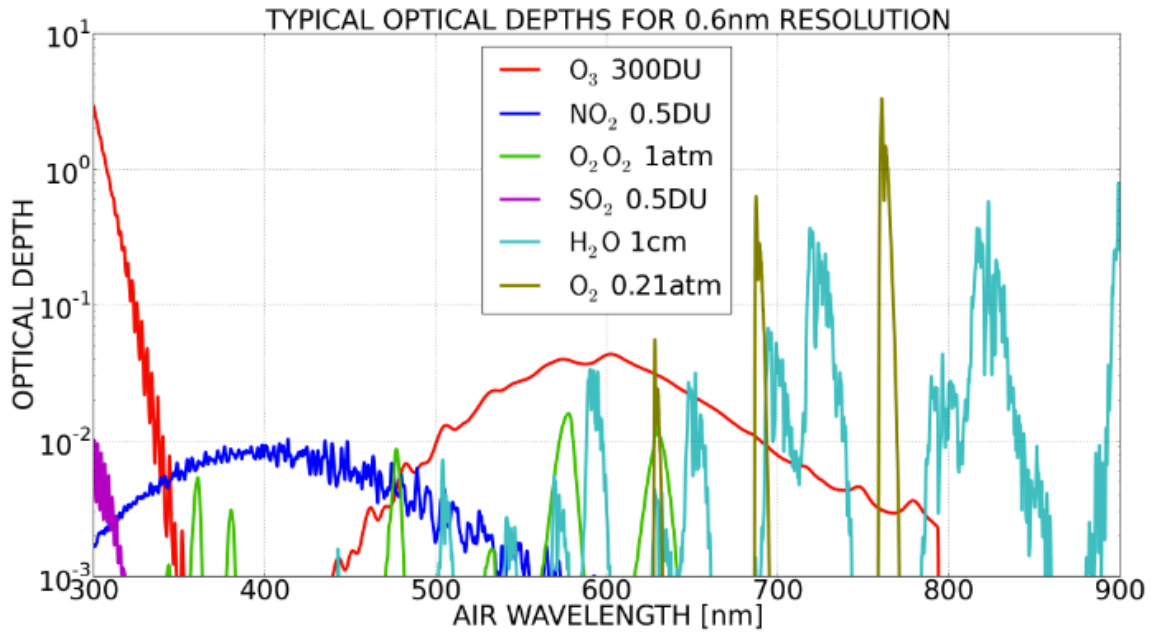

Figure 2.2 Spectral absorption optical depth in the region 300-900 nm for various atmospheric gases, as calculated for the concentrations in the legend.

The Solar spectrum is classified primary by wavelength. Different spectral regions of the radiation have effects at various processes taking place at various heights in the atmosphere. Visible radiation (400-700 nm) and infrared (>700 nm)

reaches the surface and warm it up. Ultraviolet radiation (<400 nm) is mainly absorbed at higher altitudes (>10 km). Extreme ultraviolet radiation (<120 nm) is totally absorbed at very high altitudes in the atmosphere (>100 km). Maximum energy reaching the Earth's surface is found at the visible range, as described by Wien law. Thus, solar irradiance at the top of the atmosphere differs significantly from one reaching ground level, due to the composition of the atmosphere and the stratification and concentration of its elements.

For measuring solar irradiance four basic definitions should be provided. These definitions are visualized also at figure 2.3.

Total Solar (Extraterrestrial) Irradiance (TSI), is the solar irradiance, integrated at all wavelengths, per unit area, incident on the top of the atmosphere and is measured in W/m^2. TSI depends on solar activity and orbits of planets. Major changes in TSI are very slow and recorded in scale of decades, where the most studied case is Milankovitch cycles (Kaufmman and Juselius, 2016), which are mainly explained by variations of earth's rotating plane, although there are also shorter cycles of variations observed, such as 28 cycle due to variations of sun's rotation. These long-term changes of TSI are crucial for earth's climate, explaining extreme conditions as ice age. Most used variable in atmospheric sciences is solar constant, which is the mean flux density per unit area, on a surface perpendicular to the rays at one Astronomical Unit (AU) from the sun, which is the mean earth-sun distance. Currently the most accurate value in use is 1360.8 ± 0.5 W/m^2, which was defined by combining satellite measurements and laboratory tests (Kopp and Lean, 2011, Haberreiter et al., 2014). Also there is ongoing research on the field of the solar spectrum incident at the top of the atmosphere, measured by satellite and ground instruments (eg Harder et al. 2010, Gröbner et al., 2017)

Direct Irradiance (DI), is the measured radiation on earth's surface from the direction coming just from the sun disk. DI is defined by the flux of irradiance in a solid angle with aperture of half the angular distance observer-sun (Blanc et al., 2014) and is measured in W/m^2. In order to measure DI, the exact position of the sun relatively to observer location should be defined. Azimuth and zenith angles on the spherical coordinate system of the horizon are the variables used for the sun position, which are calculated through basic astronomical relations. Under cloudless conditions, DI stands for the larger part of irradiance at ground level in the visible part of the solar spectrum.

Diffuse Horizontal Irradiance (DHI), is the radiation reaching earth's surface from scattered light in the atmosphere, thus it is measured on an horizontal surface, recording incoming irradiance from all directions higher than the horizon, excluding circumsolar radiations and is measured in W/m^2. Scattered irradiance is caused by molecules, aerosols and clouds. DHI is higher under the presence of clouds, when scattering is the main effect in the atmosphere. At clear skies, DHI is a very small part of the irradiance reaching the surface.

Global Horizontal Irradiance (GHI), it the total irradiance from the sun that reaches an horizontal surface on earth and is measured in W/m^2. Thus, it is the sum of DHI and DI multiplied with the cosine of SZA.

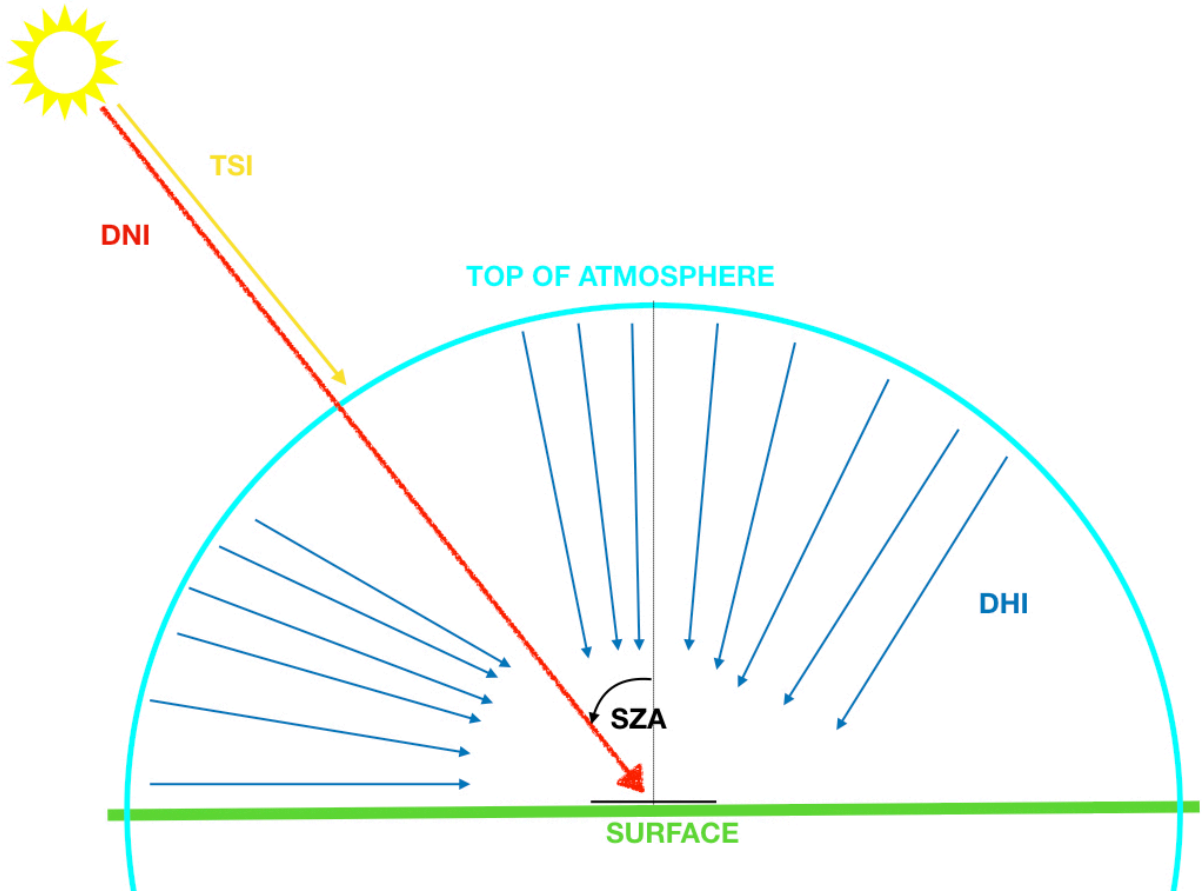

Figure 2.3 A schematic visualization of irradiances definitions and the earth's atmosphere (cyan for the top of the atmosphere) and surface (green). DHI is shown in blue, TSI in yellow, DI with red.

For calculating DI, the accurate position of the position on sky is needed and is defined by the Solar Zenith Angle (SZA) and the solar azimuth angle (ψ).

$$\cos(SZA)=\sin(\varphi) \times \sin(\delta) + \cos(\varphi) \times \cos(\delta) \times \cos(H) \quad (2.1)$$

$$\cos(\psi)=(\sin(a) \text{ X } \sin(\varphi) - \sin(\delta))/(\cos(a) \text{ X } \cos(\varphi) \quad (2.2)$$

Where φ is the geographical latitude of the observation point, δ is the solar declination, H the hour angle measured from true local solar noon and a is the solar elevation. Solar declination is the angle between earth-sun centers and the theoretical ecliptic plane, which is zero during equinoxes and has maximum value at summer solstice 23.5^o and at winter solstice -23.5. During a day, it could vary up to 0.5^o at the equator. Hour angle is the angle between observer's meridian and the solar meridian and changes about 15^o per hour. Solar elevation is the complement to the SZA and is simply calculated as

$$\alpha=1\text{-SZA} \quad (2.3)$$

From among the many available algorithms to calculate solar position, the one given by Michalsky (1988) is recommended by WMO (1996) for solar radiation measurements. It is based on trigonometric series approximations to the Astronomical Almanach for 1985 and gives apparent elevation, including refraction at sea level, to an accuracy of about 0.01° which is considered sufficient for meteorological applications. At high SZA refraction of radiation also plays an important role, thus simple trigonometric approximation is less accurate.

2.2. Basics of Sun Radiometry

Remote sensing is the acquisition of information about an object or phenomenon without making physical contact with the object. Techniques of remote sensing are very common in atmospheric sciences and are divided in passive and active. Active instruments (e.g. Radar, Lidar) provide their own energy (electromagnetic radiation) to illuminate the object or scene they observe (e.g. Wandinger, 2005, Jorgensen, and Hildebrand, 1983). They send a pulse of energy from the sensor to the object and then receive the radiation that is reflected or backscattered from that object. Passive instruments sense only radiation emitted by the object being viewed or reflected by the object from a source other than the instrument. Passive remote sensing instruments just act as receivers, recording

radiation from natural sources. Reflected sunlight is the most common external source of radiation sensed by passive instruments (Kauffman et al., 1997).

Both passive and active remote sensing techniques could by employed from the surface, from aircrafts or from satellites. First ground based active remote sensing observations were made in middle 20th century, using weather radar. Since then several active remote sensing instruments have been developed, including sodars and lidars (aerosol, wind, and ceilometer). Passive remote sensing of the atmosphere from the ground is being performed with radiometers recording either sun's or atmospheric gases' radiation, since the start of the 20th century. Also, in satellite remote sensing, most sensors are passive, recording reflected or emitted radiation from the earth (eg MODIS Aqua, AURA, MODIS Terra). More recently active instruments have been installed on satellites such as CALIOP on CALIPSO, which is a cloud and aerosol lidar, able to retrieve vertical profiles.

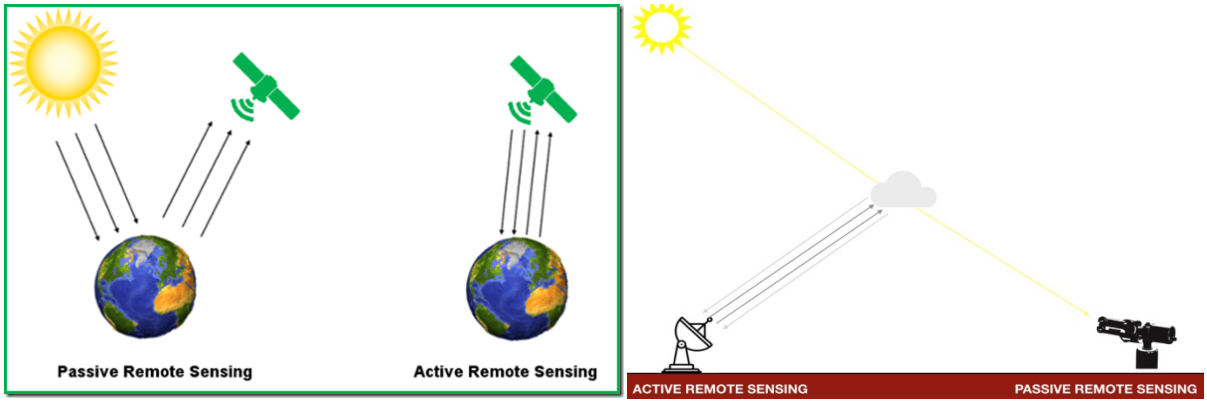

Figure 2.4 Schematic visualization of active and passive remote sensing for satellite (upper image) and ground based (lower image) instruments

Sun radiometry is a passive remote sensing technique to extract the columnar composition of the atmosphere, regarding elements that absorb or scatter the sunlight at specific spectral bandwidths. The technique is based on the assumption that the sun behaves as a source of light and the solar spectrum reaching the edge of the atmosphere is well known, thus any differences recorded at solar spectrum at the ground level is caused by atmospheric related absorption and scattering procedures. Means of this technique are constantly evolving, offering a more accurate and detailed recording of the atmospheric properties. Techniques have been also developed to retrieve atmospheric profiles of some variables, such as Ozone.

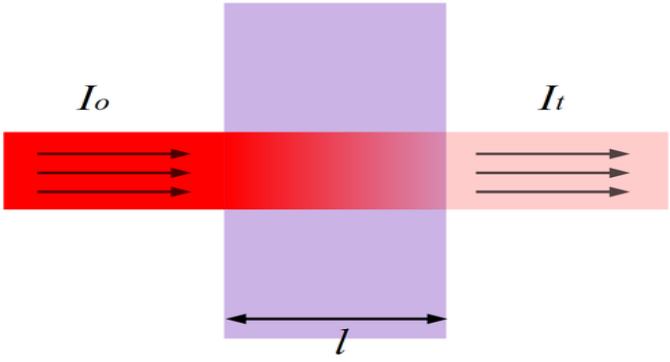

Figure 2.5. Schematic visualization of transmittance of radiation I when passing through a medium of length l.

The principle of the technique is the Beer-Lambert law, which states that the extinction process is linear in the intensity of radiation and amount of radiatively active matter, provided that the physical state is held constant. When solved for atmospheric boundary conditions is expressed as

$$I_\lambda = I_{o,\lambda} \exp(-m\tau)\, R^{-2} \quad (2.4)$$

Where I_λ is the irradiance measured at ground level at wavelength λ, $I_{o,\lambda}$ is the extraterrestrial irradiance at wavelength λ, m is the optical air mass along the line of sight connecting the observations point and the sun , τ is the total optical depth and the term R is the Sun-Earth distance in astronomical units, normalised to the variations around the mean distance.

The optical air mass is the ratio of actual path length taken by the direct solar beam to the analogous path when the Sun is overhead from the top of the atmosphere to the surface. In Sun radiometry, the optical air mass can also be interpreted as the ratio of optical thickness over optical depth, which is defined by line integrals of the extinction coefficient along the path of light. These integrals depend on the vertical profile of the scattering or absorbing coefficient, and the optical air mass will be (slightly) different for each extinction component in the same geometric path. For aerosols and water vapour, which are located mainly in the lower troposphere, a simple geometrical approximation sec(SZA) is accurate to 1% only for zenith angles smaller than about 70°. Typical scale heights for aerosol concentration are in the order of a few km (Turner et al. 2001), comparable to the scale height for water vapour, thus the formulation for water vapour optical air mass by Kasten (1966) can be used during periods of low stratospheric aerosol load. If better accuracy is required, as for Langley calibration of I_o, the path lengths must

be calculated by ray tracing through a refracting atmosphere. A more sophisticated approximation is commonly used as:

$$m_a \approx m_{H20} = 1 / (\sin(SZA)+0.0548\times(SZA +2.65)^{-1.452}) \quad (2.5)$$

Optical airmass can be prescisely calculated, by integrating the paths through all atmospheric layrers, which is a technique used to avoid approximations.

The term δ of the optical depth is describing several terms causing the extinction due to various atmospheric procedures as molecular scattering, gas absorption and aerosol extinction. These components have different vertical structures, thus their optical air mass across a refracted slant path is slightly variant. The total optical thickness τ is usually described as

$$\tau=\Sigma\ m_i\delta_{i*} \quad (2.6)$$

According to the American Meteorological Society, optical thickness means "the (dimensionless) line integral of the extinction coefficient along any path in an optical medium", while optical depth indicates "the optical thickness measured vertically above a given altitude". This definition is consistent with terminology used by the WMO (1996).

In equation (2.4) the signal of the intensity I_λ is the only measured quantity, all other terms are based on models of atmospheric extinction or of the measurement process that are approximated by relatively simple expressions for practical use. Taking the logarithm of 2.4 and re-arranging terms leads to the basic equation for determination of optical depth for each term δ_i. These optical depths refer to aerosols, trace gases as O_3 and NO_2, water vapour and molecular scattering (Rayleigh). A considerable variety of approximations to compute optical air masses m and non-aerosol optical depths δi as well as methods to determine the calibration value I_0 were proposed in the literature dealing with Sun radiometry (eg Schmid and Wehrli, 1995, Dubovik et al., 2000, Holben et al., 2001, Remer et al., 2005). While the vertical profiles of air density and ozone are more temporally constant and the corresponding optical air masses are readily calculated with good accuracy, the aerosol optical depth and the water vapour optical depth are usually treated as the unknown variable on equation 2.6. Also, it is common to apply the equation 2.6

to synchronous measurements at different wavelengths, and by combining the results to estimate the loads of various attenuators (Holben el al., 1998, King et al. 2003)

2.3 Radiative transfer

Radiative transfer is the physical phenomenon of energy transfer in the form of electromagnetic radiation. The propagation of radiation through a medium is affected by absorption, emission, and scattering processes. A quantitative description or radiative transfer is crucial for understanding the influence of radiation on atmospheric properties.

Mono-chromatic intensity of the radiance is defined as the radiant energy (dE_λ) in a given direction (defined by angle ϑ in polar coordinates) per unit time (dt) per unit wavelength (dλ) per unit solid angle (dΩ) per unit area (dA) perpendicular to the given direction (Iqbal, 1983)

$$dI_\lambda = \frac{dE_\lambda}{cos\theta \; d\Omega \; dt \; dA \; d\lambda} \; (2.7)$$

At this point, it should be noted that this monochromatic intensity is solely theoretical and it cannot be measured. Measured irradiances when described at a single wavelength, it is implied that a very narrow range of wavelengths dλ, centered at λ is recorded.

When propagating through the atmosphere, the intensity of monochromatic radiation is decreased by the dI_λ as described by Beer-Lambert law (Wallace and Hobbs, 2006)

$$dI_\lambda = -I_\lambda(\sum_i k_{\lambda i}\rho_i)ds \; (2.8)$$

where for each kind of I gas molecules or solid particles, the $k_{\lambda i}$ is the mass extinction cross section and ρi is the mass concentration, and ds is the differential path length along the ray path of the radiation. Volume extinction coefficient of I is the product $k_{\lambda i}$ ρ_i. Extinction is caused by the combined effect of absorption and scattering of radiation in the process of propagating. Following Kirchoff's each molecule or particle, emits and absorbs at wavelength λ, at the exact same rate, meaning that absorption and emission coefficient at a certain wavelength are equal.

Absorption of radiation by air molecules in the atmosphere is mainly caused by molecular oxygen (O_2) ozone (O_3), water vapour (H_2O), sulfur dioxide (SO_2) nitrogen dioxide(NO_2) methane (CH_4) and carbon dioxide (CO_2). The energy absorbed by the molecules causes changes in energy level of the atom orbits, changes in vibrational and rotational state of the molecule.

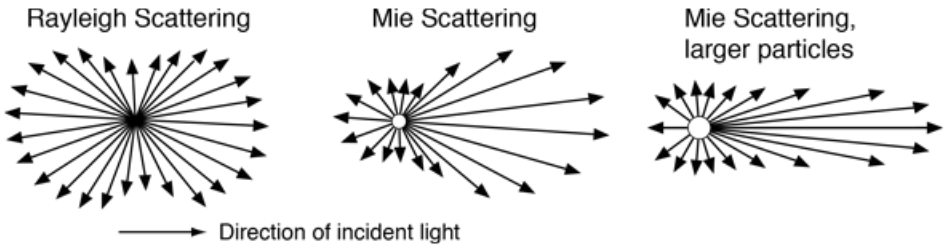

Figure 2.6 Differences of types of scattering according to particle size. Very small particles cause Rayleigh scattering and particles at the same size as the wavelength of incident light or bigger cause Mie scattering. Source: http://hyperphysics.phy-astr.gsu.edu

Scattering is the physical process where radiation is forced to deviate from a straight trajectory by one or more paths due to localized non-uniformities in the medium through which it passes. Gas molecules and particles are the cause of scattering in the atmosphere and their size define the spatial distribution of the scattered radiation. The size is considered in respect to the waveform of the radiation and when the wavelength is much larger than the effective radius of the molecules or particles, then the distribution is more uniformly and the phenomenon is described by the laws of Rayleigh (Rayleigh, 1914). The case of comparable effective radius and wavelengths or even larger particles, causes more radiation to the ray of the incident light and is described as Mie scattering (McCartney, 1971). Figure 2.6 provides a graphical visualization of these processes. Under the assumption that the scattering particle is spherical, the criterion used is the parameter x, which should be $<<1$ in case of Rayleigh scattering.

$$x = \frac{2\pi r}{\lambda} \quad (2.9)$$

where r is the radius of the spherical particle and λ is the wavelength of incident radiation. At figure 2.7 a graphical visualization from Wallace and Hobs (2006) provide a clear picture of the cases of each type of scattering. At this graph, it is shown that for solar radiation spectral range, the main mechanism is Rayleigh

scattering from air molecules and, Mie scattering could be observed in the presence of smoke dust or haze.

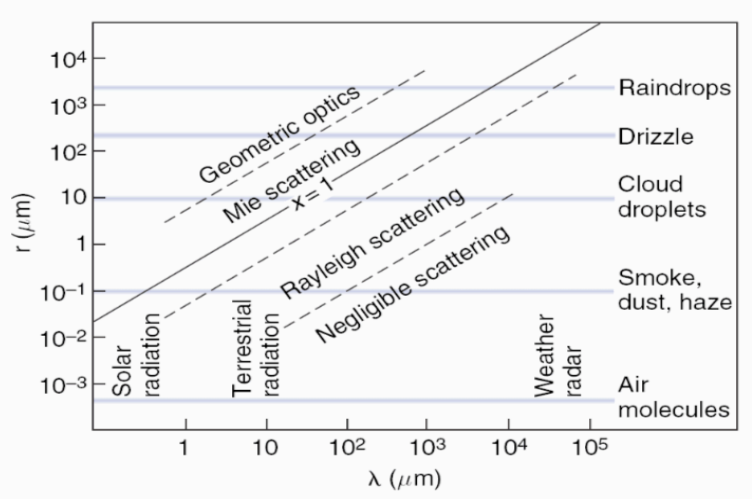

Figure 2.7. Parameter x as a function of wavelength λ of incident radiation and particle radius r source: Wallace and Hobbs (2006)

Clouds are the major attenuator of solar radiation in the atmosphere. Other important source of attenuation at solar spectral band are aerosols, ozone, water vapour and Rayleigh scattering. Also other trace gases as NO_2, SO_2 , CH_2O and O_2 have non-negligible absorption at these wavelengths. Hence, all the above could be retrieved through passive remote sensing, using the sun as source. Next paragraphs provide detailed description on all the above.

2.3.1 Aerosols

Suspensions of solid and liquid particles in the atmosphere are relevant to radiative and chemical processes. Aerosols are all the particulate matter found in earth's atmosphere and could be either natural or anthropogenic. Aerosol particles size range from thousands of a micron to several microns. Their role in the atmosphere includes cloud formation, where they serve as condensation nuclei for water droplets and ice crystals. Aerosol physical and chemical properties are determined by their sources and production processes. Fine aerosols (radius between 0.1 and 1.0 μm) are formed by coagulation of smaller nuclei or produced directly during incomplete combustion (biomass burning or coal power plants), while coarse particles (>1μm) are primarily from mechanical erosion of the earth's

surface (Levy, 2009). Figure 2.8 visualizes different type of aerosols according to diameters and their influence on physical processes.

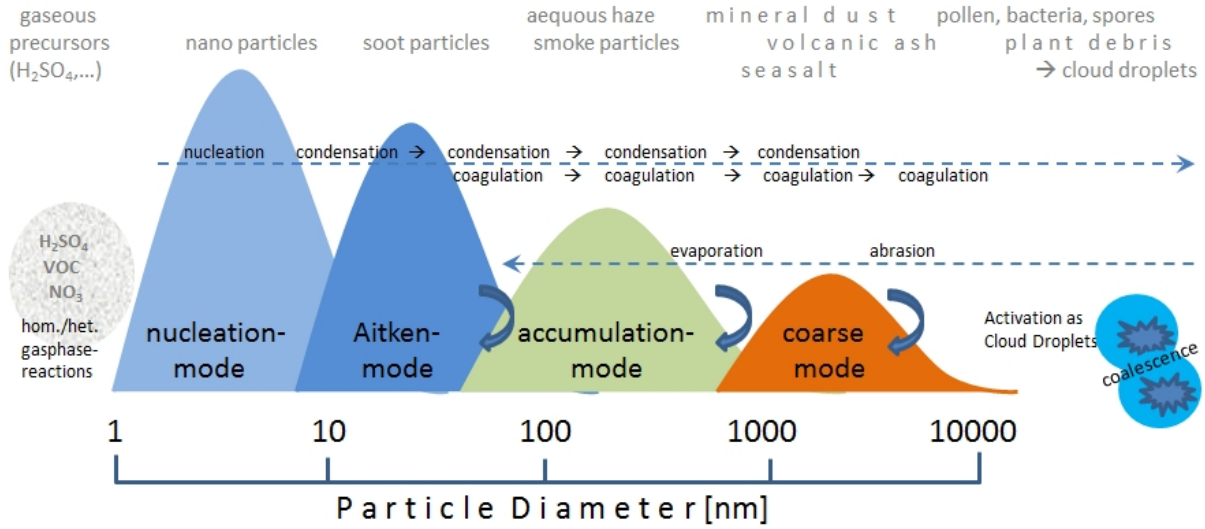

Figure 2.8 Schematic multi-modal particle size distribution with typical transformations and example particle types within each mode.

Aerosols could be emitted directly or formed by gaseous precursors. Variations of the chemical composition include inorganic species (sulphate, nitrate, ammonium, sea salt) and organic species, black carbon, mineral species and primary biological particles. Main anthropogenic emissions are linked to black carbon, sulphate, nitrate and ammonium, where the dominant natural emissions include sea salt, mineral dust and biological particles (Buscher et al., 2013).

Aerosols are mainly located in the lower troposphere and have large spatial and temporal variations. There are some aerosols in higher atmospheric layers, emitted by volcanic eruptions (McCormick et al., 1995), which could also have a major role in radiative transfer. Marine aerosols are produced by bubble bursting on sea surface, mainly during wave breaking composed by sea salt and marine organic matter (de Leeuw et al., 2011). Mineral dust is emitted from desert surfaces where large soil particles are creeped and salted before suspending in the air (Zhao et al. 2006). Biomass burning aerosols are mainly produced during forest fires (Randerson et al., 2012). Sources of biological aerosols include pollen, bacteria, fungal spores and fragments of animals and plants (Pöschl et al., 2010). Black carbon aerosol emitted directly from incomplete combustion processes such as fossil fuel and biomass burning and is the dominant anthropogenic aerosol (IPCC, 2007).

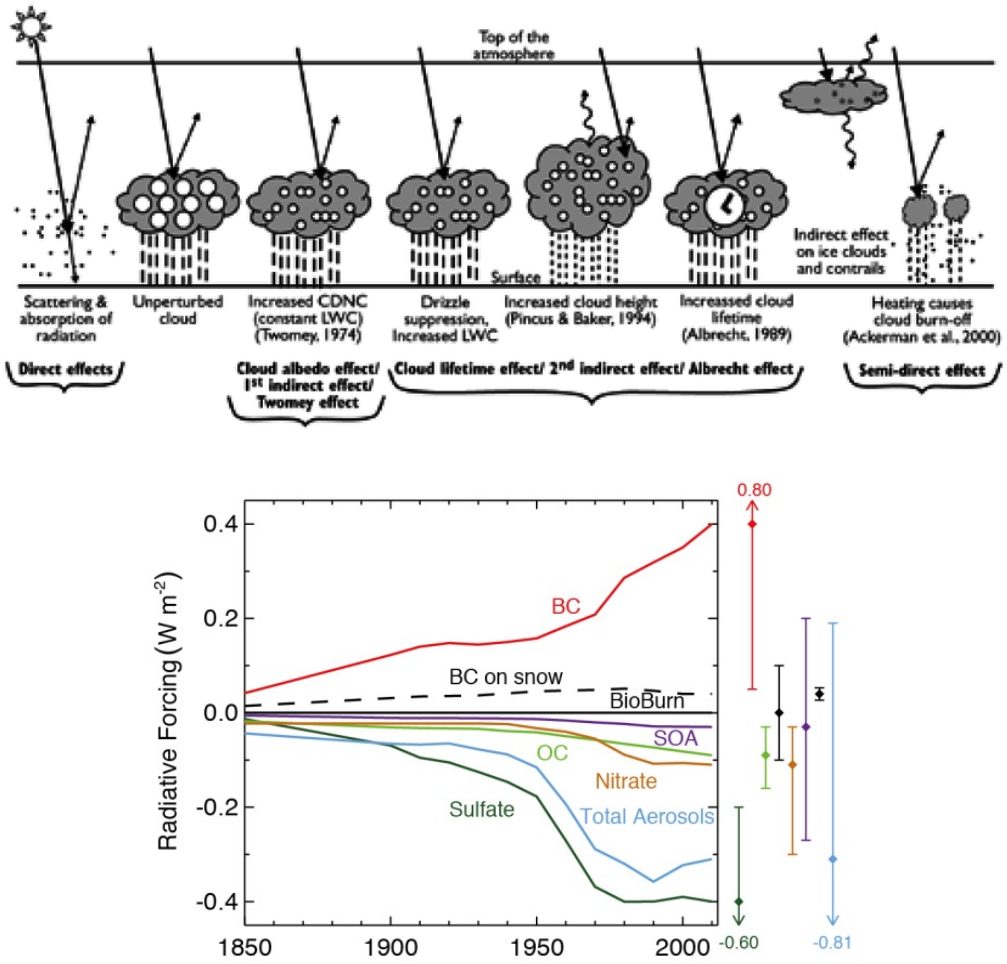

Figure 2.9 Schematic of direct/indirect effect of aerosols on radiative transfer (upper). Calculated total radiative forcing of different aerosol types in climatological terms. (IPCC, 2013)

Interaction of aerosols with radiation is caused by both scattering and absorption on the particles which alters the radiative flux. The physical process could be understood and calculated by observing the aerosol extinction coefficient, the single scattering albedo and the phase function, which are all spectral dependent variables. These variables are directly linked to the chemical properties of the aerosol mixture in the atmosphere such as size distribution, shape, composition and mixing state. Secondary, this interaction is influenced by surface properties (albedo), by atmospheric trace gases and clouds. Most of the research has focused

on this interaction on the spectral region of solar spectrum but there are not many studies on the long-wave radiation (eg Bharmal et al. 2009). This interaction is the direct effect of aerosols on radiative budget. In addition aerosol have an indirect effect on radiation by acting cloud condensation nuclei and influencing clouds properties as lifetime, height and liquid water content. A visualization of these interaction is provided in figure 2.9 upper plot, and a climatological total radiative forcing for different aerosol types, as estimated from IPCC (2013) is presented in figure 2.9 lower plot.

Table 2.1 Key aerosol properties in the troposphere. The estimated lifetimes are based on AeroCom model. Source IPCC 2013 report WG1AR5

Aerosol Species	Size Distribution	Main Sources	Main Sinks	Tropospheric Lifetime	Key Climate Relevant Properties
Sulphate	Primary: Aitken, accumulation and coarse modes Secondary: Nucleation, Aitken, and accumulation modes	Primary: marine and volcanic emissions. Secondary: oxidation of SO_2 and other S gases from natural and anthropogenic sources	Wet deposition Dry deposition	~ 1 week	Light scattering. Very hygroscopic. Enhances absorption when deposited as a coating on black carbon. Cloud condensation nuclei (CCN) active.
Nitrate	Accumulation and coarse modes	Oxidation of NO_x	Wet deposition Dry deposition	~ 1 week	Light scattering. Hygroscopic. CCN active.
Black carbon	Freshly emitted: <100 nm Aged: accumulation mode	Combustion of fossil fuels, biofuels and biomass	Wet deposition Dry deposition	1 week to 10 days	Large mass absorption efficiency in the shortwave. CCN active when coated. May be ice nuclei (IN) active.
Organic aerosol	POA: Aitken and accumulation modes. SOA: nucleation, Aitken and mostly accumulation modes. Aged OA: accumulation mode	Combustion of fossil fuel, biofuel and biomass. Continental and marine ecosystems. Some anthropogenic and biogenic non-combustion sources	Wet deposition Dry deposition	~ 1 week	Light scattering. Enhances absorption when deposited as a coating on black carbon. CCN active (depending on aging time and size).
... of which brown carbon	Freshly emitted: 100–400 nm Aged: accumulation mode	Combustion of biofuels and biomass. Natural humic-like substances from the biosphere	Wet deposition Dry deposition	~ 1 week	Medium mass absorption efficiency in the UV and visible. Light scattering.
... of which terrestrial PBAP	Mostly coarse mode	Terrestrial ecosystems	Sedimentation Wet deposition Dry deposition	1 day to 1 week depending on size	May be IN active. May form giant CCN
Mineral dust	Coarse and super-coarse modes, with a small accumulation mode	Wind erosion, soil resuspension. Some agricultural practices and industrial activities (cement)	Sedimentation Dry deposition Wet deposition	1 day to 1 week depending on size	IN active. Light scattering and absorption. Greenhouse effect.
Sea spray	Coarse and accumulation modes	Breaking of air bubbles induced e.g., by wave breaking. Wind erosion.	Sedimentation Wet deposition Dry deposition	1 day to 1 week depending on size	Light scattering. Very hygroscopic. CCN active. Can include primary organic compounds in smaller size range
... of which marine POA	Preferentially Aitken and accumulation modes	Emitted with sea spray in biologically active oceanic regions	Sedimentation Wet deposition Dry deposition	~ 1 week	CCN active.

Aerosol absorption important because it determines the total warming or cooling effect of the particles (visualized in figure 2.10). Radiation that reaches the ground is decreased when scattered by aerosols, which leads to atmospheric cooling. On the other hand, when radiation is absorbed by aerosols, the air mass containing them is heated while the radiation reaching the surface is also decreased and the surface layer cooled. Thus, in that case there is more complicated thermal mechanism to define the final cooling/warming of the system after redistributing thermal charges. This mechanism causes mainly absorbing aerosols (Black Carbon)

to have a positive radiative forcing in contrast to other aerosols that show a negative one (figure 2.9 lower plot).

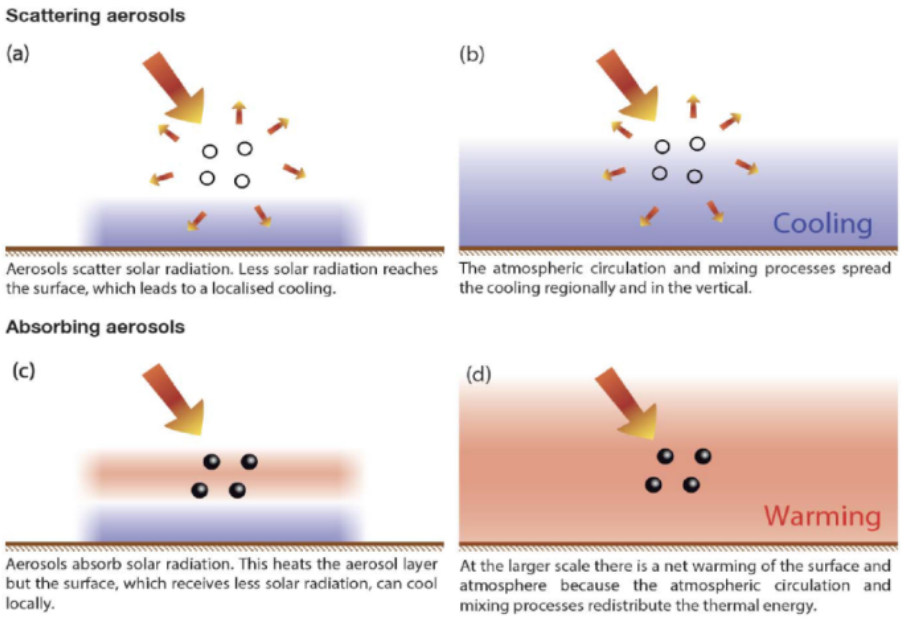

Figure 2.10 Schematic visualization of absorbing and scattering aerosols' interaction with radiation and the final warming/cooling effect.

Total extinction of irradiance at wavelength λ, caused by the presence of aerosols, is described by Aerosol Optical Depth (AOD_λ) , which is the integral of extinction ($b_{aer}(\lambda,SZA)$) over a vertical path form the surface to the top of the atmosphere (TOA), where h is the height

$$AOD_\lambda = \int_0^{TOA} b_{aer}(\lambda, h)\, dh \quad (2.9)$$

AOD is dimensionless and it describes the attenuation of the transmitted irradiance in an atmospheric column due to the presence of aerosols. Also, Ångström (1929) proposed the following formula which includes the spectral dependence of the extinction

$$AOD_\lambda = \beta\, \lambda^{-\alpha} \quad (2.10)$$

where a is the Ångström exponent, which parameterizes the spectral dependence of the extinction, and β a variable indicative of the number of particles found in the solar beam path. Common range of β values are 0 to 0.5. Ångström exponent is regularly used as an indicator of the type of aerosols (Eck et al., 1999), since different types have characteristic spectral behavior. Larger aerosols are linked to smaller values of a, while aerosol mixtures dominated by fine particles usually have a>1.5 (Kazadzis et al., 2016). Weighting a at different wavelengths, by quadratic fits, provide information on the ratio of fine aerosols to the total (O'Neil et al., 2003). Also, Ångström exponent is being used frequently to estimate the AOD at wavelengths where there are no measurements available, by extrapolation. Thus relation 2.10 for two wavelengths λ_1 and λ_2 could be solved as

$$\frac{AOD_{\lambda 1}}{AOD_{\lambda 2}} = \left(\frac{\lambda 1}{\lambda 2}\right)^{-\alpha} \quad (2.11)$$

which is also the most common approach to calculate α.

AOD shows large variations on daily seasonal and interannual scales, which caused by aerosols' short life time, the seasonality of sources and aerosols sinks defined by meteorological variables. Figure 2.11 shows the average AOD at 550 nm for the period 2002-2004, which reveals major aerosol loads over eastern Asia's megacities and relatively high over Asia's and Africa's desert regions. Generally, above the oceans there are very low loads of aerosols, which are dominated by marine particles. At South Hemisphere land regions, were AOD is significant lower than North Hemisphere, the dominant emission is biomass burning which occurs on all three continents during September-November (Remer et al., 2008). Local maximums are observed around urban areas were fossil fuel combustion emits carbon and sulphate aerosols and their variability is directly proportional to industrial and transport activities. Although most of the aerosols are found inside the boundary layer, when an aerosol plume is lifted to the free troposphere or even in the stratosphere, concentrations remain locally high for larger period of time, due to lack of efficient sinks. Maximum mean values of AOD are found in deserted arid areas (Sahara, Kalahari, Arabian, Gobi) where a lot of dust is emmited in the atmosphere. Finally, in cases of volcanic eruptions (Stenchikov et al., 2002, Ansmann et al., 2011) and forest fires (Colarco et al., 2004, Stohl et al.,2006) corresponding aerosols are emitted in the atmosphere and not include in aerosols climatology, due to their unique and random nature, but result to very high AOD recordings.

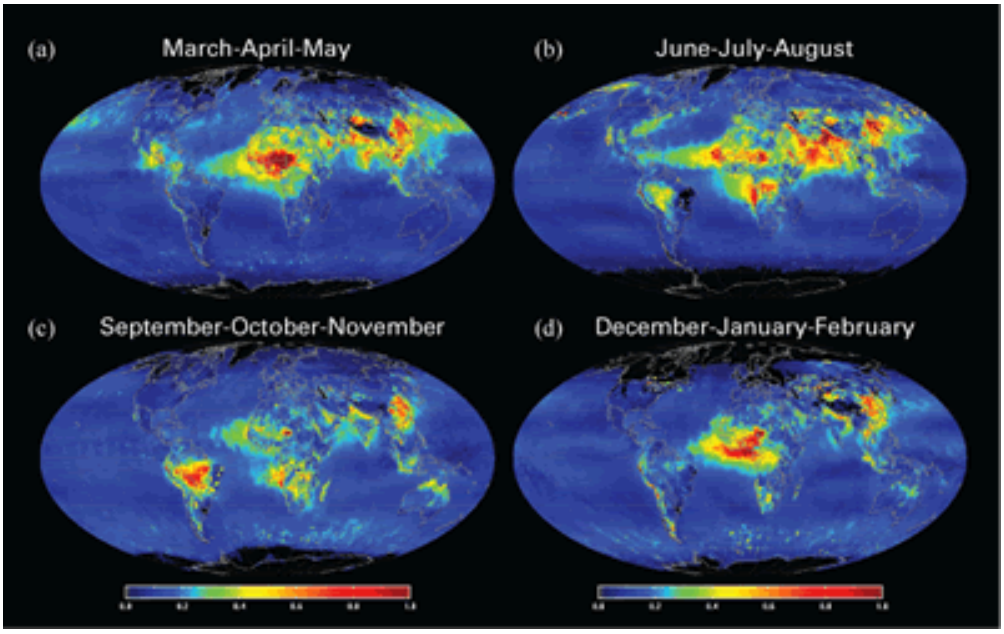

Figure 2.11. Global distribution of MODIS aerosol optical depth at 0.55 µm showing aerosol hotspots for (a) March-April-May; (b) June-July-August; (c) September-October-November; and (d) December-January-February 2005. (Hsu et al., 2004)

More recently (Taylor et al., 2015), there has been an approach to characterise atmospheric aerosol mixtures that contain different ratios of particles (figure 2.12). This has been possible using satellite products and applying a cluster analysis tool that separated the dominant mixtures found on the atmosphere. This procedure has to be applied to ground based measurement due to coherent spatial AOD biases observed (Shi et al., 2011). Marine and dusty smoke dominate around 48% of the globe. Northern hemisphere is nearly dominated by dusty Sulfate and marine dusty sulfate mixtures. Southern hemisphere is spanned by marine sulfate almost entirely below 15^{o} S.

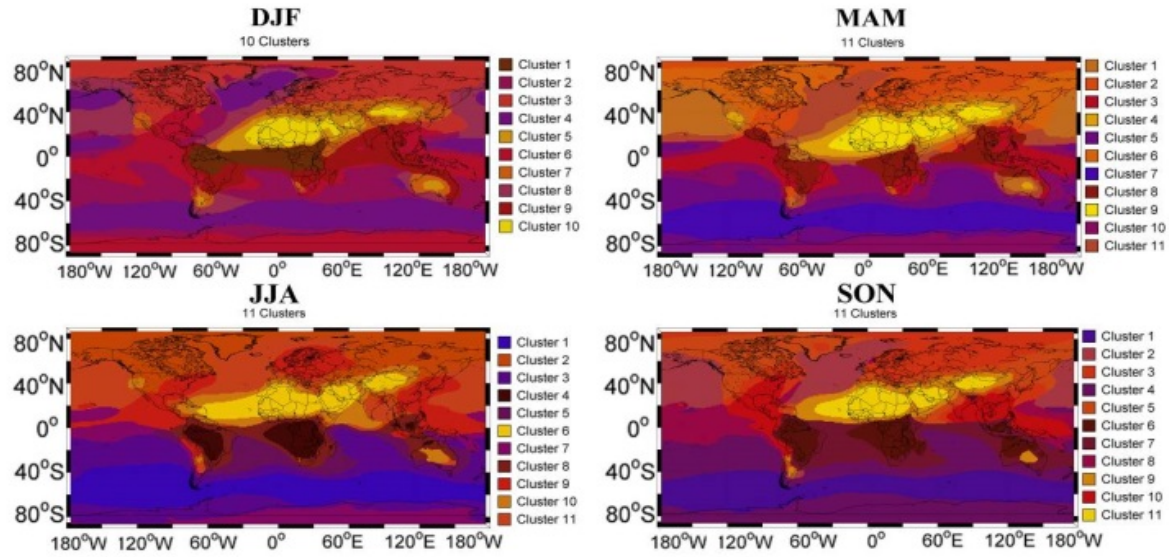

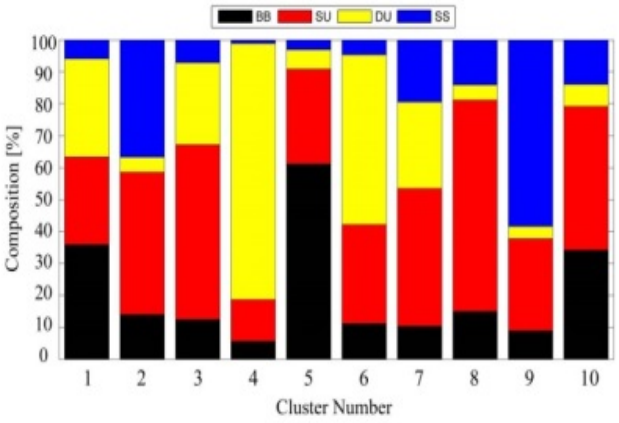

Figure 2.12 The spatial distribution of aerosol mixtures resulting from application of a clustering algorithm to the seasonal mean of global GOCART chemical data for the monthly triplets: DJF, MAM, JJA and SON. Legend of the clusters is explained in the left figure where Sulfate (SU), dust (DU), sea salt (SS) and Black Carbon (BB) AOD participation in the final composition of the mixture. Source: Taylor et al., 2015

One important variable for the radiative transfer calculations is Single Scattering Albedo (SSA), which is defined as the ratio of scattering to total extinction. Thus, it is linked to the chemical composition and the structure of the particles. SSA at a wavelength λ is defined as the relative contribution of aerosol scattering extinction (b_{sca}) to total extinction ($b_{sca}+b_{abs}$), thus indirectly is describing also the absorption contribution (b_{abs})

$$SSA(\lambda)=(b_{sca}(\lambda))/(b_{sca}(\lambda)+b_{abs}(\lambda)), \quad (2.12)$$

Values of SSA range from 0 to 1 by definition; yet, in Earth's atmosphere, they are rarely lower than 0.65 (Corr et al., 2009). High SSA signifies more scattering aerosols, while lower values are linked to more absorbing types. SSA value determines the cooling/warming outcome of the aerosol radiative forcing effect (Reid and Hobbs., 1998) Thus, uncertainties in the estimation of SSA lead to changes on the sign of forcing. Also, SSA is strongly spectral depended, demonstrating different behavior according to aerosol mixture which may lead to significant changes as a function of wavelength (Russel et al., 2010). SSA used in radiative transfer model (RTM) calculations refers to the vertical profile (column) of the aerosol extinction coefficient that usually differs significantly from the in-situ measured one (Kazadzis et al., 2016). These profiles of the extinction coefficient can be retrieved by airborne in situ vertical profiling of aerosols (Schwarz et al., 2010, Skeie et al., 2011, Andrews et al., 2017), but this approach remains very expensive and is rarely used, in experimental campaigns.

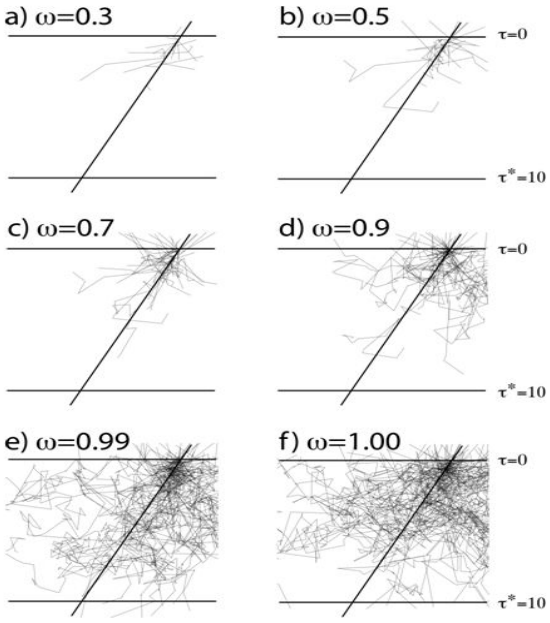

Figure 2.13 Random paths of 100 photons in plane parallel, isotropically scattering layer for variable single scattering albedo (ω).

The asymmetry parameter g, quantifies the degree of asymmetry of the angular scattering (phase function) $P_\lambda(\Theta)$, where Θ is the scattering angle

$$g_\lambda = \frac{1}{2}\int P_\lambda(\Theta)cos\Theta\ sin\Theta\ d\Theta \quad (2.13)$$

Values of g could vary between -1 for entirely backscattered light to 1 to entirely forward scattering, while for Rayleigh scattering g=0. For aerosols in earth's atmosphere, g usually varies between 0.6 and 0.7, having lower values in dry ambient conditions (Andrews et al., 2006).

Real aerosol mixtures in earth's atmosphere are quite commonly described by size distribution. Particle's diameter is the most defining characteristic for each aerosol. Though, having a large collection of particles is impossible to count each diameter, thus a distribution fitting in a histogram representing the number of particles in intervals of diameters. Size distribution could be defined by

surface area: dA/dlnDp (2.14)

volume: dV/dlnDp (2.15)

mass : dM/dlnDp (2.16)

where N is the particle number concentration, Dp the particle diameter. Different definitions apply to specific measuring techniques (eg Yamamoto and Tanaka, 1969 Hoppel,1978, Wolfenbarger and Seinfeld, 1990), but under the assumption of spherical particles all three of them could be calculated. Coarse aerosols are usually less in number but contain the largest part of mass and volume. Because of their size, coarse particles are usually quickly deposed on the ground, near the source of emmision, but in cases of strong convection could be lift higher in the troposphere and be transported from prevailing winds. Fine mode aerosols contain the dominant part of aerosol surface area, so they are the most important scatterers of solar irradiance. Finally, the size distribution of aerosol mixture is very important to the scattering effect, since diameter of the particles affects directly the scattering cross-sections.

2.3.2 Water Vapour

Water Vapour is water in gaseous phase. Water Vapour is the main greenhouse effect gas in the atmosphere and its contribution to the effect is considered to be two to three times higher than the one of CO_2. Also, Water Vapour is involved in cloud formation, radiative transfer and energy exchange in the atmosphere-ocean system. Most of the water vapour is emitted in the atmosphere by evapouration at ocean surface, which is more intense near the equators. Additional water in vapour form, is emitted by human activities, such as evapouration from agriculture, power plant cooling and combustion of fossil fuels. Still all these procedures are a very small – practically negligible - part of the water vapour flux, and thus it is categorized as a natural gas contribution to radiative forcing. But the behavior of water vapour in the atmosphere is fundamentally different from other greenhouse gases (CO_2) because it can condense and precipitate, which are control from the physical properties of the atmosphere and thus it is considered as a feedback agent for climate change. Water Vapour is a very important component of the thermodynamic state of the atmosphere (Hartman et, al 2013), being a greenhouse gas with relatively high concentrations. The quantity of water in the vapour state depends on temperature thus, from a climate change perspective, it is considered as a feedback agent (Soden and Hled, 2006). Also, it is an important component of the hydrological cycle and estimations of it are used in meteorological forecast models (eg. Hong et al., 2015, Bock et al., 2016). Finally, a robust estimation is needed to study microphysical processes that lead to the formation of clouds and determine their composition (water droplets or ice crystals) as well as the statistical shape and size of these components (Reichard et al., 1996, Yu et al., 2014). Water Vapour is found almost exclusively in the troposphere, with concentrations of 1ppb at the tropopause and decreases very quickly with height, so that more than 95% of it is located in the first 3 km from the surface.

Integrated Water Vapour (IWV) in the vertical atmospheric column is a very common variable in meteorological and climatological studies. It is defined as the height that water would stand if completely condensed and collected in a vessel of the same unit cross section (American Meteorological Society, 2015). Thus, it is the variable that is linked to the optical depth of water vapour and is more used in radiative studies. In polar regions it has almost zero values, while in the tropics, the highest values are recorded and a band of extremely humid air wobbles north and south of the equator as the seasons change. This band of humidity is part of the Intertropical Convergence Zone, where the easterly trade winds from each hemisphere converge and produce near-daily thunderstorms and clouds. The most humid are is found in western equatorial pacific, where the highest sea surface

temperature is observed and called oceanic warm pool. Further from the equator, water vapour concentrations are high in the hemisphere experiencing summer and low in the one experiencing winter. Exceptions of this zonal distribution are found over deserts, where the atmosphere is very dry. Also, water vapour amounts over land areas decrease more in winter months than adjacent ocean areas do. This is largely because air temperatures over land drop more in the winter than temperatures over the ocean. Water vapour condenses more rapidly in colder air.

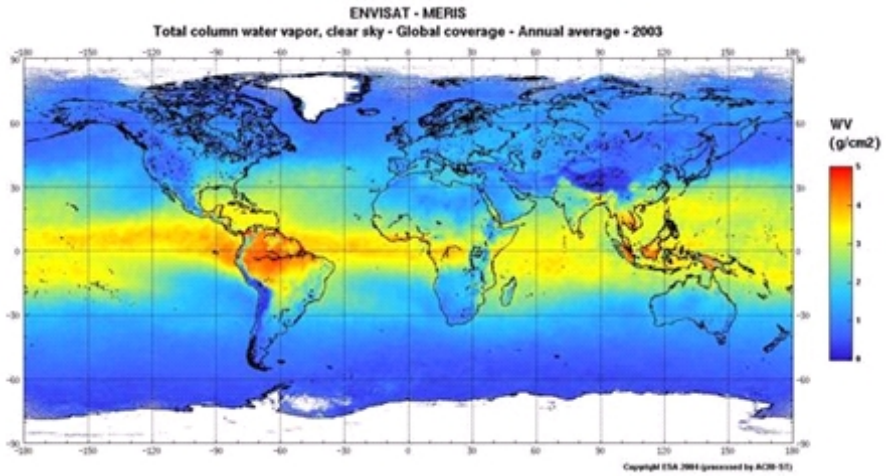

Figure 2.14 Total Column of Water Vapour (annual product 2003) (image courtesy of ACRI-ST)

2.3.3 Ozone

Ozone is the most important absorber of ultraviolet (UV) radiation in the Earth's atmosphere, and has become a focus of great scientific and public interest over the past few decades due to the growing awareness of the effects of UV on human health. Ozone in the stratosphere is produced by photochemical reaction of oxygen molecules and UV irradiance, which produces atomic oxygen and afterwards ozone. Most of the stratospheric Ozone is produced near the equator but it is transported by air mass movement toward the poles, where the mechanism is described in detail by Brewer-Dobson circulation model (Brewer, 1949, Dobson, 1956). Favoured by the extensive poleward air currents, ozone reaches its highest values over the Canadian Arctic and over Siberia. During winter in the southern hemisphere, a nearly symmetrical cold air polar vortex prevents the ozone- rich air from the tropics from reaching southernmost latitudes. Ozone concentration remains high over middle latitudes until the austral summer. these specific meteorological conditions over Antarctica and the presence of large amounts of reactive chlorine facilitate ozone destruction. Tropopause is the layer separating

troposphere and stratosphere, and usually is the lowest height of the ozone layer. Smaller amounts of ozone are produced in the troposphere by photochemical reactions involving natural gases and gases from pollution sources, such hydrocarbon, nitrogen oxides and ozone. Parts of stratospheric ozone are sometimes transported to the troposphere and influence tropospheric ozone, especially in remote unpolluted areas.

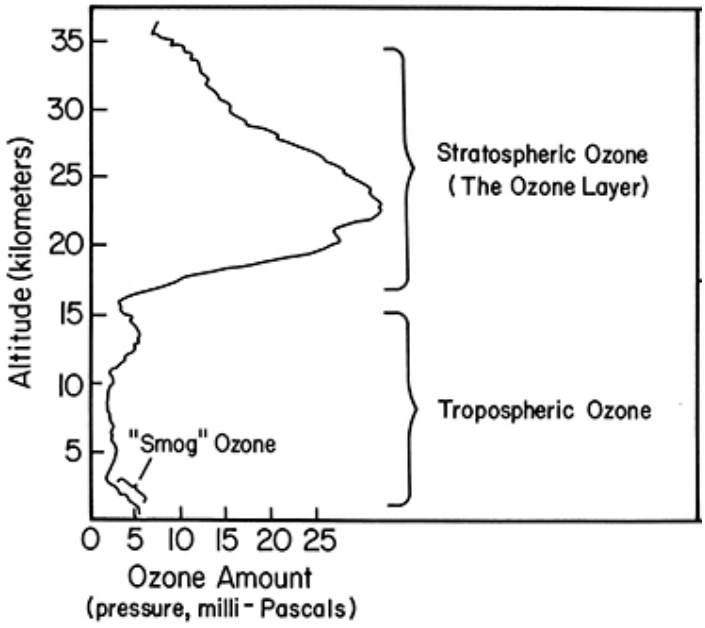

Figure 2.15 Cross section of typical vertical ozone profile at the tropics, source WMO

Absorption by ozone is becoming more important at shorter wavelengths as the absorption cross sections of ozone decrease with increasing wavelength and decreasing temperature (Bass and Paur, 1985; Molina and Molina, 1986). However, the cross sections that better describe the spectral absorption of UV radiation in the atmosphere are still under discussion (Fragkos et al., 2013; Redondas et al., 2014). Towards the end of the twentieth century, a significant reduction of stratospheric ozone was observed by various studies, both at the global scale (e.g. Staehelin et al., 1994, Fioletov 2008; Mäder et al. 2007) and also locally, e.g. over Greece (Varotsos, Kondratyev, and Cracknell 2000; Zerefos 2002). After the ratification of the Montreal Protocol on 1 January 1989, the concentration of ozone-depleting substances worldwide has reduced (WMO 2006); however, local exceptions to this trend are the subject of active research. For example, extremely low ozone values were observed in the Arctic during early 2011 (e.g. Varotsos, Cracknell, and Tzanis 2012). Monitoring stratospheric ozone is crucial for detecting other local perturbations such as these and for analysing future trends, in particular the

influence of ozone concentrations on incoming UV irradiance and climate change. Importantly, over northern mid-latitudes, a decline of ≈ 3.5% has been recorded in UV radiation in the recent years relative to the 1964–1980 mean value (Bais et al. 2014).

Total Ozone Column (TOC) is a variable used to describe the amount of ozone in an atmospheric column, which is defined as being equal to the amount of ozone contained in a vertical column of base 1 cm^2 at standard pressure and temperature (Dobson and Harrison, 1929). It is expressed in length units, but the most common unit is Dobson Unit (DU) that corresponds to an ozone layer of 0.01 mm thickness. TOC sums up all the ozone in the atmosphere, but the largest part is usually in the stratosphere, so it is used as an indicator for stratospheric ozone. In records it varies from 230 to 500 DU, having the lowest values over the equatorial belt and increasing with latitude. A brief climatology of Stratospheric Ozone found in Ziemke et al., (2011) is presented in figure 2.12. Maximum values are observed in North Hemisphere from February to April, and in South Hemisphere during September-October. At North Hemisphere, maximum monthly values are about 50 DU higher than ones at the South Hemisphere. Also over the Antarctic there are values below 150 DU, occurring in September-October linked to the ozone hole. This climatology could have inter-annual variations due to sudden stratospheric warming events or due to the breakup of the middle atmosphere polar vortex. Also, mid-latitude stratospheric ozone demonstrates a significant increase the last two decades linked to the changes after Montreal Protocol (Chipperfield et al., 2017).

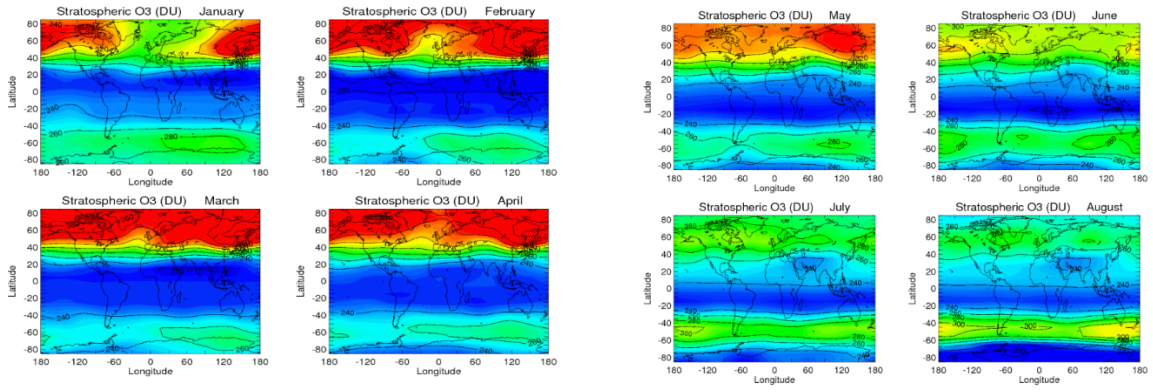

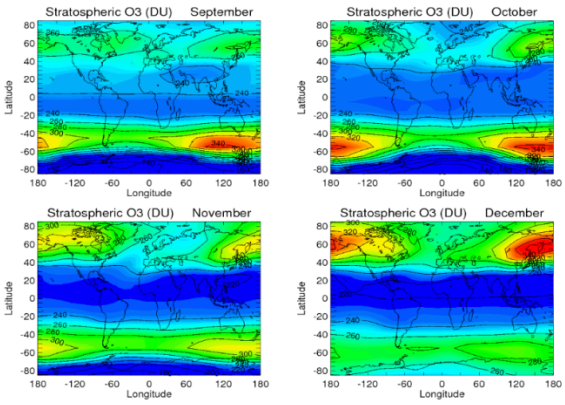

Figure 2.16 Mean Monthly Stratospheric Ozone in DU, as calculated by OMI/MLS residual ozone measurements 2004-2010. Source Ziemke et al., 2011

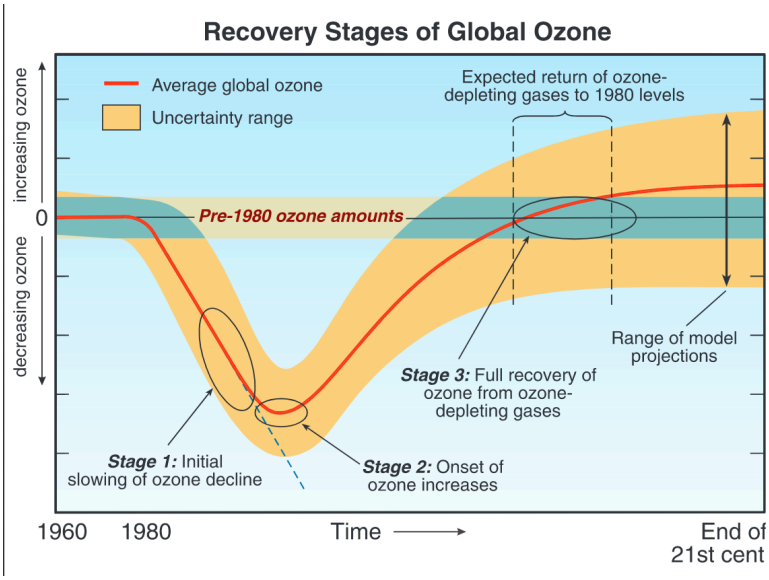

Figure 2.17 Global ozone amounts and modeled estimations of recovery. Source (Braathen, 2012)

2.3.4 Rayleigh Scattering

Scattering of solar radiation by the air molecules in the atmosphere, can be described by Rayleigh's scattering theory for particles much smaller than the wavelength of light and is the main mechanism that causes DHI. Rayleigh scattering is an approximate solution for the Mie theory of scattering of an electromagnetic plane wave by an homogeneous sphere, which in the atmosphere is applied also in particles with comparable diameters to the wavelength of the radiation (Rayleigh, 1914). Under that assumption, molecules can be represented by ideal dipoles that are excited by an incident plane wave of intensity to emit – according to Huygens principle (Maron, 1967) – a spherical wave, the scattered

radiation. The scattering amplitude is proportional to the square of the frequency and to the polarizability of the dipole, and its angular distribution depends on the polarization of the incident wave. It varies with the cosine of the scattering angle ϑ for light polarized parallel to the scattering plane and is omnidirectional for light polarized perpendicular to the scattering plane. If the incident light is unpolarized, the scattered light will be partially polarized. In the case of small particles that Rayleigh scattering applies ($x \ll 1$,) the whole surface re-radiates with the same phase. Because the particles are randomly positioned, the scattered light arrives at a particular point with a random collection of phases; it is incoherent and the resulting intensity is just the sum of the squares of the amplitudes from each particle and therefore proportional to the inverse fourth power of the wavelength and the sixth power of its size (Barnett, 1942).

The total Rayleigh scattering cross section per molecule, σ, is defined by the following formula (Bucholtz, 1995)

:

$$\sigma(\lambda) = \frac{24\pi^3\left(n_s^2-1\right)^2}{\lambda^4 N_s^2\left(n_s^2+2\right)^2}\left(\frac{6+3\rho_n}{6-7\rho_n}\right) \quad (2.17)$$

where n_s is the refractive index for standard air at wavelength λ, N_s is molecular number density ($2.54743*10^{19}$ cm^{-3}), and ρ_n is the depolarization factor which accounts for the anisotropy of the air molecule. Thus, the optical depth could be calculated using these cross sections by the formula (Bodhaine et al., 1999)

$$\tau_{ray}(\lambda) = \sigma(\lambda)\frac{p\,A}{m_a g} \quad (2.18)$$

where p is the atmospheric pressure, A is Avogadro's number, m_a is the molecular weight of air and g is gravity's acceleration. Most commonly used tables of σ(λ) are found at Penndorf (1957). A number of studies (eg Teillet 1990, Nicolet 1984, Stephens 1994) have tried to fit equations on the calculated optical depths from the σ tables. At this study, all calculations have been made with the formula found at Dutton et al. (1994)

$$\tau_{ray}(\lambda) = 0.0088\left(\frac{p}{p_0}\right)\lambda^{-4.05} \quad (2.19)$$

where p_0 is the atmospheric pressure at sea level (about 1013.25mb). Following equation, figure 2.18 visualises the Rayleigh optical depth in the spectral region 0-

2000nm. From this figure is clear that in infrared band, the phenomenon weakens very rapidly, but in the ultraviolet spectral region has a very dominant presence.

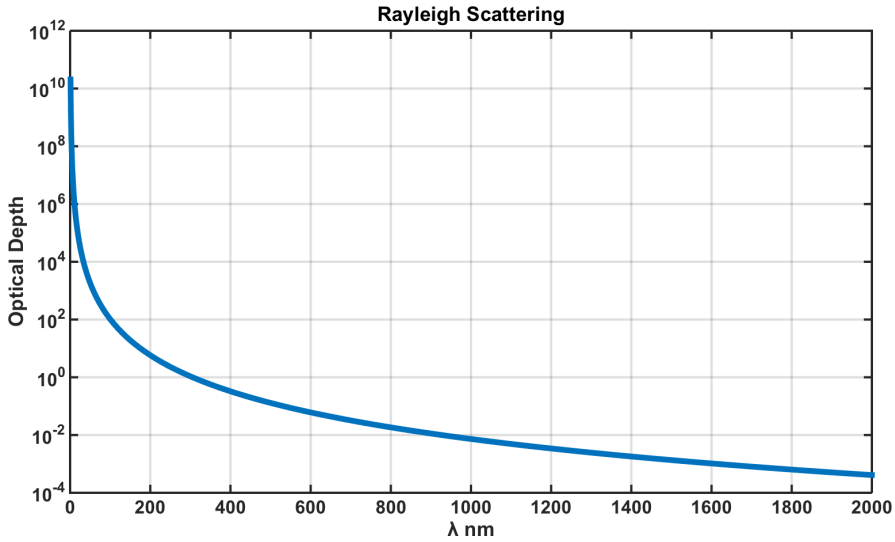

Figure 2.18 Rayleigh scattering optical depth, for the spectral region 0-2000nm as calculated by the formula suggest by Dutton et al. (1994)

2.3.5 Clouds

Clouds affect daily weather and play major role in the climate and are crucial to hydrological cycle. Clouds are formed in the atmosphere, when air cool and moisten until it reaches a supersaturation point where condensation nuclei's can be activated. Clouds could be composed by liquid water, ice or a mix of both. When droplets or ice particles in the clouds became large enough, will fall on the surface as precipitation. Clouds cover about 60% of the globe (Wielicki and Parker, 1992), while most of them are located in mid latitude oceanic storm tracks and tropical precipitation belts. Clouds participate in various atmospheric physical and chemical processes including a major influence on the solar and infrared radiation that enters and leaves the atmosphere. This influence is complex and it has the potential to act on climatic procedures (Stephens 2005). In the context of climate change, specific attention has been draught to cloud amount, cloud height (as high clouds trap longwave radiation) and cloud reflectivity (Bouscher et al., 2013).

In the visible spectral range, light is scattered evenly by clouds, hence fog and clouds appear white. Since clouds scatter all wavelengths of light, all energy that reaches the Earth's surface is blocked. Result of this procedure is that solar radiation's greatest variability is caused by cloud coverage (Kerr and Fioletov, 2008). Also, during broken clouds conditions, enhancement of recorded irradiance

has been reported (Crawford et al.,2003, de Miguel et al.,2011) This can make analyzing radiometric measurement difficult in areas prone to cloud cover. Clouds also cast shadows that change the illumination and relative reflectance of surfaces. Cloud's effect on radiative transfer depends on the fraction and part of the sky they are located and their height and synthesis (Bynyamin et al., 2010, Bais et al., 2015). Cloud transmittance is also spectral dependent (Kerr and Fioletov, 2008) and usually described by Cloud Optical Thickness (COT). A thick cloud has high COT, especially if it has a high density of moisture. Lower values of COT are found when clouds are thin or very cold. Longwave radiation is sensitive to thick clouds independently of their altitude (Bouscher at al., 2013).

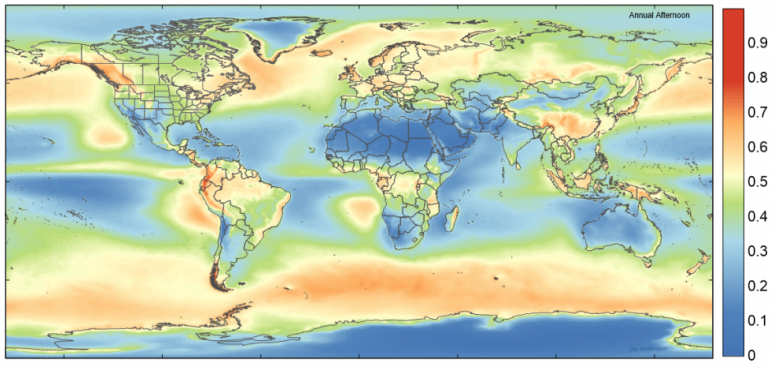

Figure 2.19 Map of global annual afternoon cloudiness derived from observations from the Aqua satellite. Source: NASA.

2.3.6 Other trace gases

Trace gases with relatively lower concentrations in earth's atmosphere, also absorb the solar radiation.

Nitrogen Dioxide (NO_2) is introduced into the environment by natural causes, including entry from the stratosphere, bacterial respiration, volcanos, and lightning, and also from anthropogenic sources mainly from fossil fuel burning andit has an important role in photochemistry, regulating tropospheric ozone concentrations. It has several effects on human health and is classifies as extremely hazardous both for respiratory and blood/heart effects. NO_2 load has been retrieved from remote sensing measurements both from satellite (OMI, Russel et al., 2012) and ground based (PANDORA, Tzortziou et al., 2015).

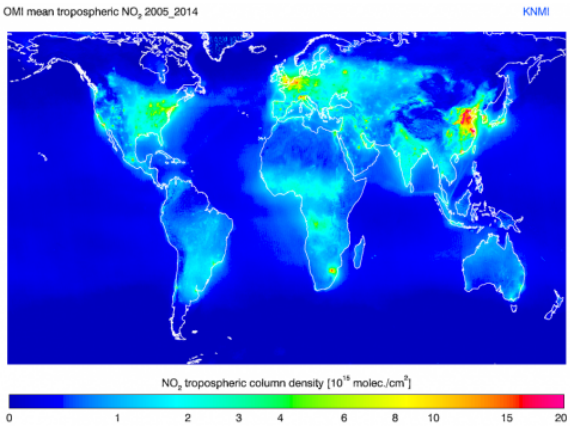

Figure 2.20 The TROPOMI NO_2 processing system is based on DOMINO, developed for the OMI NO_2 retrieval

Sulfur Dioxide (SO_2) plays an important role in atmospheric chemistry, by forming sulfate aerosols that influence weather and climate and also forms sulfuric acid (Hutchinson and Whitby, 1977) which causes acid rain. Main natural source is volcanic activity. Anthropogenic emissions include coal burning power plants, smelters and oil refineries. It is also characterized as an air pollutant and monitored for public health hazards (Longo et al., 2010). It mainly absorbs in the UV spectrum and it has been retrieved from satellites (Fioletov et al. 2015, Li et al., 2016) and ground based instruments as Brewer (Krueger et al., 1995, Bais et al., 1993) and Pandora (Fioletov et al., 2016)

Formaldehyde (HCHO) is a principal intermediate in the oxidation of hydrocarbons in the troposphere, while Oxidation of methane (CH_4) by the hydroxyl radical (OH) is the principal source of HCHO in most of the troposphere; loss of HCHO is mainly by photolysis and reaction with OH (Chance et al., 2000). In view of its widespread use, toxicity, and volatility, formaldehyde poses a significant danger to human health and been described as human carcinogen. It has been retrieved from satellite measurements from GOME (Chance et al., 2000) and OMI (Millet et al., 2006) while a number of industrial areas are facing Formaldehyde pollution problems (Garcia et al., 2006).

3. Instruments, models and data

3.1 Sites

In present study, data collected at two different measuring stations are used. The selection was based on data availability and quality and the presence of different collocated instruments that gave the opportunity to evaluate and validate retrievals.

3.1.1. Athens

Since February 2009, the ground-based Atmospheric Remote Sensing Station (ARSS) has been in continuous operation to monitor ground radiation levels and aerosol loadings over Athens (Amiridis et al., 2009). The ARSS is located on the roof of the Biomedical Research Foundation of the Academy of Athens (37.9 N, 23.0E, 130 m a.s.l.) (http://apcg.meteo.noa.gr/index.php?option=l12&client=&langid=2), which is located near the city center, 10 km from the sea (Gerasopoulos et al., 2009). The horizon view is clear at 360 degrees viewing angle. ARSS is equipped with a CIMEL CE318-NEDPS9 and an Ultraviolet MultiFilter Radiometer (UVFMR). Also, a Brewer single monochromator (Brewer #001) is installed on the same roof. The period of measurements analyzed is from July 2009 to May 2014, when all the above-mentioned instruments were fully functional. Athens is a city of 3.7 million habitants with an estimated of 2.5 million automobiles and heavy traffic, which is the single greatest source of local emissions. The area has been heavily deindustrialized the previous decades, but there are still emissions linked to factories and fossil fuels. Athens is located in a basin, where three mountains with height around 1km, trap most of the urban emissions in the greater area, due to poor ventilation. For the dispersion of pollutants the major case it the sea breeze along the NE-SW axis (Kalabokas et al. 1999). Also, there are common cases of long transport of air masses from arid areas of Northern Africa, frequently associated with dust events that affect the area (Gkikas et al., 2016). Athens has a temperate climate with warm and dry summers and wet and mild winters, typical for the Eastern Mediterranean. AERONET retrievals from Cimel sunphotometer for the period 2008-2017, show a mean AOD at 500 nm of 0.17±0.08, while maximum values are observed during April-June period and minimum on December. Average ångström exponent 440-870 nm is found at 1.31±0.18 which is typical of urban sites (Dubovik et al., 2002).

Figure 3.1 Map of Athens and greater Mediterranean region where the location of ARSS is signed with a star.

3.1.2. Lindenberg

Data recorded at Meteorologisches Observatorium Lindenberg – Richard Assmann Observatorium (MOL-RAO) from the German Meteorological Service "Deutscher Wetterdienst" (DWD) in Lindenberg (Tauche), in the North-East Germany (52° 12′ N, 14° 7′ E), have been used for the period May 2014- April 2016. MOL-RAO is a supersite for measurements of aerology and radiation, thus it provides a variety of collocated measurements that could be used for validation. MOL-RAO is exclusively devoted to instrumental measurements of the atmosphere and a numerous technical staff guarantees daily maintenance of the instruments. Sunshine at the area ranges from 55 hours/month at December to 256 hours/month during summer months on average; also, rain is recorded almost for 1/3 of days during all 12 months period (Beyrich and Adam, 2005). Minimum solar zenith angle (SZA) reaches 30^{o} during summer months while during winter it is over 70^{o}. AOD is generally very low in the area, with maximum mean monthly values of 0.25 to 0.27 during June and July. Instruments providing data for this study include Prescision Spectral Radiometer (PSR), Microwave Radiometer, CIMEL, radiosondes and a GPS receiver. MOL-RAO is located in a rural area, 90 km southeast from Berlin.

Figure 3.2 Map with the location of MOL-RAO pinpointed (left), photometric devices installed and functioning on a tracker at MOL-RAO (upper right) and a microwave radiometer along with pyranometers at MOL-RAO (lower right)

3.2Instruments

3.2.1 Ultraviolet MultiFilter Radiometer

The UVMFR (Yankee Environmental Systems, Inc) is a shadowband instrument that measures GHI and DHI in the UV part of the solar spectrum. Measurements are performed centred at 7 wavelengths (300, 305, 311, 317, 325, 332, and 368 nm) with a 2nm nominal full width at half maximum bandwidth. Signals in all channels are recorded simultaneously by different photodiode detectors passing through a single Lambertian diffuser made of Teflon, with measuring cycle lasting 10 seconds, and 1 minute average values are stored. Each measuring cycle consists of two DHI measurements, with different sun blocking positions of the shadowband and one GHI measurement. The DI component is calculated at the same time by deducting measured components. The USDA UV-B Monitoring and Research Program (UVMRP) continuously operates 31 of these instruments at sites distributed across the United States (Harrison et al., 1994, Bigelov et al. 1998, Kaye et al., 1999, Michalsky et al., 2008)

Figure 3.3 UVMFR installed and functioning at FINOKALIA, Greece.

UVMFR measurements are corrected using dark signal (Stray currents or voltages generated by the electronics in the absence of light) and angular response corrections as shown figure 3.4 (Krotkov et al., 2002).Angular response correction is linked with the non ideal (cosine) angular response of the instrument diffuser

entrance optic. Raw measurements from the instrument are saved in terms of detector voltages. YESDAS manager software applies the corrections and a provided calibration function to transform measured voltage into W/m^2.

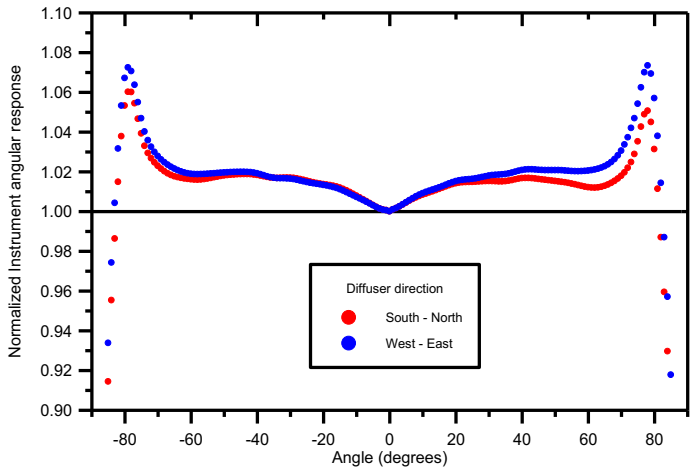

Figure 3.4. UVMFR deviation of angular response function from nominal cosine response at 368nm channel, normalized to the ideal (cosine) angular response. 2 sets of responses one from the south to north scan and one from the west to east are presented.

In order to apply further calculations and estimate the attenuators, it is needed a robust estimation of I_0. This is possible through the Langley calibration technique (Slusser et al., 2000). In order to apply this technique, equation 2.4 is written as

$$\ln(I_{0\lambda})=\ln(I_{\lambda})-\ln(T_{R\lambda}) \quad (3.1)$$

where I_{λ} is the measured in the channel corresponding to wavelength λ and $T_{R\lambda}$ is retrieved as

$$T_{R\lambda}=\exp(-m[AOD(\lambda)+\tau_{ray}(\lambda)+\tau_{O3}(\lambda)]) \quad (3.2)$$

Hence, equation 3.1 could provide an estimation of $I_{0\lambda}$ as linear regression of the other parameters. $T_{R\lambda}$ could be treated with two different approaches. Most field calibrations using Langley regression are performed at pristine high altitude sites were aerosol load is very low and stable and preferably low latitudes where ozone layer is more stable (Schmid and Werhli 1995, Wilson and Forgan, 1995). In that

case a collection of measurements at cloudless conditions at different SZA, in a time interval of few hours –usually half a day in order to have negligible variations in TOC, is used to extrapolate equation 3.1 to m=0 and retrieve $I_{0\lambda}$. In Athens such low aerosol loads are rarely observed, but using collocated AERONET AOD retrievals, half-days with low AOD (<0.1) and the technique was applied. Figure 3.5 has an example of the extrapolation on14 August 2013 during morning hours. For this study extraterrestial values were retrieved only for the 368 and 332 nm channels, where the influence of TOC is negligible (Bass and Paur, 1984). Though it is common to observe a drift in $I_{0\lambda}$ in long term datasets, due to instrumental decay, values retrieved for Athens dataset seem to have a small variation through the five year period.

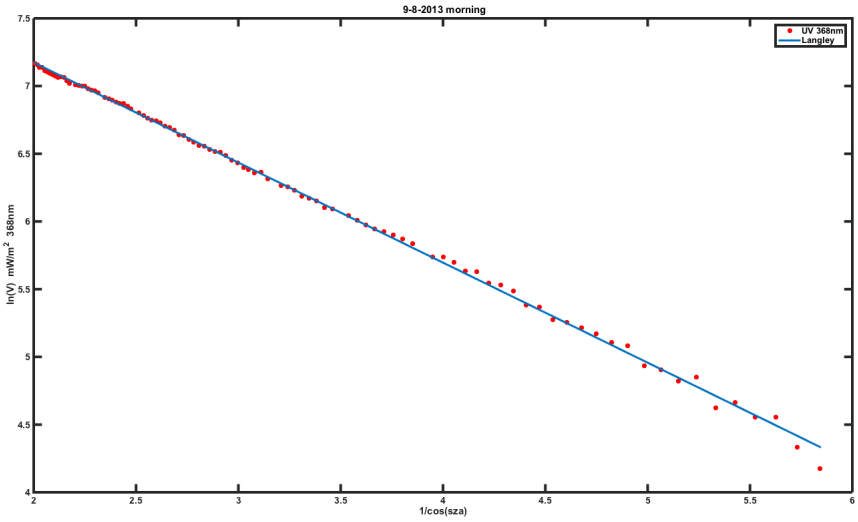

Figure 3.5 Langley plot of 368nm measurements from UVMFR on 14 August 2013 during morning hours.

Another approach is to extrapolate AOD from another instrument and use this in equation 3.2 (Kroktov et al., 2005a). Benefit from this approach is that it can be used in any aerosol load, even in heavy polluted areas. Though the main drawback is that method just transfers the calibration of the other instrument, and retrievals should not be treated as independent.

In order to examine the consistency of the values found with Langley regression, $I_{0\lambda}$ was also calculated with the second approach, by using AERONET retrievals, (see ch. 3.2.2) for the same days. Both independent approaches appear stable through the years, with no obvious drift or change, so we decided to use a single ETC for the whole period for each wavelength.

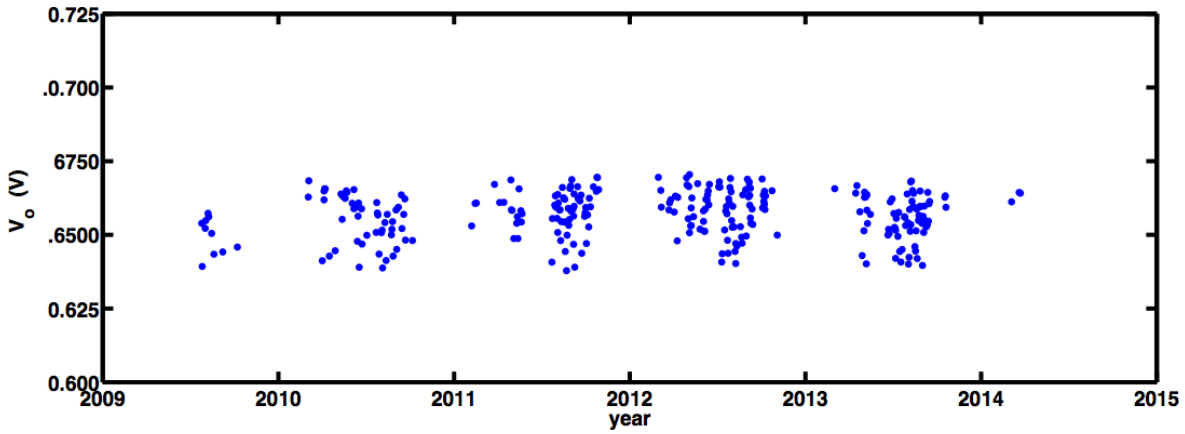

Figure 3.6. Extraterrestrial constant values at 368nm, calculated using Langley plots of UVMFR measurements, and Using Cimel extrapolated AOD's as input, for selected (low AOD's and clear sky) days for the whole period

GHI measurements from the UVMFR have been used in order to distinguish cloud free conditions for each of the one minute measurements. Clouds are detectable in the measured UVMFR GHI (at 368nm) since they cause larger variability than aerosols. In order to distinguish between cloudy and cloud free conditions, we applied an updated version of the method of Gröbner et al. (2001) which is based on a comparison of the measured DNI with RTM calculations in cloud free conditions. The method is based on the comparison of the measured GHI with radiative transfer calculations for cloud free conditions and quality assurance is checked by the following criteria:

a. The measured GHI has to lie within the modeled (cloud free) GHI for a range of aerosol loads (AOD at 500 nm of 0.1 and 0.8, respectively), corresponding to the 5th and 95th percentile of the AERONET data for the examined location and period

b. The rate of change in the measured GHI with SZA has to be within the limits depicted by the modeled cloud free GHI, otherwise the measurements are assumed cloud contamination.

c. All measured GHI values within a time window (dt= ±10 min) should be within 5% of the modeled cloud free GI, and adjusted to the level of the measurement, using an integral over time interval.

If at least 85% of the points in the time window pass tests a) – c), then the central point is flagged as cloud free. In this study, a tolerance level of ±10% was allowed for tests a) and b) in order to compensate for differences between the

modeled GHI and measured GHI due to instrumental uncertainties, as well as for usage of average climatological parameters (SSA, TOC e.t.c.) as inputs to the model. The method was limited to SZA<70^o to avoid uncertainties related with low solar radiation levels. An example of the results of the method is presented in figure 2 for a day with variable cloudiness. It should be noted that in all CIMEL-UVMFR comparisons, using synchronous measurements, both the above method and AERONET cloud screening algorithm (presented by Smirnov, et al, 2000) are considered.

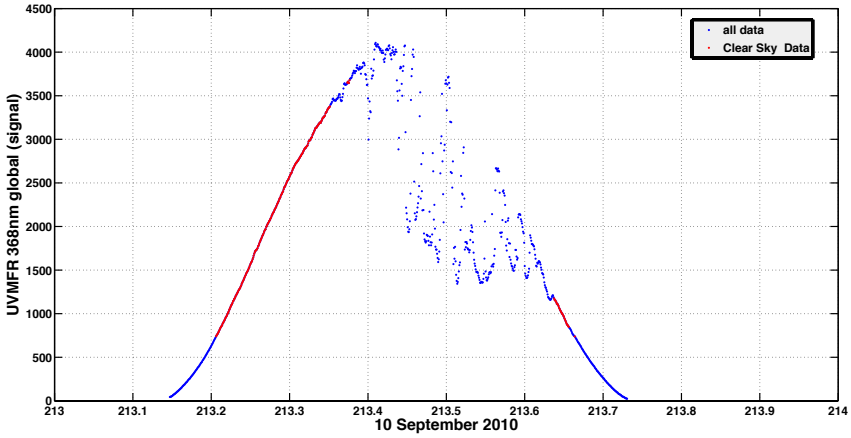

Figure 3.7. Determination of cloudless 1-minute measurements (red), from all measurements (blue) for a day with variable cloudiness in the afternoon.

3.2.2 CIMEL solar radiometer

The CIMEL sun-photometer is a filter radiometer developed by Cimel Electronics (Paris, France), which performs direct sun and sky radiance measurements.. Measurements are performed at eight nine bandpass filters between 340 and 1064 1640 nm (8 of them dedicated to AOD retrieving and one used for IWV). Direct measurements are performed usually every 10-15 minutes. These measurements are processed centrally and are widely available through Aerosol Robotic Network (AERONET) (Holben et al., 1998). AERONET data provide globally distributed observations of spectral aerosol optical depth (AOD), inversion products and IWV in diverse aerosol regimes. Aerosol optical depth data are computed for three data quality levels: Level 1.0 (unscreened), Level 1.5 (cloud screened), and Level 2.0 (cloud-screened and quality-assured).

Figure 3.8 Cimel sun photometer installed and running at NOA's Actinometric station.

Cimel sunphotometer measures direct solar irradiance by first pointing the collimator toward the approximate position of the sun (provided it is aligned properly) based on an in-built program that takes into account the time of the year and the coordinates of the location. A 4-quadrant detector then positions the sun at the center of the fields of view of the collimators by using a feedback control loop. The filter wheel rotates in front of the detector to obtain a measurement sequence. A sequence takes about 10 seconds. In order to discriminate against the presence of thin cirrus clouds, which may be non-uniform, three measurement sequences are performed (called as a triplet), lasting about 35 seconds.

Almucantar sky radiance is obtained by scanning the sky at the solar zenith angle but different azimuth angles to obtain the angular variation of skylight in 4 filters.

Solar principal plane sky measurement is obtained by scanning the sky in a plane containing the sun and the instrument and normal to the surface. Data are taken more frequently near the sun since the intensity varies rapidly in the solar aureole. The sky brightness data is inverted by radiative transfer routines to derive aerosol size distribution, SSA and phase function (Dubovik and King, 2000, Dubovik et al., 2002, 2006). The inversion procedure includes assumptions as

- Plane parallel atmosphere
- Particles are portioned in spherical and non-spherical components, and have the same complex index of refraction for all sizes (Dubovik et al., 2006).
- Homogeneous vertical distribution for almucantar inversions

- The statistically optimized inversion and corresponding retrieval error estimates are obtained under the assumption of uncorrelated log normally distributed errors (Dubovik , 2004).

Quality control for Level 2.0 inversion retrievals, have some strict criteria to reject data, because of the above assumptions and the high uncertainties introduces. These criteria includes the symmetry of radiance in all angles not to exceed 20%, all residuals from the models should not exceed 10%, sky residual errors as function of AOD440 to be less than 1.5%, and SZA>50^o and for SSA , AOD440 to be greater than 0,4 (Dubovik et al.,2000).

Direct sun measurements at 940 nm are used to retrieve IWV. At this channel the Full Width Half Maximum is 10nm, (Schmid et al., 2001) which means that the solar signal recorded represents a relatively wide spectral region. The method used to retrieve it IWV is described in detail in Smirnov et al. (2004).

AERONET currently operates hundreds stations around the globe, and some of them have been operating more than 20 years, establishing the network as the most important for columnar atmospheric aerosol observation. Centralized calibration of all CIMEL sunphotometers are performed every year, at specific sites (in U.S.A or Europe), which guarantees the quality and the comparability of retrieved data.

The CIMEL data for ARSS and MOL-RAO has been directly downloaded from AERONET website (https://aeronet.gsfc.nasa.gov/).

3.2.3 Precision Spectral Radiometer (PSR)

A new generation of solar spectrophotometers, the Precision Solar Spectroradiometer (PSR), has been developed at PMOD/WRC to eventually replace current filter based sunphotometers. It is based on a temperature stabilized grating spectroradiometer with a 1024 pixel Hamamatsu diode-array detector, operated in a hermetically sealed nitrogen-flushed enclosure. The spectroradiometer is designed to measure the solar spectrum in the 320 to 1040 nm wavelength range with a spectral resolution of about 2 nm full width at half maximum. The optical bench with the optical elements was optimized to reduce the temperature dependence of the solar measurements to less than 1%K over the whole wavelength range. The design benefits from the experience gained from successive generations of the successful Precision Filter Radiometer (PFR), including: an in-built solar pointing sensor, an ambient pressure sensor and temperature sensors to provide routine quality control information which allow autonomous operation at remote sites with state-of-the-art data exchange via

Ethernet interfaces. This includes both optical properties of aerosols and trace gases and variables useful for energy applications and earth's radiative budget.

Figure 3.9 A PSR (left) installed at NOA's actinometric station (Athens), alongside with a Pandora and a CIMEL.

The PSR that used in this study is the PSR#006, which is installed on the MOL-RAO site. This instrument has been calibrated at PMOD/WRC using a 1000 W transfer standard lamp source, in May 2014 and October 2015 (figure 3.10). A comparison between the two calibrations showed relative differences less than 1% for most spectral channels and more than 2% only in the region above 980nm (Kouremeti et al. , 2015). Moreover, stray light corrections have been applied and absolute DI time series are available for all 1024 available channels (Gröbner et al., 2014). The cycle of routine measurements during this period was in a set of 5 direct solar Irradiance and 5 dark current measurements and the average values for each pixel was saved at 1minute resolution.

Figure 3.10 PSR calibration at PMOD/WRC laboratory. (Left) Calibration reference lamp used for PSR calibrations in PMOD/WRC laboratory (Right).

An evaluation of AOD retrievals from PSR have been performed during the 4th Filter Radiometer Comparison (WMO, 2016, Kazadzis et al., 2018). Twenty-nine filter radiometers and spectro-radiometers from twelve countries have participated in this campaign, between September 28 and October 16, 2015, at Davos, Switzerland . Instruments included CIMEL, MFR, SPO and POM. The instruments have been measuring DI and then deriving AOD for the inter-comparison assigned wavelength bands (Channels 368±3nm, 412±3nm, 500±3nm, 865±5nm). Measurements of AOD were compared with the reference triad of PFR instruments of the World aerosol Optical depth research and calibration center (WORCC) which is part of the World Radiation Center (WRC)(Wehrli, 2005). The calibration of the triad was based on the Langley calibration technique and was applied to measurements from these instruments in Izaña, Spain and Mauna Loa, Hawai, USA. During FRC-IV, there were five days (September 28 – 30, October 1 and 12) with sunshine and only very limited presence of clouds. Measurements from these days have been used to compare the participating instruments. Cloudy intervals have been filtered out from all datasets. During the five inter-comparison days, AOD varied from 0.02 up to 0.12 at 500 nm, which can be considered as normal values for the area. The comparison has been based on the criterion defined by WMO as 96% of measured data should be within 0.005±0.001/m. which is noted by the grey line at figure 3.11. 24 out of 29 instruments achieved this limit at 500nm (Kazadzis et al. 2018). Statistics for PSR 006 are presented at table 1 and all available data are plotted as differences from PFR triad average on figure 3.11. A stable performance is observed for all channels, where all wavelengths are inside the designated WMO uncertainty limits, except for few measurements up to 10

measurements at 865 nm, with maximum difference of 0.02 on 29 September. Correlation coefficient is above 0.99 for 368, 412 and 500 nm and 0.98 for 865 nm (lower due to the few data above WMO limits).

Table 3.1 Statistics of Comparisons between PSR 006 and PFR triad during FRC-IV campaign.

Bandwidth (nm)	Median ±1σ	Percentile [5,95]	Correlation Coefficient	Linear Fit Slope, Intercept	N of data
368	+0.005 ± 0.007	[+0.002 , +0.008]	0.996	1.009, 0.005	822
412	-0.000 ± 0.007	[-0.003 , +0.002]	0.997	1.020, -0.001	822
500	+0.000 ± 0.007	[-0.003 , +0.003]	0.993	1.037, -0.001	822
865	+0.004 ± 0.008	[+0.002 , +0.006]	0.983	1.102, 0.002	822

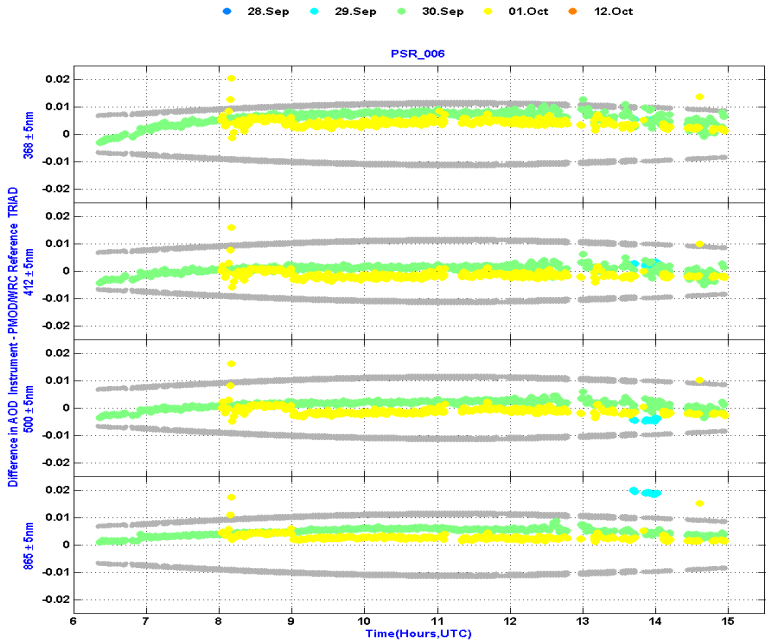

Figure 3.11, PSR 006 AOD retrievals compared to PFR triad, for the days of FRC-IV campaign. Grey dots show the WMO uncertainty limits.

3.2.4 Brewer

Measurements of global and direct spectral UV irradiance have been routinely conducted at the roof of ARSS, since July 2003 on daily basis by a Brewer MKIV monochromator measuring solar radiation in the UV and the visible part of the solar spectrum. The instrument measures columnar amounts of ozone (TOC), SO2 and NO2. It is also, measuring GHI in the UV-B part (290-315 nm) of the spectrum at 0.5 nm intervals. In the usual UV routine, the instrument scans from 290 to 325 nm, integrating approximately ls for each channel (Fioletov et al., 2001). For total column ozone measurements, the instrument is designed to take direct sun measurements at five nominal wavelengths 306.3, 310.l, 313.5, 316.8 and 320.0 nm, four of which are used with the standard algorithm to retrieve columnar ozone measurements from Brewer spectrophotometers and the shortest one is used to retrieve SO_2. In order to perform direct sun measurements, the tracker rotates the spectrometer towards the sun and solar beam reaches the sensor through a flat quartz window. TOC is calculated from these spectral measurements by the differential absorption retrieval method (Kerr et al., 1981,Staehelin et al., 2003).

$$TOC = (M_{S9} - B_1)/(A_1 * M_2) \quad (3.3)$$

And

$$M_{S9} = M_{S5} - 0.5\ M_{S6} - 1.7\ M_{S7} \quad (3.4)$$

where M_{S5}, M_{S6}, M_{S7} are the measurements of the intensities at the different wavelengths (Ratios of wavelengths pairs used in the Brewer total ozone algorithm: M_{S4}: 306.3/316.8; M_{S5}: 310.1/316.8; M_{S6}: 313.5/316.8; M_{S7}: 320.1/316.8). B_1 is the extra-terrestrial constant for the wavelengths used for ozone measurements and A1 is the differential ozone absorption coefficient for the ozone measurements determined by a linear combination of ozone absorption coefficients of different wavelengths selected by the slit mask for ozone measurements (see below for calibration). M_2 is the optical air mass, determined by:

$$M_2=\sec(\arcsin((R/(R+Z))*\sin(SZA))) \quad (3.5)$$

where R=6,371.009km is the Earth's radius and Z=22km is the ozone layer height. B1 and A1 are instrumental constants that are determined by comparisons with a standard instrument and checked or updated by the inter-comparison with the traveling standard instrument

In addition, the instrument was used to derive AOD in the visible part of the solar spectrum (Diemoz et al., 2016). In this study, spectral UV irradiance measurements at 324 nm and TOC from the Athens Brewer instrument are used, for the period January 2009 to December 2014. The Brewer spectroradiometer is calibrated regularly by means of a standard radiometer of the same type. The last three calibrations were performed at the Academy of Athens in July 2007, October 2010 and October 2013 by the travelling standard Brewer #017 (International Ozone Services Inc., Mr. Ken Lamb and Dr. Volodya Savastiouk). Lamp tests are performed every day as part of the recommended program of automatic measurements, which can be adapted by the operators (Staehelin et al., 2003). In general, the total uncertainty of Brewer derived TOC is considered in the order of 1% (Kerr et al., 1988). However, a number of studies have reported differences in the order of 3% between TOC retrieved from different Brewers (eg. Fountoulakis et al., 2017, Berjón et al., 2017, Pulli et al.,2017, Egli et al., 2016, Stübi et al., 2017,), implying underestimated inconsistencies.

Figure 3.12 A Brewer spectroradiometer installed in Antarctica.

3.2.5 The Ozone Monitoring Instrument (OMI)

Aura satellite launched in 2004 by NASA carries the Ozone Monitoring Instrument (OMI). OMI scans the entire earth's surface in 15 orbits, with a ground spatial resolution of ~13X24km2, measuring reflected radiation in 20 bandwidth channels in the spectral region of 270-500nm (Ahn et al., 2008). Aura is in a sun-synchronous orbit with ascending node Equator crossing time of 13:45 (Torres et al, 2007). OMI continues the TOMS record for total ozone and other atmospheric parameters related to ozone chemistry and climate.

The theoretical basis of the OMI ozone product algorithm for deriving the TOC from spectral scattered radiances can be found in Bhartia and Wellemeyer (2002). The main procedures include a fitting of ozone absorption cross-section to the measured spectrum, an estimation of air mass factor and corrections of clouds effects. A detailed description of the OMI instrument, some procedures of data processing, quality control/quality assurance procedures, calibration, and characterization can be found in Veefkind et al., (2006).

UV aerosol index, AOD and SSA are retrieved at 342.5 and 388nm using OMAERO (Ozone Monitoring Instrument Aerosol Product) algorithm, while there are also aerosol products from the OMAERUV algorithm which are a continuation of the Total Ozone Mapping Spectrometer time series (Torres et al., 1998) The algorithm has been revised, by adding a more sophisticated carbonaceous aerosol model (Jethva and Torres, 2011) and by including a spectral dependent imaginary index as a proxy for organics in the mixture (Kirchstetter et al., 2008). This satellite product has major sources of uncertainty caused by cloud contamination, the height of aerosol layer and the hypothesis of surface albedo, especially in desert areas (Jethva et al. , 2014).In the present study, we have used SSA and AOD from OMAERO, averaged at monthly level, using only 2009-2014 data, for the pixel

including the location of the ground-based instruments. These data are available at https://disc.gsfc.nasa.gov/datasets/OMAERO_V003/summary.

OMI products have been validated in several studies. Buchard et al. (2008) validated TOC and UV irradiance against ground based spectroradiometer installed at two sites in France and found a root mean square of TOC differences at 4.1% and 6.5% for UV at 324 nm. McPeters et al. (2007) performed a comparison with an average of 76 Dobson and Brewer ground stations between 25° and 55°N and showed that the OMI retrived TOC averages 0.4% higher than the station aver-age. Balis et al. (2007) compared OMI TOC with brewer stations, and found no significant dependence on solar zenith angle, cloud fraction and reflectivity, and global mean differences of 0.6% and revealed a pattern of an overestimation when TOC is lower than 220 DU.

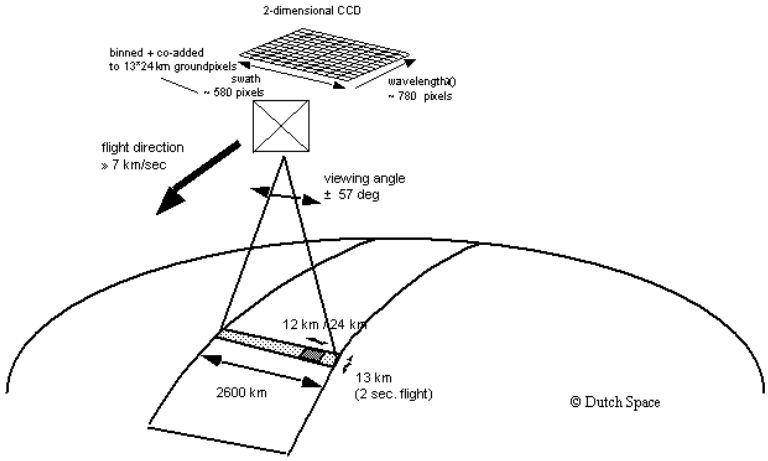

figure 3.13 Schematic of OMI functioning. source: http://projects.knmi.nl/omi/research/instrument/characteristics.php

3.2.6 Microwave Radiometer Profiler (MWP)

At MOL-RAO, a 22-channel MWP, MP-3000A /Radiometrics (Ware et al., 2003) provides vertical temperature and humidity profiles. MWP is a multi-frequency microwave radiometer that is based on a highly stable, tunable, and synthesized, local oscillator in the receiver. This design overcomes errors caused by receiver frequency drift, while allowing observation of a large number of frequencies across wide tuning ranges. The total power receiver has a highly stable noise diode that is used as a gain reference. The radiometer observes atmospheric brightness temperatures in five frequency bands from 22 to 30 GHz, and in seven bands from 51 to 59 GHz at 7 elevation angles (Cimini et al., 2003). In principle, observations from these instruments are based on recording the down-welling thermal emission of the atmosphere in the region between 22 and 30 GHz, using a zenith sky looking sensor. Emitting of atmospheric gases at well-defined bandwidths is estimated by microwave radiation received at the surface. Algorithms for retrieving IWV, are based on inversion techniques, which are using retrieved temperature profiles – derived from oxygen emission lines - fitted to model profiles either by neural networks (Churnside et al., 1994), Kalman filtering (Ledskam and Staelin, 1978) or regression (Askne and Westwater, 1986). Advantages of MWP is that retrieved profiles are continuous under all weather conditions and even Liquid Water Content profiles are recorded when clouds are present. A detailed description of the Water Vapour retrieval methodology of MWP could be found at Westwater et al. (2005). Cadeddu et al. (2013) have estimated the uncertainty of this technique in the order of 5% for IWV less than 10mm.

Figure 3.14 MWP, MP-3000A installed at MOL-RAO

3.2.7 Meteorological radiosonde (RS)

Meteorological radiosondes (RS) are launched in many places around the world, recording vertical profiles of various meteorological variables (Temperature, Wind Speed, Humidity etc). Water Vapour profiles provided by the soundings can be used to calculate IWV. This is the most objective approach for validating ground based remote sensing techniques, since water vapour is measured in-situ during the ascending procedure. Uncertainty for IWV retrieval in this approach is introduced by the nature of the method, as the total ascending of a radiosonde to stratosphere takes approximately an hour and also the path of the radiosonde in the atmosphere is determined by winds; thus, it is not directly comparable to sun-photometric estimations, which retrieve water vapour on the sun-point of observation optical path. High uncertainties -up to 20%- for relative humidity, caused by warming due to sunlight and thermal lag, have been reported (Pratt, 1985). Also, studies have reported differences due to the use of different sensors (e.g. Soden and Lanzante 1996). Vaisalla RS92 radiosondes are used in this study for which an uncertainty in the order of 5% for the RH (Relative Humidity) measurements, during daytime in the Troposphere, has been reported (Miloshevich et al., 2009). Radiosondes from MOL-RAO are launched 4 times per day (00h, 06h, 12h, 18h UTC). So, for this study 1-3 daytime soundings, per day, can be used, depending on the season. Corrections, as suggested by Vömel et al. (2007) for the dependence of the humidity sensor on temperature and radiation, were applied.

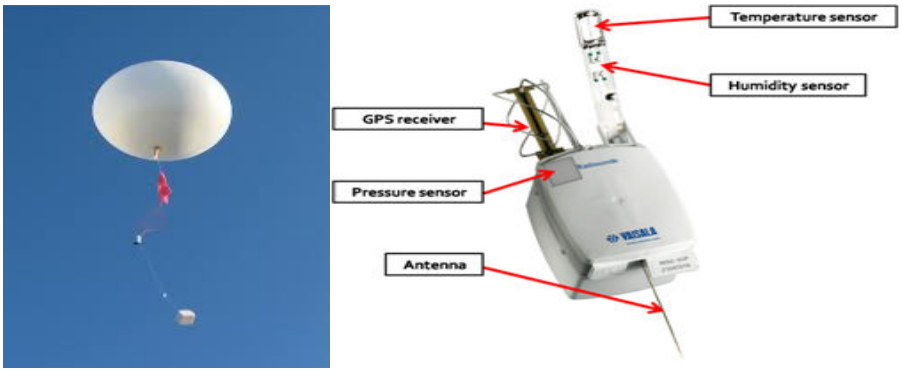

Figure 3.15 A radiosonde: left a functional balloon, right a sensor with all the parts pinpointed

3.2.8 Global Positioning System (GPS)

GPS is a space based system that uses the signal transmitted from specific satellite instrumentation in order to define the location of ground based receivers. The signal delays could be separated into dry (dependent on dry air gases) and wet (water vapour) component. Although the biggest fraction of the delay is caused by the dry component, it is estimated by hydrostatic equations, using the surface pressure, and subtracting it from the total delay. This is considered as a very accurate retrieval of the wet component, to which IWV is directly proportional (Bevis et al, 1992). Wang et al. (2007) showed that the random error of GPS IWV retrievals is in the order of 0.7 mm. GPS IWV retrievals are very valuable, since this method could be applied to any receiver and obtain a very reliable and dense dataset of frequent observations, both for daytime and night time, without being affected by cloud conditions. Differences among GPS and sun-photometric retrievals are expected, as different optical paths are used in each case and different air masses are detected: GPS path is a quasi-random path depending on the position of the satellites while the sun-photometer path is defined by the sun-instrument's relative positions

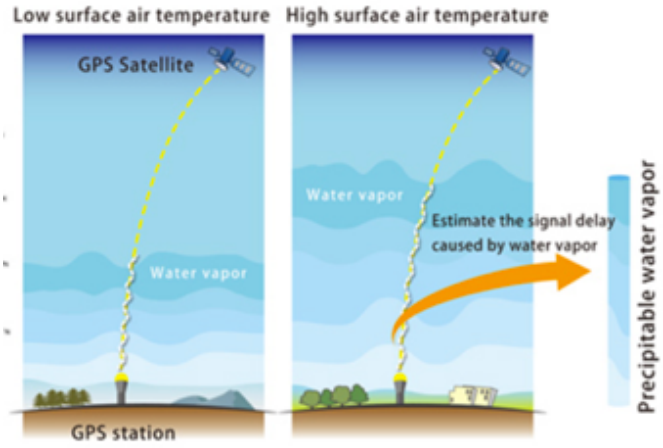

Figure 3.16 Schematic figures of GPS precipitable water vapour and interaction with GPS signal.
source:https://www.jamstec.go.jp/e/about/press_release/20170706/

3.3 Radiative Transfer Models

Radiative Transfer Models (RTM) are packages of codes that solves the equations of electromagnetic radiation propagation in the atmosphere. The development and the improvement of computer power in recent years allowed the development of RTM with very high frequencies and very dense spectra. RTMs provide simulations of several radiometric quantities (spectral and broadband) at different atmospheric levels based on measurements or estimations of the main parameters that determine the levels of the solar UV radiation. They are useful for several UV-related applications. Some of them are: estimation of the surface UV irradiance from satellite data and simulations of health and biologically related quantities over areas where measurements of the UV radiation are not available, study of the impact of changes in variables that affect the levels of UV radiation (e.g. surface reflectivity, ozone, aerosols), simulations of the past and the future levels of UV radiation, risk assessment from possible changes and information of the public. Depending on the scope of its application each model has specific characteristics. The main characteristics of the RTMs can be summarized in the following section.

3.3.1 LIBRADTRAN

Libradtran is collection of C and Fortran functions and programs for calculation of solar and thermal radiation in the Earth's atmosphere. LibRadtran is freely available under the GNU General Public License. The main tool used for calculations is *uvscpec*, which is the older version of the same package, used only for UV and visible spectral range (Mayer and Kylling, 2005). Spectral resolution could be treated either by line by line calculations, by correlated-k distribution or pseudospectral calculations.

In this study various LookUp Tables (LUT) have been constructed from libRadtran (Mayer and Kylling, 2005; Emde et al., 2016), outputs for different applications. Runs were made using the default aerosol model according to Shettle (1989), the code for spectral irradiance (COSI) developed in 1-Direction for the extraterrestrial solar source spectrum, the parameterization of molecular bands provided by LOWTRAN for the gas absorption, and finally the SDISORT radiative transfer solver (Dahlback & Stamnes, 1991). The RTM simulations were calculated using a band parameterization method based on the correlated-k approximation (Kato et al., 1999) and the exponential sum fitting technique. Inputs to the simulations included SZA and AOD, Ångström Exponent, SSA, IWV and TOC. Since the aim was to study measurements from sun radiometric instruments, no

calculations for clouds were made. Output variables were GHI, DI and DHI in a spectral region 285 to 2800nm at 1 nm resolution.

3.3.2 MODTRAN

MODerate resolution atmospheric TRANsmisson Radiative Transfer (MODTRAN) (Berk et al., 1998, Berk et al., 2005) is an atmospheric radiative transfer model co-developed by the US Air Force Research Laboratory and Spectral Sciences Inc. covering a spectral region from thermal infrared to UV infrared (0 - 50,000 cm^{-1}), providing resolution as fine as 0.2 cm^{-1}.. The atmosphere is modeled as stratified horizontal layers and molecular and particulate constituent profiles may be defined either using built-in models or by user-specified vertical profiles. MODTRAN model includes flux and atmosphere scattered solar calculations of high accuracy in the near infrared spectral region. Spherical refraction geometry effects are incorporated into calculation of path sums and scattering angles, although multiple scattering radiances are based on plane-parallel models. Approximate corrections are made for the effects of inhomogeneous distributions of temperature and species concentrations within the atmospheric layers (Berk et al., 1998). MODTRAN is widely used to retrieve various products from satellites (Gonzales and Velez-Reyes, 1998, Green et al., 1998, Berk et al., 2002, Jackson et al., 2004 Anderson et al., 2007, Goetz, 2009).

At this study, MODTRAN was used to calculate transmittance in near infrared in order to calculate IWV. For this purpose the mid-latitude built in model atmosphere was used, in the spectral region 0.7 to 1.0 μm. The selection of MODTRAN was based on the higher accuracy in this solar spectral region.

3.4 Statistical tools

In this chapter a summary of statistical variables used for the validations and comparisons in the present study is given.

Standard deviation σ is a measure that is used to quantify the amount of variation or dispersion of a set of data values. A low standard deviation indicates that the data points tend to be close to the mean. It is calculated as

$$\sigma = \sqrt{\frac{\sum_1^N |x_i - \langle x \rangle|^2}{N-1}} \quad (3.6)$$

where N is the sample size, x_i are the values of the datasets and $\langle x \rangle$ is their average value.

Pearson correlation coefficient or Pearson's r, is a measure of the linear correlation between two variables X and Y. It has a value between +1 and −1, where 1 is total positive linear correlation, 0 is no linear correlation, and −1 is total negative linear correlation. It is calculated as

$$r = \frac{1}{N-1} \sum_1^N \left(\frac{x_i - \langle x \rangle}{\sigma_x}\right)\left(\frac{y_i - \langle y \rangle}{\sigma_y}\right) (3.7)$$

where N is the sample size, x_i and y_i are the values of the datasets and $\langle x \rangle$ $\langle y \rangle$ is their average value σ_χ and σ_y are the corresponding standard deviations.

The coefficient of determination R^2 has been used to evaluate the performance of different methodologies, and was calculated as below:

$$R^2 = 1 - \frac{\sum_i (y_i - f_i)^2}{\sum_i (y_i - \langle y \rangle)^2} \quad (3.8)$$

where y_i are values from the other datasets $\langle y \rangle$ is the average of those values and f_i are the values from the tested method.

Root mean square error (RMSE) is used to measure the differences between values predicted by a model and the observed values.

$$RMSE = \sqrt{\frac{\sum_1^N (y_i - f_i)^2}{N-1}} \quad (3.9)$$

where yi are the observed values, <y> is the average of those values and fi are the values from the model.

The **t-test** is any statistical hypothesis test in which the test statistic follows a Student's t-distribution under the null hypothesis. The two-sample t-test is a parametric test that compares the location parameter of two independent data samples. Where the datasets are x and y with sizes m and σ_χ and σ_y are the corresponding standard deviations, the t score parameter is calculated as

$$t = \frac{<x> - <y>}{\sqrt{\frac{\sigma_\chi}{m} + \frac{\sigma_v}{n}}} \quad (3.10)$$

where small t values mean that datasets are similar. The exact threshold values for accepting the null hypothesis is depending on the confidence level and can be found in statistical bibliography tables (eg http://www.sjsu.edu/faculty/gerstman/StatPrimer/t-table.pdf).

4. Total Ozone Column retrieved using an Ultraviolet MultiFilter Radiometer

This chapter is based on the publication Raptis, P.I., Kazadzis, S., Eleftheratos, K., Kosmopoulos, P., Amiridis, V., Helmis, C. and Zerefos, C., 2015. Total ozone column measurements using an ultraviolet multi-filter radiometer. International Journal of Remote Sensing, 36(17), pp.4469-4482.

For monitoring total column ozone (TOC), Dobson and Brewer spectrophotometers are the primary ground-based instruments in use (Staehelin et al., 2009). Although these measurements provide long multi-decadal time series at high temporal resolution, their spatial coverage of the planet is low, over the last years a decline of stations recording TOC from surface has been recorded (Braathen, 2012, figure 4.1) leading to crucial gaps on the monitoring process.

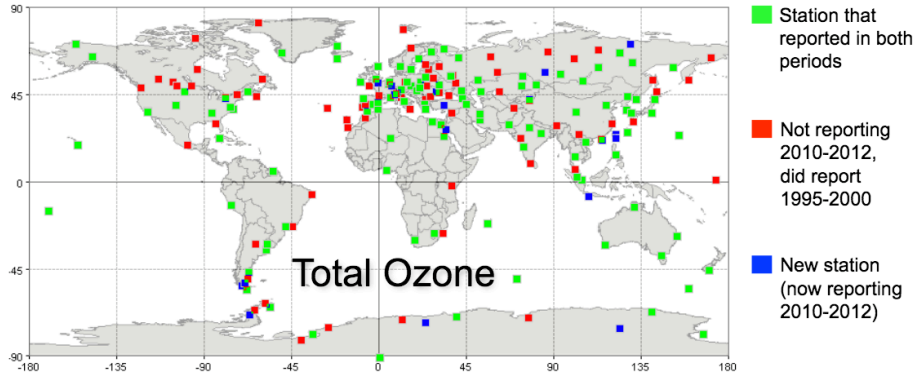

Figure 4.1, Stations providing Total Ozone measurements for WMO-GAW program, source: Braathen,2012

Under the need of spatial denser global measurements of TOC, portable multi-filter radiometers could help fill in data gaps in the global spatio-temporal record by providing high temporal resolution measurements. In particular, the Ultraviolet Multi-filter rotating shadowband Radiometer (UVMFR) is an instrument designed to DHI, GHI and DI with high accuracy and frequency and wass described in detail in 3.2.1 . In addition to its portability, the main advantages of this instrument are the automatic calibration procedures and the low operational cost. Compared to Brewer spectrophotometers, low effort is needed with UVMFRs for quality assurance and quality control (Bigelow and Slusser 2000; Slusser et al. 2005).

In this chapter, based on the approaches of Gao et al. (2001) and Slusser et al. (1999) a simple method has been developed using DI measurements at two wavelengths (305 and 325 nm) and the radiative transfer model (RTM) LUTs to

retrieve high-accuracy TOC estimates. The method is applied to five years of high-frequency UVMFR measurements to retrieve TOC at a complex (in terms of aerosol load) site in the centre of Athens, Greece. We examine the effect of AOD and ozone effective temperature on our method and introduce corrections that improve the results. Finally, we have compared this method's results with synchronous and co-located Brewer and OMI TOC retrievals.

4.1 Methodology

The corrected direct UVMFR measurements –as described in 3.2.1 - are used in order to calculate AOD (at 368nm) through frequent Langley calibrations and comparisons with a CIMEL sun-photometer that is operating at ARSS. In this work, in order to ensure the consistency of the ratio of the DI at 305nm and 325nm, Langley calibrations at low AOD (<0.1) conditions have been used.

GHI from the UVMFR have been used in order to distinguish cloud free conditions for each of the one minute measurements. Clouds are detectable in the measured UVMFR global irradiance (at 368nm) since they cause larger variability than aerosols. In order to distinguish between cloudy and cloud free conditions, we applied an updated version of the method of Gröbner et al. (2001) which is described in 3.2.1. More details about this quality control of the UVMFR measurements are presented in the next section in the context of Brewer spectrophotometer measurements.

In addition to the ground-based measurements, TOC data from the OMI on board of AURA satellite were also analyzed for the study period. OMI is a nadir-viewing ultraviolet/visible solar backscatter spectrometer on-board the Aura satellite. OMI TOC is co-located overpass data with respect to the ARSS data and has a synchronization window of 60 minutes and satellite-station spatial distances lower than 50 Km. A detailed description of the OMI instrument, some procedures of data processing, quality control/quality assurance procedures, calibration, and characterization can be found in Veefkind et al., (2006). The theoretical basis of the OMI ozone product algorithm for deriving the TOC from spectral scattered radiances can be found in Bhartia and Wellemeyer (2002).

In parallel, libRadtran RTM code have been used (Mayer and Kylling 2005) in order to simulate DI ratios from the UVMFR by performing a grid of runs whose basic input parameters include: the SZA, AOD, TOC and absorption ozone cross section and whose outputs comprise high resolution DI spectra with a spectral resolution of 0.01 nm. For each run, a constant aerosol profile (US Standard Atmosphere, 1976) and single scattering albedo of 0.91 which is the mean value

derived from AERONET at 440 nm, for this period (see details in chapter 6) have been used. In order to accurately simulate the UVMFR direct sun measurements, retrieved DI scans were weighted with the spectral response of the UVMFR instruments (for 305nm and 325nm). LUTs were then produced using the following relation between the calculated DI ratio (305/325nm) and the model input parameters:

$$DI_{305}/DI_{325} = f(SZA, TOC, AOD) \quad (4.1)$$

SZA is calculated as described in section 2.1. An overview of the method is visualised in figure 4.2.

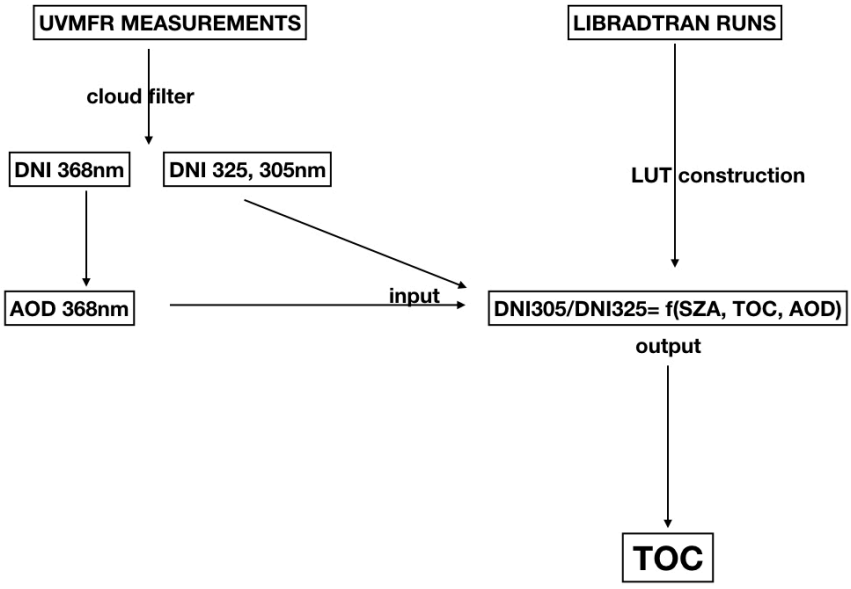

Figure 4.2 A schematic overview of the methodology used to retrieve TOC.

In Fig. 4.3 an example of the variation of the DI ratio from the LUT as a function of varying SZA and TOC for the aerosol-free case (AOD=0) is presented. Ratios for this case varies from 0 to 0.3. While the higher ratios are found at low ozone and low solar angles where the spectral dependence among 305 nm and 325 nm becomes higher. For SZA higher than 70°, all ratios are almost zero, making very difficult to retrieve TOC using this approach. This fact is a potential drawback for the methodology when used in higher latitudes. From the LUT and the quality controlled data set of DI measurements, a primary TOC dataset was constructed for the study period.

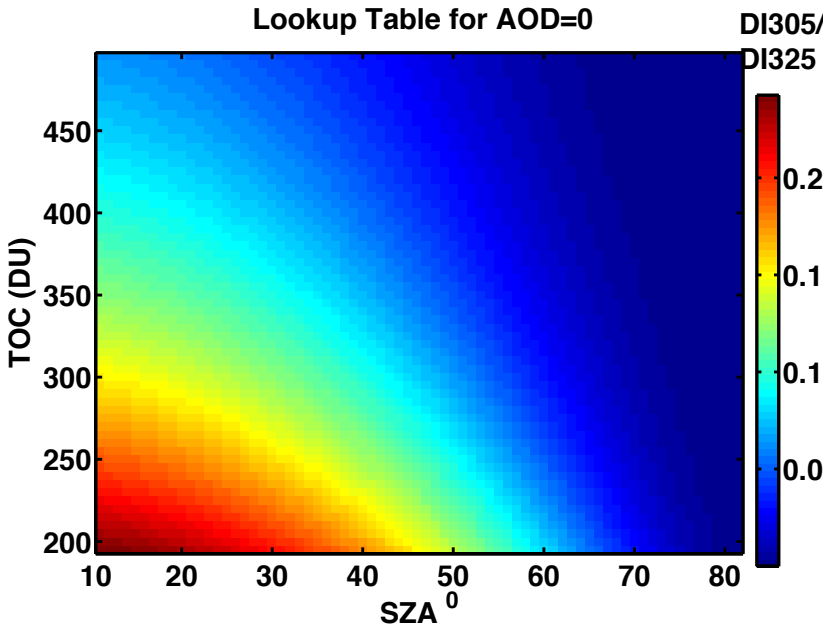

Figure 4.3 The variation of DI ratio (305:325) as a function of TOC and SZA (for AOD = 0) as calculated by RTM simulations.

4.2.1 Sensitivity to aerosols

Aerosol effect on the retrieved TOC have been studied, by calculating the AOD at 368nm (this wavelength is preferable because ozone absorption is negligible) from UVMFR irradiance measurements via the Beer-Lambert's law:

$$AOD_{368}=1/\mu\ (\ln I_{o\ 368}/\ln I_{368})-\tau_{ray368} \quad (4.2)$$

where μ is air mass factor, τ_{ray368} is Rayleigh scattering optical depth at 368nm which is calculated (Bodhaine et al, 1999) as described in 2.2 and in 2.3.4 accordingly. In order to investigate the sensitivity of the TOC retrieval to AOD, RTM runs have been perfomed for different AOD_{368} values in the range 0 to 1.2 with a 0.05 step size. Then, TOC dataset have been recalculated by interpolating the corresponding AOD LUTs. Fig. 4.4 presents the difference between TOC retrievals obtained with and without AOD_{368} for the whole study period, which can be seen to be strongly linear (R^2=0.98). Averaging differences in 0.05 bins, a change in TOC of the order of 1 (±0.4) DU is observed for each 0.1 change in AOD_{368}. It is evident that for environments having high AOD variability such as the city of Athens (Kazadzis et al, 2012), the AOD correction presented here is essential for improving the accuracy

of the TOC retrieval. The potential of using synchronous UVMFR data to retrieve the AOD is a great advantage of this method.

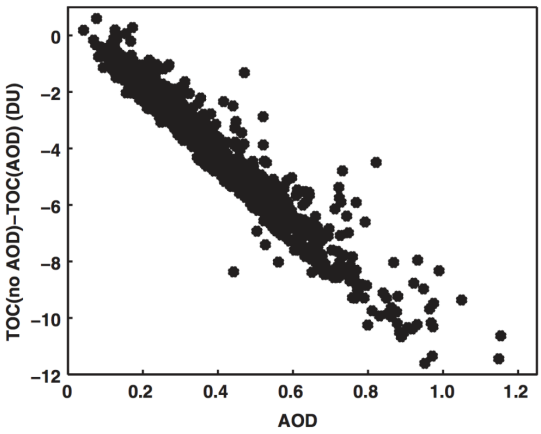

Figure 4.4 Bias of TOC calculated with and without aerosols, with respect to AOD at 368 nm.

4.2.2 Sensitivity to ozone effective temperature

For the case of sensitivity of the TOC retrieval to Ozone effective temperature, the Ozone absorption coefficients provided by Bass and Paur (1985) using different temperatures, have been set as inputs to the libRadtran RTM. These coefficients are temperature-dependent and by ignoring them, this lead to a seasonal error (Redondas et al, 2014) on TOC retrieval. Recent studies have also calculated the effect of temperature variation on ground based measurements of the TOC (Redondas et al, 2014, Fragkos et al, 2013). The most accurate approach requires ozonesonde data to calculate ozone effective temperature and then to apply absorption coefficients. In order to provide a stand-alone and simpler method for retrieving the TOC, the following procedure was followed: The yearly variability of mid-latitude stratospheric temperature is around 16K and the European centre for medium-range weather forecasts (ECMWF) provides a mean value of 224K over Greece (Parrish et al, 2013). Following this climatology , Ozone cross-sections for the range of temperatures 216K up to 232K were calculated . Fig. 4.5 presents TOC values calculated at SZA=60^o and AOD_{368} =0.5 for different temperatures using this approach. TOC at 224K was compared to all tables for same SZA, and AOD_{368}, and a change in the calculated TOC of 0.5% per degree K was found in the temperature range of interest. Then, a correction to the calculated TOC dataset was introduced using climatological values of stratospheric temperature.

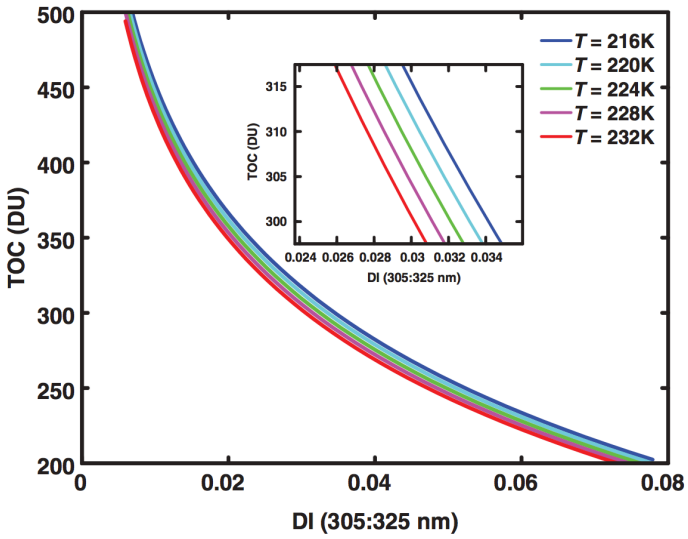

Figure 4.5 TOC as a function of the ratio of DI (305/325 nm) for Bass–Paur cross sections at different temperatures.

4.3. Retrievals comparison

For validation of our results, synchronous Brewer TOC retrievals have been used, described in 3.2.4. The comparison was further assessed by studying the UVFMR/Brewer TOC ratios and the correlation coefficient between the two datasets. Results are presented in Table 4.1. A strong positive correlation is observed between UVMFR and Brewer coincident measurements (R=0.98) and with and with a mean total ozone ratio equalling 1.00 and a standard deviation of 0.03 95% confidence interval at ±0.002. Comparison with coincident OMI satellite retrievals also revealed strong positive correlations but with a small overestimation of the total ozone with the UVMFR compared with OMI, and a slight underestimation in the case of the Brewer instrument.

Table 4.1: Comparative statistics for TOC (Pearson product-moment correlation coefficient) and the total ozone ratio (mean, standard deviation σ) between the UVMFR and Brewer instruments retrievals for each OMI overpass data.

	Correlation coefficient	Mean ratio	σ
UVMFR-BREWER	0.98	1.00	0.03
UVMFR-OMI	0.93	1.03	0.04

BREWER-OMI	0.96	0.99	0.03

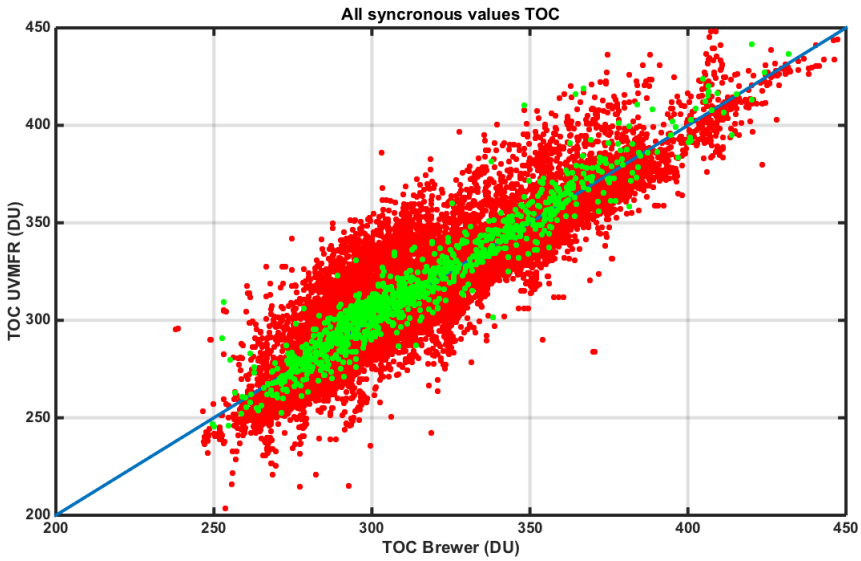

Figure 4.6 Scatterplot of all quality assured and synchronous values of Brewer, and UVMFR TOC retrievals, in red and in green, all and daily values accordingly. Linear regression for daily values with r = 0.97. r^2 and ax+b data

First all the values retrieved from UVMFR were compared, to the corresponding synchronous Brewer retrievals. For each Brewer measurement, averages of 5 (minute) UVMFR recordings were calculated. Measurements for SZA higher than 70^o have not been used in the study in order to avoid uncertainties linked with the non ideal angular response of the UVMFR instrument. In total 24723 cases of cloudless sky synchronous measurements were studied and presented in figure 4.65, from which we determined a coefficient R^2 of 0.94. The average ratio is 1.024, with a standard deviation of 0.034. In addition, daily TOC values from the UVMFR and the Brewer has been calculated and are superimposed in figure 4.5. While mean median and standard deviations of the TOC ratio UVMFR/Brewer of the TOC ratio UVMFR/Brewer and UVMFR/OMI are presented in table 4.2 for each month. Brewer and UVMFR TOC retrievals seem to have a uniform behaviour through the year, while OMI seems to overestimate constantly during summer months.

Table 4.2: Comparative statistics for TOC ratio (mean, standard deviation σ) between the UVMFR and Brewer instruments retrievals for each OMI overpass data per month

<TOC	σ	TOC	<TOC	σ	TOC

	UVMFR/Brewer>	UVMFR/Brewer	UVMFR/OMI>	UVMFR/OMI
JANUARY	1.02	0.04	1.02	0.03
FEBRUARY	1.00	0.03	0.98	0.02
MARCH	0.99	0.03	0.98	0.03
APRIL	0.98	0.02	0.98	0.04
MAY	1.02	0.03	1.03	0.06
JUNE	1.04	0.04	1.06	0.05
JULY	1.02	0.03	1.04	0.05
AUGUST	1.03	0.05	1.04	0.05
SEPTEMBER	1.02	0.03	1.03	0.03
OCTOBER	1.00	0.02	1.01	0.02
NOVEMBER	0.99	0.02	1.00	0.02
DECEMBER	1.00	0.04	1.01	0.03

In addition, in figure 4.7 relative frequency histograms for TOC ratio among UVFMR and Brewer for all synchronous values (blue) and daily values (red) is visualised. Difference in the skewness is observed, revealing a slight UVMFR overestimation when using all values statistics. Using a t-test distribution 95% confidence intervals were calculated as 1.0085±0.0003 for all values and 1.0075±0.0020 for daily values. This slight difference in the distribution could be explained by the fact that more commonly ratios larger than 1 were recorded in summer months, when more measurements are available.

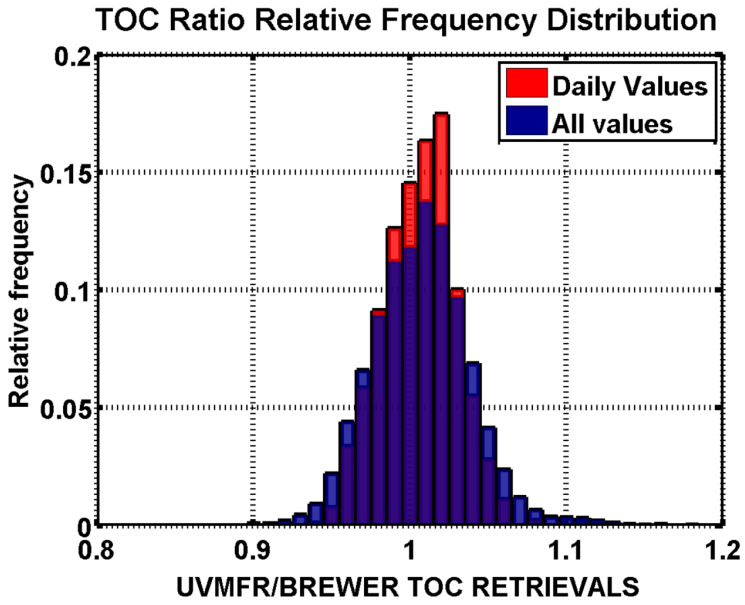

Figure 4.7 Relative frequency histogram of all TOC ratio (UVFMR:Brewer) values and daily values correspondingly.

In order to investigate the error sources linked with the TOC retrieval, the UVMFR/brewer ratio with respect to SZA is shown in figure 4.8. It appears that both the ratio and scatter of values are independent of the solar zenith angle. A slight overestimation of the UVMFR retrievals appears around 45^{o}. Overall it can be seen that the errors are within ±3.5% for all solar zenith angles. The non solar zenith angle dependent ratios reveal the ability of the UVMFR to simulate accurately the DI and using the presented methodology to simulate TOC for SZA up to 70 degrees. Cosine correction of global irradiance measurement at UVB spectral range is up to 2% (Gröbner et al., 1996). Kroktov et al. (2005a) have estimated for UVMFR all the sources of errors and found a measuring uncertainty up to 1%. Measuring errors propagate an uncertainty of 1.6% to the final calculation. UVMFR AOD retrieval at 368 nm compared to CIMEL transferred AOD from 440 nm to this bandwidth reveal maximum differences of 0.04 (chapter 6.1, Kazadzis et al., 2016,), which would lead to errors up to 0.4 DU in present approach.

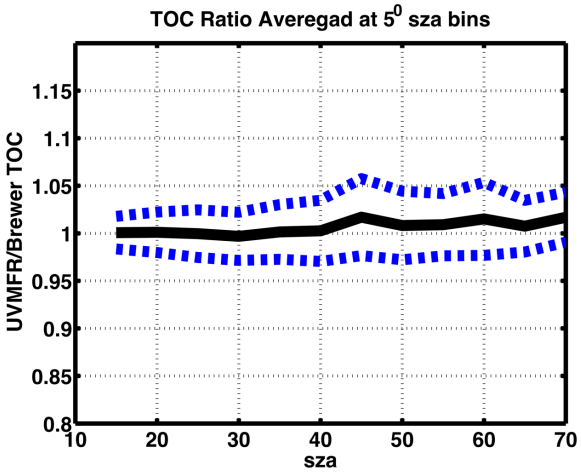

Figure 4.8 UVMFR/Brewer TOC all values ratio, averaged at 5^{o} sza bins. Blue dash lines indicate ±1 standard deviation.

Since UVMFR measurements have much higher measurement frequency than Brewer ozone measurements, interesting daily features could be identified. In Fig. 4.9 for example, daily TOC variability features are captured. Such information is crucial when using TOC for the calculation of other parameters such as UV Index that its daily variability is required. Diurnal stratospheric ozone variation has been found to exhibit an afternoon peak at mid-latitudes related to the formation of tropospheric ozone near the earth's surface at populated urban locations (e.g., Anton et al., 2010).

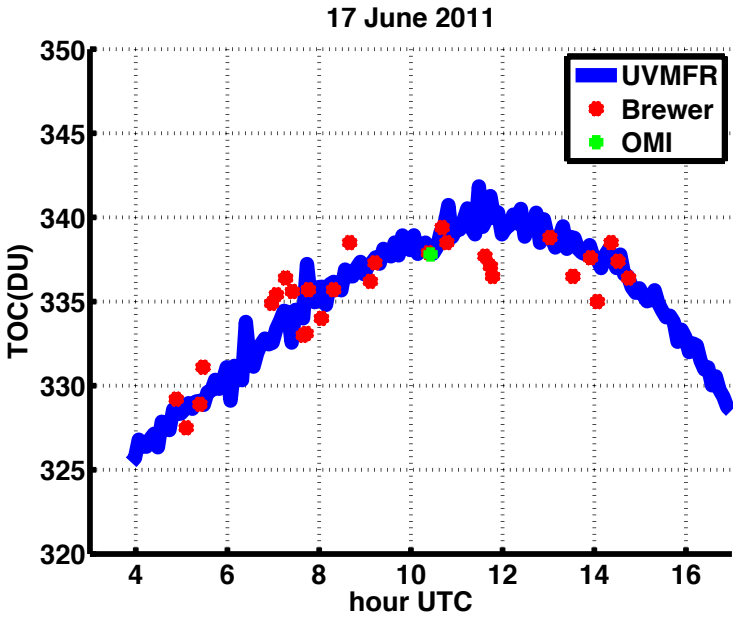

Figure 4.9 Brewer, UVMFR and OMI overpass TOC data on 17 June 2011

In Fig. 4.10, mean hourly values for both instruments are shown during the month of June where an afternoon peak is visible in both datasets despite the high standard deviation calculated for both instruments. The physical explanation for this diurnal pattern is likely caused by the daily variability of photochemical processes related with ozone formation and destruction in the lower troposphere especially for urban areas(Logan et al., 1985). According to Anton et al., 2010, these diurnal fluctuations in tropospheric ozone could explain part of diurnal TOC variations (between 20% and 70% depending on the mixing layer height).

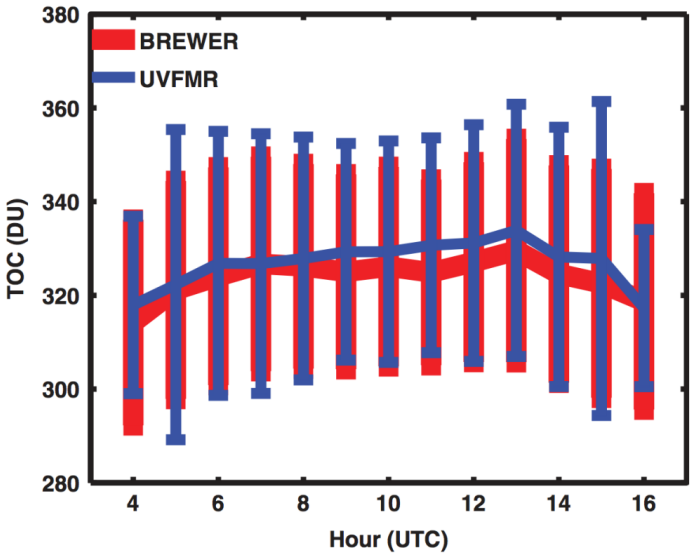

Figure 4.10 Average Hourly TOC values for both instruments, recorded during the month of June during 2011.

Examining the time series of the ratio among the UVMFR and Brewer time series it appears a small remaining seasonality of the order of 3%, whereas at winter months UVMFR underestimating and overestimating at summer months. This difference suggests that despite the fact that the seasonal correction is applied, there is remaining seasonal dependence on the calculated TOC.

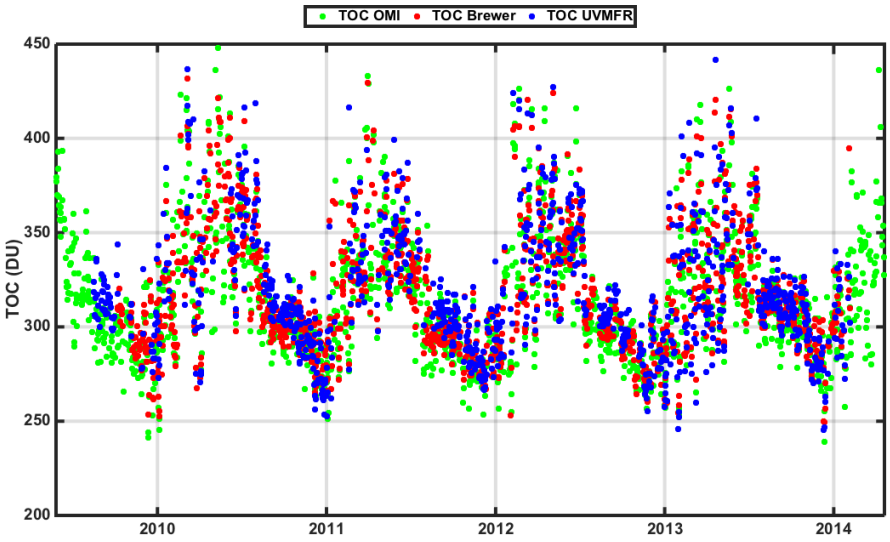

Figure 4.11 Daily TOC retrievals from OMI, Brewer and UVFMR measurements over the period 2009-2014 at Athens, Greece

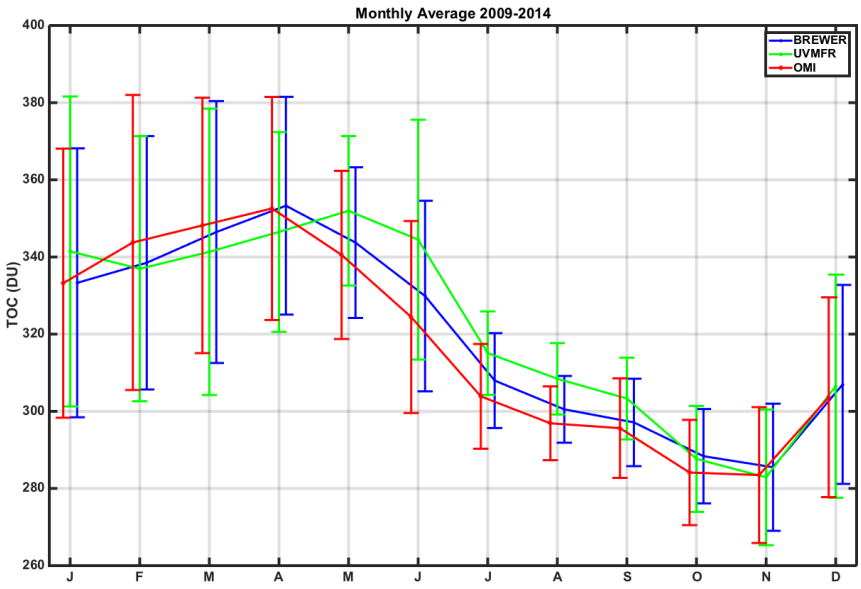

Figure 4.12. Monthly average TOC retrieved by Brewer and UVMFR and the corresponding OMI overpass means, 2009-2014

In order to compare OMI-based and ground-based TOC measurements, UVMFR and Brewer daily values have been produced by averaging TOC measurements in a 2 hour window around OMI overpass (figure 4.11 and 4.12). The annual variability of mainly stratospheric TOC is captured from all instruments. Hence, this approach can provide a satisfactory representation of the atmospheric TOC state. The results are presented in figure 4.9 alongside with OMI retrievals. Data presented here capture a span of 5 years (2009-2014) of continuous ozone measurements from the two surface-based instruments. It seems that UVMFR

retrievals are overestimated during summer months, which is possibly explained by an erroneous estimation of ozone effective temperature for these months in the retrieved method. All 3 methods show the same ozone related seasonal cycle over Athens, with maximum values on April-May and minimum at October-November, which is better visualized in figure 4.10. This figure reveals a slight overestimation of OMI around summer months and an underestimation on spring, which is caused by the different Ozone cross sections used for the TOC retrieval. Balis et al, (2007) had found average biases among OMI's TOC retrievals and Brewer measurements, to be less than 3%. Also, Anton et al. (2009) have compared OMI and Brewer retrieval's in multiple locations and found an underestimation up to 3%, and Ialongo et al. (2008) showed biases up to 2% for Rome. Our results show a good agreement between the Brewer and the satellite total ozone, which is the order of 2.7% with a standard deviation of 4%. Similar results have been found comparing TOC from OMI and UVMFR.

4.5.Conclusions

A simple method using RTM lookup tables and UVMFR measurements at two wavelengths can be used to calculate TOC and provides results comparable to other standard methods. A sensitivity study and a validation of such UVMFR based algorithms were perfomed, introducing improvements based on AOD and ozone effective temperature described effects, on the retrieval algorithm. In addition, to the previous works using TOC-UVMFR retrievals, this is the first work using a long term (5 years) time series of TOC data. This is crucial in order to explore further the limitations of such retrieval, especially linked with long term stability of the UVMFR instruments and their use for monitoring purposes.

Main advantages of the use of such a method include: the low cost and relatively easier maintenance of the UVMFR compared with Brewer or Dobson TOC measuring spectroradiometers, the potential of high frequency retrievals and the ability to calculate synchronous AOD that are needed for improving the TOC retrievals. A 5 year UVMFR time series were analysed and compared to collocated Brewer retrievals in Athens, Greece and found a correlation in the order of 98%, mean ratio of synchronous values at 1 and a standard deviation of 0.003. In the case of neglecting AOD variations an error of 1DU per 0.1 change in AOD is introduced. Look up tables were constructed that included SZA, AOD and DI ratios of 305 and 325nm. UVMFR retrievals slightly overestimate TOC in the summer and underestimate during winter, compared with the Brewer TOC retrievals. This

seasonality was investigated and found that using Bass-Paur ozone absorption coefficient should influence TOC by 0.5% per K degree. Climatological values of Ozone Effective temperature were used to apply a correction on the retrieval. Also, we compared to OMI product and found differences in the order of ±3%. UVMFR irradiance measurements can be used to investigate diurnal variations of TOC.

Brewer retrieval should be considered more reliable as using multiple bandwidths ratios to eliminate random errors. All results from UVMFR method stand in less than ±2% from Brewer measurement, while average statistics show very slight differences (σ=0.003). While Brewer established uncertainty for TOC retrieval is assumed up to 3% (Anton et al., 2013).

5. Columnar Water Vapour retrieved with a Precision Spectral Radiometer

This chapter is based on the publication: Raptis, P.I., Kazadzis, S., Gröbner, J., Kouremeti, N., Doppler, L., Becker, R. and Helmis, C., 2018. Water vapour retrieval using the Precision Solar Spectroradiometer. Atmospheric Measurement Techniques, 11(2), pp.1143-1157.

Water Vapour is a very important component of the thermodynamic state of the atmosphere (Hartman et al., 2013), being a greenhouse gas with relatively high concentrations. IWV in the vertical atmospheric column, defined as the height that water would stand if completely condensed and collected in a vessel of the same unit cross section (American Meteorological Society, 2015). IWV is a crucial parameter for meteorology, by defining the potential of cloud formation. Although GPS ground receivers offer a robust retrieval, there is no unified way to process the signals and retrieve easily IWV. Radiosondes provide the most reliable measurements, by measuring in situ humidity and providing the water vapour's profile, but the usage is not so wide and usually there are only few launches per day. Microwave profile radiometers provide also a robust estimation, by recording water vapour's profile, but these instruments are expensive and not widespread. Hence, a lot of available data are provided by filter sunphotometers using a channel with high absorption for water vapour.

Technological advances of the recent years have made feasible the manufacturing of operational spectral sun-photometers for environmental monitoring. The Precision Solar Spectroradiometer (PSR), designed and manufactured at PMOD/WRC, Davos, Switzerland, is described in chapter 3.2.3 . In this study developed tools were developed to retrieve IWV using PSR recordings, adopting two different approaches; one using single wavelength channels and another retrieving from a wider spectral region, the latter being impossible with filter radiometers. Retrievals in different channels and spectral windows in the water vapour absorbing region of near infrared spectrum were evaluated and selected. Both methods were applied to a 2-year long PSR dataset at the German Meteorological Service (Deutscher Wetterdienst, DWD) site in Lindenberg, Germany and results have been compared with sun-photometric (CIMEL), GPS, radiosonde and MWP IWV datasets from the same station. Present study gives the technical details of all instrumentation used, describes all the details of the development of these two methodological approaches and estimates the uncertainties linked to them and finally all the comparisons for the 2 year dataset are reported.

5.1.Instrumentation

Methodologies for retrieving IWV were applied to PSR measurements at Meteorologisches Observatorium Lindenberg – Richard Assmann Observatorium (MOL-RAO) from the German Meteorological Service "Deutscher Wetterdienst" (DWD) in Lindenberg (Tauche), where a 2-year long PSR dataset is available (May 2014- April 2016). MOL-RAO is described in detail at 3.1.2 chapter. AOD in the area is generally low, with maximum mean monthly values of 0.25 and 0.27 during June and July. PSR instrument is described in detail in 3.2.3. Also data from IWV GPS (3.2.8), Radiosondes (3.2.7) and MWP (3.2.6) have been used.

Figure 5.1. PSR#004 and PSR#006 installed on a sun tracking device at MOL-RAO,

Cimel IWV data was also used in this study. The method used to retrieve it IWV is described in detail in Smirnov et al. (2004). The principle of this method is to calculate a two constants' fit, using radiative transfer model calculationsin order to retrieve IWV from the transmittance recorded at 940 nm. The precision of this retrieval was investigated by Alexandrov et al. (2009) who showed an error in the region of 0.05-0.18cm depending on the amount of IWV.

The CIMEL Level 2 AOD data for MOL-RAO has been directly downloaded from AERONET website (https://aeronet.gsfc.nasa.gov/). During the 2 years of this study, the station has been equipped with three different instruments:

Cimel CE318N, #787

Cimel CE318N, #873 supplying #787 during its AERONET calibration

Cimel CE318T ("Triple") since October 2015, instrument of higher temporal resolution (~1 minute)

5.2 Methodology

In the near infrared measuring spectral region of PSR the most important water absorption has been found in the 700-1000 nm wavelength region. Figure 5.2 shows the transmittance from Rayleigh scattering, aerosols and IWV, as calculated by the MODerate resolution atmospheric TRANsmisson Radiative Transfer Model (MODTRAN RTM) (Berk et al., 1987, Berk et al., 1999). Aerosols direct effect on irradiance is measured through Aerosol Optical Depth (AOD), which is the integrated extinction coefficient of the vertical column due to aerosols. Spectral variation of AOD at different wavelengths is measured through Ångström Exponent. For the example on figure 5.2, Ångström Exponent equal to 1.5 was considered and aerosol of AOD 0.1 and 0.2. Inclination of aerosol transmittance lines is proportional to Ångström Exponent and higher AOD will lead to lower absolute values. WMO (2004) recommends 719, 817 and 946 nm central wavelengths to retrieve IWV, which appears as significant drops in the solar transmittance spectra in Figure 5.2. Ingold et al. (2000) investigated the quality of the retrievals at these wavelengths and found that the one at 946 nm is the most robust, which could be translated as the wavelength range with the strongest absorption of IWV. Considering that absorption of water vapour is higher in the 910-950 nm region, all calculations were performed for PSR channels in the spectral range. Example of DI spectra in the 700-1000 nm spectral region are visualized in figure 5.4.

MODTRAN was selected instead of LIBRADTRAN which is used in the rest of this dissertation, because of reported overestimation of LIBRADTRAN libraries in the near infrared spectral region, while MODTRAN is documented to have higher accuracy at this bandwidth. An example of spectra calculated with both codes is provided in figure 5.3, where expected DI drops due to water vapour are almost negligible when LIBARADTRAN is used.

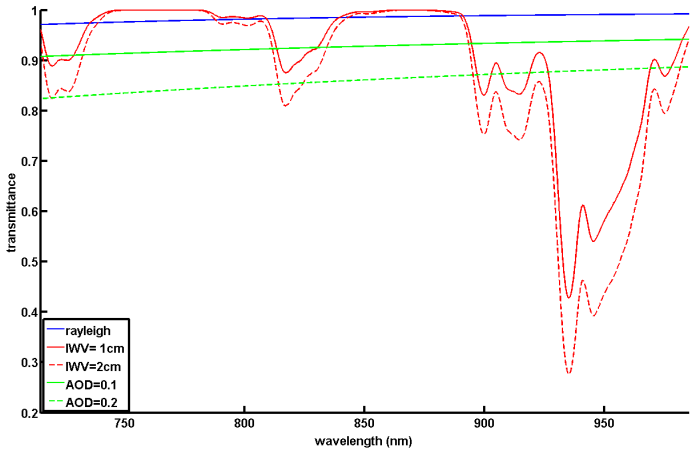

Figure 5.2. Transmittance of Water Vapour, Aerosols and Rayleigh scattering in the spectral region 700-1000 nm, calculated using MODTRAN set at 0.1 nm resolution, at SZA=0° IWV=1cm, IWV=2cm and AOD=0.1 and AOD=0.2 at 700nm using an Ångström Exponent of 1.5. Black vertical dotted lines represent WMO recommendations for IWV retrieval.

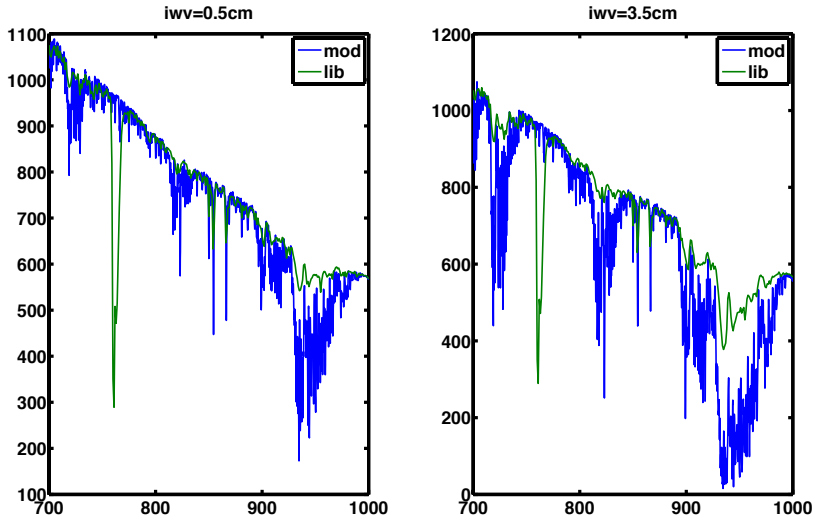

Figure **5.3** DI Spectra in the near infrared region (700-100nm) for no AOD and SZA=45°, calculated with MODTRAN (blue) and LIBRADTRAN (green), for IWV=0.5 and 3.5 cm.

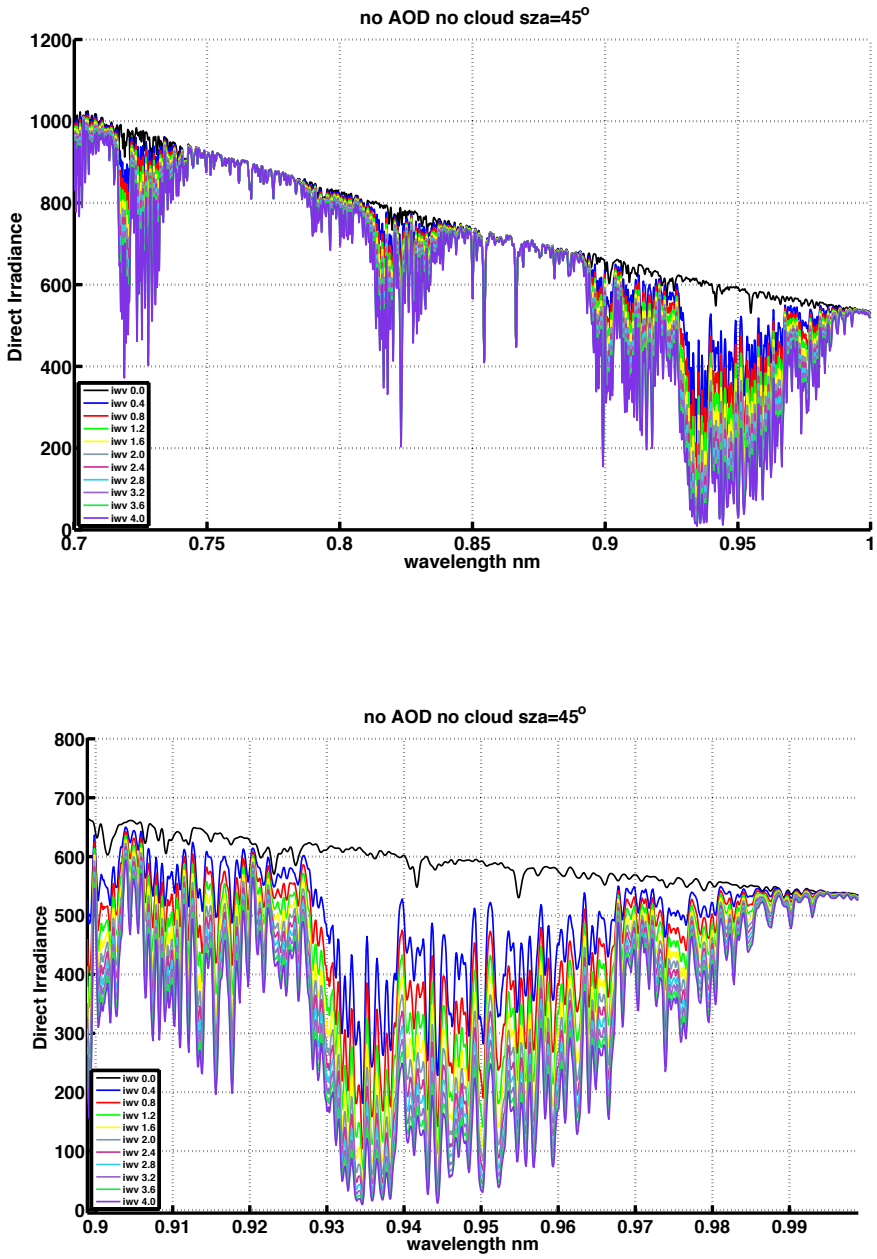

Figure 5.4 DI Spectra in the) for no AOD and SZA=45°, calculated with MODTRAN, with different IWV, for 700-100nm region (upper) and zoomed in 900-1000 (lower).

5.2.1 Monochromatic Approach

The methodology in use is described in detail by Ingold et al. (2000) and it is the most common procedure to calculate IWV for sun-photometric devices using individual wavelength (filter) measurements. It is labeled as monochromatic in contrast to the second approach presented in Section 3.2, although it is calculated

for a spectral region defined by the instrument's slit function or the limits of its bandpass filter.

The first step of the procedure is to calculate the Water Vapour transmittance Tw in the spectral window of use and afterwards to develop empirical formulas using RTM calculations to determine the IWV from the calculated transmittance.

For specific spectral regions in the near infrared, where absorption of dominant trace gases can be considered negligible, we can express the transmittance of the Atmosphere (T_{atmo}) as follows:

$$T_{atmo} = \frac{I_\lambda}{I_{0,\lambda}} \qquad (5.1)$$

where I_λ is the recorded spectral irradiance at wavelength λ (in Wm-2nm-1) and Io,λ is the value of the solar irradiance at the top of the atmosphere at the same wavelength.

The Beer-Lambert law (Swinehart, 1962) could be expressed with respect to water vapour transmittance as follows:

$$T_{atmo} = e^{(-m_{ray}\tau_{ray,\lambda} - m_a\tau_{a,\lambda})} * T_w \qquad (5.2)$$

$$T_w = \frac{I_\lambda e^{(m_{ray}\tau_{ray,\lambda} + m_a\tau_{a,\lambda})}}{I_{0,\lambda}} \qquad (5.3)$$

where T_w is the transmittance of water vapour, τ_{ray} is the Rayleigh scattering optical depth, τ_a is the aerosol optical depth (AOD), m is the relative optical air mass of aerosol and Rayleigh scattering accordingly. For the Rayleigh scattering cross-section the formula found at Bodhaine et al. (1999) has been used.

Also, for $I_{0\lambda,}$ extraterrestrial values calculated for each of the PSR wavelengths measured have been used and are presented by Gröbner et al. (2017a, 2017b). Spectral AODs were calculated using the Beer-Lambert law and the above extraterrestrial solar spectrum (Kouremeti and Gröbner, 2012). For calculating AOD at the wavelengths in the 920-950nm region, where direct sun measurements are affected by water vapour, we have applied a least square quadratic spectral extrapolation, using ln(AOD) as function of ln(wavelength) and the PSR AODs at 500 - 865 nm following Eck et al. (1999) suggestion for AERONET retrievals.

In order to convert Tw into IWV we have used the three-parameter expression found in Ingold et al. (2000):

$$T_w = ce^{-a\chi^b} \qquad (5.4)$$

where

$$\chi = \frac{u\, m_w}{u_0} \qquad (5.5)$$

with u_o = 10 kg/m^2 , u representing IWV, m_w as the H_2O air mass and a,b,c the three wavelength dependent coefficients. At this step the coefficients of equation (5.4) can be estimated. For that purpose, MODTRAN multiple runs have been performed for solar zenith angle (SZA) in the region of 0^o to 85^o with steps of 2.5^o. The mid-latitude built in model atmosphere have been used, in the spectral region 0.7 to 1.0 μm and IWV from 0 to 40 mm with steps of 2 mm for site elevation set at 110m (MOL-RAO). The modeled spectra were convolved by the spectrally dependent instrument slit function in order to derive comparable (model-PSR) results. Then T_w retrieved from the output spectra was calculated as a function of Slant Water Vapour Path (m_w*u), and a fit of these values is used to estimate the coefficients (a, b, c) of equation (5.4). This procedure was repeated for all PSR channels in the whole spectral region of 900-950 nm. In figure 5.5, corresponding fits for wavelengths 935.5 and 946 nm are presented. Fits for wavelengths lower than 926 nm were unsatisfactory (R^2<0.7), suggesting that a different parameterization should be used in this area instead of equation (5.4).

After determining the coefficients a,b,c, equations could be solved in order to calculate the IWV :

$$IWV = \frac{1}{m_w}\left(\frac{ln\left(T_w/c\right)}{-a}\right)^{1/b} \qquad (5.6)$$

Thus, IWV now depends only on T_w and air mass, although the coefficients depend on the altitude of the measurement site; so, different RTM runs are needed for each installation.

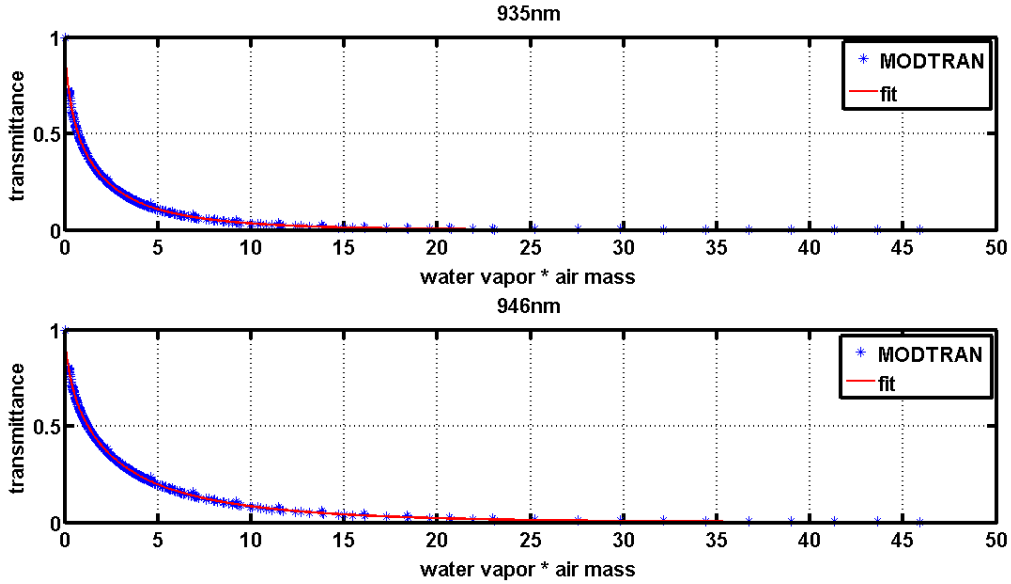

Figure 5.5. Transmittance of IWV versus Slant Water Vapour Path (mw*u) calculated by MODTRAN, and three-parameters expression fit for 935 and 946nm bandpasses.

In order to test the above methodology, IWV has been retrieved on September 30th 2015, for each PSR channel in the 920-950 nm region separately, after calculating wavelength dependent a, b, and c coefficients. Also, aerosol and Rayleigh transmissions were calculated separately for each wavelength. An average value of all wavelengths in the regions 920-948nm is shown in Figure 3 for one day alongside with GPS IWV retrievals. The standard deviation of the residuals retrieved from different wavelengths is 0.11. The IWV retrievals at 946 and 935.5 nm have the smallest deviations compared to the GPS and CIMEL retrievals, because at these wavelengths the absorption due to water vapour absorption is higher. At these two wavelengths, the agreement with CIMEL measurements is very good, with correlations (expressed as the R^2 coefficient) of 0.94 and 0.93 respectively. The lowest R^2 is found for wavelengths shorter than 928 nm which is in the order of 0.6. At figure 5.6 the mean IWV from all wavelengths for one day (30 September 2015) is presented as an example, alongside with the standard deviation of all monochromatic retrievals and retrievals at 946 nm are presented as reference. The standard deviation of the residuals retrieved from different wavelengths is 0.11. Following WMO guidelines, retrievals at 946 nm were selected to use for this study and the monochromatic approach.

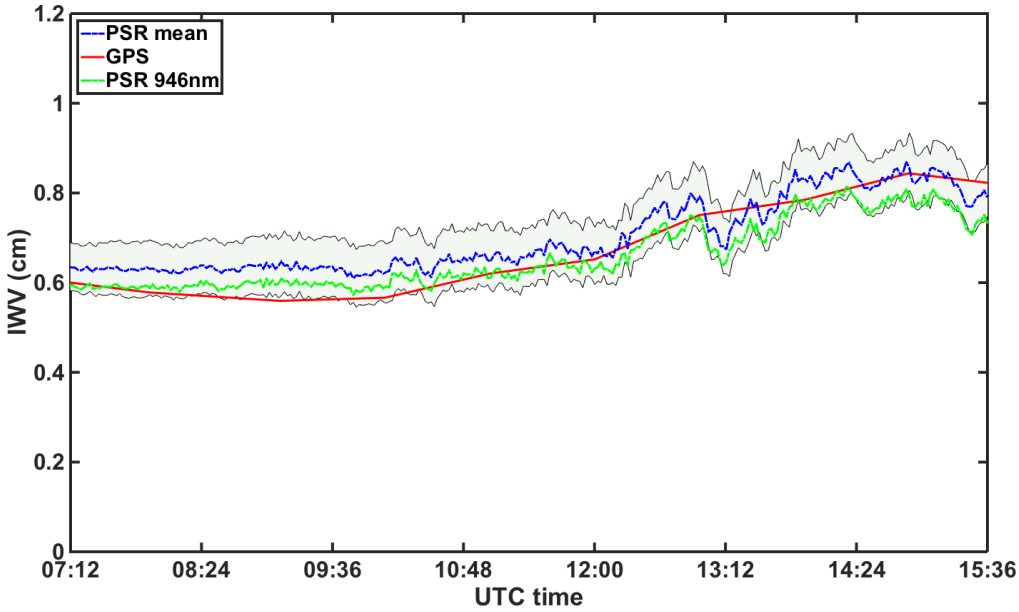

Figure 5.6 Retrievals of monochromatic approach on 30th September 2015 at various wavelengths. Average IWV retrieved using the monochromatic approach at different wavelengths represented by blue line; the shaded area represents the standard deviation (1σ) of retrievals at different wavelengths, green line represent retrievals at suggested 946 nm and the red curve represents the IWV retrieved from GPS.

5.2.2 IWV retrieval using integrated spectral windows

In order to benefit from the high resolution spectral measurements available from the PSR, a method was developed that utilizes direct sun integrated irradiances for a spectral window in contrast to individual/single wavelengths as previously described. This methodology is expected to improve the IWV retrieval, since the large variability found in the IWV retrievals at different wavelengths suggests that an approach that combines different wavelengths could possibly be more accurate. Figure 5.7 shows two theoretical spectra in the region of 700-1000 nm (calculated using MODTRAN), at SZA=0^o with no aerosol load and with 0 and 2 cm of IWV respectively. In this approach we have used the transmittance of the whole spectral window, and then equation (5.3) can be written as follows:

$$T_{w,\Delta\lambda} = \frac{\int_{\lambda_1}^{\lambda_2} \frac{I(\lambda)\exp\left(m_{ray}\tau_{ray}(\lambda)+m_a\tau_a(\lambda)\right)}{I_0(\lambda)} d\lambda}{\Delta\lambda} \qquad (5.7)$$

Where λ_1 and λ_2 are the area wavelength limits, and $\Delta\lambda=\lambda_2-\lambda_1$.

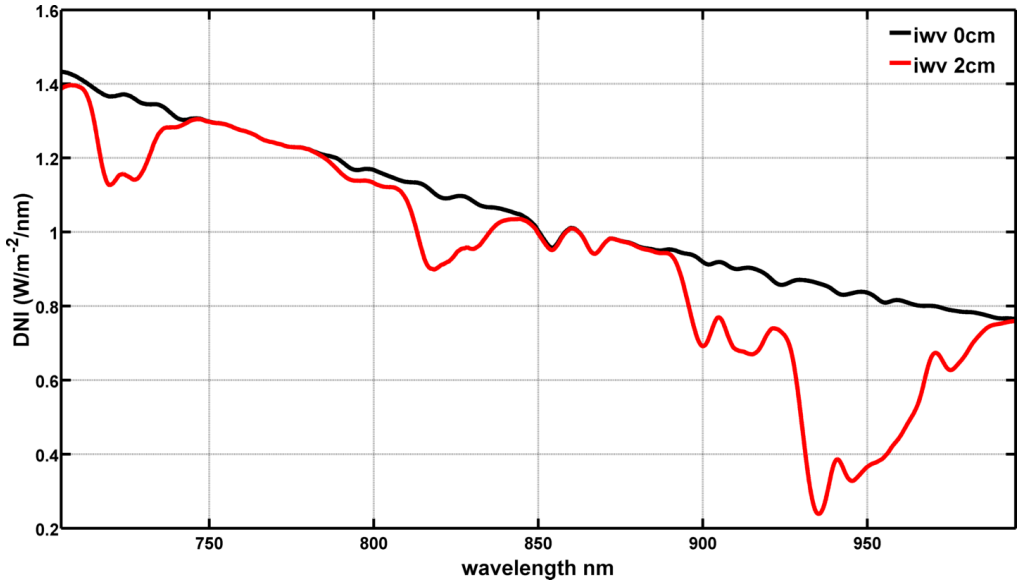

Figure 5.7. Calculated Spectra of Direct Solar Irradiance, at SZA=0^o with AOD=0 and IWV=0 cm (black) and 2 cm (red), as calculated from MODTRAN 5.2.1 RTM.

A similar methodology for converting transmittance to IWV, as in the monochromatic approach described above is applied again in order to calculate a third order polynomial function, valid for the wide spectral region. The same MODTRAN outputs were used as in the monochromatic approach but integrated over each spectral window, and the coefficients for equation (5.4) were calculated accordingly. Calculations have been performed for spectral windows with variable wavelength limits. An investigation on the selection of spectral window has been performed because, as monochromatic retrievals suggested (figure 5.6), the IWV calculation depends on the wavelength region in use. This investigation was made by changing the window, keeping the upper limit fixed at 948 nm and having the lower one varying between 930 to 946 nm with a step of 1 nm. This selection was made based on the water vapour absorption features as shown in Figure 5.7, so that the spectral window always includes the high absorption region of 943-947 nm. Longer than 947 nm wavelengths was avoided as there were higher uncertainties in the PSR calibration (Kouremeti et al., 2015, Gröbner et al., 2017). As demonstrated in Figure 5.8 (for the 934 - 948 nm window), fitting of the 3-parameter equation had results of similar statistics with the monochromatic approach in that region. Residuals from fitting at this window are at average at 0.007 but there are also some up to 0.04. So, for each spectral window a new 3-parameter function is calculated.

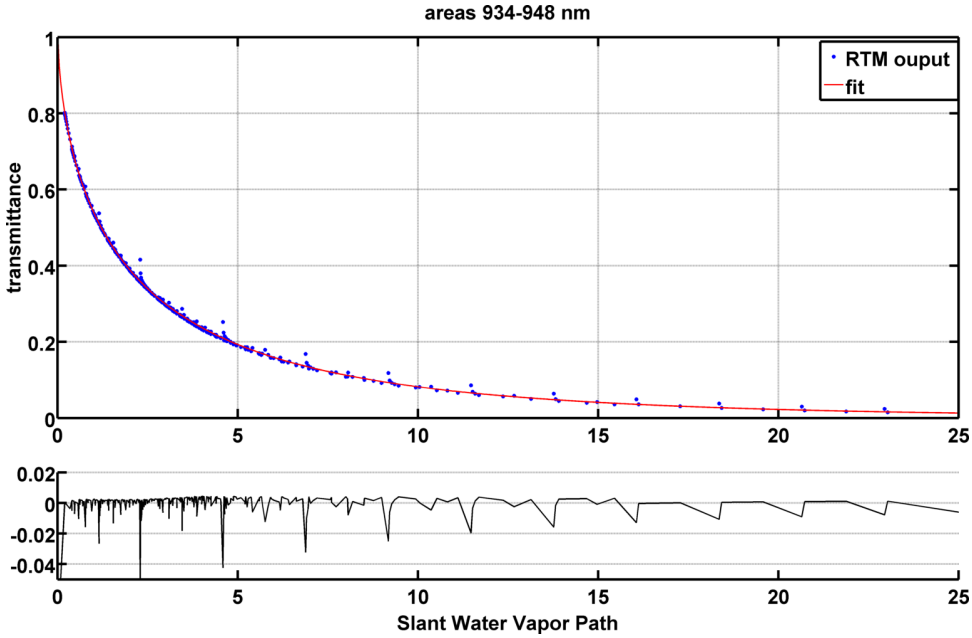

Figure 5.8. Integrated Transmittance of IWV in the 934-948 nm window versus Slant Water Vapour Path (mw*u) calculated by MODTRAN, and Third order polynomial fit.

In figure 5.9 results from different spectral windows have been compared to other instruments' retrievals for the whole MOL-RAO dataset, using R^2 coefficient of determination to evaluate the performance. Horizontal axis of figure 5.9 represents the shorter limit of the spectral window, the longer being always fixed at 948 nm. The aim of this step is to find out which spectral window produces the more robust IWV retrieval results. These comparisons suggest that different spectral windows selection lead to different coefficients of determination for IWV retrieval compared with different instruments. However, results converge to defining a lower wavelength limit between 932 and 936 nm that will provide the best agreement for all the comparisons. The window 934-948 nm was selected to be used for further analysis, as a median of the above mention area.

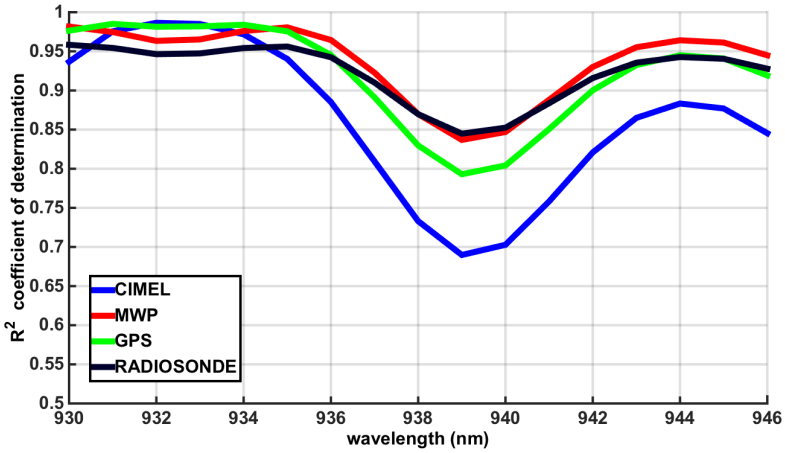

Figure 5.9, IWV retrievals from PSR using spectral approach with different spectral windows, using fixed upper boundary at 946 nm and moving lower boundary at x axis, compared to synchronous ones of CIMEL, GPS, MWP and radiosonde, for the full 2-year measuring period.

It is interesting to observe different R^2 of the PSR IWV retrievals as compared using different instruments. Especially the fact that by minimizing the spectral window the R^2s decrease showing a minimum at window 939-946 nm. For this particular range all R^2s are below 0.85 with the one of CIMEL-PSR showing a minimum. The differences observed when comparing the PSR using different instruments can be partly explained based on the results of section 5.4.

5.3. Uncertainty budget of IWV retrievals

Uncertainty estimation of the IWV retrieval is very crucial for evaluating our comparing comparison results. Beginning from equations (5.3) and (5.7) and the calculations of Tw, errors as introduced from each variable are estimated and their propagation to the total uncertainty of IWV retrieval is calculated.

$$T_w = \frac{I_\lambda e^{(m_{ray}\tau_{ray,\lambda}+m_a\tau_{a,\lambda})}}{I_{0,\lambda}} \quad (5.3)$$

From equation (5.3), the term that introduces the higher uncertainty in the retrieval of the IWV through the use of Beer-Lamber law is the AOD. A benefit from the methodology applied in this case is that the same set of Io are used for calculating Tw and AOD, and so errors related to the determination of I_o do not

propagate in the calculations. PSR AOD retrievals at 865 nm have been found in accordance with prototype PFR triad when compared during FRC IV, 2015 (Filter Radiometer Comparison (GAW, 2016)) with average AOD differences at 865nm less than 0.02. Also, a calibration stability study of the PSR was performed (Kouremeti et al., 2015) and showed that the instrument was stable in the 2-year dataset of MOL-RAO, demonstrating a mean difference of 0.3% with maximum of 4% in some channels. In addition, comparison with different CIMEL instruments for longer periods in all cases showed differences smaller than 0.03 at AOD at visible and near infrared wavelengths (Kouremeti and Gröbner, 2014). So, the AOD related uncertainty calculated in all studies for the PSR is in at maximum 0.03.

Rayleigh optical depths in this spectral region are very low (~0.01 for 1000 mb pressure) and the uncertainty is 1% (Teillet, 1990) and, thus, we may consider it negligible for the IWV retrieval. Air masses were calculated using the formula found in Kasten (1966), which assumes a standard vertical profile of humidity in the troposphere and introduces an error of 10% at SZA higher than 85°, due to variations in real atmospheric conditions but is negligible for SZA lower than 75° (Tomasi et al., 1998).

Coefficients a, b, c derived from fitting of MODTRAN outputs introduce an uncertainty that is related to the goodness of the calculated fit. For the monochromatic approach at 946nm, Root Mean Square Error (RMSE) is 0.0021 and for the spectral approach at window 934-948nm it is 0.0029. So, the uncertainties introduced using the empirical equation to estimate IWV from Tw is 0.2% and 0.3% for each approach accordingly, due to the fitting.

Uncertainty is also introduced by the extrapolation of AOD from the 865 nm and lower wavelength region to water absorbing wavelengths in the range of 934-948 nm. A sensitivity analysis of the IWV retrieval in respect to fluctuations in AOD caused by the uncertainty of AOD was performed. The uncertainty of this extrapolation was calculated to be 0.03.

Figure 5.10 shows the total expected uncertainty of IWV retrieval with respect to SZA, for the case of AOD=0.3 at 865 nm and the case of IWV equal to 2 cm. Highest uncertainties are expected for higher than 75° SZA, when IWV is very low or AOD very high. Very low IWV values could be found only at very dry atmospheres and even then, those are rarely below 0.2 cm. In the range of values found in the dataset of MOL-RAO (0.3 - 4.5cm), the maximum uncertainty is 0.28cm. For the 0.3 - 0.5cm values in our dataset, absolute uncertainty is calculated as 0.08-0.12 cm. Thus, the maximum expected uncertainty of the method, using PSR

instruments, is found at the range of 15%, when the solar zenith angle is very high (SZA>75^{o}) and AOD higher than 0.9.

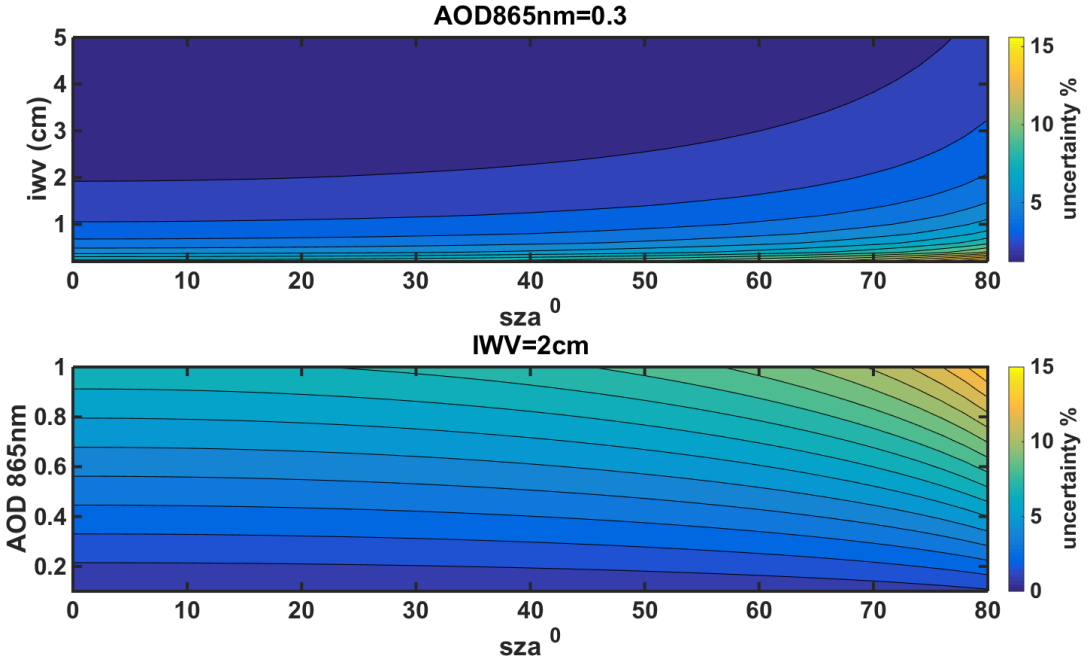

figure 5.10. Uncertainty (%) of IWV retrieved using monochromatic approach at 946 nm, for various Solar Zenith Angles (^{o}) test figure, in respect to AOD (when IWV=2cm) in lower plot, and with respect to IWV (when AOD=0.3) in upper plot.

5.4. Results

In order to validate the results retrieved from both methodologies, different IWV datasets recorded at MOL-RAO have been used. Calculations have been performed for all PSR measurements, but we have used only the ones synchronous to CIMEL level data in order to avoid cloud contamination (Smirnov et al., 2000). So indirectly the AERONET cloud screening procedure (Smirnov et al., 2000) has been used. For each CIMEL data point we have calculated the synchronous PSR value by averaging all values in a ±5 min interval. This approach produced a dataset of 3501 synchronous data points between PSR and CIMEL, 2507 between PSR and GPS and 2964 between PSR and MWP. For radiosondes, in order to have a robust coincidence criterion, the approach of Schneider et al. (2010) was followed, averaging PSR measurements for ±20 min from the time that the radiosonde reaches a 4 km height, in order to minimize spatial and temporal PSR and radiosonde measurement differences.

For all the comparisons statistics are calculated for the differences

$$D_X = IWV_X - IWV_{PSR} \quad (5.8)$$

where x is the corresponding instrument/method, μ_X is the average value for D_X and

$$\sigma = \sqrt{\frac{\sum_1^N |D_{xi} - \mu_x|^2}{N-1}} \quad (5.9)$$

where N is the number of available, quality controlled observations.

For the monochromatic approach at 946 nm, the comparison is presented in Figure 5.11 and corresponding statistics in Table 5.1. Better agreement was found when compared to MWP retrievals, but at similar level as for the comparisons to CIMEL and to GPS retrievals. Mean absolute difference is slightly lower when compared to GPS (0.02 01 cm), but the spread of the differences is almost the same for CIMEL, GPS and MWP (standard deviation between 0.16 17 cm and 0.18 cm). Differences with CIMEL retrieval are within the CIMEL uncertainty range. It appears that PSR overestimates the IWV compared to CIMEL for IWV larger than 3 cm, which causes the different slope in the graphs. This feature is not shown in the comparison with GPS and MWP at these IWV values. Schneider et al. (2010) also observed a different behavior of CIMEL retrievals as compared to other methods, regarding dry or wet conditions in the atmosphere and linked to filter characterization errors. Radiosonde retrievals had largest deviations and more scattered differences, which is expected because of the different temporal and spatial scale of the RS retrieval. Percentiles 10-90 of the differences are also presented in table 1 and GPS, MWP and CIMEL retrievals have a spread of differences in the range of the uncertainties described for these instruments. In general RS retrievals demonstrate the most spread differences from the PSR retrievals, though the average and median are in the uncertainty range of the instruments. The high spread of the differences is explained by the random error introduced by the temporal variability of IWV in the time range averaged (±20min) and by the different paths of the sounding.

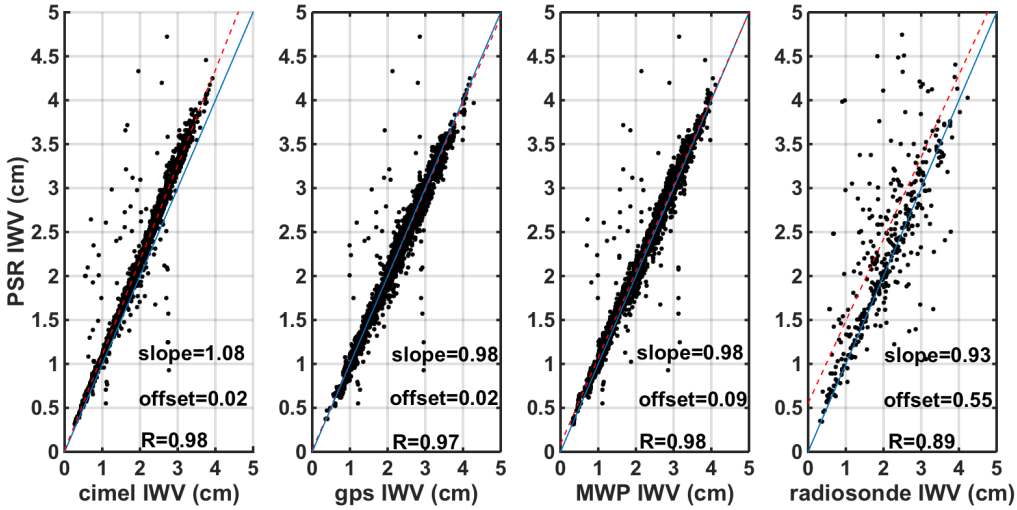

Figure 5.11: IWV retrievals from PSR using monochromatic approach at 946 nm compared to synchronous ones of CIMEL, GPS, MWP and radiosonde, for the full 2-years measuring period.

A histogram of relative difference of this retrieval compared to GPS is demonstrated in Figure 5.12. Also, IWV retrievals relative differences are shown against other parameters (AOD, SZA and IWV from GPS). A normal distribution with mean at 0.024 cm and standard deviation of 0.084 is fitted to the differences and passed the One-sample Kolmogorov-Smirnov test (Marsaglia et al., 2003). Thus 95% of the absolute differences are lower than 0.16cm. IWV differences against AOD at 865 nm show that almost all absolute relative differences higher than 0.2 cm (20%) are linked to AOD values higher than 0.5. This pattern could be connected to the higher error introduced larger uncertainty of AOD calculated by the extrapolation of AOD at 946 nm, using different wavelengths when AOD values are higher. Furthermore, it appears that most of the large differences appear at high SZA, but there are also some individual points showing large differences at lower SZA that could be linked to AOD uncertainty. Compared to IWV retrieved from the GPS it appears that extreme differences are linked to overestimation from PSR when the absolute value is above 2 cm, and to underestimation when below , though GPS retrievals are not optimal at more dry conditions (Schneider et. al., 2010).

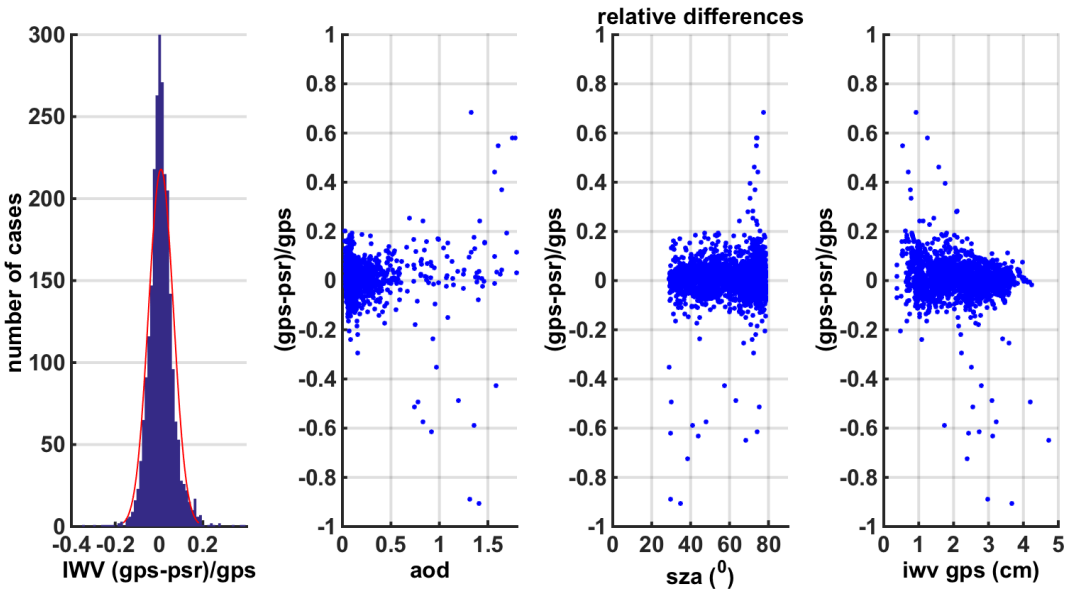

figure 5.12. Histogram of relative difference among synchronous GPS and PSR retrievals – using monochromatic approach at 946 nm- and plotted against AOD (retrieved from PSR at 865 nm), solar zenith angle and IWV (retrieved from GPS).

Table 5.1. Statistics of the differences among retrievals from PSR using Monochromatic approach at 946 nm, and retrievals from other instruments for the whole dataset.

	N	*mean (cm)*	*standard deviation(CM)*	*median (cm)*	*percentile 10-90 (CM)*	*mean relative (%)*	R^2
CIMEL	3501	-0.16	0.18	-0.14	-0.30 -0.04	-3.3	0.92
GPS	2507	0.01	0.17	0.01	-0.11 0.14	0.4	0.94
MWP	2964	-0.05	0.17	-0.04	-0.16 0.07	-0.4	0.95
RS	414	-0.41	1.03	-0.10	-1.42 0.22	-2.7	0.79

Comparison of the PSR spectral method with other instruments is presented in Figure 5.13 and corresponding statics statistics in Table 5.2. The spread of differences with all methods is significantly lower than for the monochromatic approach. All comparisons are found with R^2 between 0.96 and 0.98. CIMEL seems to underestimate, compared to this method, but also compared with the other instruments at higher IWV values. Although the slope caused by the overestimation is still presented in this approach, the spread of the differences among CIMEL and PSR retrievals is significantly lower than any other comparison, with σ=0.07 and

10-90 percentiles of differences in a range of -0.23–0.02. Differences with GPS and MWP retrievals have the same spread and statistical behavior. Radiosonde data are in significantly better agreement with the spectral approach retrieval than with the monochromatic approach. Standard deviation of the differences is at least halved as compared to the monochromatic approach and all mean relative differences when compared to any other instrument are lower than 0.7%. Comparison with RS' dataset has still significantly larger standard deviation than other comparisons but it is less than 1/4 of the monochromatic approach. Extreme values observed with the monochromatic approach are significantly reduced and the standard deviation is reduced to values from 0.07 for CIMEL to 0.18 for RS retrievals. A wider spread is observed at higher SZA, which is explained by the increase of the instrument related uncertainty at these angles.

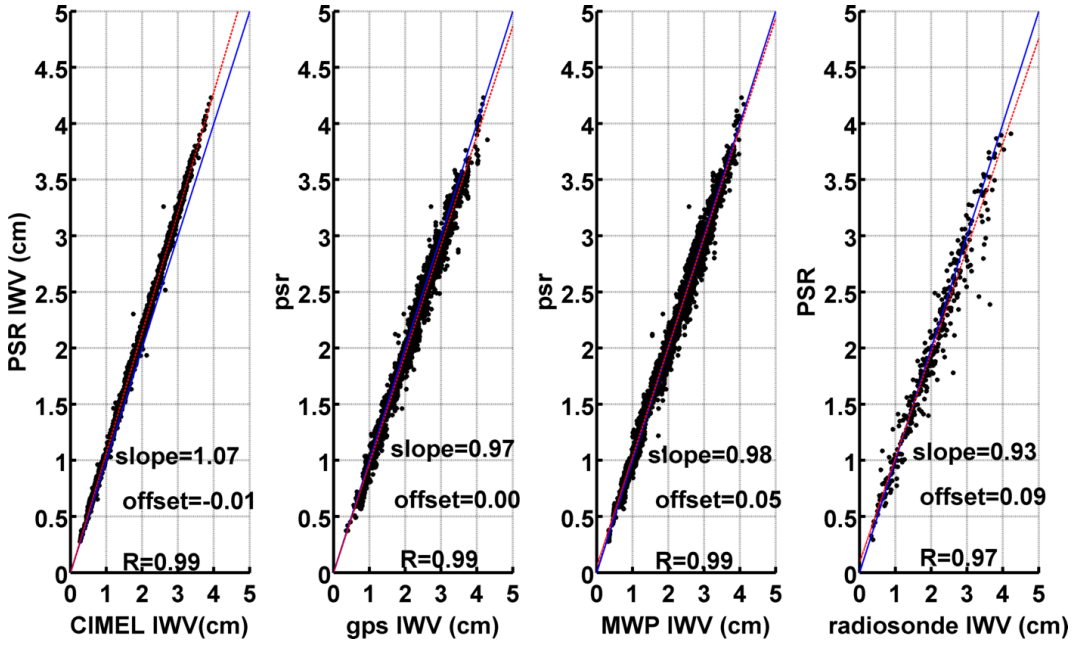

Figure 5.13 IWV retrievals from PSR using spectral approach at 934-948 nm region, compared to synchronous ones of CIMEL, GPS, MWP and radiosonde, for the full 2-year measuring period.

Figure 5.14 displays a histogram of relative differences of the spectral approach for the spectral window 934-948 nm the GPS dataset and a relative IWV comparison against: AOD at 865nm, SZA and GPS' IWV. A normal distribution with mean at 0.021cm and σ at 0.042 is fitted at the data, passed the One-sample Kolmogorov-Smirnov test (Marsaglia et al., 2003) and 95% of differences are lower than 0.08 cm. The quality of spectral retrieval shows no dependence on absolute IWV values, as the distribution of differences in figure Figure 5.14 is independent

of IWV. When the IWV relative difference is shown against AOD, higher relative differences than 0.1 are more frequent for AOD lower than 0.2.

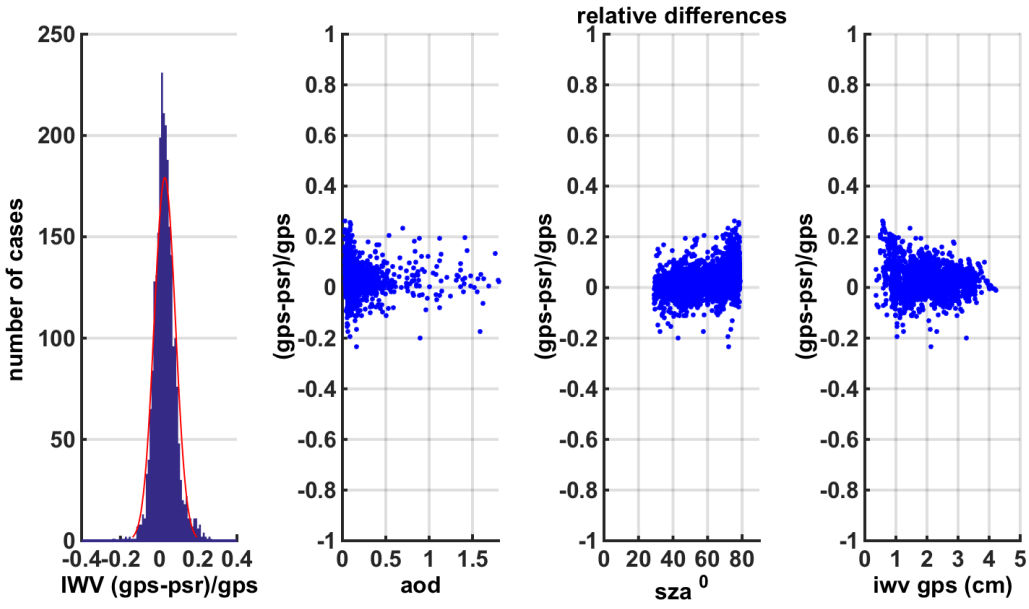

figure 5.14. Relative difference among synchronous GPS and PSR retrievals – using spectral approach at 934-948nm region- plotted against (a) AOD (retrieved from PSR at 865nm), (b) solar zenith angle and (c) IWV (retrieved from GPS).

Table 5.2. Statistics of differences among retrievals from PSR using Spectral Approach at 934-948 nm window, and retrievals from other instruments for the whole dataset.

	N	*mean (cm)*	*standard deviation (CM)*	*median (cm)*	*percentile 10-90 (CM)*	*mean relative (%)*	R^2
CIMEL	3501	-0.11	0.07	-0.10	-0.23 -0.02	-0.7	0.97
GPS	2507	0.05	0.10	0.04	-0.06 0.18	0.4	0.97
MWP	2964	-0.04	0.10	0.01	-0.12 0.12	0.3	0.98
RS	414	0.04	0.18	0.02	-0.13 0.25	0.5	0.95

5.5. Conclusions

The aim of the work presented in this chapter was to develop methodologies and tools in order to retrieve IWV from PSR spectral measurements. The methods which were developed can be applied to provide long term time-series of IWV using any direct sun spectroradiometer able to measure at the 930-950 spectral range.

Two approaches to retrieve IWV from PSR spectral direct solar irradiance measurements have been developed. The first one is the monochromatic approach using an individual wavelength, and the second use a spectral window. For both methods the corresponding Water Vapour Transmittance has been retrieved from the PSR measurements, from which IWV can be calculated using a three-parameter formula following the principles of Ingold's (2000) work.

The dependence of the retrievals to other parameters has been investigated for both approaches and found to be affected in cases of low (<0.2) AOD coincidencies. Larger deviations were observed at high Solar Zenith Angles, which are linked to higher uncertainties in those retrievals.

Comparisons to other instruments (CIMEL, MWP) and methods (GPS, radiosondes) have been performed to select the optimum wavelength and spectral window for the IWV retrieval of the PSR. All the channels in the infrared region of 900-950 nm were tested for monochromatic approach and 946 nm bandpass was selected as giving significantly better results than other channels. For the spectral approach all possible spectral windows limits combinations were tested and the spectral window of 934-948 nm was finally chosen.

Uncertainties of the methodologies have been investigated and in more frequent atmospheric conditions have been found less than 5%, while might reach up to 15% in cases of very high AOD, very low IWV and SZA higher than 75o combined. In general, absolute uncertainty is found to be in the range of 0.08-0.3 cm.

Retrievals from a 2-year long time-series at MOL-RAO in Lindenberg, Germany showed that the monochromatic approach had differences in the order of 0.4% compared to GPS and MWP, in the order of 2.7% compared to RS, and 3.3% compared to CIMEL. 95% of differences with GPS retrievals are less than 0.15 cm.

Spectral approach's retrievals showed better agreement with other datasets, having differences of 0.7% compared to CIMEL, 0.4% compared to GPS, 0.3% compared to MWP and 0.5% when compared to RS. Also , the differences to other retrievals were always at least half spread compared to monochromatic approach.

Differences with GPS retrievals were less than 0.08cm in 95% of the dataset. Differences among the other instruments found independent of other variables, suggesting robust appliance of the method.

6. Single Scattering Albedo in UV spectral region, retrieved using an Ultraviolet Moving Filter Radiometer

This chapter is based on the publication Kazadzis, S., Raptis, P., Kouremeti, N., Amiridis, V., Arola, A., Gerasopoulos, E. and Schuster, G.L., 2016. Aerosol absorption retrieval at ultraviolet wavelengths in a complex environment. Atmospheric Measurement Techniques, 9(12), p.5997.

The role of aerosols, both natural and anthropogenic, is extremely important for regional and global climate change studies as well as for overall pollution mitigation strategies (e.g., IPCC,2013). However, a considerable amount of work still needs to be carried out, particularly as it appears that climate change is accelerating, with aerosols impacting at local, regional and global scales. Furthermore, the components controlling aerosol forcing, account for the largest uncertainties in relation to anthropogenic climate change (IPCC, 2013). Comprehensive measurements are crucial to understand their effects and to reduce SSA uncertainties that propagate into aerosol radiative forcing estimates. SSA calculated here differs from in situ SSA values retrieved from absorption and scattering measurements at a single altitude level (e.g., at the ground), in that it is a columnar measurement, arising from solar irradiance transfer in the atmosphere.

Although, there are several retrievals in the visible and near infrared pars of the spectrum (including AERONET and SKYNET retrievals in hundreds of stations around the globe), observations in the UV part are quite rare and mainly focused on experimental campaigns.

In this work, for the calculation of the UV-SSA, a methodology based on the idea of Krotkov et al. (2005a), Krotkov et al. (2005b) and Corr et al. (2009) is adopted. The methodology, together with the retrieval tools used and technical assumptions made are presented in section 6.2. Results of UV-SSA measurements and their comparison with synchronous AERONET retrievals in the visible range are presented in section 6.3. Finally, discussion of the observed diurnal SSA patterns in Athens, SSA wavelength dependency as well as overall conclusions are presented in the last section of this work.

6.1 Methodology

In this work estimates of SSA are presented at two independently retrieved UV wavelengths 332nm and 368 nm for an urban site situated in Athens, Greece. The period of measurements analyzed is from July 2009 to May 2014. All measurements took place using a UVMFR and a CIMEL at Atmospheric Remote Sensing Station (ARSS – more details at 3.1)

6.1 Retrieval methodology

SSA is a key aerosol optical property and describes the portion of solar irradiance that is scattered from the main direct beam passing through the atmosphere. Changes in SSA influence only the diffuse radiation reaching the earth's surface, while they don't effect direct radiation. Model calculations can be used for retrieving SSA when global and/or diffuse spectral irradiance, solar zenith angle (SZA), total column ozone, and AOD are known (Krotkov et al., 2005b; Kazadzis et al., 2010; Ialongo et al., 2010; Corr et al., 2009; Bais et al., 2005). Present retrieval methodology is based on the approach that is described in detail in the Corr et al. (2009), Krotkov et al. (2005a) and Krotkov et al. (2005b). This approach consists of measurements of the Direct Irradiance (DI) to Global Horizontal Irradiance (GHI) ratios (DGR) and AODs measured with the UVMFR instrument for our case, that are used as basic input parameters to the RTM for the calculation of the SSA at 332nm, and 368nm. These wavelengths are selected for having the lowest ozone absorption from the seven available (Bass and Paur , 1985). The advantage of this method is that the same detector and filter measure DI and GHI, thus there is no need for absolute irradiance calibration and raw voltage measurements -corrected for nighttime voltages and angular response - could be used.

GHI measurements from the UVMFR have been used in order to distinguish cloud free conditions for each of the one minute measurements as described in 3.2.1.

Measurements of the DHI and GHI from the UVMFR have been used in order to retrieve DI at 332nm and 368nm. ETC from these measurements was derived as described in 3.2.1. and AODs at 332 nm and 368 were calculated accordingly. C. In contrast with the Krotkov et al., 2005a approach ,CIMEL Extraterrestrial Constant (ETC) was not transferred to the UVMFR measurements; rather, independently calculated (UVMFR-based) AODs were estimated. Validation of the results was performed based on synchronous UVMFR and CIMEL measurements. The mean AOD calculated from the 1 minute UVMFR measurements within ±5 minutes from the CIMEL measurement (when the UVMFR 10 minute period is characterized by cloudless conditions) has been defined as synchronous. Since the CIMEL instrument provides measurements of AOD at 340 nm and 380 nm, CIMEL derived AOD at 332 nm and 368 nm was estimated by applying least square quadratic spectral extrapolation, using ln(AOD) as function of ln(wavelength) for AERONET measurements at 340nm 380nm, 440nm and 500nm. (Eck et al, 1999).

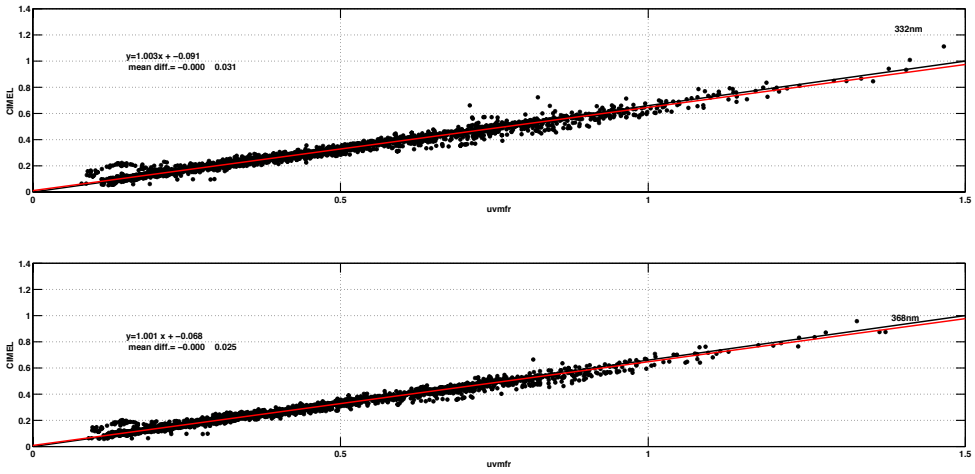

Figure 6.1. Comparison of CIMEL and UVMFR retrieved AODs for synchronous measurements for 332 nm (top panel) and 368 nm (bottom panel). Red lines indicate 1-1 curve, and black ones are the corresponding 1st order linear fits.

The results of this comparison have a Pearson product moment correlation coefficient equal to 0.96 and 0.98 respectively for 332nm and 368nm AODs. Mean differences were zero, with standard deviations of 0.031 and 0.025 for the respective wavelengths, comparable with the CIMEL AOD retrieval uncertainty of ±0.02. The quality of the data produced can be verified by comparing the AOD's retrieved by the two instruments as a function of SZA (figure 6.2). Also lower plot at figure 6.2, shows the number of UVMFR data in each 5^o SZA bin, where only 15^o has less than 10000 data points. Stability of the AOD differences as a function of SZA verifies the validity of the calibration of the UVMFR AOD's and the fact that no SZA-dependent errors (that would be directly related with an erroneous ETC determination) are found in this procedure. In figure 6.2, AOD's have been grouped in bins of 5 degrees (of SZA). The differences shown in figure 5 include ETC determination accuracy, the extrapolation of CIMEL AOD at 368nm, together with instrumental/measurement errors. Using a single UVMFR ETC for the whole period provides very good agreement between the two instruments. However, this may not be the case for all UVMFR instruments using this approach as ETC may suddenly or gradually change especially for years-long time series due to instrumental (filter related) changes. AODs deviations could lead to large errors in SSA calculations, so this comparison ensures that these errors are minimized.

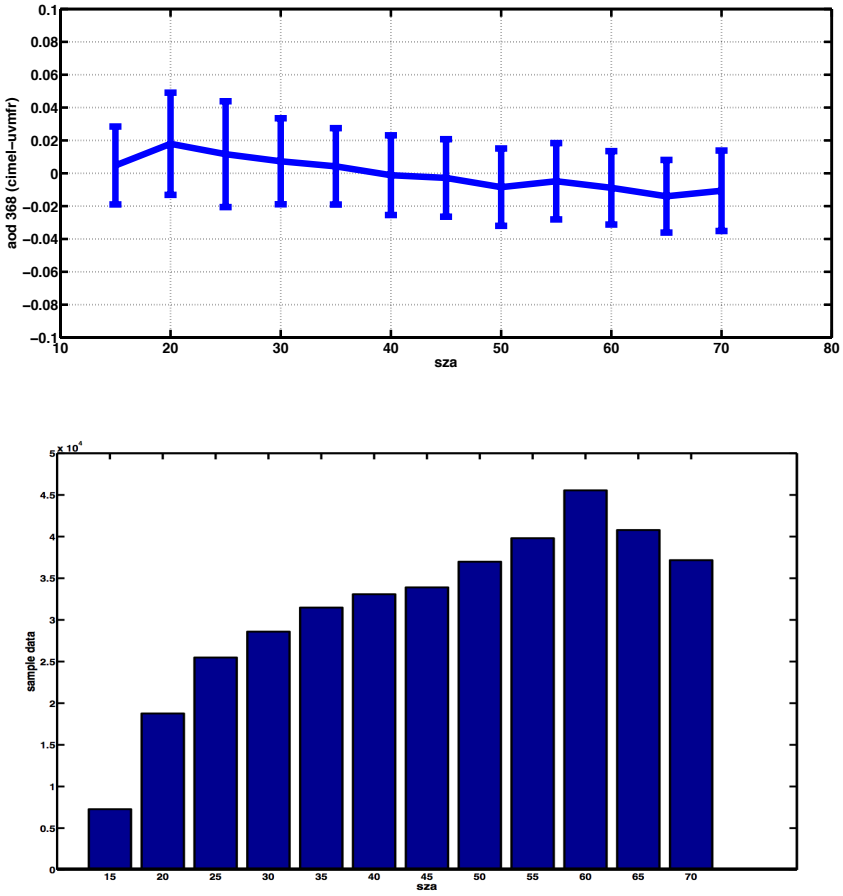

Figure 6.2 AOD differences between CIMEL and UVMFR at 368 nm, as a function of solar zenith angle (upper plot). Number of data on each 5° SZA bin.

Look up tables (LUT) DGR at 368nm and 332nm as a function of SZA, AOD, SSA, asymmetry factor (g) and total column ozone were calculated using the RTM libradtran. Climatological–satellite derived NO_2 and O_3 values were used for construction of the LUT (ones used for AERONET AOD retrieval), while for g, input value was set to mean daily as retrieved at 440nm from the CIMEL instrument measurements when available and the mean value of the whole period equal to 0.7 (2σ standard deviation of the g during this period was 0.04) otherwise. Using the above inputs, matching SSA values for each individual UVMFR DGR measurement were calculated. LUT examples are visualized in figure 6.3, for clarification of the method. For known SZA and AOD (in cloudless sky conditions), the variability of the DGR is caused by SSA other than AOD, . At low aerosol loads this variation is nearly negligible, but it becomes more important at higher aerosol load. More absorbing aerosols lead to smaller values of DGR. It is crucial to observe the range of SSAs in the two examples. For low AOD's, accurate SSA determination requires

very low uncertainty of the DGR and the AOD measurement. While for high AOD's the range of DGRs for a particular SZA is quite large.

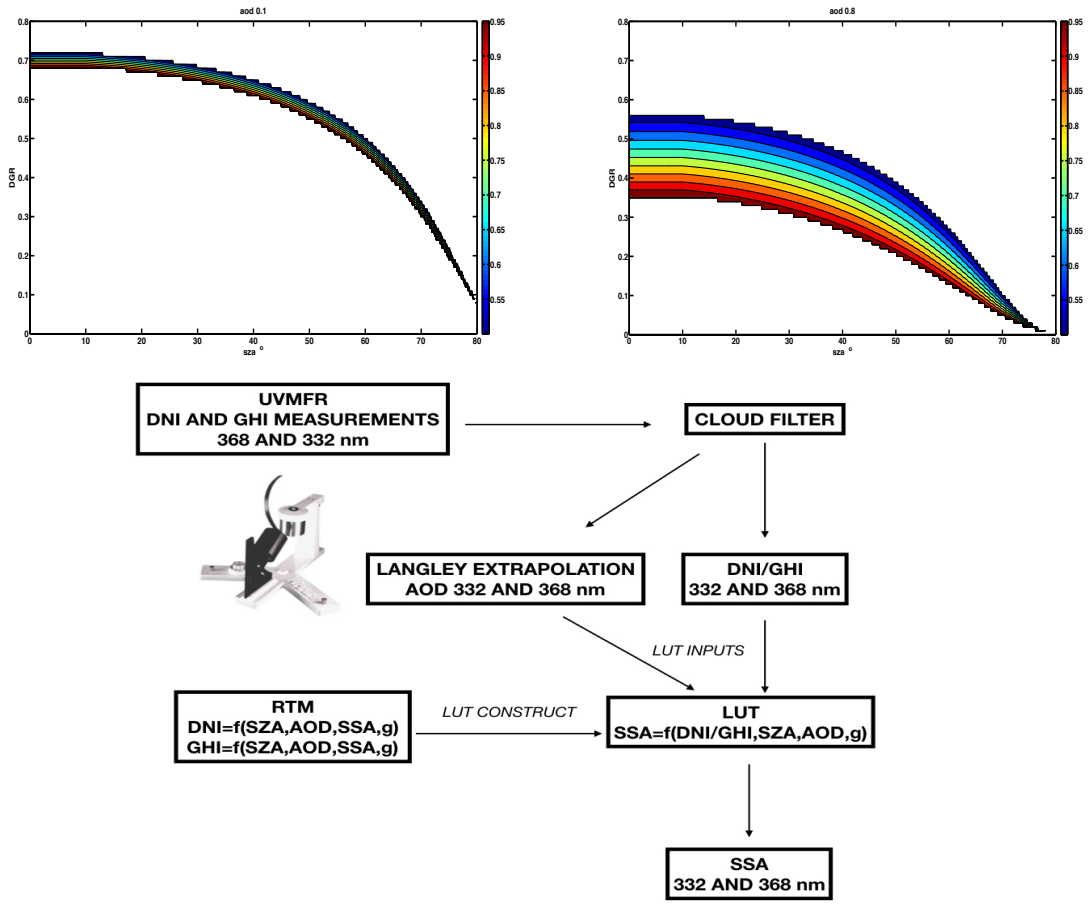

Figure 6.3 LUT of direct to global ratio at 368nm, as calculated for AOD 0.1 (left) and 0.8 (right) with respect to SZA (g=0.7), colorbar represents assumed SSA values (upper). Flow chart of the methodology followed to retrieve SSA from UVFMR measurements (lower)

6.1.2 Retrieval Uncertainties

The CIMEL sunphotometer provides SSA inversion retrievals characterized as Level 1.5 and Level 2.0 data. Level 2.0 (L2) data are recommended by AERONET as they have less uncertainty but are restricted in measurement to SZA>50 degrees, AOD at 440 nm> 0.4 and homogeneous sky conditions. These limitations make AERONET SSA L2 worldwide measurements unsuitable for:

a. climatological studies due to the AOD restriction that limits analyses only to areas having large average annual AODs, or to cases of moderate to high aerosol episodes in specific areas. As an example, for the urban site of Athens, which is one

of the most polluted cities in Europe, the number of measurements is limited to an average 11 cases per month for the whole analysis period.

b. diurnal variation studies due to the SZA restriction. For mid and low latitude sites, this limitation leads to a severe lack of information on diurnal SSA patterns as there are only few wintertime measurements and close to zero measurements at local noon.

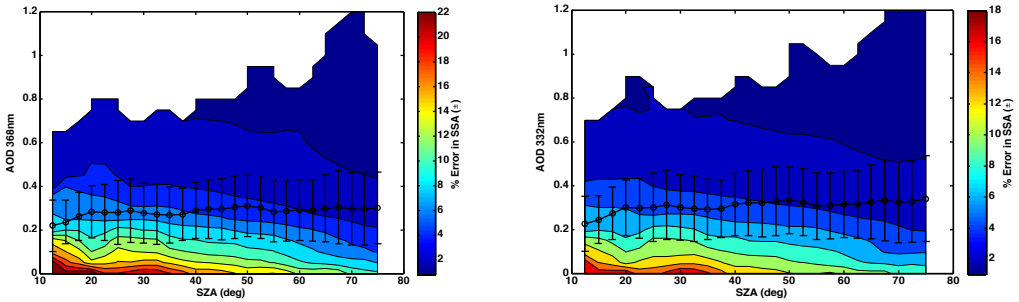

Figure 6.4 Relative Uncertainty estimate (color) for the SSA retrieval from UVMFR as a function of AOD and solar zenith angle for 368nm (left panel) and 332nm (right panel), based on DGR and AOD uncertainties. Superimposed, mean AODs for 2.5 degree bins of solar zenith angle are shown.

Level 1.5 data: AERONET Level 1.5 (L1.5) SSA data are provided by AERONET for all AOD's and at all SZA that almucantar scans are performed. In this work L1.5 data were used, but with an extra quality control. We have ignored SSA L1.5 data when L2 size distribution is not available. Thus we have an enhanced L1.5 SSA data set with AOD<0.4, but with L2 cloud screening, calibrations and quality controls. Data has been compared with UVMFR retrieved SSAs taking into account limitations related with the retrieval uncertainties. Khatri et al (2016) studied AERONET SSA retrieval uncertainties, in order to compare with SKYNET and found that AOD errors introduce the largest variations. They also found that the sky irradiance calibration has a primary role in the uncertainty of the retrieval, and they investigated influence of surface albedo and sphericity of aerosols, that was found negligible.

For the UVMFR data the uncertainty of the UVMFR SSA retrieval is mainly related to:

- direct to global irradiance measurements uncertainties.
- RTM input data accuracy.

DI to GHI measurement uncertainties can result to a range of SSA values rather than a single value, that would produce a close match between the measurement and the RTM DGR outputs. This range broadens at low SZA and high aerosol level

cases, as shown in Figure 6.3, when the effect of the scattering/absorbing nature of aerosols in radiation is greater . The RTM inputs that were used for the SSA LUT construction include also an uncertainty budget (ETC,AOD, surface albedo, constant aerosol vertical profile, asymmetry factor), where the biggest source of uncertainty was linked to AOD retrieval at UVMFR channels. Following the uncertainty analysis of Krotkov et al. (2005b), the total relative uncertainty of the DGR measurement was calculated to be ±3%. AOD absolute uncertainty is considered as 0.02 for 368nm and 0.04 for 332nm, following the analysis of previous section. The impact of this on the SSA calculation is directly connected with AOD levels and the SZA. In figure 6.4 UVMFR SSA retrieval uncertainty was calculated for different AODs and solar zenith angles, caused by DGR and AOD uncertainty. DGR and AOD uncertainty ranges from previous paragraph were used to calculate the possible SSA range and the expected error. In this figure, the mean AODs, for each SZA bin (errorbars equal to one standard deviation) for Athens measured by the UVMFR at each solar angle, are presented. In addition figure 6.5 shows mean values and 1σ of retrieved SSA, where no angular deviated behavior is observed.

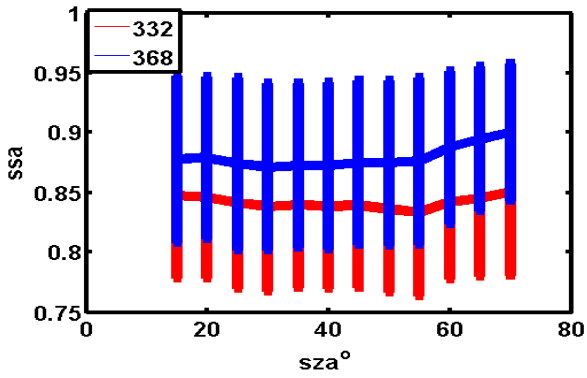

Figure 6.5 Mean SSA at 332 and 368 nm and 1σ errobars , retrieved from UVMFR, averaged at 5° SZA bins.

6.2 SSA retrieval results

Using the methodology described in the previous section SSA at 332nm and 368nm was calculated using 1 minute data from the UVMFR. For the period under investigation, also calculated the daily mean SSA's at these two wavelengths in the UV band and also the mean daily SSA's in the visible band derived from data provided by the CIMEL (L1.5 data) operating in Athens' AERONET station (figure 6.6).

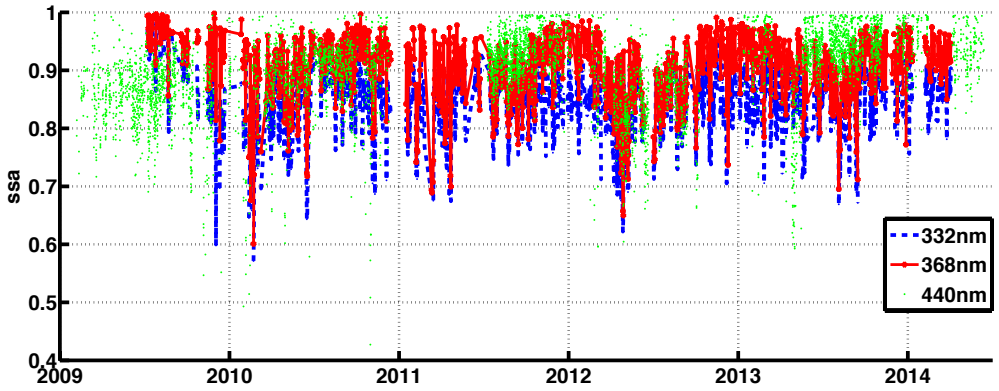

Figure 6.6 Daily mean SSAs in the UV (UVMFR) at two wavelengths and at 440nm(CIMEL) for Athens area.

The variability of SSA during this period is quite high, ranging from 0.75 (0.62) to 0.98 (0.97) for 368nm (3332nm) (2 standard deviations) with mean values of 0.90, 0.87 and 0.83 for 440nm, 368nm and 332nm respectively. In figure 6.7 mean monthly values of SSA at UV wavelengths and standard deviations were calculated for the whole period to examine the annual variability. The lowest SSA values were found for the period from February to May at both wavelengths, which should be linked to the usual dust events during this period for the area, and also the presence of brown carbon. Paraskevopoulou, et al (2014), have found maximum values of Organic and Elemental Carbon, in February and November, in a 5 year (2008-2013) data set of in-situ measurements, at center of Athens. However, most months have similar SSAs, with differences that lie well within the SSA variability of each month. A t-student test was applied to differences between 368 and 332 nm for each month and all differences are proved to bestatistical significant. All months have very large collections of data (in the order of 20000 in winter months to 100000 for summer months). Very small p was calculated for mean difference statistics. A boxplot of these differences is presented in 6.7 lower plot.

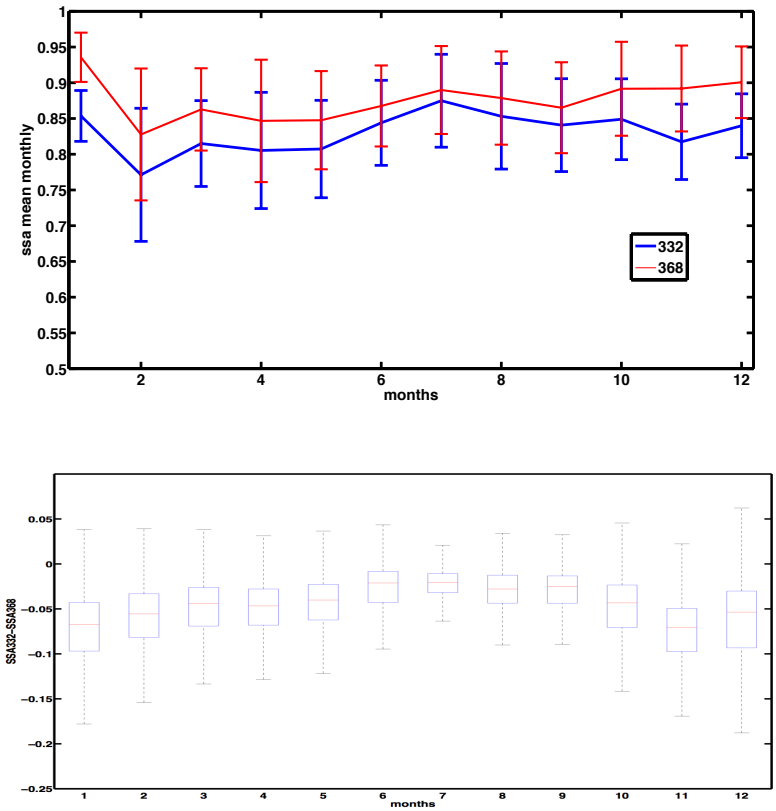

Figure 6.7 Mean monthly SSAs in the UV (UVMFR) at two wavelengths for the whole 5-year period, at Athens, errorbars equal 1σ (upper plot). Difference between SSA_{332} and SSA_{368} averaged for each month (lower plot)

When calculating diurnal patterns of the SSA at UV and visible wavelengths for the Athens area, we observed a mean diurnal pattern with a variability of the order of 0.02 to 0.05 and having highest absorption (lowest SSA's) ±2 hours around noon (figure 6.8). Similar behavior can also be seen from AERONET retrieved SSA's having higher values observed during the early morning and late evening. However, the SZA limitation of the AERONET retrieval methodology leads to lack of measurement points around noon. To investigate the uncertainty in relation to UVMFR retrievals, the diurnal pattern was calculated for different SSA bins according to the analysis in the previous section. In general, the daily pattern is clear for each bin and is mirrored by the AERONET inversion retrievals. However, the statistical 1σ bars are quite large. These bars describe the variability of the SSA's during each hourly bin, but also include the uncertainty of the retrieved value.

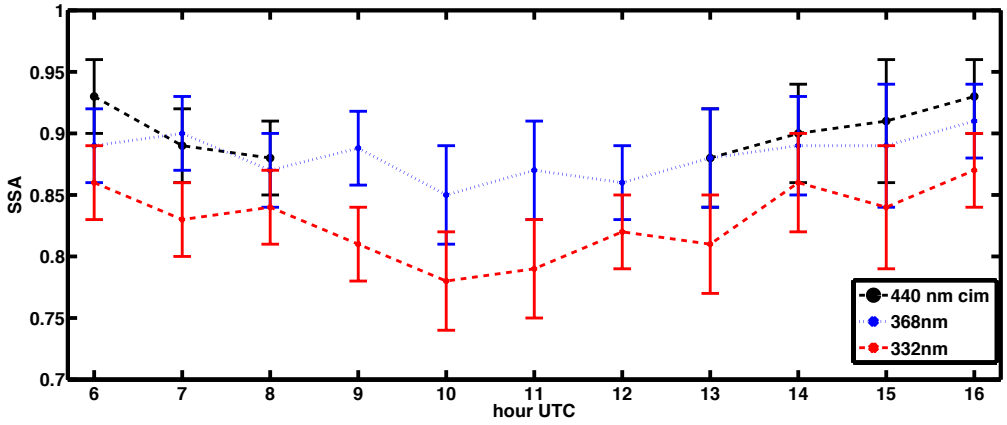

Figure 6.8 Diurnal patterns of SSA derived from the UVMFR and CIMEL measurements. Mean values per hour plotted with errorbars at one standard deviation. Local time in Athens is UTC+2(winter) UTC+3(summer)

In order to investigate the possible dependence of SSA on AOD, figure 6.9 shows the synchronous UVMFR and CIMEL SSA retrievals plotted against AOD at 440nm. In general, SSA decreases with a decrease in optical extinction, although lower AOD's are also linked to higher uncertainties of retrieved SSA. We believe that this behavior reflects seasonal changes in the average aerosol composition in Athens. Indeed, the annual cycle of SSA is the same as the AOD annual cycle having a maximum in summer and a minimum in winter. Studies of the SSA annual variability for other cities such as Ispra, Italy and Thessaloniki, Greece (Arola et al., 2005, Bais et al., 2005) revealed the same trend, with low SSA values (high absorption) associated with low AOD and reminiscent of mostly wintertime cases. It has to be noted that due to low AOD, uncertainties associated with the data obtained from both retrieval techniques (AERONET and UVMFR), are quite high. For higher AOD (>0.7), CIMEL retrievals show an almost constant value of the SSA ~0.92, while lower values have been retrieved at smaller AODs . Similar results were reported by Krotkov et al. (2005b) when analyzing measurements derived at at AERONET calibration site in Greenbelt, Maryland USA.

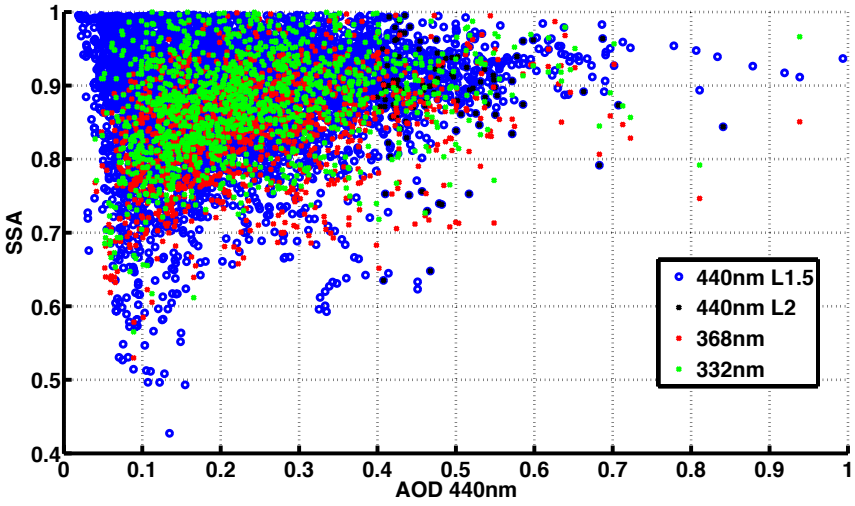

Figure 6.9 Dependence of the calculated SSA from AOD measurements

An analysis of the differences of SSAs between the visible and the UV parts of the spectrum was performed based on aerosol characteristics using synchronous CIMEL and UVMFR SSA retrievals and an aerosol classification scheme described in detail in Mielonen et al. (2009). There, a classification of AERONET data was used in order to derive 6 aerosol types based on the SSA measurement at 440nm and the AE that was derived in the 440-870 nm wavelength range. Mielonen et al. (2009) used a visualization of this characterization, by plotting AE versus SSA for individual sites, and compared their results with the CALIPSO (Omar et al., 2005) aerosol classification scheme obtaining good agreement. In addition, the difference between SSA at 440 nm and 1020 nm (similar to the approach applied by Derimian et al. (2008)), was implemented to better distinguish fine absorbing aerosols from coarse ones. The main idea was to fill this SSA versus AE aerosol type related "space" with the differences of SSA_{440}-SSA_{368} (SSA_{DIFF}) to investigate a possible link between SSA wavelength dependence and aerosol type. In figure 6.10 using the Mielonen et al. (2009) aerosol typing approach, SSA_{DIFF} is plotted for different classes (colored scale), and separate aerosol types by areas in the SSA/AE plot . In addition, actual points of SSA_{440} retrieved by the CIMEL instrument are shown in order to categorize Athens results according to the classification scheme.

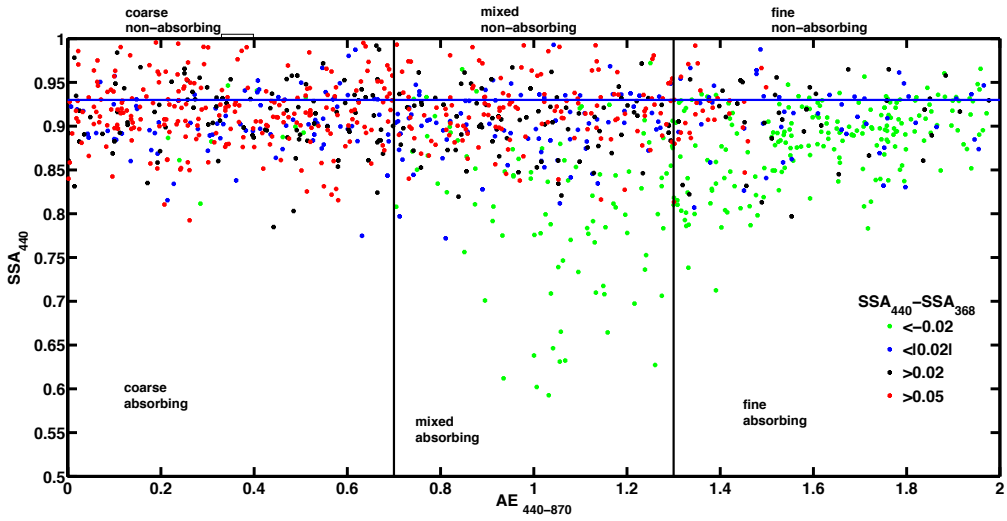

Figure 6.10 Daily average SSA440 (CIMEL) versus $AE_{(440\text{-}870nm)}$. Colors represent different bins of the spectral differences of SSA440nm- SSA368nm.

The results in figure 6.10 show that a mixture of aerosol types characterizes the ARSS site in Athens, with SSA_{440} values spanning all 6 sub-spaces. Analyzing the wavelength dependence of the SSA, by defining SSA_{DIFF} as the difference SSA_{440} – SSA_{368}, there is evidence that high negative SSA_{DIFF} values (that means that the SSA at UV wavelengths is equal or relatively higher than SSA_{440}) tend to occur towards high AEs. For these cases (green color in figure 11) we observe high absorption cases with AE's around 1, which can be attributed to polluted dust aerosol events. Also the majority of cases which comply with the condition AE < 0.7 are found with lower SSA at UV by at least 0.05 compared to SSA_{440}. More specifically, dust cases (mainly during spring) can be identified due to the proximity of Athens to the Saharan desert (Gerasopoulos, et al., 2010), explaining this behavior of absorbing aerosols at UV with low AE. Russel, et al. (2010) reported results obtained from diverse datasets showing SSA wavelength dependency from the IR down to visible wavelengths. In addition, Bergstrom et al. (2007) presented SSA spectra for dust-containing aerosols campaigns (PRIDE and ACE-Asia) including AERONET measurements at sites that are affected by dust such as Cape Verde, Bahrain (Persian Gulf) and the Solar Village (Saudi Arabia). Both studies concluded that the SSA spectra for AERONET locations, dominated by desert dust decrease with decreasing wavelength. In addition, Russel et al., (2010) reported that SSA spectra for AERONET locations dominated by urban-industrial and biomass-burning aerosols decrease with increasing wavelength in line with the results of Bergstrom et al. (2007). Figure 11 also shows that similar SSA values can be found for 440nm and 368nm and for fine aerosol cases (AE>1.4).

In order to understand the potential relative contributions of dust and brown carbon better, we applied the method of Schuster et al., (2016) to the AERONET measurements in Athens. This method separates contributions from black carbon, organic carbon, hematite and goethite, to the retrieved refractive index at all available wavelengths, even in complex mixtures. Figure 6.11 shows the fractions of total aerosol volume attributed to these components in both fine and coarse mode, as well as the volume fractions accordingly. It is evident, according to this approach, that both brown carbon and mineral dust are likely absorbing components involved in the aerosol mixture in Athens, and brown carbon playing the more dominant role. Brown carbon highly absorbs in UV wavelengths and hardly any above 0.7nm (Kirchstetter et all, 2004). BrC fraction is higher in October, but it has very large concentrations at the period March-June, which partly explains low SSA values at figure 6.6.

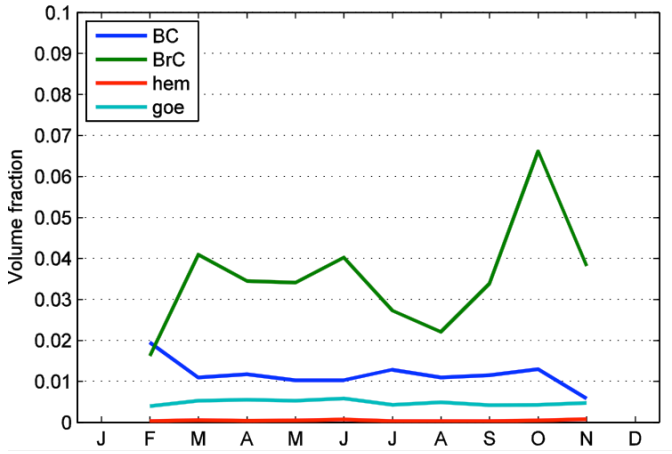

Figure 6.11. Volume fraction of absorbing aerosol components, as inferred by the method of Schuster et al. 2016. The retrieval gives the fractions for fine and coarse mode separately and here the contributions are shown as mode-weighted median value.

The utility of the AE for aerosol scattering is that its value depends primarily on the size of the particles, ranging from a value of 4 for very small particles (Rayleigh scattering) to around 0 for very large particles (such as cloud drops). Thus AE for atmospheric aerosol mixtures varies between limits specified by particle size. Various studies (e.g. Bergstrom et al., 2007) have used the Ångström Absorption Exponent (AAE) for studying the aerosol absorption wavelength dependence for different aerosol types and mixing (which is calculated similarly with the Ångström Exponent, only using Absorption Optical depth [AOD*(1-SSA)] instead of AOD). As the absorption AOD is a relatively smooth decreasing function

with wavelength, it can be approximated with a power law wavelength dependence via the AAE which is defined as the negative of the slope of the absorption on a log-log plot. Figure 6.11 shows the temporal variability of $AAE_{(440-870)}$ and $AAE_{(332-440)}$. Measurements of $AAE_{(440-870)}$ are found to lie between 0.9 and 1.5 (2σ) in accordance with the results of Bergstrom et al., (2007). $AAE_{(332-440)}$ in the UV range is very different from that in the visible, with values ranging from 1.4 to 5 (2σ). A direct comparison reveals that for the aerosol composition features of Athens, the AAEs are usually up to 4 times higher in the UV range than in the visible. This is due to a combination of the enhanced absorption (lower SSA's) that has been found in the UV, together with higher AOD's in this band.

Finally, mean CIMEL SSA was calculated for all four retrieved wavelengths (440nm, 673nm, 870nm and 1020nm) for the whole period under study, and synchronous (5 minute SSA averaged around the CIMEL measurement time) UVMFR SSAs at UV (332nm and 368nm). The results are shown in figure 6.12 with errorbars at 1σ. Datasets of SSA retrievals are separated in 3 cases accordingly: a) all points (CIMEL L1.5 and all synchronous UVMFR data), b) measurements retrieved with AOD>0.2 (reduced uncertainty), and c) SSA retrievals for $AE_{340-440}$<0.7, to identify dust events. While for all cases the calculated standard deviation is quite high (≥0.05), there is a systematic SSA decrease in the UV range, and mean differences of 0.07 and 0.02 have been found when comparing SSA at the visible range and SSA at 332nm and 368nm respectively. Dust cases show a spectral decrease in SSA with decreasing wavelength from 1022nm (CIMEL) down to 332nm (UVMFR).

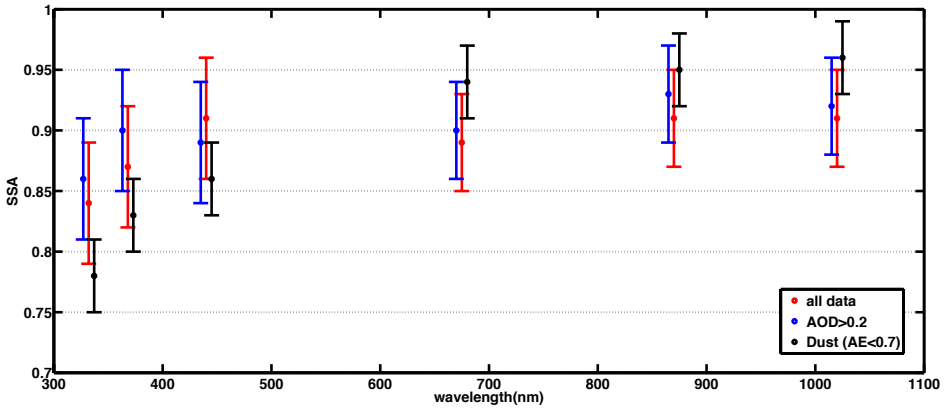

Figure 6.12 Wavelength dependence of SSA from synchronous CIMEL and UVMFR measurements. Blue points represent all data points, red data retrievals with AOD>0.2 and black data only dust aerosol cases.

The spectral dependence of the SSA from the visible to the UV wavelengths is in agreement with findings presented by Corr et al., (2009) and Krotkov et al., (2009).The same approach applied to Mexico City where measurements are also influenced by city emissions and blowing dust, Corr et al. (2009) studied the SSA behavior at UV wavelengths and showed that for AOD>0.1, SSA varied from 0.78 to 0.80 for 332nm and 368nm respectively with enhanced absorption at UV wavelengths relative to the visible wavelengths attributable to these types of aerosols. Krotkov et al., (2009) have modified a UVMFR in order to measure also at 440nm , and found strong SSA wavelength dependence across blue and near UV spectral region.

6.3 Conclusions

Advantages of measuring the aerosol absorption (SSA) in the UV with the UVMFR instrument can be summarized as follows:

- AOD, in the UV wavelength range, is higher (for the same aerosol mass) than in the visible spectral range
- SSA retrievals with the uncertainty of ±0.03 can be derived for SZA> 40 degrees and with an uncertainty of ±0.04 for all SZAs where AOD>=0.2
- SSA retrievals are stable and repeatable over the five year period

A 5 year period of UVMFR and CIMEL measurements was analyzed at the city of Athens by retrieving SSA at visible and UV wavelengths based on the effect of aerosol SSA on the DI to GHIRatio (DGR) for a given AOD and air mass. Since the CIMEL retrieval algorithm is more accurate for high SZA, the combination of the two instruments allows for an increase in measurement frequency of SSA and the ability to derive a complete diurnal cycle of aerosol absorption. In addition, the spectral differences of the aerosol absorption properties in the visible and UV wavelength range have been investigated, using synchronous CIMEL and UVMFR retrievals. Results of this work confirmed similar results found for Mexico City, Mexico (Corr et al., 2009), Washington DC, USA (Krotkov et al., 2005b) and Rome, Italy (Ialongo et al., 2010), that presented enhanced absorption of aerosols for UV wavelengths.

Retrieved dataset was used to investigate possible effects of aerosol type on observed SSA wavelength differences. The enhanced UV absorption can be mainly due to either dust or organic aerosol. Our analysis of Athens AERONET measurements suggests that the relative role of absorbing organic aerosol would be

somewhat more significant than dust. The enhanced aerosol absorption found when comparing UV and visible spectrum results, shows:

- a systematic overestimation of modeled solar UV irradiance using SSA from extrapolation from the visible range as an input to RTMs
- a possible decrease in specific days/cases of regional O_3 due to the enhanced aerosol absorption
- Satellite post-correction validation results, including aerosol absorption effects, have to take into account absorption enhancement in the UV range.
- an overestimation on the UV irradiance (UV Index) calculations on cloudless cases under dust and/or brown carbon presence when using SSA values from the visible range. This as a combination of the overestimated SSA and the high AODs during such events.

However, the spectral SSA differences, that were found, are well within the uncertainty of both retrievals as instrumental effects or absolute calibration uncertainties of sky radiances (~5% for the CIMEL almucantar measurements) might also play an important role when performing such comparisons. The coincidence of AOD measurements, from both instruments, using a single ETC for various SZA over the extended 5 year period used here, is a sign that no systematic SZA dependent factors influence the final SSA results.

7. Impact of Single Scattering Albedo in UV Solar Irradiance estimation

*This chapter is based on the publication: Raptis, I.-P.; Kazadzis, S.; Eleftheratos, K.; Amiridis, V.; Fountoulakis, I. Single Scattering Albedo's Spectral Dependence Effect on UV Irradiance. Atmosphere **2018**, 9, 364.*

Aerosols are among the major agents of Earth's radiative budget, having a crucial effect on the climate as described in chapter 2. Aerosols that show a significant absorbing behaviour are mainly black carbon, mineral dust and organic aerosols grouped as brown carbon, which are discussed in detail in chapter 6.

This work aims to quantify the impact of spectral SSA (measurements and estimations) in the UV spectral region on UVA and UVB simulations from RTMs. Datasets of SSA retrieved at UV region from UVFMR measurements, from satellites and from climatological databases, alongside with CIMEL SSA retrievals at 440 nm were used as inputs in RTM. All data were recored or refer to Athens, Greece for 2009-2014 period. Results have been compared to obtain a robust estimation of the impact of SSA on UV irradiance. Also, actual irradiance measurements from a collocated Brewer spectroradiometer at 324 nm were used to validate the RTM results for different SSA inputs.

7.1. Data and methodology

In order to quantify the effect of the absorbing and scattering nature of aerosols, the main physical variables used are SSA and AAOD defined at chapter 3. AAOD is a convenient variable for quantifying the final effect of the variations of aerosol absorption on radiative forcing, because it considers both the total extinction by aerosols and the scattering portion and, cases of high AOD and low SSA, which lead to the largest reduction of irradiance, are more clearly identified.

Ground based measurements used in this study are recorded at ARSS, Athens, and is the dataset of SSA that was used in chapter 6. This includes UVMFR retrieved SSA at 332 and 368 nm and AERONET retrievals at 440 nm. Also, AeroCom climatological SSA and OMI derived were used for validating UV output from RTM irradiance measurements from Brewer (described at 3.2.4).

The Max-Planck-Institute Aerosol Climatology version 1 (MAC-v1) provides optical properties of the total column of tropospheric aerosols, such as the AOD, the SSA and the asymmetry parameter (Kinne et al., 2013). The MAC-v1 climatology has been widely used in studies involving aerosols (Bais et al., 2015, Kinne et al., 2006, Ruiz-Arias et al., 2014). The parameters are provided on monthly timescales for the entire globe, with spatial resolution of $1^{\circ} \times 1^{\circ}$. They have been derived by combining

ground-based monthly statistics for aerosol optical properties from sun-photometer networks with the median of 15 models used Aerosol Comparison between Observations and Models (AeroCom) (Kinne et al., 2013). Climatology was initially created for the mid-visible aerosol column optical properties, since reliable ground-based measurements exist mainly for the visible range of the solar spectrum. This was later extended to other wavelengths of the solar and the far - infrared spectrum (ranging from 0.23 to 8 μm and 3.6 to 100 μm respectively) with the proper assumptions. In the UV region (UV-C, UV-B and UV-A) the optical properties are provided for 0.23, 0.3 and 0.4 μm. A linear interpolation of the desired parameters to the coordinates of ARSS were applied, since the coordinates of the ARSS do not coincide with any of the climatology grid points.

For RTM calculations, the Libradtran code (Mayer and Killing, 2005, Emde et al, 2015) was used. Multiple runs were performed to construct appropriate LUTs, for calculating SSA through DI and GHI measurements and then UV irradiance from SSA retrievals. Output spectra were set to 0.1 nm resolution for both GHI and DI. Input values for AOD were 0-1.5 with a step of 0.1, for SZA 1-81^{o} with a step of 2.5^{o}, for SSA 0.60-0.96 with a step of 0.02 and for TOC 250-400 DU with a step of 15 DU. As described in chapter 6 the output was used to calculate SSA from UVMFR measurements. Afterwards, RTM output data were used to calculate Irradiance in the UV spectral region. UVA was calculated by integrating GHI values between 315-400 nm and between 290-315 nm for UVB accordingly. Also, timeseries of irradiance at 324 nm were calculated in order to compare with Brewer measurements. Since the aim of the present work is to investigate the difference in irradiance caused by different estimation of SSA, other variables, such as TOC, NO2, and surface albedo, were used as constant inputs, using Athens climatology. Thus, the parametrization used is as follows:

$$UVA = f(AOD368, SSAi, SZA) \quad (7.1)$$

$$UVB = f(AOD332, SSAi, SZA) \quad (7.2)$$

Wherein, SZA is derived from astronomical calculations and SSAi is used differently in each of the retrieved or the climatological (AeroCom) datasets For UVA and UVB, AOD retrieved with UVMFR at 368 nm and at 332 nm were used respectively, and Ångström exponent is calculated from these data. The uncertainty of this choice is discussed later in this section. For calculating UV at 324 nm, AOD extrapolated from 332 nm was used, which adds an uncertainty lower than the one

of the measurement (0.01 AOD). TOC was set to climatological values derived from Brewer time-series. For calculating UV Irradiance at 324nm with the RTM, mean values of Brewer TOC, averaged at ±2 hours interval around cloudless Brewer measurements were used. Extra-terrestrial Irradiance spectrum of ATLAS-3 (Thuiller et al, 2003) was used and the US Standard aerosol profiles were set (US Standard Atmosphere, 1976) and maintained the same in all sets of runs to avoid any effect on the comparisons. NO2 was also set to a constant mean climatological value. Keeping constant values for all inputs, except aerosol parameters and sun elevation, provide the opportunity to study the SSA effects on UV solar irradiance, only. In order to validate the RTM outputs when comparing to Brewer measurements, RTM runs have been calculated using an Extraterrestrial Irradiance convoluted with the Brewer slit function, in order to have comparable results (Kazadzis et al., 2005) Modelled UVA and UVB values were calculated by integrating the RTM output irradiances at 315-400 nm and 290-315 nm accordingly. Comparison between RTM and Brewer UV irradiances at 324 nm was carried out using 324±1 nm integrals. The choice of this wavelength was to minimize the ozone effect on the absolute comparison differences (Fioletov et al., 1997). For the same period, asymmetry factor (g) at 440nm from AERONET at the station shows mean value of 0.69 with a standard deviation of 0.03, while 3.2% of the values are higher 0.72 and 2.9% lower than 0.66. Since measurements of g in UV spectral range are not available, these values were used in RTM (Corr et al., 2009). A sensitivity analysis on the response of RTM output on g changes revealed variations of 0.6% on both UVA and UVB, when mean AOD and SSA where used, for mean $\pm\sigma$ values for g. Mean monthly values have been used for calculations of UVA and UVB, which varied in the range 0.68-0.71. For calculating UV Irradiance at 324nm, mean daily (or monthly if not available) from CIMEL for each Brewer cloudless measurement was used. Surface albedo at UV spectral region is very low, in the order of 2-4%, in snow free conditions (Kroktov et al., 2005b) and a constant value of 0.04 was used in our calculations. Brewer measurements are considered as state of the art for TOC measurements with an uncertainty in the order of 3%. Including this uncertainty, for the 324 nm UV retrievals, the introduced error is less than 0.2%. For similar calculations at lower wavelengths, the introduced uncertainty would be much higher. All results are presented in the form of relative differences of irradiances. Hence, any uncertainty introduced by the above selections will alternate absolute values, but will be eliminated in current comparisons.

7.2 Results and discussion

5 year average SSA recorded at 332 nm and 368 nm retrieved from UVMFR and at visible bandwidths from CIMEL are presented in figure 6.12 were a systematic decrease of SSA values when moving from visible to lower wavelengths for the whole dataset is recorded. Detailed discussion about the spectral dependence is found at chapter 6 and hence explain deviations observed at this study. A lot of studies summarised by Bais et al. (2015) are in accordance with this behaviour and in this study, it is underlined that SSA extrapolation to UV wavelengths is often a reasonable approximation for scattering but less so for absorption, which is more dependent on chemical composition and that UV enhanced absorption is caused by organic material in the particles.

Based on the differences visualised in figure 6.12, the theoretical expected differences between UVB and UVA irradiances simulated by the RTM were calculated with different SSA inputs. The example shown in figure 7.1 includes two cases; the first one using the CIMEL Athens mean SSA at 440nm (SSA_{440}) (0.91) and the second using the 368 nm and 332 nm SSA mean values from UVMFR (0.86 and 0.84 respectively). A graphical representation of the differences in each case is provided for all SZAs and AODs. The difference on the solar UV irradiance between the simulations for the two cases (using SSA_{440} or SSA from the UVMFR) is shown as a function of SZA and AOD. The differences are of the order of 10-13% and 13-18% per unit of AOD for UVA and UVB respectively. Although, in Athens' dataset an AOD of 1 is very rare and it was noted that in such occasions the UVB estimations are different by 20% and this would introduce a very high error in UV index calculation and forecasts. In cases of very low AOD (<0.1) the differences are <2%, thus any differences on UVA and UVB estimations due to the spectral variability of SSA is less important. Highest relative differences are found at higher SZAs, which is linked to longer optical paths, and are expected to have a larger effect on aerosol extinction on solar irradiance.

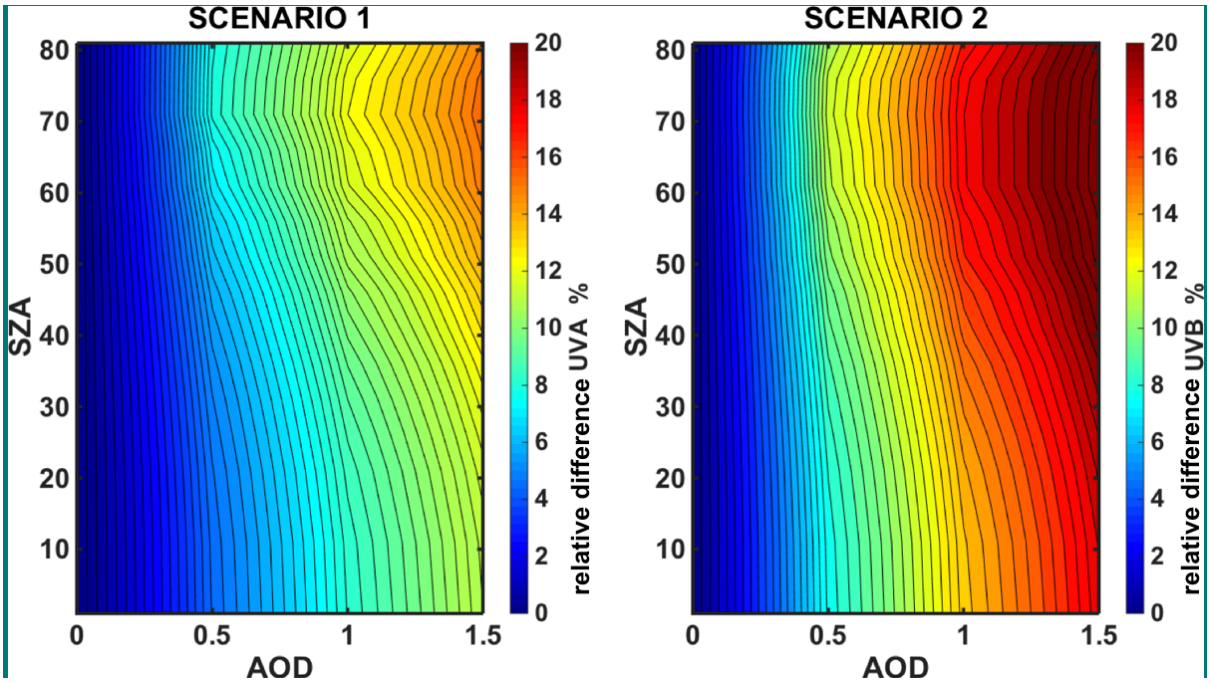

Figure 7.1. Relative differences of UVA (left) and UVB (right) irradiances for different SSAs as a function of SZA and AOD, calculated from RTM. Scenarios are calculated using mean SSA values at 332,368 and 440nm for Athens' dataset. Scenario 1 is calculated with $(SSA_{440}-SSA_{368})/SSA_{440}$ and scenario 2 with $(SSA_{440}-SSA_{332})/SSA_{440}$. Mean values for these are SSA_{440}=0.91 SSA_{368}=0.86 and SSA_{332}=0.84.

In order to perform the simulations using AOD and SSA from other available datasets, we have calculated the mean monthly values of SSA from OMAERO (388nm and 340nm), OMAERUV (388 nm) and AeroCom (300 nm) for Athens, Greece and compared them to those from UVMFR (332 nm and 368 nm) and CIMEL (440 nm) (see figure 4a). In addition, mean monthly AODs for 332, 368 and 440nm were calculated from UVMFR and CIMEL measurements respectively and presented in figure 7.2 low. All average values in both figures were calculated using data from the period 2009-2014, which provides a short-term climatology for the Athens region. All SSA values retrieved from ground observations have lower values during the period of February to May, which in chapter 6 was attributed to frequent dust events and high brown carbon emissions within the urban area. Meanwhile, the highest monthly values are recorded during the summer months, peaking in August. OMAERUV at 338 nm retrieves clearly higher values, even from visible wavelengths (CIMEL 440 nm) except from January and December, where the values from both instruments are similar. UVMFR retrievals have the lowest values all year, excluding the months of January and April when AeroCom retrieves slightly lower ones and January when CIMEL is lower. AeroCom monthly values calculated at 300 nm, deviate from those of other retrievals and noticeably

from those of UVMFR at 332 nm. OMAERO practically provides the same values all year, except in November but still the values are significantly higher than any other retrieval. AOD at all wavelengths peaks in July, showing higher values during the summer months. Lowest AOD is recorded in December and January. Mean AOD at 332 nm is higher during the whole year, showing differences from AOD at 440nm ranging from 0.05 in December up to 0.13 in July.

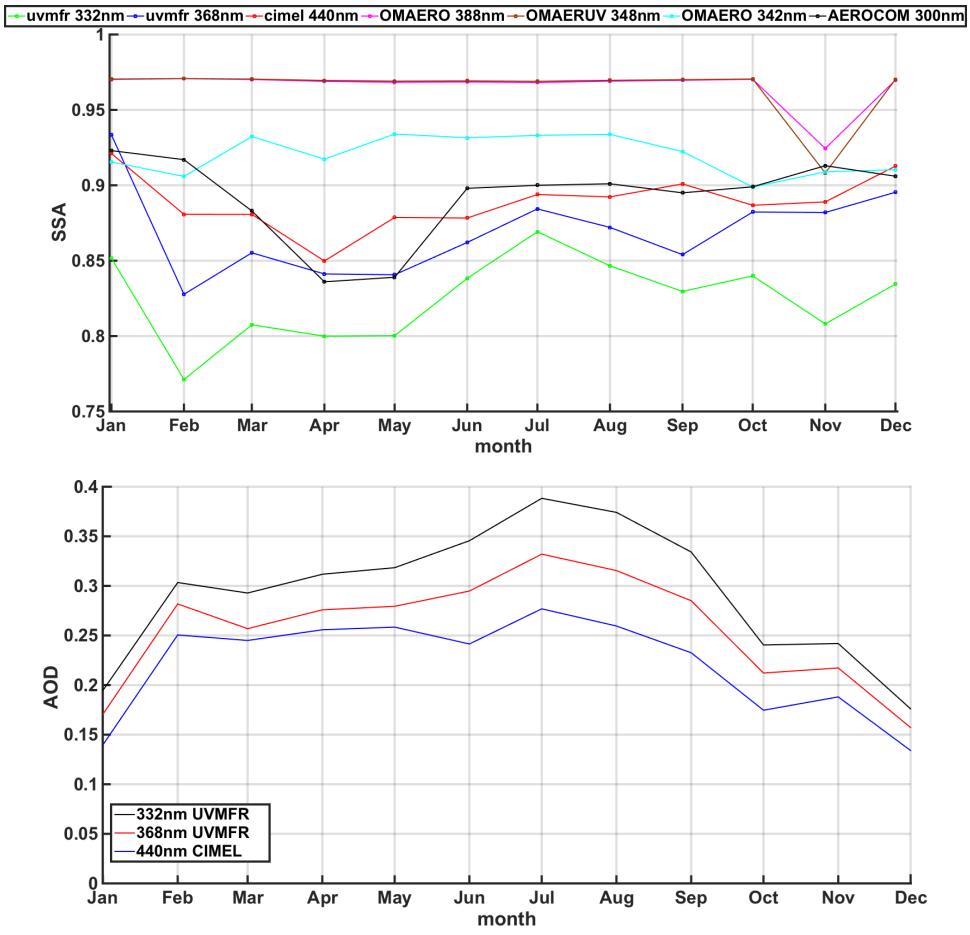

Figure 7.2. Top: Mean Monthly SSA values calculated by CIMEL and UVMFR time series and extracted from OMAERO, OMAERUV and AeroCom databases, for Athens during the 2009-2014 period. Bottom: mean monthly values of AOD calculated using CIMEL and UVMFR time series.

The differences between the simulations of UVB and UVA irradiance using UVMFR and CIMEL SSA inputs have been assessed. The inputs and model outputs presented here can be seen in table 1. We have decided to keep the AOD inputs

common (332 nm for UVB RTM integrals and 368 nm for UVA RTM ones) for all different data sources of SSAs to assess only the effect of differences in the SSA on simulated solar UV and not to mix or enhance these differences by using (the slightly different but within the measurement uncertainty [see chapter 6]), different AODs. However, this way guarantees a more robust comparison of the results, isolating SSA spectral related effects on UV irradiances.

Table 7.1: UVA and UVB Output Datasets of RTM runs, characterized by SSA and AOD used in each case. Result names are characterized by the SSA dataset used.

Name	AOD input (λ) (nm, instr.)	SSA input (λ) (nm, instr.)	Output (irradiance integral)
$UVMFR_{UVA}$	368,uvmfr	368,uvmfr	UVA
$UVMFR_{UVB}$	332,uvmfr	332,uvmfr	UVB
$CIMEL_{UVA}$	368,uvmfr	440,CIMEL	UVA
$CIMEL_{UVB}$	332,uvmfr	440,CIMEL	UVB
$OMAERO_{UVA}$	368,uvmfr	342, OMAERO	UVA
$AeroCom_{UVB}$	332,uvmfr	300, AeroCom	UVB

Following this approach, mean UVA and UVB for each month was calculated for SZA=60°. This SZA selection was made to quantify the influence of different values of SSA, excluding the seasonal variability of SZA and the SZA value which was chosen as the one that can be found all year long. Relative differences of these results are presented in figure 7.3. These relative differences follow the combined seasonal variations of AOD and SSA, presenting the lowest values in February reaching -9.1% for UVA and -12.3% for UVB. Barring UVA calculated with SSA_{CIMEL} and SSA_{UVMFR} in January, all other months reveal an underestimation of irradiance

when using UVMFR inputs. This is explained by lower SSA values retrieved by the instrument. UVA calculated with SSA_{OMAERO} shows an average difference of 6.1% all year round in comparison to the one calculated with SSA_{UVMFR}. UVA calculated with SSA_{CIMEL} has a yearly difference of 2.9% from that calculated with SSAUVMFR. For UVB calculations, the relative differences are higher and are of the same order for both $SSA_{AEROCOM}$ and SSA_{CIMEL}, showing an average of -5.9% and -5.7% accordingly.

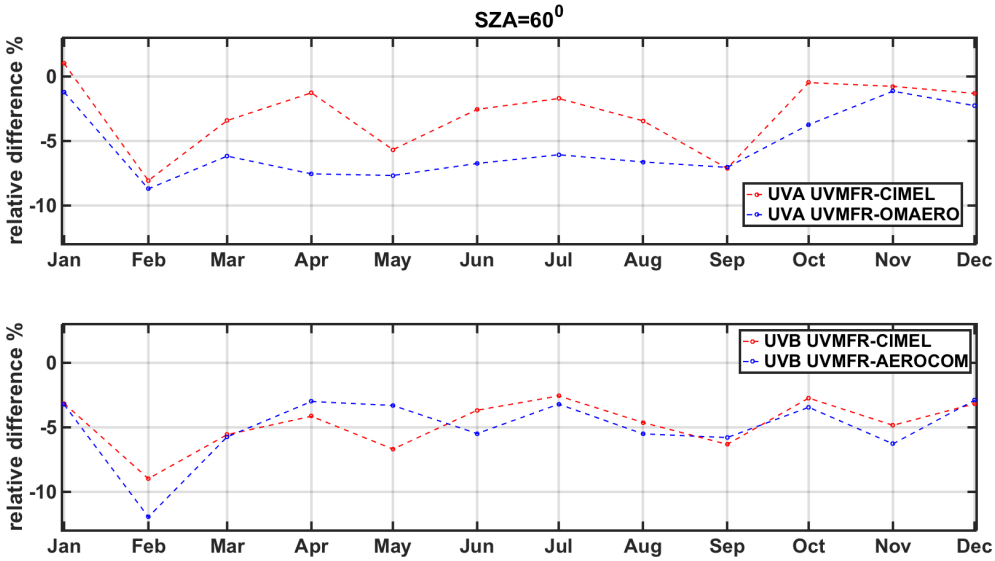

Figure 7.3: Mean Monthly Relative difference in UVA (upper plot) and UVB (lower plot), calculated with different SSA input and using time series of UVMFR SSA as reference.

Figure 7.4 shows the calculated differences for UVB and UVA outputs when using SSACIMEL and SSAUVMFR as a function of AAOD. For these calculations, we have used all the 1480 synchronous values of both UVMFR and AERONET level 1.5 inversions products (following the criterion described in chapter 6). AAOD was used for this comparison, as combined AOD and SSA changes in irradiance RTM outputs can be described by this parameter. This is because even if AODs did not differ in the compared model runs, irradiance differences are enhanced, due to higher AOD absolute values according to formula (7.2). In this particular figure, UVB and UVA calculations, using SSA_{CIMEL} and SSA_{UVMFR}, are found to decrease by ~12% per 0.05 of AAOD. When AAOD is higher than 0.04, an overestimation of outputs of SSA_{CIMEL} is the dominant case for both UVA and UVB, while the opposite appears in about 1% of the data. Although measurements of higher AAOD values would provide a more robust estimation of this behaviour, this estimation is produced using a 5 year long dataset and can be considered as representative for this urban area with moderate aerosol loads.

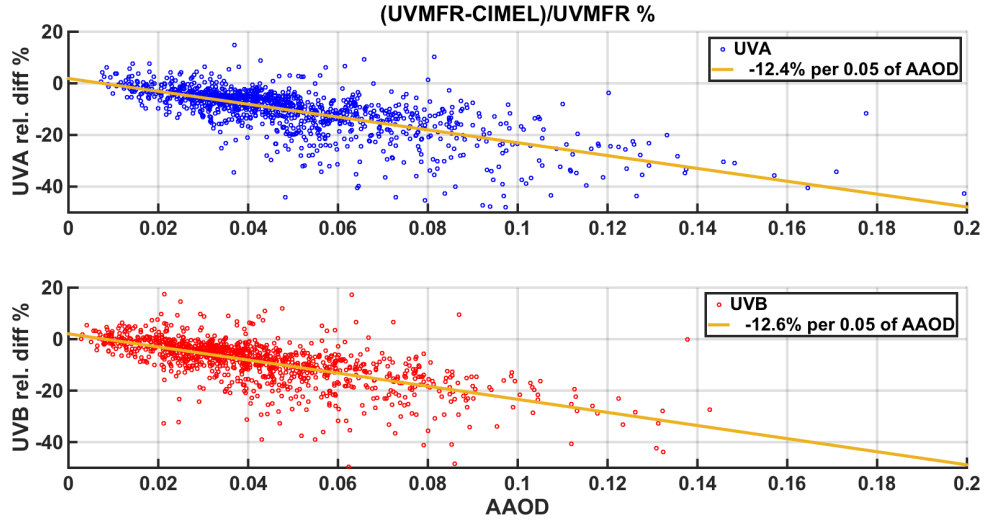

Figure 7.4. Relative difference in UVA (upper plot) and UVB (lower plot) with respect to AAOD, calculated with UVMFR and CIMEL SSA inputs as described in table 7.1

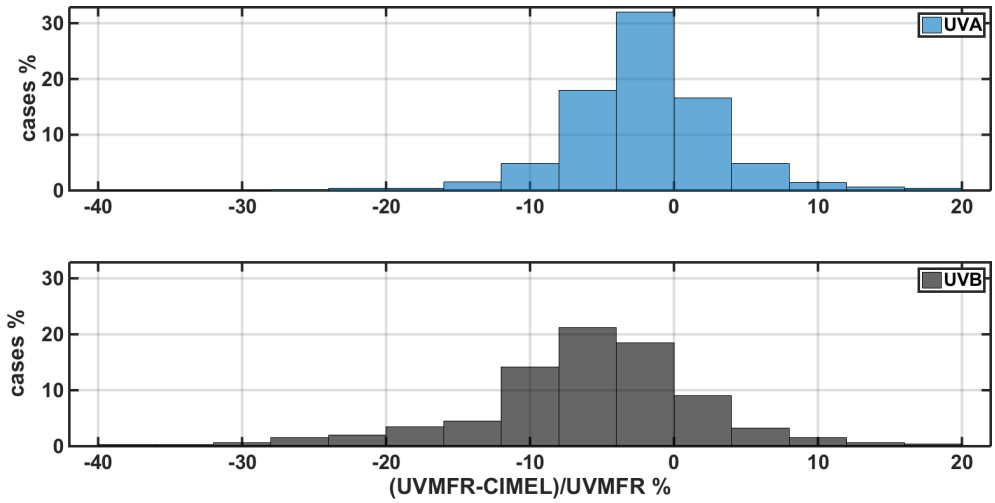

Figure 7.5. Relative Frequency Histograms of cases of UVA (upper plot) and UVB (lower plot) relative differences of GHI calculated using UVMFR and CIMEL SSA input as described in table 1, for all available synchronous data.

In figure 7.5, histograms for the comparison of the full data set of UVMFR and CIMEL synchronous 1480 retrievals, are presented. These histograms reveal a dominant overestimation of both UVA and UVB when calculated using SSA_{CIMEL}. The average relative difference for UVA is -4.7% and for UVB is -8.5%. For 77.1% and 86.4% of the cases for UVA and UVB respectively, the irradiances simulated with input from SSA_{UVMFR} are lower than those simulated with SSA_{CIMEL}. The rest of the cases are linked with aerosol mixtures that have higher SSA in UV than in 440nm. These are usually expected to be fine mode absorbing aerosols that are attributed to urban pollution. Also, there are very few cases (0.9% for UVA and

1.4% for UVB) showing absolute differences higher than 25%. In chapter 6 (and in Kazadzis et al., 2016) most these cases are linked to Ångstrom Exponents lower than 0.7, thus to severe dust events.

Aiming to verify the above results using actual solar irradiance measurements, RTM simulated solar UV irradiances were compared with synchronous cloud free Brewer UV measurements at 324 nm from the Brewer MKIV instrument. This is located on the same roof (ARSS) as the UVMFR and CIMEL instruments. For this simulation, AOD_{UVMFR} and SSA_{UVMFR} at 332nm were used as input. In order to validate the agreement between RTM and BREWER recorded Irradiance at 324nm, a statistical approach was selected. A comparison of 4297 synchronous cloud free (based on the cloud detection algorithm used for UVMFR [described at chapter 3.2.1]) Brewer measurements and UV324nm model runs – with UVMFR input data - is shown in figure 7.6, demonstrating an R^2 of 0.96 and RMSE of 0.013W/m^2. The results reveal a good agreement with differences that can be mainly attributed to model inputs as well as measurement and absolute calibration uncertainties of the Brewer.

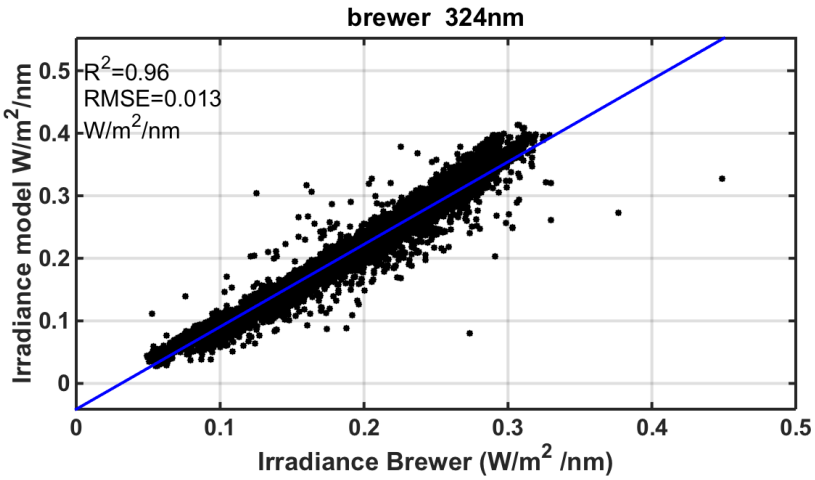

Figure 7.6: Cloudless synchronous retrievals of Global UV at 324nm, measured from Brewer and calculated from model using UVMFR SSA and AOD at 332nm inputs.

Finally, RTM runs were performed with CIMEL, AeroCom and UVMFR 332nm SSA as well as UVMFR 332 nm AOD and compared with Brewer recordings. At this scenario, AeroCom values for the corresponding month, was used for all the synchronous UVMFR-BREWER data points. The distribution of differences of the three different scenarios is presented in Figure 7.7 and table 7.2. From these statistics, it was concluded that irradiance calculated with SSA_{UVMFR} has the smallest absolute mean and median difference in comparison to the ones calculated with SSA_{CIMEL} and $SSA_{AEROCOM}$. Results reveal a similar average difference with the ones

presented in figure 7.4. Standard deviations of the differences are in the order of 6.5% to 7.5%. It is interesting that AeroCom provides a slightly better agreement than AERONET, having smaller absolute mean and median differences. This is mainly because $SSA_{AEROCOM}$ is calculated at 300 nm. However, it is expected to have higher variation when using a constant climatological monthly value. It should be noted that the dominant case is the overestimation of simulated irradiance as compared to recorded values, which indicates that SSA at 324 nm should be lower than any of these values. All three distributions have comparable range of values, with less than 10 cases of relative differences higher than 20%. Concluding the comparison, it appears that using SSA_{UVMFR} at 332 nm in RTM UV 324nm calculation provides the closest to Brewer measured results.

Table 7.2: Statistics of RTM calculated Irradiance at 324nm compared to Brewer recordings at 324 nm for all available data.

UV(Brewer-Modelx)/Brewer	Mean difference %	Standard Deviations %	Median %	5-95 percentile %
UVMFR	-0.85	6.78	-1.86	-9.72 – 11.24
CIMEL	-4.91	6.62	-5.58	-12.07 – 4.33
AeroCom	-4.15	7.50	-5.34	-12.47 – 7.72

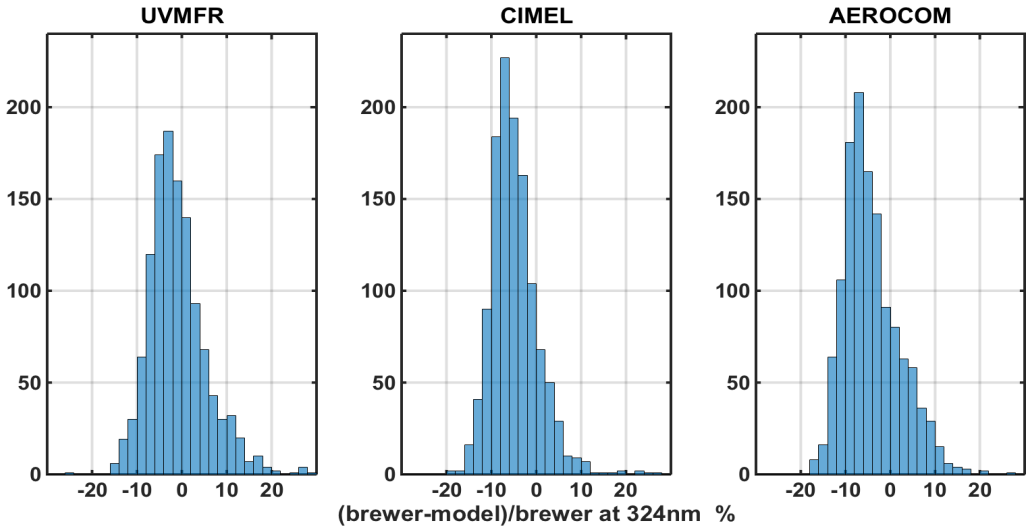

Figure 7.7. Number of cases of relative difference between Brewer recorded Irradiance at 324nm and estimated through RTM calculations using SSAUVMFR at 332, SSA_{CIMEL} at 440nm and $SSA_{AEROCOM}$ at 300nm.

All the above results converge to the conclusion that retrievals of SSA at UV wavelengths are required to correctly estimate UV irradiance. Also, according to aerosol type, a detailed parametrization of SSA values in UV could lead to more valid estimation of UV irradiance. The datasets were recorded in Athens, Greece, which is a moderate polluted European city. With rare high aerosol loads and frequent Saharan dust transport events between the months of February and June, the differences in calculated irradiances should be considered as representative of these conditions. UV irradiance estimation differences in rural pristine areas with very low AOD values should be nearly negligible. On the other hand, in heavily industrialized areas and megacities with very high black and brown carbon concentrations, these differences would be magnified. Also, in areas with more frequent and more severe dust events, the effect of SSA drop in UV should be considered in all calculations. Additionally, there is a need of performing a similar study in an area were types of aerosol with different spectral behavior dominate, especially organic particles. Although, for some types (e.g., sea salt, sulfate, and nitrate) the absorption is practically negligible in the whole spectrum (Bais et al. , 2015). Differences in UVA and UVB lead to change in health-related variables. In most cases, irradiances are lower than estimated which transported from visible range values, resulting to lower UV index and Vitamin D production. This should lead to different instructions for the exposure of general population.

7.3. Conclusions

The effect of spectral SSA using different data sources for calculating incoming irradiance at UV wavelengths was studied. A 5-year long data set of SSA_{UVMFR} at 368 and 332 nm, AERONET retrievals at 440 nm, SSA_{OMAERO} at 342.5 nm and climatological values from AeroCom were used as input to a RTM. Outputs were integrated to estimate UVA and UVB. Major findings are:

- SSA spectral decrease in the UV leads to a systematic overestimation of UV when SSA at visible is used, for the Athens area for the same AOD. The average difference for UVA is 4.7% and for UVB is 8.5%, between estimations using SSA_{UVMFR} and SSA_{CIMEL} inputs.

- When climatological $SSA_{AEROCOM}$ values at 300 nm were used to calculate UVB, average relative difference to the one calculated with SSA_{UVMFR} at 332 nm was found at 5.7%.

- The rate of underestimation of calculated UVA and UVB with SSA_{UVMFR} and SSA_{CIMEL}, for Athens, is -12% per 0.05 increase of AAOD. Mostly, for dust aerosol and local pollution related areas of the planet, this overestimation could be highly important. In addition, as AAOD at shorter (UVB) wavelengths is theoretically higher than the one at 332 nm, the effect of using extrapolating SSA_{440} could have larger discrepancies in the UVB irradiance calculation compared to the results presented in this study.

- UV Irradiance at 324 nm from a Brewer was compared to RTM calculations using different SSA input. This was performed to validate the RTM results. The results revealed that using SSA_{UVMFR} at 332nm in the simulations provides closer to measured values with a mean difference of 0.85%, compared to 4.91% when transferring SSA from the visible and 4.11% when using climatological values.

To summarize, spectral aerosol optical depth is the most important parameter that can describe the UV attenuation due to aerosols. In addition, there is a lack of SSA measurements worldwide for the UV range. This is because the densest ground-based aerosol sun-photometric network (AERONET) provide SSA at 440nm (lowest wavelength). UV irradiance – aerosol interaction studies and services (for example UV Index forecasts) does not take in to account the findings of various studies (especially in urban and high AOD areas). This presents higher absorption in the UV compared to the visible. This can lead to a systematic overestimation of the UV Index (when all other parameters like TOC, AOD have been correctly used in the UV Index forecast models), due to this SSA spectral dependence.

8. General Conclusions

The main objective of this work was the contribution to the atmospheric composition measurement related science, through the improvement of aerosols, ozone and water vapour related columnar measurements. This was achieved through the development of new tools and algorithms related with global horizontal and direct solar spectral measurements. In this frame, state of the art methods have been established for retrieving SSA at UV wavelength using data from a UVMFR, for retrieving TOC using data from UVFMR and for retrieving IWV spectrally from PSR data. Additionally, a study for the influence of using SSA retrieved from UV measurements on calculating UV irradiance has been performed.

TOC describes the amount of ozone in an atmosphere, hence it is the most used variable to monitor ozone from ground based measurements. The method developed in this study for TOC retrievals showed good agreement with both Brewer (up to ±2% differences) and OMI (up to 3% differences) retrievals. Considering advantages such as the instrument's mobility, the method could be easily adopted by any UVMFR instrument operating worldwide, so it can be used in order to increase the low geographical coverage of current TOC instrumentation. Especially in the tropics where only few instruments are deployed such initiatives could be a useful tool for TOC related future networks. Comparing the difference on the cost and the maintenance needed for UVMFR and standard Brewer instruments, the use of UVMFR instrumentations together with developed algorithms such as the one presented in this work could be a step towards filling such surface-based TOC monitoring gaps. One crucial factor that has to be addressed is the instrument quality assurance and quality control especially regarding the calibration stability through methods that have been presented here. Future work on this field include the establishment of TOC measurements in multiple locations using UVMFR and use of the data for climatological stratospheric ozone monitoring studies and satellite validation. Also, the possibility of retrieving other trace gases that absorb significantly in the UV region (such as NO_2) with similar approach, should be investigated. This could be achieved with hardware modifications using filters with different/adequate for NO_2 retrieval wavelength bandpasses.

IWC is a variable used both for meteorology and climatology, as water vapour is the most important greenhouse gas dominating atmospheric thermodynamics. The accuracy of IWV retrieval using PSR data is in the same order of the other well established methods and devices. The spectral approach, benefiting from the characteristics of PSR, provided statistically better results (up

to 0.75% mean relative differences). Also, having applied the method to a 2-year dataset indicated a stable long-term performance of the instrument, which shows that it can be used for IWV calculations. The analysis in this Thesis verifies the findings of other publications showing differences of CIMEL/AERONET related IWV retrievals with other IWV measurements using different measuring principles (e.g. GPS). The PSR method that consist of a sun-photometric measuring approach verifies the GPS and other IWV levels. The IWV method development and assessment presented in this work provides an added value to the PSR instrument, being able to measure simultaneously spectral solar irradiance components (direct and horizontal), aerosol spectral optical properties (AOD, Angstrom Exponents) and IWV, constituting the PSR as a unique sun-photometric instrument. The spectral approach is a new pathway, that very recently has become technologically feasible and in the near future should be applied and tested in other spectroradiometers. Newly developed instruments such as PANDORA that measure spectrally in the same region could have this method applied for retrieving IWV. Considering the plans for global networks of spectroradiometers by ESA and NASA, this approach could become one of the possible standard approaches in the future.

Aerosol columnar absorption (here described by the SSA) plays an important role on the Earth-Atmosphere radiative balance. Columnar SSA retrieved in the UV spectral region for long term is not available in the current measurements related literature, as few instruments include this option and usually it has only been performed during experimental campaigns. The extended SSA at 332 and 368 nm dataset retrieved in this study significantly improves comparative statistics and provides additional information on the effect of varying background aerosol conditions and higher aerosol absorption than that provided by previous studies. CIMEL/AERONET instruments currently does not provide SSA in the UV region. In addition, various assumption such as the AOD limitations (>0.4) make the SSA retrieval possible only in very high aerosol polluted areas or significant aerosol related episodes. Mean values of SSA for the period were 0.83, 0.87 and 0.90 for 332, 368 and 440 nm accordingly. In conclusion, the combined use of CIMEL sun and sky radiance measurements in the visible, with UVMFR total and diffuse irradiance measurements in the UV, provides an important advantage for remote measurements of column aerosol absorption over the UV-Visible spectral range. Brown carbon and dust cases have been identified by combining variables as Ångström exponent and refractive index. Future work could include a deeper analysis on the spectral signature of different aerosol mixture on these and other columnar optical properties, aiming to investigate the possibility of characterizing

mixes based on photometric measurements. Since there is need of more data of SSA in the UV spectral region, future work should aim to retrieve it from other instruments that also measure at these bandwidths (e.g. PSR, PANDORA).

UV Irradiance estimation is crucial for health-related parameters such as UV Index that is a standard modelling output for all meteorological and forecasting products for public awareness concerning UV exposure and skin cancer. It appears to be crucial for modelled UVA and UVB irradiance calculations to have a proper estimation of absorbing aerosol related columnar parameters such as SSA, especially when AOD is higher than 0.4. Although TOC is the major factor at UV wavelengths, especially in UVB region, SSA spectral dependence could lead to changes of more than 15% per unit of AOD. In the dataset recorded at Athens and studied in this work, differences up to 20% were found when SSA at visible wavelengths was used instead of SSA_{UV}. In the absence of SSA_{UV} measurements worldwide, currently used estimations for UV forecasts have a non-negligible uncertainty caused by using visible wavelength based SSA values. All the findings present the need of more detailed information on the aerosol absorbing properties in the UV range when UV related variables are estimated (UVA, UVB, UV Index, Vitamin D production), especially for high AOD areas. Future work on this field should be focused on the having more SSA_{UV} datasets and assimilate them in UV forecasting tools, also absorption effect on UV related health indices should be estimated separately to any of them.

9.References

Ahn, C., Torres, O. and Bhartia, P.K., 2008. Comparison of ozone monitoring instrument UV aerosol products with Aqua/Moderate Resolution Imaging Spectroradiometer and Multiangle Imaging Spectroradiometer observations in 2006. Journal of Geophysical Research: Atmospheres, 113(D16).

Alexandrov, M.D., Schmid, B., Turner, D.D., Cairns, B., Oinas, V., Lacis, A.A., Gutman, S.I., Westwater, E.R., Smirnov, A. and Eilers, J., Columnar water vapour retrievals from multifilter rotating shadowband radiometer data. Journal of Geophysical Research: Atmospheres, 114(D2), 2009.

Alfaro, S. C., Lafon, S., Rajot, J. L., Formenti, P., Gaudichet, A., and Maillé, M.: Iron oxides and light absorption by pure desert dust: An experimental study, Journal of Geophysical Research D: Atmospheres, 109, D08208 08201-08209, 10.1029/2003jd004374, 2004.

American Meteorological Society, Precipitable Water Vapour, Glossary of Meteorology, 2015.

Amiridis, V., Kafatos, M., Perez, C., Kazadzis, S., Gerasopoulos, E., Mamouri, R. E., Papayannis, A., Kokkalis, P., Giannakaki, E., Basart, S., Daglis, I., and Zerefos, C.: The potential of the synergistic use of passive and active remote sensing measurements for the validation of a regional dust model, Ann. Geophys., 27, 3155-3164, doi:10.5194/angeo-27-3155-2009, 2009

Andrews, E., Ogren, J. A., Kinne, S., and Samset, B.: Comparison of AOD, AAOD and column single scattering albedo from AERONET retrievals and in situ profiling measurements, Atmos. Chem. Phys., 2017, 17, 6041-6072, https://doi.org/10.5194/acp-17-6041-2017.

Andrews, E., Sheridan, P.J., Fiebig, M., McComiskey, A., Ogren, J.A., Arnott, P., Covert, D., Elleman, R., Gasparini, R., Collins, D. and Jonsson, H., 2006. Comparison of methods for deriving aerosol asymmetry parameter. Journal of Geophysical Research: Atmospheres, 111(D5).

Ansmann, A., Tesche, M., Seifert, P., Gross, S., Freudenthaler, V., Apituley, A., Wilson, K.M., Serikov, I., Linné, H., Heinold, B. and Hiebsch, A., 2011. Ash and fine-mode particle mass profiles from EARLINET-AERONET observations over central Europe after the eruptions of the Eyjafjallajökull volcano in 2010. Journal of Geophysical Research: Atmospheres, 116(D20).

Antón, M., López, M., Serrano, A., Bañón, M., & García, J. A. (2010). Diurnal variability of total ozone column over Madrid (Spain). Atmospheric Environment, 44(24), 2793-2798.

Arola, A., Kazadzis, S., Krotkov, N., Bais, A., Gröbner, J., and Herman, J. R.: Assessment of TOMS UV bias due to absorbing aerosols, Journal of Geophysical Research D: Atmospheres, 110, 1-7, 2005.

Askne J. and E.R. Westwater, "A Review of Ground-Based Remote Sensing of Temperature and Moisture by Passive Microwave Radiometers," IEEE Transactions on Geoscience And Remote Sensing, G3-24, 1986, pp. 340-352

B. M. Herman, S. R. Browning, and J. J. DeLuisi, "Determination of the effective imaginary term of the complex refractive index of atmospheric dust by remote sensing: the diffuse-direct radiation method," J. Atmos. Sci. 32, 918–925, 1975.

Bais AF, Kazantzidis A, Kazadzis S, Balis D, Zerefos CS, Meleti C, Effects of aerosol optical depth and single scattering albedo on surface UV irradiance, Atmos Environ, 2005, 39,1093–1102

Bais, a F., McKenzie, R. L., Bernhard, G., Aucamp, P. J., Ilyas, M., Madronich, S., & Tourpali, K. (2014). Ozone depletion and climate change: impacts on UV radiation. Photochemical & Photobiological Sciences : Official Journal of the European Photochemistry Association and the European Society for Photobiology. doi:10.1039/c4pp90032d

Bais, a F., McKenzie, R. L., Bernhard, G., Aucamp, P. J., Ilyas, M., Madronich, S., & Tourpali, K. (2014). Ozone depletion and climate change: impacts on UV radiation. Photochemical & Photobiological Sciences : Official Journal of the European Photochemistry Association and the European Society for Photobiology. doi:10.1039/c4pp90032d

Bais, A. F., Kazantzidis, A., Kazadzis, S., Balis, D. S., Zerefos, C. S., and Meleti, C.: Deriving an effective aerosol single scattering albedo from spectral surface UV irradiance measurements, Atmospheric Environment, 39, 1093-1102 2005.

Bais, A.F., Zerefos, C.S., Meleti, C., Ziomas, I.C. and Tourpali, K., 1993. Spectral measurements of solar UVB radiation and its relations to total ozone, SO2, and clouds. Journal of Geophysical Research: Atmospheres, 98(D3), pp.5199-5204.

Balis, D., Kroon, M., Koukouli, M. E., Brinksma, E. J., Labow, G., Veefkind, J. P., & McPeters, R. D. (2007). Validation of Ozone Monitoring Instrument total ozone column measurements using Brewer and Dobson spectrophotometer ground-based observations. Journal of Geophysical Research, 112(D24), D24S46. doi:10.1029/2007JD008796

Balis, D., Kroon, M., Koukouli, M.E., Brinksma, E.J., Labow, G., Veefkind, J.P. and McPeters, R.D., 2007. Validation of Ozone Monitoring Instrument total ozone column measurements using Brewer and Dobson spectrophotometer ground-based observations. Journal of Geophysical Research: Atmospheres, 112(D24).

Barnard, J. C., Volkamer, R., and Kassianov, E. I.: Estimation of the Mass Absorption Cross section of the organic carbon component of aerosols in the Mexico City Metropolitan Area, Atmospheric Chemistry And Physics, 8, 6665-6679, 2008.

Barnett, C.E. (1942). "Some application of wavelength turbidimetry in the infrared". J. Phys. Chem. **46** (1): 69–75. doi:10.1021/j150415a009.

Bass, A. M., & Paur, R. J. (1985). The ultraviolet cross-sections of ozone: I. The measurements II. Results and temperature dependence, in atmospheric ozone. In C. Zerefos & A. Ghazi (Eds.), Proceedings of the Quadrennial Ozone Symposium, Halkidiki, Greece (pp. 606–616).

Bergstrom, R. W., Pilewskie, P., Schmid, B., and Russell, P. B.: Estimates of the spectral aerosol single scattering albedo and aerosol radiative effects during SAFARI 2000, Journal of Geophysical Research D: Atmospheres, VOL. 108, 8474, pp. 11, doi:10.1029/2002JD002435, 2003

Bergstrom, R.W., Pilewskie, P., Russell, P. B., Redemann, J., Bond, T. C., Quinn, P. K., and Sierau, B.: Spectral absorption proper- ties of atmospheric aerosols, Atmos. Chem. Phys., 2007, 7, 5937–5943, https://doi.org/10.5194/acp-7-5937-2007,

Berjón, A., Redondas, A., Sildoja, M., Nevas, S., Wilson, K., León-Luis, S.F., El Gawhary, O., and Fountoulakis, I.: Characterization of the instrument temperature dependence of Brewer total ozone column measurements, Atmos. Meas. Tech. Discuss., https://doi.org/10.5194/amt-2017-406, 2017.

Berk, A., Adler-Golden, S.M., Ratkowski, A.J., Felde, G.W., Anderson, G.P., Hoke, M.L., Cooley, T., Chetwynd, J.H., Gardner, J.A., Matthew, M.W. and Bernstein, L.S., 2002, July. Exploiting MODTRAN radiation transport for atmospheric correction: The FLAASH algorithm. In Information Fusion, 2002. Proceedings of the Fifth International Conference on (Vol. 2, pp. 798-803). IEEE.

Berk, A., Anderson, G.P., Acharya, P.K., Bernstein, L.S., Muratov, L., Lee, J., Fox, M., Adler-Golden, S.M., Chetwynd, J.H., Hoke, M.L. and Lockwood, R.B., 2005, June. MODTRAN 5: a reformulated atmospheric band model with auxiliary species and practical multiple scattering options: update. In Algorithms and technologies for multispectral, hyperspectral, and ultraspectral imagery XI (Vol. 5806, pp. 662-668). International Society for Optics and Photonics.

Berk, A., Anderson, G.P., Bernstein, L.S., Acharya, P.K., Dothe, H., Matthew, M.W., Adler-Golden, S.M., Chetwynd Jr, J.H., Richtsmeier, S.C., Pukall, B. and Allred, C.L., MODTRAN 4 radiative transfer modeling for atmospheric correction. In Proceedings of SPIE- The International Society for Optical Engineering (Vol. 3756, pp. 348-353),1999.

Berk, A., Bernstein, L.S. and Robertson, D.C., MODTRAN: A moderate resolution model for LOWTRAN (No. SSI-TR-124). SPECTRAL SCIENCES INC BURLINGTON MA, 1987.

Bevis, M., S. Businger, T. A. Herring, C. Rocken, R. A. Anthes, and R. H. Ware. "GPS Meteorology: Remote Sensing of Atmospheric Water Vapour Using the Global Positioning System." Journal of Geophysical Research, Vol. 97, No. D14, , pp. 15,787-15,801, October 20, 1992

Beyrich, F., and W. K. Adam, Site and Data Report for the Lindenberg Reference Site in CEOP - Phase I. Berichte des Deutschen Wetterdienstes, 230, Offenbach am Main, Germany, 55 pp, 2007.

Bharmal, N.A., Slingo, A., Robinson, G.J. and Settle, J.J., 2009. Simulation of surface and top of atmosphere thermal fluxes and radiances from the radiative atmospheric divergence using the ARM Mobile Facility, GERB data, and AMMA Stations experiment. Journal of Geophysical Research: Atmospheres, 114(D13).

Bhartia, P. K. and Wellemeyer, C. W.: TOMS-V8 total O3 algo- rithm, in OMI Algorithm Theoretical Basis Document, NASA Goddard Space Flight Cent., Greenbelt, MD, USA, 2002.

Bigelov D.S., J. R. Slusser, A. F. Beaubien, and J. R. Gibson, ‘‘The USDA ultraviolet radiation monitoring program,’’ Bull. Am. Meteorol. Soc. 79, 601–615, 1998

Bigelow, D. S., & Slusser, J. R. (2000). Establishing the stability of multifilter UV rotating shadow-band radiometers. Journal of Geophysical Research: Atmospheres (1984–2012), 105(D4), 4833-4840.

Blanc, P., Espinar, B., Geuder, N., Gueymard, C., Meyer, R., Pitz-Paal, R., Reinhardt, B., Renné, D., Sengupta, M., Wald, L. and Wilbert, S., 2014. Direct normal irradiance related definitions and applications: The circumsolar issue. Solar Energy, 110, pp.561-577.

Bock, O., Bosser, P., Pacione, R., Nuret, M., Fourrié, N. and Parracho, A. : A high-quality reprocessed ground-based GPS dataset for atmospheric process studies, radiosonde and model evaluation, and reanalysis of HyMeX Special Observing 30 Period. Q.J.R. Meteorol. Soc., 142: 56–71. doi:10.1002/qj.2701, 2016.

Bodhaine, B. A. ., Wood, N. B., Dutton, E. G., & Slusser, J. R. (1999). On Rayleigh Optical Depth Calculations, 1854–1861.

Bodhaine, B. A., Wood, N. B., Dutton, E. G., and Slusser, J. R.: On Rayleigh optical depth calculations, J. Atmos. Ocean. Tech., 16(11), Part 2, pp 1854–1861, 1999.

Bodhaine, B. A., Wood, N. B., Dutton, E. G., and Slusser, J. R.: On Rayleigh optical depth calculations, J. Atmos. Ocean. Tech., 16(11), Part 2, pp 1854–1861, 1999.

Bornman, J.F. and Teramura, A.H. Effects of ultraviolet-B radiation on terrestrial plants. In Environmental UV-Photobiology, Young, A.R., Björn, L.O., Moan, J. and Nultsch, W. (eds.), Plenum Press, New York, pp. 427-471.1993.

Boucher, O., D. Randall, P. Artaxo, C. Bretherton, G. Feingold, P. Forster, V.-M. Kerminen, Y. Kondo, H. Liao, U. Lohmann, P. Rasch, S.K. Satheesh, S. Sherwood, B. Stevens and X.Y. Zhang, 2013: Clouds and Aerosols. In: Climate Change 2013: The Physical Science Basis. Contribution of Working Group I to the Fifth Assessment Report of the Intergovernmental Panel on Climate Change Stocker, T.F., D. Qin, G.-K. Plattner, M. Tignor, S.K. Allen, J.

Boschung, A. Nauels, Y. Xia, V. Bex and P.M. Midgley (eds.)]. Cambridge University Press, Cambridge, United Kingdom and New York, NY, USA

Braathen, G.O., 2012, November. Ozone Layer Monitoring. In *Montreal Protocol Seminar on Protecting our Atmosphere for Generations to Come, Geneva* (Vol. 11).

Brewer, A.W., 1949. Evidence for a world circulation provided by the measurements of helium and water vapour distribution in the stratosphere. Quarterly Journal of the Royal Meteorological Society, 75(326), pp.351-363.

Buchard, V., Brogniez, C., Auriol, F., Bonnel, B., Lenoble, J., Tanskanen, A., Bojkov, B. and Veefkind, P. Comparison of OMI ozone and UV irradiance data with ground-based measurements at two French sites. Atmospheric Chemistry and Physics, 8(16), pp.4517-4528, 2008.

Bucholtz, A., 1995. Rayleigh-scattering calculations for the terrestrial atmosphere. Applied Optics, 34(15), pp.2765-2773.

Butz, A., Galli, A., Hasekamp, O., Landgraf, J., Tol, P. and Aben, I., 2012. TROPOMI aboard Sentinel-5 Precursor: Prospective performance of CH4 retrievals for aerosol and cirrus loaded atmospheres. Remote sensing of environment, 120, pp.267-276.

Cadeddu, M. P., J. C. Liljegren, and D. D. Turner, The Atmospheric Radiation Measurement (ARM) program network of microwave radiometers: Instrumentation, data and retrievals, Atmos. Meas. Tech., 6, 2359–2372, doi:10.5194/amt-6-2359-2013, 2013.

Campanelli, M., Estellés, V., Smyth, T., Tomasi, C., Martínez- Lozano, M. P., Claxton, B., Muller, P., Pappalardo, G.,Pietruczuk, A., Shanklin, J., Colwell, S., Wrench, C., Lupi, A., Mazzola, M., Lanconelli, C., Vitale, V., Congeduti, F.,Dionisi, D., and Cacciani, M.: Monitoring of Eyjafjallajoekull volcanic aerosol by the new European SkyRad users(ESR) sun-sky radiometer network, Atmos. Environ., 48, 33–45, 2012.

Campanelli, M., Mascitelli, A., Sanò, P., Diémoz, H., Estellés, V., Federico, S., Iannarelli, A. M., Fratarcangeli, F., Mazzoni, A., Realini, E., Crespi, M., Bock, O., Martínez-Lozano, J. A., and Dietrich, S.: Precipitable water vapour content from ESR/SKYNET sun–sky radiometers: validation against GNSS/GPS and AERONET over three different sites in Europe, Atmos. Meas. Tech., 11, 81-94, https://doi.org/10.5194/amt-11-81-2018, 2018.

Campanelli, M., Nakajima, T., Khatri, P., Takamura, T., Uchiyama, A., Estellés Leal, V., Liberti, G.L. and Malvestuto, V., Retrieval of characteristic parameters for water vapour transmittance in the development of ground based sun-sky radiometric measurements of columnar water vapour. Atmospheric Measurement Techniques, 2014, num. 7, p. 1075-1087,2014.

Castro, T., Madronich, S., Rivale, S., Muhlia, A., and Mar, B.: The influence of aerosols on photochemical smog in Mexico City, Atmospheric Environment, 35, 1765-1772, 2001.

Chance, K., Palmer, P.I., Spurr, R.J., Martin, R.V., Kurosu, T.P. and Jacob, D.J., 2000. Satellite observations of formaldehyde over North America from GOME. Geophysical Research Letters, 27(21), pp.3461-3464.

Chance, K.V. and Spurr, R.J., 1997. Ring effect studies: Rayleigh scattering, including molecular parameters for rotational Raman scattering, and the Fraunhofer spectrum. Applied Optics, 36(21), pp.5224-5230.

Che, H., Gui, K., Chen, Q., Zheng, Y., Yu, J., Sun, T., Zhang, X. and Shi, G., Calibration of the 936 nm water-vapour channel for the China aerosol remote sensing NETwork (CARSNET) and the effect of the retrieval water-vapour on aerosol optical property over Beijing, China. Atmospheric Pollution Research, 7(5), pp.743-753, 2016.

Churnside, J. H., T. A. Stermitz, and J. A. Schroeder, “Temperature Profiling with Neural Network Inversion of Microwave Radiometer Data,” Journal of Atmospheric and Oceanic Technology, 11, pp.105-109, 1994.

Cimini D. , J. A. Shaw, Y. Han, E. R. Westwater, V. Irisov, V. Leuski, and J. H. Churnside, “Air Temperature Profile and Air-Sea Temperature Difference Measurements by Infrared and Microwave Scanning Radiometers,” Radio Science, 38, 3, 8045, doi:10.1029/2002RS002632, 2003.

Colarco, P.R., Schoeberl, M.R., Doddridge, B.G., Marufu, L.T., Torres, O. and Welton, E.J., 2004. Transport of smoke from Canadian forest fires to the surface near Washington, DC: Injection height, entrainment, and optical properties. Journal of Geophysical Research: Atmospheres, 109(D6).

Corr CA, Krotkov N, Madronich S, Slusser JR, Holben B, Gao W, Flynn J, Lefer B, Kreidenweis SM , Retrieval of aerosol single scattering albedo at ultraviolet wavelengths at the T1 site during MILAGRO. Atmos Chem Phys, 2009, 9, 5813–5827. doi:10.5194/acp-9-5813-2009

Corr CA, Krotkov N, Madronich S, Slusser JR, Holben B, Gao W, Flynn J, Lefer B, Kreidenweis SM , Retrieval of aerosol single scattering albedo at ultraviolet wavelengths at the T1 site during MILAGRO. Atmos Chem Phys, 2009, 9, 5813–5827. doi:10.5194/acp-9-5813-2009

Corr, C. A., Krotkov, N., Madronich, S., Slusser, J. R., Holben, B., Gao, W., Flynn, J., Lefer, B., and Kreidenweis, S. M.: Retrieval of aerosol single scattering albedo at ultraviolet wavelengths at the T1 site during MILAGRO, Atmospheric Chemistry And Physics, 9, 5813-5827, 2009.

Crawford, J., Shetter, R.E., Lefer, B., Cantrell, C., Junkermann, W., Madronich, S. and Calvert, J., 2003. Cloud impacts on UV spectral actinic flux observed during the International Photolysis Frequency Measurement and Model Intercomparison (IPMMI). Journal of Geophysical Research: Atmospheres, 108(D16).

Dahlback, A. and Stamnes, K., 1991. A new spherical model for computing the radiation field available for photolysis and heating at twilight. Planetary and Space Science, 39(5), pp.671-683.

de Leeuw, G., et al., 2011: Production flux of sea spray aerosol. Rev. Geophys., 49, RG2001.

De Miguel, A., Román, R., Bilbao, J. and Mateos, D., 2011. Evolution of erythemal and total shortwave solar radiation in Valladolid, Spain: Effects of atmospheric factors. Journal of Atmospheric and Solar-Terrestrial Physics, 73(5-6), pp.578-586.

den Outer, P. N., Slaper, H., and Tax, R. B.: UV radiation in the Netherlands: Assessing long-term variability and trends in relation to ozone and clouds, J. Geophys. Res., 110, D02203, 10.1029/2004jd004824, 2005.

Derimian, Y., J.-F. Léon, O. Dubovik, I. Chiapello, D. Tanré, A. Sinyuk, F. Auriol, T. Podvin, G. Brogniez, and B. N. Holben, Radiative properties of aerosol mixture observed during the dry season 2006 over M'Bour, Senegal (African Monsoon Multidisciplinary Analysis campaign), J. Geophys. Res., 113, D00C09, doi:10.1029/2008JD009904, 2008.

Dickerson, R. R., Kondragunta, S., Stenchikov, G., Civerolo, K. L., Doddridge, B. G., and Holben, B. N.: The impact of aerosols on solar ultraviolet radiation and photochemical smog, Science, 278, 827-830, 1997.

Diémoz, H., Eleftheratos, K., Kazadzis, S., Amiridis, V. and Zerefos, C.S., 2016. Retrieval of aerosol optical depth in the visible range with a Brewer spectrophotometer in Athens. Atmospheric Measurement Techniques, 9(4), pp.1871-1888.

Diffey, B. L.: Solar Ultraviolet-Radiation Effects On Biological-Systems, Physics In Medicine And Biology, 36, 299-328, 1991.

Dobson, G.M.B. and Harrison, D.N., 1926. Measurements of the amount of ozone in the Earth's atmosphere and its relation to other geophysical conditions. Proc. R. Soc. Lond. A, 110(756), pp.660-693.

Dobson, G.M.B., 1956. Origin and distribution of the polyatomic molecules in the atmosphere. Proceedings of the Royal Society of London. Series A. Mathematical and Physical Sciences, 236(1205), pp.187-193.

Dubovik, O., A. Smirnov, B. N. Holben, M. D. King, Y. J. Kaufman, T. F. Eck, and I. Slutsker. "Accuracy assessments of aerosol optical properties retrieved from Aerosol Robotic Network (AERONET) Sun and sky radiance measurements." Journal of Geophysical Research: Atmospheres 105, no. D8 (2000): 9791-9806.

Dubovik, O., and King, M. D.: A flexible inversion algorithm for retrieval of aerosol optical properties from Sun and sky radiance measurements, Journal Of Geophysical Research-Atmospheres, 105, 20673-20696, 2000.

Dubovik, O., B. N. Holben, T. Lapyonok, A. Sinyuk, M. I. Mishchenko, P. Yang, and I. Slutsker, Non-spherical aerosol retrieval method employing light scattering by spheroids, Geophys. Res. Lett., 29(10), 1415, doi:10.1029/2001GL014506, 2002.

Dubovik, O., Holben, B., Eck, T.F., Smirnov, A., Kaufman, Y.J., King, M.D., Tanré, D. and Slutsker, I., 2002. Variability of absorption and optical properties of key aerosol types observed in worldwide locations. Journal of the atmospheric sciences, 59(3), pp.590-608.

Dutton, E. G., P. Reddy, S. Ryan, and J. J. DeLuisi, 1994: Features and effects of aerosol optical depth observed at Mauna Loa,Hawaii: 1982–1992.J. Geophys. Res.,99,8295–8306

Eck T. F., B. N. Holben, I. Slutsker, and A. Setzer, "Measurements of irradiance attenuation and estimation of aerosol single scattering albedo for biomass burning aerosols in Amazonia," J. Geophys. Res. 103, 31865–31878, 1998

Eck, T. F., Holben, B. N., Ward, D. E., Mukelabai, M. M.,Dubovik, O., Smirnov, A., Schafer, J. S., Hsu, N. C., Piketh,S. J., Queface, A., and Roux, J. L.: Variability of biomass burning aerosol optical characteristics in southern Africa duringthe SAFARI 2000 dry season campaign and a comparison of single scattering albedo estimates from radiometricmeasurements, J. Geophys. Res.-Atmos., 108, 2156–2202,doi:10.1029/2002JD002321, 2003.

Eck, T.F., Holben, B.N., Ward, D.E., Mukelabai, M.M., Dubovik, O., Smirnov, A., Schafer, J.S., Hsu, N.C., Piketh, S.J., Queface, A. and Roux, J.L., 2003. Variability of biomass burning aerosol optical characteristics in southern Africa during the SAFARI 2000 dry season campaign and a comparison of single scattering albedo estimates from radiometric measurements. Journal of Geophysical Research: Atmospheres, 108(D13).

Eck, T.F., Holben, B.N., Reid, J.S., Dubovik, O., Smirnov, A., O'Neill, N.T., Slutsker, I. and Kinne, S., "Wavelength dependence of the optical depth of biomass burning, urban and desert dust aerosols," J. Geophys. Res. 104, 31333–31350. 1999.

Egli, L., Gröbner, J., Köhler, U., Redondas, A., Carreño, V., and Henri Diemoz: A simulation-tool to model ozone retrieval uncertainties of Brewer and Dobsons instruments, UVNews 11, 36 – 41 http://metrology.tkk.fi/uvnet/reports.htm, (2016)

Elminir, H. K.: Sensitivity of ultraviolet solar radiation to anthropogenic air pollutants and weather conditions, Atmospheric Research, 84, 250-264, 29 January 2012, 2007.

Fioletov V.E.(2008) Ozone climatology, trends, and substances that control ozone, Atmosphere-Ocean,46:1, 39-67, DOI: 10.3137/ao.460103

Fioletov, V.E., McArthur, L.J.B., Kerr, J.B. and Wardle, D.I., 2001. Long-term variations of UV-B irradiance over Canada estimated from Brewer observations and derived from ozone and pyranometer measurements. Journal of Geophysical Research: Atmospheres, 106(D19), pp.23009-23027.

Fioletov, V.E., McLinden, C., Krotkov, N. and Li, C., 2015. Lifetimes and emissions of SO2 from point sources estimated from OMI. Geophysical Research Letters, 42(6), pp.1969-1976.

Fioletov, V.E., McLinden, C.A., Cede, A., Davies, J., Mihele, C., Netcheva, S., Li, S.M. and O'Brien, J., 2016. Sulfur dioxide (SO 2) vertical column density measurements by Pandora spectrometer over the Canadian oil sands. Atmospheric Measurement Techniques, 9(7), pp.2961-2976.

Flores, J. M., Washenfelder, R. A., Adler, G., Lee, H. J., Segev, L., Laskin, J., Laskin, A., Nizkorodov, S. A., Brown, S. S., and Rudich, Y.: Complex refractive indices in the near-ultraviolet spectral region of biogenic secondary organic aerosol aged with ammonia, Phys. Chem. Chem. Phys., 16, 10629–10642, doi:10.1039/C4cp01009d, 2014.

Fountoulakis, I., Redondas, A., Lakkala, K., Berjon , A., Bais, A. F., Doppler, L., Feister, U., Heikkila, A., Karppinen, T., Karhu, J. M., Koskela, T., Garane, K., Fragkos, K., and Savastiouk, V.: Temperature dependence of the Brewer global UV measurements, Atmos. Meas. Tech., 10, 4491-4505, https://doi.org/10.5194/amt-10-4491-2017, 2017

Fragkos, K., Bais, a. F., Balis, D., Meleti, C., & Koukouli, M. E. (2013). The Effect of Three Different Absorption Cross-Sections and their Temperature Dependence on Total Ozone Measured by a Mid-Latitude Brewer Spectrophotometer. Atmosphere-Ocean, 0(0), 1–10. doi:10.1080/07055900.2013.847816

Gao, W., Slusser, J., Gibson, J., Scott, G., Bigelow, D., Kerr, J., & McArthur, B. (2001). Direct-Sun column ozone retrieval by the ultraviolet multifilter rotating shadow-band radiometer and comparison with those from Brewer and Dobson spectrophotometers. Applied Optics, 40(19), 3149–55.

Garcia, A.R., Volkamer, R., Molina, L.T., Molina, M.J., Samuelson, J., Mellqvist, J., Galle, B., Herndon, S.C. and Kolb, C.E., 2006. Separation of emitted and photochemical formaldehyde in Mexico City using a statistical analysis and a new pair of gas-phase tracers. Atmospheric Chemistry and Physics, 6(12), pp.4545-4557.

GAW Report-No 231,Fourth WMO Filter Radiometer Comparison (FRC-IV) 28 September-16 October 2015; Davos ,Switzerland, https://library.wmo.int/opac/doc_num.php?explnum_id=3369, WMO, 2016

Gerasopoulos, E., Amiridis, V., Kazadzis, S., Kokkalis, P., Eleftheratos, K., Andreae, M. O., Andreae, T. W., El-Askary, H., and Zerefos, C. S.: Three-year ground based measurements of aerosol optical depth over the Eastern Mediterranean: the urban environment of Athens, Atmos. Chem. Phys., 11, 2145–2159, doi:10.5194/acp-11-2145-2011, 2011.

Gerasopoulos, E., Kokkalis, P., Amiridis, V., Liakakou, E., Perez, C., Haustein, K., Eleftheratos, K., Andreae, M. O., Andreae, T. W., and Zerefos, C. S.: Dust specific extinction cross-sections over the Eastern Mediterranean using the BSC-DREAM model and sun photometer data: The case of urban environments, Annales Geophysicae, 27, 2903-2912, 10.5194/angeo-27-2903-2009, 2009.

Gkikas, A., Basart, S., Hatzianastassiou, N., Marinou, E., Amiridis, V., Kazadzis, S., Pey, J., Querol, X., Jorba, O., Gassó, S. and Baldasano, J.M., 2016. Mediterranean intense desert dust outbreaks and their vertical structure based on remote sensing data. Atmospheric Chemistry and Physics, 16, pp.8609-8642.

Goering, C. D., L'Ecuyer, T. S., Stephens, G. L., Slusser, J. R., Scott, G., Davis, J., Barnard, J. C., and Madronich, S.: Simultaneous retrievals of column ozone and aerosol optical properties from direct and diffuse solar irradiance measurements, J. Geophys. Res., 110, D05204, 10.1029/2004jd005330, 2005.

Goetz, A.F., 2009. Three decades of hyperspectral remote sensing of the Earth: A personal view. Remote Sensing of Environment, 113, pp.S5-S16.

Green, R.O., Eastwood, M.L., Sarture, C.M., Chrien, T.G., Aronsson, M., Chippendale, B.J., Faust, J.A., Pavri, B.E., Chovit, C.J., Solis, M. and Olah, M.R., 1998. Imaging spectroscopy and the airborne visible/infrared imaging spectrometer (AVIRIS). Remote sensing of environment, 65(3), pp.227-248.

Green, R.O., Eastwood, M.L., Sarture, C.M., Chrien, T.G., Aronsson, M., Chippendale, B.J., Faust, J.A., Pavri, B.E., Chovit, C.J., Solis, M. and Olah, M.R., 1998. Imaging spectroscopy and the airborne visible/infrared imaging spectrometer (AVIRIS). Remote sensing of environment, 65(3), pp.227-248.

Gröbner, J., Kazadzis, S., Kouremeti, N., Doppler, L., Tagirov, R. and Shapiro, A.I., February. Spectral solar variations during the eclipse of March 20th, 2015 at two European sites. In AIP Conference Proceedings (Vol. 1810, No. 1, p. 080008). AIP Publishing, 2017a.

Gröbner, J., Kouremeti, N., Coulon, E., Durig, F., Gyo, M., Soder, R., Wasser, D., Spectroradiometer for Spectral Aerosol Optical Depth and Solar Irradiance Measurements, annual report PMOD/WRC, page 13, http://pmodwrc.ch/annual_report/2012_PMODWRC_Annual_Report.pdf, 2012.

Gröbner, J., Kouremeti, N., Nevas, S., Blattner, P., Characterisation Studies of Precision Solar Spectroradiometer, PMOD-WRC Annual Report 2014, p26 http://pmodwrc.ch/annual_report/2014_PMODWRC_Annual_Report.pdf, 2014

Gröbner, J., Kröger, I., Egli, L., Hülsen, G., Riechelmann, S. and Sperfeld, P., 2017. The high-resolution extraterrestrial solar spectrum (QASUMEFTS) determined from ground-based solar irradiance measurements. Atmospheric Measurement Techniques, 10(9), pp.3375-3383.

Gröbner, J., Kröger, I., Egli, L., Hülsen, G., Riechelmann, S., and Sperfeld, P.: The high-resolution extraterrestrial solar spectrum (QASUMEFTS) determined from ground-based solar irradiance measurements, Atmos. Meas. Tech., 10, 33753383,https://doi.org/10.5194/amt-10-3375-2017, 2017.

Gröbner, J., Kröger, I., Egli, L., Hülsen, G., Riechelmann, S., and Sperfeld, P.: The high-resolution extraterrestrial solar spectrum (QASUMEFTS) determined from ground-based solar irradiance measurements, Atmos. Meas. Tech., 10, 3375-3383, https://doi.org/10.5194/amt-10-3375-2017, 2017b.

Gröbner, J., N.Kouremeti, and D.Rembges: A systematic comparison of solar UV radiation spectra with radiative transfer calculations, 8th European Symposium on Physico-Chemical Behaviour of Air Pollutants, A Changing Atmosphere EC, ORA/POST 62172, 2001.

Güldner, J. and Spänkuch, D., Remote sensing of the thermodynamic state of the atmospheric boundary layer by ground-based microwave radiometry. Journal of Atmospheric and Oceanic Technology, 18(6), pp.925-933, 2001.

Güldner, J.: A model-based approach to adjust microwave observations for operational applications: results of a campaign at Munich Airport in winter 2011/2012, Atmos. Meas. Tech., 6, 2879-2891, doi:10.5194/amt-6-2879-2013, 2013.

Haberreiter, M., Delouille, V., Mampaey, B., Verbeeck, C., Del Zanna, G. and Wieman, S., 2014. Reconstruction of the solar EUV irradiance from 1996 to 2010 based on SOHO/EIT images. Journal of Space Weather and Space Climate, 4, p.A30.

Haberreiter, M., Delouille, V., Mampaey, B., Verbeeck, C., Del Zanna, G. and Wieman, S., 2014. Reconstruction of the solar EUV irradiance from 1996 to 2010 based on SOHO/EIT images. Journal of Space Weather and Space Climate, 4, p.A30.

Halthore, R.N., Eck, T.F., Holben, B.N. and Markham, B.L., , Sun photometric measurements of atmospheric water vapour column abundance in the 940-nm band. Journal of Geophysical Research: Atmospheres, 102(D4), pp.4343-4352, 1997.

Harder, J. W., Thuillier, G., Richard, E. C., Brown, S. W.,Lykke, K. R., Snow, M., McClintock, W. E., Fontenla, J. M.,Woods, T. N., and Pilewskie, P.: The SORCE SIM solar spectrum: comparison with recent observations, Sol. Phys., 263, 3–24, https://doi.org/10.1007/s11207-010-9555-y, 2010

Hartmann, D., Klein Tank, A., Rusticucci, M., Alexander, L., Brönnimann, S., Charabi, Y., Dentener, F., Dlugokencky, E., Easterling, D., Kaplan, A., Soden, B., Thorne, P.,Wild, M., and Zhai, P.: Observations: Atmosphere and Surface, in: Climate Change 2013: The Physical Science Basis. Contribution of Working Group I to the Fifth Assessment Report of the Intergovernmental Panel on Climate Change, edited by Stocker, T., Qin, D., Plattner, G., Tignor, M., Allen, S., Boschung, J., Nauels, A., Xia, Y., Bex, V., and Midgley, P., Cambridge University Press, Cambridge, United Kingdom and New York, NY, USA, 2013.

Holben, B. N., Eck, T. F., Slutsker, I., Tanre, D., Buis, J. P., Setzer, A., … Smirnov, A. (1998). AERONET — A Federated Instrument Network and Data Archive for Aerosol Characterization. Remote Sensing of Environment, 4257(98).

Holben, B. N., Eck, T. F., Slutsker, I., Tanré, D., Buis, J. P., Setzer, A., Vermote, E., Reagan, J. A., Kaufman, Y. J., Nakajima, T., Lavenu, F., Jankowiak, I., and Smirnov, A.: AERONET-A Federated Instrument Network and Data Archive for Aerosol Characterization, Remote Sens. Environ., 66, 1–16, 1998.

Holben, B. N., Tanré, D., Smirnov, A., Eck, T. F., Slutsker, I., Abuhassan, N., Newcomb, W. W., Schafer, J. S., Chatenet, B., Lavenu, F., Kaufman, Y. J., Castle, J. V., Setzer, A., Markham, B., Clark, D., Frouin, R., Halthore, R., Karneli, A., O'Neill, N. T., Pietras, C., Pinker, R. T., Voss, K., and Zibordi, G.: An emerging ground-based aerosol climatology: Aerosol optical depth from AERONET, J. Geophys. Res., 2001, 106, 12067–12097, https://doi.org/10.1029/2001JD900014.

Holben, B.N., Eck, T.F., Slutsker, I., Tanre, D., Buis, J.P., Setzer, A., Vermote, E., Reagan, J.A., Kaufman, Y.J., Nakajima, T. and Lavenu, F., AERONET—A federated instrument network and data archive for aerosol characterization. Remote sensing of environment, 1998, 66(1), pp.1-16.

Holben, B.N., Eck, T.F., Slutsker, I., Tanre, D., Buis, J.P., Setzer, A., Vermote, E., Reagan, J.A., Kaufman, Y.J., Nakajima, T. and Lavenu, F., 1998. AERONET—A federated instrument network and data archive for aerosol characterization. Remote sensing of environment, 66(1), pp.1-16.

Holben, B.N., Tanre, D., Smirnov, A., Eck, T.F., Slutsker, I., Abuhassan, N., Newcomb, W.W., Schafer, J.S., Chatenet, B., Lavenu, F. and Kaufman, Y.J., 2001. An emerging ground-based aerosol climatology: Aerosol optical depth from AERONET. Journal of Geophysical Research: Atmospheres, 106(D11), pp.12067-12097.

Hong L., Yunchanga C., Xiaominb W., Zhifangb X., Haishena W., Henga H., Meteorological applications of precipitable water vapour measurements retrieved by the national GNSS network of China, Geodesy and Geodynamics, vol 6 no 2, 135-142. http://dx.doi.org/10.1016/j.geog.2015.03.001, 2015.

Hoppel, W.A., 1967. Theory of the electrode effect. Journal of Atmospheric and Terrestrial Physics, 29(6), pp.709-721.

Hoppel, W.A., 1978. Determination of the aerosol size distribution from the mobility distribution of the charged fraction of aerosols. Journal of Aerosol Science, 9(1), pp.41-54.

Hoppel, W.A., Frick, G.M. and Larson, R.E., 1986. Effect of nonprecipitating clouds on the aerosol size distribution in the marine boundary layer. Geophysical Research Letters, 13(2), pp.125-128.

Hutchinson, T.C. and Whitby, L.M., 1977. The effects of acid rainfall and heavy metal particulates on a boreal forest ecosystem near the Sudbury smelting region of Canada. Water, Air, and Soil Pollution, 7(4), pp.421-438.

Ialongo, I., Buchard, V., Brogniez, C., Casale, G. R., and Siani, A. M.: Aerosol single scattering albedo retrieval in the UV range: An application to OMI satellite validation, Atmospheric Chemistry And Physics, 10, 331-340, 2010.

Ingold, T., Schmid, B., Matzler, C., Demoulin, P., & Kampfer, N, Modeled and empirical approaches for retrieving columnar water vapour from solar transmittance measurements in the 0.72, 0.82, and 0.94 mu m absorption bands. Journal of Geophysical Research., 105(D19), 24327–24343. http://doi.org/10.1029/2000JD900392, 2000.

IPCC, 2013: Climate Change 2013: The Physical Science Basis. Contribution of Working Group I to the Fifth Assessment Report of the Intergovernmental Panel on Climate Change [Stocker, T.F., D. Qin, G.K. Plattner, M. Tignor, S.K. Allen, J. Boschung, A. Nauels, Y. Xia, V. Bex and P.M. Midgley (eds.)]. Cambridge University Press, Cambridge, United Kingdom and New York, NY, USA, 1535 pp, doi:10.1017/CBO9781107415324.

IPCC: Climate Change 2013: The Physical Science Basis. Contribution of Working Group I to the Fifth Assessment Report of the Intergovernmental Panel on Climate Change, edited by: Stocker, T. F., Qin, D., Plattner, G. K., Tignor, M., Allen, S. K., Boschung, J., Nauels, A., Xia, Y., Bex, V., and Midgley, P. M., Cambridge University Press, Cambridge, United Kingdom and New York, NY, USA, 1535 pp., doi:10.1017/CBO9781107415324, 2013. Jacobson

Iqbal, M., 1983. An introduction to solar radiation. Elsevier.

Jackson, T.J., Chen, D., Cosh, M., Li, F., Anderson, M., Walthall, C., Doriaswamy, P. and Hunt, E.R., 2004. Vegetation water content mapping using Landsat data derived normalized difference water index for corn and soybeans. Remote Sensing of Environment, 92(4), pp.475-482.

Jacobson, M. Z. (1999), Isolating nitrated and aromatic aerosols and nitrated aromatic gases as sources of ultraviolet light absorption, J. Geophys. Res.,104, 3527–3542.

Jethva, H. and Torres, O.: Satellite-based evidence of wavelength-dependent aerosol absorption in biomass burning smoke inferred from Ozone Monitoring Instrument, Atmos. Chem. Phys., 2011, 11(20), 10541–10551, doi:10.5194/acp-11-10541-2011.

Jorgensen, D.P., Hildebrand, P.H. and Frush, C.L., 1983. Feasibility test of an airborne pulse-Doppler meteorological radar. Journal of Climate and Applied Meteorology, 22(5), pp.744-757.

Kalabokas, P.D., Viras, L.G. and Repapis, C.C., 1999. Analysis of the 11-year record (1987–1997) of air pollution measurements in Athens, Greece. Part I: Primary air pollutants. Global Nest: The International Journal, 1(3), pp.157-168.

Kassianov, E. I., Barnard, J. C., and Ackerman, T. P.: Retrieval of aerosol microphysical properties using surface MultiFilter Rotating Shadowband Radiometer (MFRSR) data: Modeling and observations, Journal of Geophysical Research D: Atmospheres, 110, 1-12, 10.1029/2004jd005337, 2005.

Kasten, F., 1966: A new table and approximation formula for the relative optical air mass, Arch.Meteo.Geophys.Bioklim Ser.B, 14, 206-223

Kasten, F., A new table and approximation formula for the relative optial air mass. Archiv für Meteorologie, Geophysik und Bioklimatologie, Serie B, 14(2), pp.206-223, 1965 .

Kato, S., Ackerman, T.P., Mather, J.H. and Clothiaux, E.E., 1999. The k-distribution method and correlated-k approximation for a shortwave radiative transfer model. Journal of Quantitative Spectroscopy and Radiative Transfer, 62(1), pp.109-121.

Kaufman, Y.J., Tanré, D. and Boucher, O., A satellite view of aerosols in the climate system ,Nature, 2002. 419(6903), p.215.

Kaufman, Y.J., Tanré, D., Gordon, H.R., Nakajima, T., Lenoble, J., Frouin, R., Grassl, H., Herman, B.M., King, M.D. and Teillet, P.M., 1997. Passive remote sensing of tropospheric aerosol and atmospheric correction for the aerosol effect. Journal of Geophysical Research: Atmospheres, 102(D14), pp.16815-16830.

Kaufmann, R.K. and Juselius, K., 2016. Testing competing forms of the Milankovitch hypothesis: A multivariate approach. Paleoceanography, 31(2), pp.286-297.

Kaufmann, R.K. and Juselius, K., 2016. Testing competing forms of the Milankovitch hypothesis: A multivariate approach. Paleoceanography, 31(2), pp.286-297.

Kaye JA, Hicks BB, Weatherhead EC, Long CS and Slusser JR, US interagency UV monitoring program established and operating, EOS (Wash. D.C.) 80 (10), 114-116, 1999

Kazadzis, S., Bais, A., Balis, D., Kouremeti, N., Zempila, M., Arola, A., Giannakaki, E., Amiridis, V., and Kazantzidis, A.: Spatial and temporal UV irradiance and aerosol variability within the area of an OMI satellite pixel, Atmospheric Chemistry And Physics, 9, 4593, 2009.

Kazadzis, S., Gröbner, J., Arola, A., and Amiridis, V.: The effect of the global UV irradiance measurement accuracy on the single scattering albedo retrieval, Atmos. Meas. Tech., 3, 1029-1037, 10.5194/amt-3-1029-2010, 2010.

Kazadzis, S., Kouremeti, N., Diémoz, H., Gröbner, J., Forgan, B. W., Campanelli, M., Estellés, V., Lantz, K., Michalsky, J., Carlund, T., Cuevas, E., Toledano, C., Becker, R., Nyeki, S., Kosmopoulos, P. G., Tatsiankou, V., Vuilleumier, L., Denn, F. M., Ohkawara, N., Ijima, O., Goloub, P., Raptis, P. I., Milner, M., Behrens, K., Barreto, A., Martucci, G., Hall, E., Wendell, J., Fabbri, B. E., and Wehrli, C.: Results from the 4th WMO Filter Radiometer Comparison for aerosol optical depth measurements, Atmos. Chem. Phys. Discuss., https://doi.org/10.5194/acp-2017-1105, in review, 2017.

Kazadzis, S., Kouremeti, N., Diémoz, H., Gröbner, J., Forgan, B.W., Campanelli, M., Estellés, V., Lantz, K., Michalsky, J., Carlund, T. and Cuevas, E., Results from the Fourth WMO Filter Radiometer Comparison for aerosol optical depth measurements. Atmospheric Chemistry and Physics, 2018, 18(5), pp.3185-3201.

Kazadzis, S., Raptis, P., Kouremeti, N., Amiridis, V., Arola, A., Gerasopoulos, E. and Schuster, G.L., Aerosol absorption retrieval at ultraviolet wavelengths in a complex environment, Atmospheric Measurement Techniques, 2016, 9(12), p.5997.

Kazadzis, S., Raptis, P., Kouremeti, N., Amiridis, V., Arola, A., Gerasopoulos, E. and Schuster, G.L., Aerosol absorption retrieval at ultraviolet wavelengths in a complex environment, Atmospheric Measurement Techniques, 2016, 9(12), p.5997.

Kerr, J.B. and Fioletov, V.E., 2008. Surface ultraviolet radiation. Atmosphere-ocean, 46(1), pp.159-184.

Kerr, J.B., Asbridge, I.A. and Evans, W.F.J., 1988. Intercomparison of total ozone measured by the Brewer and Dobson spectrophotometers at Toronto. Journal of Geophysical Research: Atmospheres, 93(D9), pp.11129-11140.

Kerr, J.B., McElroy, C.T. and Olafson, R.A., 1981. Measurements of ozone with the Brewer ozone spectrophotometer. In Quadrennial International Ozone Symposium, Boulder, CO (pp. 74-79).

Khatri, P., T. Takamura, T. Nakajima, V. Estellés, H. Irie, H. Kuze, M. Campanelli et al. "Factors for inconsistent aerosol single scattering albedo between SKYNET and AERONET." Journal of Geophysical Research: Atmospheres (2016).

King, M.D., Menzel, W.P., Kaufman, Y.J., Tanré, D., Gao, B.C., Platnick, S., Ackerman, S.A., Remer, L.A., Pincus, R. and Hubanks, P.A., 2003. Cloud and aerosol properties, precipitable water, and profiles of temperature and water vapour from MODIS. IEEE Transactions on Geoscience and Remote Sensing, 41(2), pp.442-458.

Kirchstetter, T. W., T. Novakov, and P. V. Hobbs, Evidence that the spectral dependence of light absorption by aerosols is affected by organic carbon, J. Geophys. Res., 109, D21208, doi:10.1029/2004JD004999, 2004.

Kirchstetter, T.W., Aguiar, J., Tonse, S., Fairley, D. and Novakov, T., 2008. Black carbon concentrations and diesel vehicle emission factors derived from coefficient of haze measurements in California: 1967–2003. Atmospheric Environment, 42(3), pp.480-491.

Kopp, G. and Lean, J.L., 2011. A new, lower value of total solar irradiance: Evidence and climate significance. Geophysical Research Letters, 38(1).

Kopp, G. and Lean, J.L., 2011. A new, lower value of total solar irradiance: Evidence and climate significance. Geophysical Research Letters, 38(1).

Kosmopoulos, P.G., Kazadzis, S., Taylor, M., Raptis, P.I., Keramitsoglou, I., Kiranoudis, C. and Bais, A.F., Assessment of surface solar irradiance derived from real-time modelling techniques and verification with ground-based measurements, Atmospheric Measurement Techniques,2018, 11(2), pp.907-924.

Kouremet, J., Blumthaler, M. and Ambach, W., 1996. Experimental investigation of spectral global irradiance measurement errors due to a non ideal cosine response. Geophysical research letters, 23(18), pp.2493-2496.

Kouremeti , J., and J. B. Kerr (2001), Ground-based determination of the spectral ultraviolet extraterrestrial solar irradiance: Providing a link between space-based and ground-based solar UV measurements, J. Geophys. Res., 106(D7), 7211–7217, doi:10.1029/2000JD900756.

Kouremeti, N., Gröbner, J., Doppler, L., Stability of the Precision Solar Spectroradiometer, PMOD-WRC Annual Report 2015, p40 http://pmodwrc.ch/annual_report/2015_PMODWRC_Annual_Report.pdf, 2015

Kouremeti, N., Gröbner, J., Spectral Aerosol Optical Depth from a Precision Spectroradiometer, PMOD-WRC Annual Report 2012, p33 http://pmodwrc.ch/annual_report/2012_PMODWRC_Annual_Report.pdf, 2012

Kouremeti, N., Gröbner, J., Spectral Aerosol Optical Depth From a Precision Solar Spectroradiometer During Three Field Campaigns, PMOD-WRC Annual Report 2014, p30 http://pmodwrc.ch/annual_report/2014_PMODWRC_Annual_Report.pdf, 2014

Krotkov ,N., Labow ,G., Herman,Slusser,Tree, R., Janson,G.,Durham, Eck,T., Holben,B., Aerosol column absorption measurements using co-located UV-MFRSR and AERONET CIMEL instruments. Proc. SPIE 7462, Ultraviolet and Visible Ground and Space-based Measurements, Trace Gases, Aerosols and Effects VI, 746205 (August 20, 2009); doi:10.1117/12.826880.

Krotkov, N. A., Bhartia, P. K., Herman, J. R., Fioletov, V., and Kerr, J.: Satellite estimation of spectral surface UV irradiance in the presence of tropospheric aerosols 1. Cloud-free case, Journal of Geophysical Research D: Atmospheres, 103, 8779-8793, 1998.

Krotkov, N. A., Bhartia, P. K., Herman, J. R., Slusser, J. R., Labow, G., Scott, G. R., Janson, G. T., Eck, T. F., and Holben, B. N.: Aerosol ultraviolet absorption experiment (2002 to 2004), part 1: ultraviolet multifilter rotating shadowband radiometer calibration and intercomparison with CIMEL sunphotometers, Opt. Eng., 2005 , 44, 041004, https://doi.org/10.1117/1.1886818.

Krotkov, N. A., Bhartia, P. K., Herman, J. R., Slusser, J., Scott, G., Labow, G., Eck, T.F , Holden, B. N. (2002). UV aerosol absorption experiment (2002-04): 1 . UV-MFRSR calibration and performance at GSFC, 1–24.

Krotkov, N. A., Bhartia, P. K., Herman, J., Slusser, J., Labow, G., Scott, G., Janson, G., Eck, T. F., and Holben, B.: Aerosol ultraviolet absorption experiment (2002 to 2004), part 1: Ultraviolet multifilter rotating shadowband radiometer calibration and intercomparison with CIMEL sunphotometers, Optical Engineering, 44, 1-17, 2005a.

Krotkov, N.A., Bhartia, P. K., Herman, J., Slusser, J., Scott, G., Labow, G., Vasilkov, A. P., Eck, T. F., Dubovik, O., and Holben, B. N.: Aerosol ultraviolet absorption experiment (2002 to 2004), part 2: Absorption optical thickness, refractive index, and single scattering albedo, Optical Engineering, 44, 1-17, 2005b.

Krueger, A.J., Walter, L.S., Bhartia, P.K., Schnetzler, C.C., Krotkov, N.A., Sprod, I.T. and Bluth, G.J.S., 1995. Volcanic sulfur dioxide measurements from the total ozone mapping spectrometer instruments. Journal of Geophysical Research: Atmospheres, 100(D7), pp.14057-14076.

Kudo, R., Uchiyama, A., Yamazaki, A., Kobayashi, E., and Nishizawa, T.: Retrieval of aerosol single-scattering properties from diffuse and direct irradiances: Numerical studies, J. Geophys. Res., 113, D09204, 10.1029/2007jd009239, 2008.

L. Harrison, J. Michalsky, and J. Berndt, "Automated Multi-Filter Rotating Shadowband Radiometer: An instrument for Optical Depth and Radiation Measurements", Appl. Optics, 33, 5118-5125, 1994.

Ledskam W.M. and D. H. Staelin, "An Extended Kalman-Bucy Filter for Atmospheric Temperature Profile Retrieval with a Passive Microwave Sounder," Journal of Applied Meteorology, 17, pp. 1023-1033,1978

Levelt, P. F., Oord, G. H. J. Van Den, Dobber, M. R., Mälkki, A., Visser, H., Vries, J. De, et al (2006). The Ozone Monitoring Instrument. IEEE Transaction on Geoscience and Remote Sensing, 44(5), 1093–1101.

Levy, R.C., 2009. The dark-land MODIS collection 5 aerosol retrieval: algorithm development and product evaluation. In Satellite aerosol remote sensing over land (pp. 19-68). Springer, Berlin, Heidelberg.

Li, C., Krotkov, N.A., Carn, S., Zhang, Y., Spurr, R.J. and Joiner, J., 2017. New-generation NASA Aura Ozone Monitoring Instrument (OMI) volcanic SO 2 dataset: Algorithm description, initial results, and continuation with the Suomi-NPP Ozone Mapping and Profiler Suite (OMPS). Atmospheric Measurement Techniques, 10(2), pp.445-458.

Lide, David R., ed. (2004). "Properties of the Solar System". CRC Handbook of Chemistry and Physics (85th ed.). CRC Press. p. 14-2. ISBN 9780849304859.

Liu S, AC Aiken, K Gorkowski, MK Dubey, CD Cappa, LR Williams, SC Herndon, P Massoli, EC Fortner, PS Chhabra, WA Brooks, TB Onasch, JT Jayne, DR Worsnop, S China, N Sharma, C Mazzoleni, L Xu, NL Ng, D Liu, JD Allan, JD Lee, ZL Fleming, C Mohr, P Zotter, S Szidat, and ASH Prévôt, Enhanced light absorption by mixed source black and brown carbon particles in UK winter, Nature Communications, 6, 8435, doi:10.1038/ncomms9435, 2015.

Logan, J.A., 1985. Tropospheric ozone: Seasonal behavior, trends, and anthropogenic influence. Journal of Geophysical Research: Atmospheres, 90(D6), pp.10463-10482.

Longo, B.M., Yang, W., Green, J.B., Crosby, F.L. and Crosby, V.L., 2010. Acute health effects associated with exposure to volcanic air pollution (vog) from increased activity at Kilauea Volcano in 2008. Journal of Toxicology and Environmental Health, Part A, 73(20), pp.1370-1381.

M. King and B. M. Herman, "Determination of the ground albedo and the index of absorption of atmospheric particles by remote sensing. Part I: Theory," J. Atmos. Sci. 36, 163–173. 1979

M. King, "Determination of the ground albedo and the index of absorption of atmospheric particles by remote sensing. Part II: Application," J. Atmos. Sci. 36, 1072–1083, 1979

Mäder, J. A., Staehelin, J., Brunner, D., Stahel, W. A., Wohltmann, I., & Peter, T. (2007). Statistical modeling of total ozone: Selection of appropriate explanatory variables. Journal of Geophysical Research: Atmospheres (1984–2012), 112(D11).

Marom E., "Rayleigh–Huygens Diffraction Formulas: Boundary Conditions and Validity of Approximations," J. Opt. Soc. Am. **57**, 1390_1-1392 (1967)

Marsaglia, G., W. Tsang, and J. Wang. "Evaluating Kolmogorov's Distribution." Journal of Statistical Software. Vol. 8, Issue 18, 2003.

Martins, J. V., Artaxo, P., Kaufman, Y. J., Castanho, A. D., and Remer, L. A.: Spectral absorption properties of aerosol particles from 350–2500 nm, Geophys. Res. Lett., 2009, 36, L13810, https://doi.org/10.1029/2009GL037435, .

Mayer, B., & Kylling, a. (2005). Technical note: The libRadtran software package for radiative transfer calculations – description and examples of use. Atmospheric Chemistry and Physics Discussions, 5, 1319–1381. doi:10.5194/acpd-5-1319-2005

Mayer, B., and Kylling, A.: Technical note: The libRadtran software package for radiative transfer calculations - Description and examples of use, Atmospheric Chemistry and Physics, 5, 1855-1877, 2005.

McCartney, E.J., 1976. Optics of the atmosphere: scattering by molecules and particles. New York, John Wiley and Sons, Inc., 1976. 421 p.

McCormick, M.P., Thomason, L.W. and Trepte, C.R., 1995. Atmospheric effects of the Mt Pinatubo eruption. Nature, 373(6513), p.399.

McPeters, R., Kroon, M., Labow, G., Brinksma, E., Balis, D., Petropavlovskikh, I., Veefkind, J.P., Bhartia, P.K. and Levelt, P.F., 2008. Validation of the Aura Ozone Monitoring Instrument total column ozone product. Journal of Geophysical Research: Atmospheres, 113(D15).

McPeters, R., Kroon, M., Labow, G., Brinksma, E., Balis, D., Petropavlovskikh, I., Veefkind, J.P., Bhartia, P.K. and Levelt, P.F., 2008. Validation of the Aura Ozone Monitoring Instrument total column ozone product. Journal of Geophysical Research: Atmospheres, 113(D15).

Medina, R., Fitzgerald, R. M., & Min, Q. (2012). Retrieval of the single scattering albedo in the El Paso-Juarez Airshed using the TUV model and a UV-MFRSR radiometer. Atmospheric Environment, 46, 430–440. doi:http://dx.doi.org/10.1016/j.atmosenv.2011.09.028

Meleti, C., Bais, A. F., Kazadzis, S., Kouremeti, N., Garane, K., & Zerefos, C. (2009). Factors affecting solar ultraviolet irradiance measured since 1990 at Thessaloniki, Greece. International Journal of Remote Sensing, 30(15-16), 4167-4179.

Michalsky, J.J. and Kiedron, P.W.,. Comparison of UV-RSS spectral measurements and TUV model runs for clear skies for the May 2003 ARM aerosol intensive observation period. Atmospheric Chemistry and Physics, 8(6), pp.1813-1821, 2008.

Michalsky, J.J., 1988. The astronomical almanac's algorithm for approximate solar position (1950–2050). Solar energy, 40(3), pp.227-235.

Michalsky, J.J., 1988. The astronomical almanac's algorithm for approximate solar position (1950–2050). Solar energy, 40(3), pp.227-235.

Mielonen, T., Arola, A., Komppula, M., Kukkonen, J., Koskinen, J., de Leeuw, G., and Lehtinen, K. E. J.: Comparison of CALIOP level 2 aerosol subtypes to aerosol types derived from AERONET inversion data, GEOPHYS. RES. LETT., 36, L18804, 10.1029/2009gl039609, 2009.

Millet, D.B., Jacob, D.J., Turquety, S., Hudman, R.C., Wu, S., Fried, A., Walega, J., Heikes, B.G., Blake, D.R., Singh, H.B. and Anderson, B.E., 2006. Formaldehyde distribution over North America: Implications for satellite retrievals of formaldehyde columns and isoprene emission. Journal of Geophysical Research: Atmospheres, 111(D24).

Miloshevich, L.M., Vömel, H., Whiteman, D.N. and Leblanc, T., Accuracy assessment and correction of Vaisala RS92 radiosonde water vapour measurements. Journal of Geophysical Research: Atmospheres, 114(D11), 2009

Mok, J., Krotkov, N.A., Arola, A., Torres, O., Jethva, H., Andrade, M., Labow, G., Eck, T.F., Li, Z., Dickerson, R.R. and Stenchikov, G.L.,. Impacts of brown carbon from biomass burning on surface UV and ozone photochemistry in the Amazon Basin. Scientific reports, 2016, 6,p.36940.

Mok, J., Krotkov, N.A., Torres, O., Jethva, H., Li, Z., Kim, J., Koo, J.H., Go, S., Irie, H., Labow, G. and Eck, T.F., Comparisons of spectral aerosol single scattering albedo in Seoul, South Korea, Atmospheric Measurement Techniques, 2018, 11(4), p.2295.

Moosmüller, H., J. P. Engelbrecht, M. Skiba, G. Frey, R. K. Chakrabarty, and W. P. Arnott (2012), Single scattering albedo of fine mineral dust aerosols controlled by iron concentration, J. Geophys. Res., 117, D11210, doi:10.1029/2011JD016909.

Müller, D., Wandinger, U., and Ansmann, A.: Microphysical particle parameters from extinction and backscatter lidar data by inversion with regularization: Simulation, Applied Optics, 38, 2358-2368, 1999.

Nakajima, T., Tonna, G., Rao, R., Boi, P., Kaufman, Y., & Holben, B. (1996). Use of sky brightness measurements from ground for remote sensing of particulate polydispersions. Applied Optics, 35(15), 2672-2686.

Nakajima, T., Tonna, G., Rao, R., Boi, P., Kaufman,Y., and Holben, B.: Use of sky brightness measurements from ground for remote sensing of particulate polydispersions, Appl. Optics, 1996 , 35, 2672– 2686, https://doi.org/10.1364/AO.35.002672.

Nakajima, T., Yoon, S.-C., Ramanathan, V., Shi, G.-Y., Takemura, T., Higurashi, A., Takamura, T., Aoki, K., Sohn, B.-J., Kim, S.-W., Tsuruta, H., Sugimoto, N., Shimizu, A., Tanimoto, H., Sawa, Y., Lin, N.-H., Lee, C.-T., Goto, D., and Schutgens, N.: Overview of the Atmospheric Brown Cloud East Asian Re- gional Experiment 2005 and a study of the aerosol direct radiative forcing in east Asia, J. Geophys. Res., 2007 , 112, D24S91, https://doi.org/10.1029/2007JD009009.

Nicolet, M., 1984: On the molecular scattering in the terrestrial atmosphere: An empirical formula for its calculation in the homosphere.Planet. Space Sci.,32,1467–1468.

Nikitidou, E., Kazantzidis, A., De Bock, V., De Backer, H., The aerosol forcing efficiency in the UV region and the estimation of single scattering albedo at a typical West European site, Atmospheric Environment (2013), doi: 10.1016/j.atmosenv.2012.12.035

Nyeki, S., Vuilleumier, L., Morland, J., Bokoye, A., Viatte, P., Mätzler, C., & Kämpfer, N. , A 10-year integrated atmospheric water vapour record using precision filter radiometers at two high-alpine sites. Geophysical Research Letters, 32(23), 1–4, http://doi.org/10.1029/2005GL024079 , 2005.

O'Neill, N.T., T.F.Eck, , A.Smirnov, B.N.Holben, and S.Thulasiraman, Spectral discrimination of coarse and fine mode optical depth, J. Geophys. Res., 108(D17), 4559, doi:10.1029/2002JD002975, 2003.

Omar, A. H., Won, J. G., Winker, D. M., Yoon, S. C., Dubovik, O., and McCormick, M. P.: Development of global aerosol models using cluster analysis of Aerosol Robotic Network (AERONET) measurements, Journal Of Geophysical Research-Atmospheres, J. Geophys. Res. 110: D10S14, doi: 10.1029/2004JD0048, 2005.

Paraskevopoulou, D., Liakakou, E., Gerasopoulos, E., Theodosi, C., & Mihalopoulos, N. (2014). Long-term characterization of organic and elemental carbon in the PM 2.5 fraction: the case of Athens, Greece. Atmospheric Chemistry and Physics, 14(23), 13313-13325.

Parrish, D. D., Law, K. S., Staehelin, J., Derwent, R., Cooper, O. R., Tanimoto, H., Volz-Thomas A, Glige S., Scheel H.E. , Streinbacher M and Chan E.(2013). Lower tropospheric ozone at northern midlatitudes: Changing seasonal cycle. Geophysical Research Letters, 40(8), 1631-1636.,DOI: 10.1002/grl.50303

Paur, R. J., and A. M. Bass. 1985. “The Ultraviolet Cross-Sections of Ozone: II. Results and Temperature Dependence.” In Atmospheric Ozone, edited by C. S. Zerefos and A. Ghazi, 611– 616. Dordrecht: Springer.

Penndorf, R., 1957: Tables of the refractive index for standard air and the Rayleigh scattering coefficient for the spectral region between 0.2 and 20.0M and their application to atmospheric optics.J. Opt. Soc. Amer.,47,176–182.

Petters, J. L., Saxena, V. K., Slusser, J. R., Wenny, B. N., and Madronich, S.: Aerosol single scattering albedo retrieved from measurements of surface UV irradiance and a radiative transfer model, Journal of Geophysical Research D: VOL. 108, NO. D9, 4288, doi:10.1029/2002JD002360, 2003.

Pöschl, U., et al., 2010: Rainforest aerosols as biogenic nuclei of clouds and precipitation in the Amazon. Science, 329, 1513–1516

Pöschl, U., Martin, S.T., Sinha, B., Chen, Q., Gunthe, S.S., Huffman, J.A., Borrmann, S., Farmer, D.K., Garland, R.M., Helas, G. and Jimenez, J.L., 2010. Rainforest aerosols as biogenic nuclei of clouds and precipitation in the Amazon. science, 329(5998), pp.1513-1516.

Pratt, R.W., Review of radiosonde humidity and temperature errors. Journal of Atmospheric and Oceanic Technology, 2(3), pp.404-407, 1985.

Pulli, T., Kärhä, P., Karppinen, T., Karhu j.m., Lakkala, K., Vaskuri, A., Shpak, M, and Mes, J.: Out-ofrange stray light characterization of single-monochromator Brewer spectrophotometer, UVNews 11, 20 – 23, http://metrology.tkk.fi/uvnet/reports.htm, (2016).

Randerson, J. T., Y. Chen, G. R. van der Werf, B. M. Rogers, and D. C. Morton, 2012: Global burned area and biomass burning emissions from small fires. J. Geophys. Res., 117, G04012.

Rayleigh, L., 1914. On the theory of long waves and bores. Proceedings of the Royal Society of London. Series A, Containing Papers of a Mathematical and Physical Character, 90(619), pp.324-328.

Redondas, a., Evans, R., Stuebi, R., Köhler, U., & Weber, M. (2014). Evaluation of the use of five laboratory-determined ozone absorption cross sections in Brewer and Dobson retrieval algorithms. Atmospheric Chemistry and Physics, 14(3), 1635–1648. doi:10.5194/acp-14-1635-2014

Reichard, J., U. Wandinger, M. Serwazi, and C. Weitkamp , Combined Raman lidar for aerosol, ozone and moisture measurements, Opt. Eng., 35, 1457–1465, 1996.

Reid, J. S. and Hobbs, P. V.: Physical and optical properties of young smoke from individual biomass fires in Brazil, J. Geophys. Res.-Atmos., 1998, 103, 32013–32030, 6448, 6457

Remer, L.A., Kaufman, Y.J., Tanré, D., Mattoo, S., Chu, D.A., Martins, J.V., Li, R.R., Ichoku, C., Levy, R.C., Kleidman, R.G. and Eck, T.F., 2005. The MODIS aerosol algorithm, products, and validation. Journal of the atmospheric sciences,2005, 62(4), pp.947-973.

Remer, L.A., Kleidman, R.G., Levy, R.C., Kaufman, Y.J., Tanré, D., Mattoo, S., Martins, J.V., Ichoku, C., Koren, I., Yu, H. and Holben, B.N., 2008. Global aerosol climatology from the MODIS satellite sensors. Journal of Geophysical Research: Atmospheres, 113(D14).

Reuder, J., and Schwander, H.: Aerosol effects on UV radiation in nonurban regions, Journal of Geophysical Research D: Atmospheres, 104, 4065-4077

Routh, S., Bhattacharya, A., Saha, S. and Kahyap, M., 2018. Propagation Characteristics of Acoustic Wave in Non-Isothermal Earth's Atmospheres. Mapana-Journal of Sciences, 17(1).

Russell, A.R., Valin, L.C. and Cohen, R.C., 2012. Trends in OMI NO 2 observations over the United States: effects of emission control technology and the economic recession. Atmospheric Chemistry and Physics, 12(24), pp.12197-12209.

Russell, P. B., Bergstrom, R. W., Shinozuka, Y., Clarke, A. D., DeCarlo, P. F., Jimenez, J. L., Livingston, J. M., Redemann, J., Dubovik, O., and Strawa, A.: Absorption Angstrom Exponent in AERONET and related data as an indicator of aerosol composition, Atmospheric Chemistry And Physics, 10, 1155-1169, 10.5194/acp-10-1155-2010, 2010.

Schmid, B. and Wehrli, C., 1995. Comparison of Sun photometer calibration by use of the Langley technique and the standard lamp. Applied Optics, 34(21), pp.4500-4512.

Schmid, B., Michalsky, J.J., Slater, D.W., Barnard, J.C., Halthore, R.N., Liljegren, J.C., Holben, B.N., Eck, T.F., Livingston, J.M., Russell, P.B. and Ingold, T., Comparison of columnar water-vapour measurements from solar transmittance methods. Applied Optics, 40(12), pp.1886-1896, 2001.

Schneider, M., Romero, P. M., Hase, F., Blumenstock, T., Cuevas, E., & Ramos, R., Continuous quality assessment of atmospheric water vapour measurement techniques: FTIR, Cimel, MFRSR, GPS, and Vaisala RS92. Atmospheric Measurement Techniques, 3(2), 323–338. http://doi.org/10.5194/amt-3-323-2010,2010.

Schuster, G. L., Dubovik, O., & Arola, A. (2016). Remote sensing of soot carbon – Part 1 : Distinguishing different absorbing aerosol species, 1565–1585. doi:10.5194/acp-16-1565-2016

Schwarz, J. P., Spackman, J. R., Gao, R. S., Watts, L. A., Stier, P., Schulz, M., Davis, S. M., Wofsy, S. C., and Fahey, D. W.: Global-scale black carbon profiles observed in the atmosphere and compared to. models, Geophys. Res. Lett., 2010, 37, L18812, doi:10.1029/2010GL044372.

Shi, Y., Zhang, J., Reid, J.S., Holben, B., Hyer, E.J. and Curtis, C., 2011. An analysis of the collection 5 MODIS over-ocean aerosol optical depth product for its implication in aerosol assimilation. Atmospheric Chemistry and Physics, 11(2), pp.557-565.

Skeie, R. B., Berntsen, T. K., Myhre, G., Tanaka, K., Kvalevåg, M. M., and Hoyle, C. R.: Anthropogenic radiative forcing time series from pre-industrial times until 2010, Atmos. Chem. Phys., 2011, 11, 11827–11857, doi:10.5194/acp-11-11827-2011.

Slusser, J., Gibson, J., Bigelow, D., Kolinski, D., Disterhoft, P., Lantz, K. and Beaubien, A., 2000. Langley method of calibrating UV filter radiometers. Journal of Geophysical Research: Atmospheres, 105(D4), pp.4841-4849.

Slusser, J., Gibson, J., Bigelow, D., Kolinski, D., Mou, W., Koenig, G., & Beaubien, a. (1999). Comparison of

column ozone retrievals by use of an UV multifilter rotating shadow-band radiometer with those from Brewer and Dobson spectrophotometers. Applied Optics, 38(9), 1543–51. Retrieved from http://www.ncbi.nlm.nih.gov/pubmed/18305778

Slusser, J., Labow, G., Scott, G., Krotkov, N., Bhartia, P. K., Eck, T. F., ... & Janson, G. (2005). Aerosol ultraviolet absorption experiment (2002 to 2004), part 1: Ultraviolet multifilter rotating shadowband radiometer calibration and intercomparison with CIMEL sunphotometers. Optical Engineering, 44(4), 041004-041004.

Smirnov, A, Holben, B.N., Lyapustin A., Slutsker, I. and Eck, T.F., AERONET processing algorithms refinement, AERONET Workshop, El Arenosillo, Spain , May 10 - 14, 2004.

Smirnov, A., Holben, B. N., Eck, T. F., Dubovik, O., & Slutsker, I. (2000). Cloud-screening and quality control algorithms for the AERONET database. Remote Sensing of Environment, 73(3), 337-349.

Smirnov, A., Holben, B.N., Eck, T.F., Dubovik, O. and Slutsker, I.,Cloud-screening and quality control algorithms for the AERONET database. Remote Sensing of Environment, 73(3), pp.337-349, 2000.

Soden, B. J., and J. R. Lanzante, An assessment of satelliteand radiosonde climatologies of upper-tropospheric water vapour, J. Climate, 9, 1235–1250, 1996.

Soden, B.J. and Held, I.M., An assessment of climate feedbacks in coupled ocean–atmosphere models. Journal of Climate, 19(14), pp.3, 2006.

Staehelin J., Kerr, J., Evans, R., and Vanicek, K.: Comparison of total ozone measurements of Dobson and Brewer spectrophotometers and recommended transfer functions, WMO TD No. 1147, No 149, 2003.

Staehelin J., Vogler C., Brönnimann S. (2009) The Long History of Ozone Measurements: Climatological Information Derived from Long Ozone Records. In: Zerefos C., Contopoulos G., Skalkeas G. (eds) Twenty Years of Ozone Decline. Springer, Dordrecht

Staehelin, J., Thudium, J., Buehler, R., Volz-Thomas, A. and Graber, W., 1994. Trends in surface ozone concentrations at Arosa (Switzerland). Atmospheric Environment, 28(1), pp.75-87.

Stenchikov, G., Robock, A., Ramaswamy, V., Schwarzkopf, M.D., Hamilton, K. and Ramachandran, S., 2002. Arctic Oscillation response to the 1991 Mount Pinatubo eruption: Effects of volcanic aerosols and ozone depletion. Journal of Geophysical Research: Atmospheres, 107(D24), pp.ACL-28.

Stohl, A., Andrews, E., Burkhart, J.F., Forster, C., Herber, A., Hoch, S.W., Kowal, D., Lunder, C., Mefford, T., Ogren, J.A. and Sharma, S., 2006. Pan-Arctic enhancements of light absorbing aerosol concentrations due to North American boreal forest fires during summer 2004. Journal of Geophysical Research: Atmospheres, 111(D22).

Stübi, R., Schill, H., Klausen, J., Vuilleumier, L., and Ruffieux, D.:Reproducibility of total ozone column monitoring by the Arosa Brewer spectrophotometer triad, J. Geophys. Res.-Atmos., 122,4735–4745, https://doi.org/10.1002/2016JD025735, 2017

Swinehart, D.F., The beer-lambert law. J. Chem. Educ, 39(7), p.333 , 1962.

Tanskanen, A., Lindfors, A., Määttä, A., Krotkov, N., Herman, J., Kaurola, J., Koskela, T., Lakkala, K., Fioletov, V., Bernhard, G., McKenzie, R., Kondo, Y., O'Neill, M., Slaper, H., den Outer, P., Bais, A. F., and Tamminen, J.: Validation of daily erythemal doses from Ozone Monitoring Instrument with ground-based UV measurement data, Validation of daily erythemal doses from ozone monitoring instrument with ground-based UV measurement data,~J. Geophys. Res., 112, D24S44, doi:10.1029/2007JD008830, 2007

Taylor, M., Kazadzis, S., Amiridis, V. and Kahn, R.A., 2015. Global aerosol mixtures and their multiyear and seasonal characteristics. Atmospheric environment, 116, pp.112-129.

Taylor, T. E., L'Ecuyer, T. S., Slusser, J. R., Stephens, G. L., and Goering, C. D.: An operational retrieval algorithm for determining aerosol optical properties in the ultraviolet, J. Geophys. Res., 113, D03201, 10.1029/2007jd008661, 2008.

Teillet, P. M., 1990: Rayleigh optical depth comparisons from various sources.Appl.Opt., 29,1897–1900

Teillet, P.M., Rayleigh optical depth comparisons from various sources. Applied Optics, 29(13), pp.1897-1900.354-3360, 1990.

Tomasi, C., Vitake, V. and De Santis, L.V., Relative optical mass functions for air, water vapour, ozone and nitrogen dioxide in atmospheric models presenting different latitudinal and seasonal conditions. Meteorology and Atmospheric Physics, 65(1), pp.11-30, 1998.

Torres, O., A. Tanskanen, B. Veihelmann, C. Ahn, R. Braak, P. K. Bhartia, P. Veefkind, and P. Levelt (2007), Aerosols and surface UV products from Ozone Monitoring Instrument observations: An overview, J. Geophys. Res., 112, D24S47,doi:10.1029/2007JD008809

Torres, O., Bhartia, P.K., Herman, J.R., Ahmad, Z. and Gleason, J., 1998. Derivation of aerosol properties from satellite measurements of backscattered ultraviolet radiation: Theoretical basis. Journal of Geophysical Research: Atmospheres, 103(D14), pp.17099-17110.

Tree , M R and Slusser , J, Comparison of column ozone retrievals obtained by UV multifilter rotating shadowband radiometer with those from Brewer and Dobson spectrophotometers, Proc. SPIE 5545, Ultraviolet Ground- and Space-based Measurements, Models, and Effects IV, 81 (October 14, 2004); doi:10.1117/12.562500; http://dx.doi.org/10.1117/12.562500

Trenberth, K.E., Fasullo, J. and Smith, L., 2005. Trends and variability in column-integrated atmospheric water vapour. Climate dynamics, 24(7-8), pp.741-758.

Turner, D. D., R. A. Ferrare, and L. A. Brasseur, 2001: Average aerosol extinction and water vapour profiles over the Southern Great Plains, Geophys. Res. Letters, 28, 4441 – 4444

Tzortziou, M., Herman, J.R., Cede, A., Loughner, C.P., Abuhassan, N. and Naik, S., 2015. Spatial and temporal variability of ozone and nitrogen dioxide over a major urban estuarine ecosystem. Journal of Atmospheric Chemistry, 72(3-4), pp.287-309.

UNEP, Van der Leun, J. C., Tang, X., and Tevini, M.: Environmental effects of ozone depletion: 1998 assessment, Journal of Photochemistry and Photobiology B: Biology, 46, 10.1016/s1011-1344(98)00195-x, 1998.

UNEP, Van Der Leun, J., Bornman, J. F., and Tang, X.: Environmental effects of ozone depletion and its interactions with climate change: 2006 Assessment, Photochem. Photobiol. Sci., 2007,6, 209-209, DOI: 10.1039/B700016B. 2007.

UNEP: Environmental effects of ozone depletion and its interactions with climate change: 2002 assessment, executive summary, Photochem. Photobio. S., 2, 1–4, 2003.

Van Weele, M., Martin, T. J., Blumthaler, M., Brogniez, C., Den Outer, P. N., Engelsen, O., Lenoble, J., Mayer, B., Pfister, G., Ruggaber, A., Walravens, B., Weihs, P., Gardiner, B. G., Gillotay, D., Haferl, D., Kylling, A., Seckmeyer, G., and Wauben, W. M. F.: From model intercomparison toward benchmark UV spectra for six real atmospheric cases, Journal of Geophysical Research D: Atmospheres, 105, 4915-4925, 2000.

Varotsos, C. a., Cracknell, A. P., & Tzanis, C. (2012). The exceptional ozone depletion over the Arctic in January–March 2011. Remote Sensing Letters, 343–352. doi:10.1080/01431161.2011.597792

Varotsos, C. a., Kondratyev, K. Y., & Cracknell, a. P. (2000). New evidence for ozone depletion over Athens, Greece. International Journal of Remote Sensing, 2951–2955. doi:10.1080/01431160050121366

Veefkind, J. P., J. F. de Haan, E. J. Brinksma, M. Kroon, and P. F. Levelt (2006), Total ozone from the Ozone Monitoring Instrument (OMI) using the OMI DOAS technique, IEEE Trans. Geosci. Remote Sens., 44(5), 1239–1244.

Veefkind, J.P., Aben, I., McMullan, K., Förster, H., De Vries, J., Otter, G., Claas, J., Eskes, H.J., De Haan, J.F., Kleipool, Q. and Van Weele, M., 2012. TROPOMI on the ESA Sentinel-5 Precursor: A GMES mission for global observations of the atmospheric composition for climate, air quality and ozone layer applications. Remote Sensing of Environment, 120, pp.70-83.

Vömel, H., Selkirk, H., Miloshevich, L., Valverde-Canossa, J., Valdés, J., Kyrö, E., Kivi, R., Stolz, W., Peng, G. and Diaz, J.A., Radiation dry bias of the Vaisala RS92 humidity sensor. Journal of Atmospheric and Oceanic Technology, 24(6), pp.953-963,2007.

Wallace, J.M. and Hobbs, P.V., 2006. Atmospheric science: an introductory survey (Vol. 92). Elsevier.

Wandinger, U., 2005. Raman lidar. In Lidar (pp. 241-271). Springer, New York, NY.

Wang, J., Zhang, L., Dai, A., Van Hove, T., and Van Baelen, J.: A near-global, 2-hourly dataset of atmospheric precipitable water from ground-based GPS measurements, J. Geophys. Res., 1 12, D11107, doi:10.1029/2006JD007529, 2007.

Ware, R., Carpenter, R., Güldner, J., Liljegren, J., Nehrkorn, T., Sol- heim, F., andVandenberghe, F.:Amulti-channel radiometric pro- filer of temperature, humidity and cloud liquid, Radio Sci., 38, 8079, doi:10.1029/2002RS002856, 2003.

Westwater, E. R., Crewell, S., Mätzler, C., and Cimini, D.: Principles of surface-based microwave and millimeter wave radio- metric remote sensing of the troposphere, Quaderni della Societa Italiana di Elettromagnetismo, 1, 50–90, 2005.

Wilson, S.R. and Forgan, B.W., 1995. In situ calibration technique for UV spectral radiometers. Applied optics, 34(24), pp.5475-5484.

WMO: Guide to meteorological instruments and methods of obser- vation, 6. Edn. WMO no. 8, Secretariat of the World Meteorological Organization, 1996

WMO: Scientific Assessment of Ozone Depletion: 2002. Global Ozone Research and Monitoring Project - Report No. 47, Geneva,Switzerland, 498 pp, 2003.

WMO/GAW Report No. 231, The Fourth WMO Filter Radiometer Comparison (FRC-IV), November 2016

WMO/GAW: Experts workshop on Global Surface-based Networkm for long term observations of column aerosol optical properties,Davos, Switzerland, 8–10 March 2004. GAW report No. 162,WMO TD No. 1287, 153 pp., available at: http://www.wmo.int/pages/prog/arep/gaw/gaw-reports.html (last access: 21 October 2016), 2005,

Wolfenbarger, J.K. and Seinfeld, J.H., 1990. Inversion of aerosol size distribution data. Journal of Aerosol Science, 21(2), pp.227-247.

World Meteorological Organization (WMO): Global ozone research and monitoring project, Tech. Rep. 50, Sci. Assess. of Ozone Depletion, Geneva, Switzerland, 2006

Yamamoto, G. and Tanaka, M., 1969. Determination of aerosol size distribution from spectral attenuation measurements. Applied optics, 8(2), pp.447-453.

Yu, H., Kaufman, Y. J., Chin, M., Feingold, G., Remer, L. A., Anderson, T. L., Balkanski, Y., Bellouin, N., Boucher, O., Christopher, S., DeCola, P., Kahn, R., Koch, D., Loeb, N., Reddy, M. S., Schulz, M., Takemura, T., and Zhou, M.: A review of measurement-based assessments of the aerosol direct radiative effect and forcing, Atmospheric Chemistry And Physics, 6, 613-666, 2006.

Yu, S., Alapaty, K., Mathur, R., Pleim, J., Zhang, Y., Nolte, C., Eder, B., Foley, K. and Nagashima, T., Attribution of the United States “warming hole”: Aerosol indirect effect and precipitable water vapour. Scientific reports, 4, 2014.

Zerefos C. S. , Kourtidis A. K., Melas D., Balis, D., Zanis P., Katsaros, L., Mantis H. T., et al (2002). Photochemical Activity and Solar Ultraviolet Radiation (PAUR) Modulation Factors: An overview of the project. Journal of Geophysical Research, 107(D18), 8134. doi:10.1029/2000JD000134

Zerefos, C. S. (2002). Long-term ozone and UV variations at Thessaloniki, Greece. Physics and Chemistry of the Earth, Parts A/B/C, 27(6-8), 455–460. doi:10.1016/S1474-7065(02)00026-8

Zerefos, C. S. and Eleftheratos, K.: The Atmospheric Environment Division of the Center of Environmental Health & Biophysics of the Biomedical Research Foundation of the Academy of Athens, in Bio Academy, A Quarterly Bulletin of the Biomedical Research Foundation, Academy of Athens, October–December 2007, Issue 1, 10–13, 2007.

Zerefos, C. S., Tourpali, K., Eleftheratos, K., Kazadzis, S., Meleti, C., Feister, U., Koskela, T., and Heikkilä, A.: Evidence of a possible turning point in solar UV-B over Canada, Europe and Japan, Atmospheric Chemistry And Physics, 12, 2469-2477, 10.5194/acp-12-2469-2012, 2012.

Zhao, T.L., Gong, S.L., Zhang, X.Y., Blanchet, J.P., McKendry, I.G. and Zhou, Z.J., 2006. A simulated climatology of Asian dust aerosol and its trans-Pacific transport. Part I: Mean climate and validation. Journal of Climate, 19(1), pp.88-103.

Ziemke, J.R., Chandra, S., Labow, G.J., Bhartia, P.K., Froidevaux, L. and Witte, J.C., 2011. A global climatology of tropospheric and stratospheric ozone derived from Aura OMI and MLS measurements. Atmospheric Chemistry and Physics, 11(17), pp.9237-9251.